ECOLOGICAL AND EVOLUTIONARY CONSEQUENCES OF EXOMETABOLITES FOR MICROBIAL INTERACTIONS

By

John Luke Chodkowski

A DISSERTATION

Submitted to
Michigan State University
in partial fulfillment of the requirements
for the degree of

Microbiology and Molecular Genetics – Doctor of Philosophy

2021

ABSTRACT

ECOLOGICAL AND EVOLUTIONARY CONSEQUENCES OF EXOMETABOLITES FOR MICROBIAL INTERACTIONS

By

John Luke Chodkowski

Interspecies interactions have fundamental roles in shaping microbial communities. Microbial community members can produce and release a diverse set of extracellular small molecules, collectively referred to as exometabolites. Interspecies interactions that result from exometabolites can alter the response and behaviors of microbial community members. This dissertation work demonstrates the establishment of a synthetic community system that facilitates the study of exometabolite-mediated interspecies interactions. This system was then used to understand the consequences of exometabolite-mediated interactions in a 3-member synthetic microbial community over stationary phase using a multi-omics approach. Lastly, an experimental evolution showed the consequences of long-term exometabolite interspecies interactions on the evolution of antibiotic resistance. This work advances knowledge on the dynamic response and behaviors of microbial community members' during non-growth states. This work also demonstrates how bacterial-bacterial interactions in a simple environment can lead to the emergence of antibiotic resistance.

This dissertation is dedicated to my sister, Nicole. Your passion for science inspired my pursuit of becoming a scientist.

ACKNOWLEDGEMENTS

I would first like to thank my family. To my mother, Susan Chodkowski, my father, William Chodkowski, and my sister, Nicole Chodkowski, you have all provided unwavering support during my graduate studies. Your collective encouragement motivated my efforts. I would also like to thank the friends I made during this journey. I am forever grateful for the times we shared.

I thank my committee members, Dr. Richard Lenski, Dr. George Mias, and Dr. Neal Hammer. Your constructive criticisms helped hone my research skills. I would also like to thank the entire Microbiology and Molecular Genetics Department for providing a welcoming and encouraging environment for scientific inquiry. I must also give a special shoutout to Roseann Bills. Thank you for keeping me on track.

To the Shade Lab members, past and present, I am grateful to have you as colleagues and friends. You all immensely supported my research and provided a welcoming environment for scientific engagement and discovery. I would especially like to thank my PhD mentor, Dr. Ashley Shade. I keenly remember watching your research presentation at the BMS research forum and being inspired to join your lab. I'm lucky that our paths aligned. Thank you for your guidance, your patience, and trust in me to develop a major arm in your research program. I have developed into the scientist I am today because of your mentorship.

TABLE OF CONTENTS

LIST OF TABLES

LIST OF FIGURES

KEY TO ABBREVIATIONS

AHL – Acyl-homoserine lactones

ANOVA – Analysis of variance

BiNGO - Biological Networks Gene Ontology tool

BLAST – Basic local alignment search tool

bp – Base pair

BSGC – Biosynthetic gene cluster

COG - Clusters of Orthologous Groups of proteins

CDS – Coding sequence

DCM - Dichloromethane

DNA – Deoxyribonucleic acid

dNTPs - Deoxynucleotide triphosphates

DOE JGI -Department of Energy Joint Genome Institute

gDNA – Genomic deoxyribonucleic acid

GNPS - Global Natural Product Social Molecular Networking

GO – Gene ontology

ITSD – Internal standard

kbp – kilobase pair

KEGG – Kyto encyclopedia of genes and genomes

LFC – log2 fold change

MIBig - Minimum Information about a Biosynthetic Gene cluster

MS – Mass spectrometry

MS/MS – Tandem mass spectrometry

MSI - Metabolomics Standards Initiative

NRPS – Nonribosomal Peptide Synthetases

PBS – Phosphate buffered saline

PCoA – Principal coordinates analysis

PCR – Polymerase chain reaction

PERMANOVA – Permutational multivariate analysis of variance

PKS - Polyketide synthase

RNA – Ribonucleic acid

rpm – Rotations per minute

RT-PCR – Reverse transcription polymerase chain reaction

TSA50 – 50% trypticase soy agar

TSB50 – 50% trypticase soy broth

UPLC-MS – Ultraperformance liquid chromatography mass spectrometry

CHAPTER 1 : Introduction

Overview

Microbes have numerous mechanisms to interact with surrounding neighbors (1). These interactions affect the functioning of microbial communities and ultimately, ecosystem processes. Extracellular chemical exchange is one method by which microbial interactions is facilitated. The production and release of these extracellular small molecules is referred to as the study of exometabolites (2). Exometabolites include both primary and secondary metabolites that are produced in response to the surrounding environment (4). Intra/Interspecies exometabolite exchanges result in ecological engagements that range from cooperative to competitive interactions (4). With technological advances in metabolite characterization, we are now capable of characterizing hundreds of metabolites from environments of interest (5). This has enabled researchers to study exometabolites in more complex environments and identify potentially novel compounds. Despite the development of new technologies for chemical characterization, we still lack simplistic experimental systems to study exometabolite-mediated interactions. In addition, knowledge gaps exist characterizing exometabolite production under physiologically relevant conditions and how exometabolite-mediated interaction alter population-level behaviors in a community setting. Lastly, limited knowledge is known in regard to the impact of exometabolite interactions on evolutionary outcomes. This dissertation established a new synthetic system to study exometabolite-mediated interactions. After establishment, the study system was then used to observe population-level and community outcomes resulting from exometabolite interactions. This was performed as a longitudinal study on ecological

timescales over the course of stationary phase. Finally, the evolutionary consequences of long-term exometabolite interactions was examined with implications for antibiotic resistance.

Classes of exometabolites and the interaction types they facilitate

Two broad classes of exometabolites exist- primary and secondary metabolites. Primary metabolites are directly involved in central metabolism. Thus, they are required for cell survival (see section below). Secondary metabolites, on the other hand, are not required for survival but aid in the survival of a microorganism through interactions with the surrounding environment. Primary metabolites are produced during exponential phase growth, when resources are converted to biomass production. As carrying capacity of a population is reached, due to nutrient exhaustion/inaccessibility or through waste product accumulation, microbial populations enter stationary phase. During this phase, molecules from primary metabolism are used as substrates to produce secondary metabolites. The enzymes responsible for the formation of secondary metabolites are organized as a cluster of genes referred to as a biosynthetic gene cluster (BSGC) (6). Aside from enzymes involved in the formation of a secondary metabolite, these clusters will also contain genes involved in molecule transport, regulation, and resistance genes such that a molecule does not become self-damaging. Once released into the environment, the collection of exometabolites can facilitate a range of interaction outcomes. Microbes can engage in various types of interactions. These interaction types are outlined in **Table 1.1** and described, below.

Table 1.1. Types of microbial interactions and exometabolites that facilitate them.

Ecological interaction	Effect on microbe 1	Effect on microbe 2	Exometabolite example
Mutualism	Beneficial	Beneficial	Nodulation factors
Synergism	Beneficial	Beneficial	Acyl homoserine lactones
Commensalism	Unaffected	Beneficial	SCFA
Predation	Harmful	Beneficial	H_2O_2
Amensalism	Unaffected	Harmful	Lactic acid
Competition	Beneficial/Harmful	Harmful	Antibiotics/Siderophores

Mutualism

Both members benefit from a mutualistic interaction and the presence of each member is necessary for their individual survival. A seminal example of this involves exometabolites that mediate cross-kingdom interactions. Legumes release flavonoids as root exudates. In response to the flavonoids, rhizobia secrete lipo-chitooligosaccharide exometabolites referred to as Nod factors. The mutual exchange of these exometabolites allow for successful root nodulation and the establishment of a plant-microbe symbiosis (7). Additional exometabolite exchanges are proposed between plants and their root microbiome (8).

Synergism

As with mutualism, both members benefit from the interaction but partner presence is not required for survival. Another classic example of exometabolite-mediated symbiosis involves the Hawaiian bobtail squid, *Euprymna scolopes* and *Aliivibrio fischeri*. *A. fishceri* is provided a nutrient-rich niche in the squid's light organ. In return, the population of *A. fishceri* creates a counter-illumination camouflage for the squid at night to protect it from predation (9). This anti-predation mechanism is achieved through *A. fishceri* bioluminescence via population-dependent quorum sensing. Acyl homoserine lactones (AHLs) serve as the exometabolite to active bioluminescence genes in *A. fishceri* (10).

Commensalism

Commensalism creates a benefit for one member while the other member, typically the exometabolite producer, is unaffected. In the developing infant gut, the establishment of

beneficial microbiota in early life is essential to the long-term health outcomes (11,12). Two species found in the infant gut include *Bifidobacterium longum subsp. infantis* and *Anaerostipes caccae. B. infantis* is able to metabolize carbohydrate sources provided in breast milk, such as human milk oligosaccharides (HMOs). *A. caccae* cannot grow on HMOs but can grow in co-culture with *B. infantis*. *B. infantis* facilitates *A. caccae* growth from short-chain fatty acid production (e.g. acetate and formate), produced as an exometabolite by-product of HMO fermentation (13). Commensalism can be found in most environments with complex carbon sources that create a trophic cascade of cross-feeding interactions (14-16).

Predation

Predation occurs when waste products from one microbe are metabolized by another microbe that in turn, creates an inhibitory exometabolite against the first microbe. This type of interaction is highlighted in the oral cavity. *Streptococcus mutans*, the microbe responsible for dental caries, produces lactate as a waste product from fermentable sugars scavenged from the host diet. *Streptococcus oligofermentans* converts *S. mutans*-produced lactate to hydrogen peroxide through the activity of lactate oxidase, resulting in the inhibition of *S. mutans* (17).

Amensalism

In amensalism, one microbe is harmed while the other, usually the producer of the exometabolite, is unaffected. Amensalism is commonly observed in scenarios involving fermentation. For example, the simultaneous production of lactic and lactobionic acids by *Lactobacillus casei* and *Pseudomonas taetrolens*, respectively, was studied for its industrial

potential to produce a synbiotic. When these microbes were co-cultured in residual cheese whey, it was observed that *P. taetrolens* was inhibited. Fermentation by-products, such as lactic acid, accumulated as an exometabolite to the extent that it prohibited *P. taetrolens* growth. The overall growth of *L. casei and* production of lactic acid was unaffected (18).

Competition

Competition can be beneficial to one microbe and harmful to the other or both microbes can be harmed by the interaction. In addition, two types of competition exist, exploitative and interference competition. In the former, exometabolites are released to scavenge resources from the environment and reduce resources to the opposing microbe. The production of siderophores represent an exometabolite that results in exploitative competition for iron (19). At one extreme, strain-specific siderophores and transport systems diverge within strains of the same species, creating exclusive, isogenic scavenging mechanisms (20). On the other hand, the siderophore producer may be at a competitive disadvantage if other microbes retain the transport mechanisms for siderophore production without the ability to produce the siderophore (21). Siderophore production also results in interspecies interactions, where the competitive depletion of iron can result in alterations in colony morphology (22).

In interference competition, microbes produce exometabolites that directly harm their neighbor. This is generally the case for the bioactivity associated with antibiotics (23). The competition sensing hypothesis suggests antibiotic production is closely tied to stressors associated with ecological competition. In other words, the stress regulatory networks that sense nutrient depletion and cell damage are commonly tied to antibiotic production while

this correlation is not observed with abiotic stressors such as heat and osmotic stress (24). Responding to biotic stressors through antibiotic production does not always guarantee success. For example, an antibiotic-receiver microbe may incur damage from a microbe initiates competition via antibiotic production. The receiver microbe can respond via upregulation of BSGCs but will be at a disadvantage if the BSGC repertoire possessed by the antibiotic-receiver does contain a bioactive molecule against the initiator. The antibiotic-initiator in this scenario benefits by expanding spatial growth and resource acquisition as a result of the growth detriment and/or lysis of the antibiotic-receiver. Competition can also result in mutual destruction. In response to damage from bacteriocins, closely related strains respond with a bacteriocin counter-attack to also inhibit their neighbor (25). The discovery of biosynthetic gene clusters and antibiotic resistance mechanisms in pristine environments provides credence to the importance of competition in the eco-evolutionary trajectories of microbial communities (26,27).

Other notable exometabolites that do not fulfill a specific ecological interaction

While most of the aforementioned exometabolites appear to serve a particular ecological engagement, other exometabolites have displayed a variety of bioactive versatility. One notable example are (cyclo)dipeptides. These are non-ribosomal peptides synthesized by either cyclodipeptides synthases (CDPSs) and non-ribosomal peptide synthetases (28). These exometabolites exhibit broad bioactivities relating to chemotactic responses (29), quorum-sensing (30), antimicrobial (31), anti-biofim (32), and cross-kingdom signaling for plant growth promotion (33). Dipeptides display a wide diversity of chemical structures

but diverse bioactivities are still observed from a single cyclodipeptide (e.g. quorum-sensing and cross kingdom signaling). The prospect of other exometabolite classes displaying various bioactivities is in the realm of possibility. It is likely that bioactivities may be better understood if microbes are studied in settings that best replicate their natural environment (34). Furthermore, bioprospecting natural environments is revealing the dearth of untapped biosynthetic potential of microbes (35). Advances in sequencing, isolation methods, and chemical characterization will expand the exometabolite field.

Methods for exometabolite characterization

Mass spectrometry (MS)

Mass spectrometry is an analytical technique used to measure the mass-to-charge ratio (m/z) of ions, representing a collection of compounds in a sample. The m/z can be used to determine the molecular weight of compounds and the quantity of these compounds. In addition, compounds fragmentation in MS can allow one to determine the structure of unknown compounds. There are three components to a mass spectrometer: 1) Ionization source 2) Mass analyzer 3) Ion detection system. For purposes of simplicity, work in this dissertation used mass spectrometer with electrospray ionization (ESI) and orbitrap technology. This will be described, below. See reviews for information on the array of ionization methods, mass analyzers, and detection systems used in mass spectrometry (36, 37, 38).

During electrospray ionization, charged ions in liquid phase are placed under high voltage to create an aerosol. The ions originally present in the solution enter in gas phase through solvent evaporation. Ions then enter the orbitrap, which functions as both a mass

analyzer and a detector. The orbitrap is composed of three parts: an inner spindle electrode and two concave outer electrodes. A linear electric field is created by placing a voltage potential between the inner and outer electrodes. Ions enter the orbitrap tangential to the inner electrode and at a particular potential, the ions will continuously spin around the inner electrode. The conical shape of the electrodes induces a harmonic axial oscillation of the ions. This oscillation is detected by the outer electrodes and a Fourier transform is used to convert this signal from a time domain to a frequency domain to obtain a mass spectrum. This displays the signal intensity of detected ions as a function of the mass-to-charge ratio (m/z), providing the relative abundance of compounds analyzed. The axial harmonic frequencies are proportional to the m/z of the ions (37). Chromatographic techniques can be performed prior to MS in order to provide better resolution of a complex mixture of compounds.

Liquid chromatography-MS (LC-MS): This is the most common method used for the analysis of samples containing a diversity of exometabolites. In LC-MS, metabolites are separated based on their affinity to a stationary column. Column choice reflects the types of exometabolites one want to observe. A C-18 or HILIC column can be used to separate and analyze nonpolar and polar exometabolites, respectively. The mobile phase containing separated exometabolites and then enters the mass spectrometer.

Gas chromatography-MS (GC-MS): Similar to LC-MS, GC-MS will separate exometabolites based on affinity to a stationary column. However, the stationary phase is coated on a hollow silica capillary column and the mobile phase contains a gas. Exometabolites analyzed in a GC-MS must have a low boiling point. In order to achieve this

range for analysis, exometabolites (e.g. sugar) will be derivatized prior to injection on the GC. Separated molecules will be analyzed on a mass spectrometer.

Capillary electrophoresis-MS (CE-MS): Exometabolites are separated based on electrophoretic mobility. High voltages are applied to separate ionic species. The size and charge of the exometabolite determines its retention time through the capillary. CE-MS provides a higher separation efficiency compared to LC or GC-MS but is highly sensitive to pH changes.

Imaging techniques

The previously mentioned techniques require considerable sample deconstruction to analyze the exometabolite profile. Destructive methods such as sample processing, solvent extraction, and chemical derivatization homogenizes the sample and hinders the possibility of both longitudinal and spatial exometabolite analysis. Imaging techniques allow for minimal sample processing in order to capture temporal and spatial resolution of exometabolite production. There are three methods for obtaining exometabolite ionization- desorption electrospray ionization (DESI), Matrix-assisted laser desorption/ionization (MALDI), and secondary ion mass spectrometry (SIMS). DESI uses a charged solvent to extract ions from the sample of interest. In MALDI, the sample is coated in a matrix and a laser beam is directed at the sample to generate ions. SIMS uses an ion beam bombardment on the surface of the sample, resulting in the generation of secondary ions. In all these techniques, the resulting ions are typically coupled to a mass spectrometer for exometabolite characterization (39).

Nuclear Magnetic Resonance (NMR) Spectroscopy

The principle of NMR is to use the magnetic properties of atomic nuclei to characterize compounds of interest (40). Atoms such as ^{1}H, ^{13}C, and ^{31}P are NMR active, but ^{1}H is most commonly for metabolomic studies. The sample is typically dissolved in a deuterated solvent, such as deuterated chloroform ($CDCl_3$), to minimize signal coming from the solvent. The sample is placed in a strong magnetic field which will cause nuclei to precess about the direction of the magnetic field (z-plane). Then, a short radio frequency (RF) pulse is applied perpendicular to the magnetic field, flipping the nuclei into in excited state in the xy-plane. The relaxation of the nuclei after the RF pulse releases energy as an exponentially decaying sine wave as the nuclei realign with the original magnetic field. This observed decay pattern is referred to as free-induction decay (FID). Nuclei in a compound will display different FIDs depending on the electron density in their chemical environment. A Fourier transform can convert the time domain data captured by the FID to a frequency domain. An NMR spectrum is then formed by plotting frequency against signal intensity. Thus, each compound will have unique NMR spectra that allows one to identify exometabolites in a sample. Simple sample preparation and fast analysis time make NMR a suitable choice for metabolomics experiments (41).

Approaches for studying exometabolite interactions in synthetic communities

Synthetic microbial communities are laboratory-scale assemblages of cultivable microbial isolates. This approach has become a suitable method to test and understand underlying principles of microbial community ecology (42). Prior to contemporary advances in sequencing methods and analytical techniques, microbiology was predominantly performed

with monocultures. With the advent of next-generation sequencing, it became possible to obtain the abundance and functional potential of environmental microbial communities (43). With respect to microbial ecology, synthetic communities allow for one to bridge the gap between the simplicity of monoculture experiments and the complication of deciphering the complexity of wild microbial communities. And now, with the innovations of -omics technologies, we have vastly expanded our abilities to understand causes and consequences for microbial interactions (44).

Systems for studying synthetic microbial communities are expanding. The underlying principle of these systems is that they are controllable and scalable. This allows a researcher to study select microbial isolates to disentangle how their interactions drive community dynamics and ultimately, their functions (45). Several synthetic systems of note have been deployed for use in the synthetic microbial ecology. In its simplest, yet effective form, individual wells of a 96-well plate can be mixed with different microbial isolates. Using this system, an ecological model was fit from temporal population dynamic data to conclude that pairwise interactions are major drivers of multi-species community dynamics (46). Unique systems, such as the kChip, have been purposely designed for rapid, massively parallel construction of synthetic communities. Their droplet platform enables combinatorial screening of ~10^5 synthetic microbial communities in a day (47). Bottom-up approaches facilitate causative associations between microbe-microbe interactions and their functional outcomes.

Unlike bottom-up approaches, top-down approaches can be used to study community assembly processes from native samples. Here, synthetic environments are created to observe how the environment affects community dynamics. For example, marine samples were

collected by Enke and colleagues to observe community succession dynamics on model polysaccharide particles (48). Enke and colleagues observed that marine microbial communities on model polysaccharide particles are organized in a simple trophic structure, from narrow-range degraders to broad-range consumers. Metabolic cross-feeding drives community successional dynamics, regardless of initial substrate. Importantly, these dynamics were different from the surrounding seawater, suggesting assembly processes were unique to the particle environment and the biotic interactions that emerged therein. Another top-down approach observed that microbial community structure converged at the family taxonomic level when provided single carbon sources, regardless of environmental origin (e.g. soil samples and plant leaf surfaces, 49). Ultimately, this reflected functional redundancy that was conserved at the family level. Informed from their initial top-down experiments, these researchers then assembled a bottom-up synthetic community to uncover how these species stably coexisted through metabolic cross-feeding of isolate secretions. Thus, both top-down and bottom-up are useful for uncovering broad assembly patterns and providing causation to observed phenomena, respectively.

Microbial communities can interact in a myriad of ways (1). Broadly, these interactions can be categorized as contact-dependent and contact-independent. The aforementioned synthetic community studies were not able to disentangle the contributions of these interactions methods to their experimental results. Therefore, additional study systems are also needed that focus on an interaction type of interest, such as those facilitated by exometabolites. One method to achieve this is using agar plates. Different isolates are spotted on agar in close vicinity such that colonies are physically separated but exometabolite

interactions are permitted. Imaging mass spectrometry can be used to understand the exometabolite exchanges at the interaction interface (50). A disadvantage of this approach is that it is low throughput and limited to a few interacting species. Alternatively, filters can be used in liquid medium to achieve the same purpose of only permitting exometabolite interactions. One such design created a co-culture plate to study pairwise interactions. Two chambers are separated by a semi-permeable membrane that allow for the diffusion of exometabolites between the chambers. The current design achieves 8 individual coculture chambers contained within the same dimensions as a 96-well plate. Blank and colleagues performed a proof of principle experiments coculturing *P. aeruginosa* and *Burkholderia cenocepacia* to show that *B. cenocepacia* is negatively impacted by the presence of *P. aeruginosa* (51). However, their system may be limited in terms of scalability (e.g. number of interacting isolates), and post-processing to obtain exometabolites. Thus, a simple synthetic community system that is scalable and minimizes post-processing efforts would be useful for research concerning how exometabolite interactions impact isolate behaviors and community functional dynamics.

Studying synthetic microbial communities under environmentally relevant lifestyles

Microbial molecular mechanisms and behavioral responses to stimuli have been largely studied in model organisms with exponentially growing populations. While these findings are essential to advance our understanding of microbial phenomena, microbes in particular environments exist in predominantly non-growth states. Thus, studying microbes in physiological states other than exponential phase may have more relevance to translating

laboratory findings to behaviors in the environment. For example, there are numerous examples of non-growth states such as stationary phase, long-term stationary phase (GASP phenotype), oxygen limitation, viable but non-culturable (VNBC), and persisters. Stationary phase is of interest for its common observance after exponential population growth. Details on other non-growth states are discussed in a review by Bergkessel and colleagues (52).

Stationary phase is a population-level phenomena following exponential phase growth where the carrying capacity is reached and the population abundance is relatively stable. The onset of stationary phase can result from a variety of factors such as nutrient depletion, nutrient inaccessibility, or feedback inhibition by metabolic waste products (53). Environments where stationary phase is the predominant lifestyle include soils (54), the human gut (55), and sequencing batch reactors (56). In these environments, prolonged periods starvation is punctuated with short bursts of nutrients. Thus, microbial populations in these environments predominantly exists in a stationary state.

Various molecular and physiological alterations occur at the onset of stationary phase. One major molecular alteration is the increase in sigma factor RpoS (σ^{38}), otherwise known as the stationary phase sigma factor (53). This sigma factor makes cells more adaptable and resistant to stressful conditions, such as nutrient stress. Another notable stationary phase protein is the leucine-responsive regulatory protein (Lrp). This acts as a global transcriptional regulator whose production is negatively correlated to growth rate (53). In *Escherichia coli*, it was found that ~75% of stationary phase induced genes were influenced by Lrp (57). These transcriptional alterations result in subsequent physiological alterations- the peptidoglycan layer increases in thickness, nucleoid condensation occurs for the protection of DNA, the

periplasmic space expands while the cytoplasmic space is condensed, overall protein synthesis decreases due to 100S hibernating ribosome via the dimerization of 70S subunits, truncated mRNA and deacylated tRNA accumulate, and cells become more spherical (58). Overall, coordinated transcriptional and translational events in stationary phase increase the survivability of microbial populations in a non-growth state by altering metabolism and the formation of stress-resistant cells (52).

Despite the tendency of stationary populations to shift towards stress-resistance and survival, these populations are still active. In fact, after entry into stationary phase, prolonged protein production in *E. coli* is maintained after several days (59). Alterations in metabolic activity are also associated with stationary phase. Energetically costly biomass metabolites were shown to accumulate in *E. coli* upon the induction of stationary phase by carbon-starvation (60). In line with this idea of metabolic alterations, bioactive metabolites, such as secondary metabolites, tend to be produced in stationary phase (53). An interesting concept, referred to as the competition sensing hypothesis, posits that bacterial transcriptional networks have evolved to sense and respond to ecological competition. This is evidenced by the fact that antibiotic production is linked to bacterial stress responses such as nutrient limitation and envelope damage (24). Thus, characterizing the exometabolomics response of microbes during stationary phase can unravel the nature dynamic interaction that can occur during periods of growth arrest.

Combining –omics to understand consequences for exometabolite interactions

The five major fields of -omics are genomics (61), transcriptomics (62), proteomics (63), metabolomics (64), and epigenomics (65). Each of these techniques provides a different view of the biological system in question. Combined with longitudinal studies, systems biology is moving toward being able to monitor, model, and predict the dynamics of complex biological systems (66). Furthermore, multiple studies are now integrating -omics to generate more translatable biological knowledge from their studies (67,68). Thus, multi-omics integration studies are a promising tool for the interpretation of biological systems (69,70).

Experimental evolution driven by microbial interactions

Experimental evolution has been instrumental for novel insights into evolutionary processes (71). Adaptive evolution experiments (72), in particular, can be beneficial to the study of the consequences of evolution via natural selection (e.g. antibiotic resistance). While much emphasis has been placed on the emergence of antibiotic resistance in clinical settings (73), bacteria in the environment display diverse antibiotic resistance mechanisms (74) resulting from bacterial warfare capabilities (75). Therefore, studying interspecies microbial interactions may provide insights into the coevolutionary processes shaping antibiotic resistance and antibiotic production.

Summary and aims

This dissertation aims to better understand the consequences of exometabolite interactions for microbial interactions at both ecological and evolutionary time scales. In Chapter 2, a new synthetic community system was established that facilitates experiments in Chapters 3 and 4. The new synthetic

community system is a 96-transwell plate where each well is fitted with a 0.22 μM filter bottom and a medium reservoir is fitted below the well plate. This physically separates cell populations but facilitates exometabolite-mediated interactions. The transwell systems is used in Chapter 3 to understand the transcriptomic and exometabolite dynamics of 3 microbial environmental strains in monocultures over stationary phase. In Chapter 4, these microbial environmental strains were then placed in each pairwise combination and in a 3-member synthetic community to understand the transcriptomic and metabolomic responses to interspecies interactions over stationary phase. In Chapter 5, bacterial strains were coevolved on agar plates at a distance that allowed for exometabolite interactions to occur. Genomics was used to uncover the genetic signatures to antibiotic resistance. Overall, this work advances knowledge on the dynamic interactions that can occur in microbial communities during periods of non-growth and the evolutionary repercussions to exometabolite-exchange.

CHAPTER 2 : A Synthetic Community System for Probing Microbial Interactions Driven by Exometabolites

Work presented in this chapter has been published as Chodkowski JL, Shade A. 2017. A Synthetic Community System for Probing Microbial Interactions Driven by Exometabolites. *mSystems* 2:e00129-17.

Abstract

Though most microorganisms live within a community, we have modest knowledge about microbial interactions and their implications for community properties and ecosystem functions. To advance understanding of microbial interactions, we describe a straightforward synthetic community system that can be used to interrogate exometabolite interactions among microorganisms. The filter plate system (also known as the Transwell system) physically separates microbial populations, but allows for chemical interactions via a shared medium reservoir. Exometabolites, including small molecules, extracellular enzymes, and antibiotics, are assayed from the reservoir using sensitive mass spectrometry. Community member outcomes, such as growth, productivity, and gene regulation, can be determined using flow cytometry, biomass measurements, and transcript analyses, respectively. The synthetic community design allows for determination of the consequences of microbiome diversity for emergent community properties and for functional changes over time or after perturbation. Because it is versatile, scalable, and accessible, this synthetic community system has the potential to practically advance knowledge of microbial interactions that occur within both natural and artificial communities.

Introduction

There is modest knowledge about how microorganisms interact with each other in their native habitats and whether these microbial interactions have implications for emergent community or ecosystem properties. Microorganisms can communicate chemically, and these

chemical interactions underlay a range of relationships from commensalism to antagonism (24, 76, 77). Because of the specificity of many microbe-microbe relationships, it is thought that most microorganisms produce certain chemical products only within a particular consortium (42, 45, 76, 78, 79). However, understanding of relatively well-described microbial interactions often is incomplete. For example, sensitive mass spectrometry was employed to discover new components of an interaction between *Bacillus subtilis* and *Streptomyces coelicolor* (45), which suggested that knowledge of this interaction was limited despite having been studied previously. Investigations of microbial exometabolite production have been predominantly focused on the analysis of a single taxon or pairs (80–82) of microbial taxa rather than on multimember profiling (83). However, the collective abilities of microbiomes to produce and exploit extracellular enzymes have been hypothesized to be key in discriminating situations in which microbial community structure has implications for ecosystem processes like carbon and nitrogen cycling (84, 85). These studies and others suggest that most microbial interactions remain obscure and that improved understanding of some of these interactions likely will provide important insights into microbial community functions.

Synthetic microbial systems recently have garnered reinvigorated interest because of their potential to address fundamental unknowns in microbial ecology, engineering, and systems and synthetic biology (42, 45, 86). Synthetic microbial systems are a key approach used in microbial ecology to understand how microbial interactions lead to emergent properties of communities, such as resistance and resilience (45). For example, synthetic communities have been assembled from marine waters onto artificial particles to observe community primary succession and the resulting functional changes in model heterotrophic particles (87) and

phototrophic biofilms (88), spatially constrained synthetic communities have been used to investigate reciprocal syntrophy (89), and computationally modeled synthetic communities have been applied to predict coculture growth given the metabolic needs of the members (90). Other recent work used a combination of metabolic flux analysis and multimember coculture to determine that the net outcome of complex interactions between an antagonist and a syntroph was not necessarily the sum of all expected pairwise outcomes, especially given particular spatial arrangements of the members (91). Other synthetic microbial systems are engineered to control and manipulate genetic circuitry toward required functions (92). These studies and others demonstrate that synthetic microbial communities can be applied in diverse and creative ways to provide insights into the dynamic biological and ecological interactions of microbiomes (93, 94), with the anticipation that these insights then can be applied to manage these communities toward desired outcomes.

We have developed a simple synthetic community system to interrogate exometabolite interactions among microbial community members. This synthetic community system permits direct investigation of chemical interactions among microorganisms via secondary metabolites, signaling molecules, and other exometabolites and allows for observation of behaviors that only occur when those microorganisms exist as part of a particular consortium. This system combines concepts and tools from systems biology, microbiology, biochemistry, genomics, and ecology and can provide both top-down and bottom-up approaches to investigate key questions in synthetic microbial ecology (45). Thus, it can advance understanding of microbial interactions within diverse natural and artificial microbiomes. It can also facilitate discovery of novel microbial products that are made given certain community memberships.

Materials and Methods

Filter plate preparation.

To prepare and use the filter plates for experiments, all protocols were performed using an aseptic technique in a biosafety level 2 cabinet. For the synthetic community experiments, we used sterile filter plates with 0.22-µm-pore polyvinylidene difluoride (PVDF) filter bottoms (Millipore MAGVS2210). These are also referred to as "Transwell plates" in the tissue culture literature. Prior to use, filter plates were washed three times with sterile water using a vacuum apparatus (NucleoVac 96 vacuum manifold; Clontech Laboratories). The filter of well H12 was removed with a sterile pipette tip and tweezer, and 31 ml of medium was added to the reservoir through well H12. Each well was then filled with 130 µl of culture or medium.

Validation of the synthetic community system by the quorum sensing experiment

We investigated the ability of quorum sensing molecules produced by populations arrayed in some wells to be sensed by nonproducing but receptive populations in other wells. Cv017 and Cv026 (**Table 2.1**) were inoculated in half-concentration Trypticase soy broth (TSB50) from overnight growth on half-concentration Trypticase soy agar (TSA50) in 3 replicate plates and grown at 29°C for 10 h. Cv017 was diluted to an optical density at 600 nm (OD_{600}) of 0.2, and Cv026 was diluted to an OD_{600} of 0.075. Dilutions were either inoculated into test tubes (monoculture control growth) or a filter plate containing TSB50. Wells from columns 1 to 4 were inoculated with 130 µl/well Cv017 culture, columns 5 to 8 were inoculated with 130 µl/well fresh TSB50, and columns 9 to 12 were inoculated with 130 µl/well Cv026 culture. Control cultures in test tubes were incubated at 29°C at 200 rpm (model 4353; Thermo

Scientific). After 16 h, cultures were flash-frozen in liquid nitrogen and stored at −80°C. Filter plates were incubated at 29°C with gentle shaking (0.32 relative centrifugal force [rcf]) for 26 h. After 26 h, 10 µl from 5 wells containing Cv026 and 10 µl from the shared medium reservoir were serially diluted (10^{-4}) and plated on TSA50 for 24 h at 29°C. The remaining Cv026-innoculated wells were pooled, flash-frozen in liquid nitrogen, and stored at −80°C.

Genomic DNA (gDNA) was used as a positive control in RT-PCR experiments. An overnight culture of Cv017 was grown in TSB50 at 29°C. Genomic DNA was isolated using the EZNA bacterial DNA kit (Omega Bio-Tek, Norcross, GA). We extracted RNA from the Cv017-Cv026 filter plate coculture experiment and from both test tube controls. RNA was isolated using the EZNA bacterial RNA kit (Omega Bio-Tek) according to the manufacturer's instructions and treated with RNase-free DNase (Qiagen). Purity of RNA was analyzed on a NanoDrop spectrophotometer using a 260/280 absorbance ratio and quantified using Qubit 2.0 (Life Technologies, Inc.).

Primers for *vioC* and *rpoB* were designed with Primer3 v.0.4.0 (116) using *C. violaceum* reference sequences from NCBI's GenBank (**Appendix A Table 2**). To confirm that the amplicon products were as expected, *vioC* and *rpoB* bands were excised from an agarose gel and purified using the Wizard SV gel and PCR clean-up system (Promega). Sanger sequencing was performed on the purified bands at the Michigan State Genomics Core using the forward and reverse primers from *vioC_Cv* and *rpoB_Cv*.

PCR was performed on extracted RNA to ensure proper DNase treatment using the *vioC_Cv* primers. Fifty nanograms of RNA from each sample was added to GoTaq Green 2×

master mix (containing buffer and enzyme; Promega), 0.5 µM forward and reverse primers, and nuclease-free water in a total volume of 25 µl/reaction. Thirty nanograms of Cv017 gDNA was used as a positive control and nuclease-free water as a negative PCR control. PCR conditions were as follows: 95°C for 5 min, 95°C for 15 s, 56°C for 15 s, and 72°C for 25 s, repeated 29 times from step 2, followed by 72°C for 10 min and hold at 7.4°C. Five microliters of each PCR product was run on 1% agarose gel containing 0.5× Tris-borate with EDTA (TBE) and ethidium bromide with a 100-bp DNA ladder (New England Biolabs). Electrophoresis was run for 50 min at 100 V. Gels were visualized by UV illumination.

Reverse transcription (RT) was performed using a Thermo Fisher Scientific high-capacity cDNA RT kit for both *vioC* and *rpoB* genes according to the manufacturer's instructions. Each RT reaction mixture contained ~1,500 ng template RNA, 0.625 µM reverse primer (**Appendix A Table 2**), 4 mM deoxynucleoside triphosphates (dNTPs), MultiScribe murine leukemia virus (MuLV) reverse transcriptase (50 U; Applied Biosystems), 1× RT buffer, and nuclease-free water in a total volume of 20 µl/reaction. An RT negative control was prepared for each primer using only nuclease-free water instead of template. The RT thermocycler conditions were as follows: 25°C for 10 min, 37°C for 2 h, and 85°C for 5 min, followed by hold at 4°C. cDNA was stored at −80°C.

Endpoint PCR was performed on cDNA after the reverse transcription reaction for both *vioC* and *rpoB* using the *Pfu* Turbo DNA polymerase kit (Agilent Technologies). Each reaction mixture contained 1 µl of RT product, 1× *Pfu* buffer, 0.2 mM dNTP, 1× *Pfu* DNA polymerase, 0.5 µM forward and reverse primers (**Appendix A Table 2**), and nuclease-free water in a total volume of 25 µl/reaction. Thirty nanograms of Cv017 gDNA was used as a

positive control, while a nuclease-free water sample served as a negative PCR control. The RT reaction without template DNA served as an additional negative control. PCR conditions for both primer sets were as follows: 95°C for 2 min, 95°C for 30 s, 56°C for 30 s, and 72°C for 45 s, repeated 29 times from step 2, followed by 72°C for 10 min and hold at 4°C. Twenty-five microliters of each PCR product was mixed with 6× loading dye (New England Biolabs) and run on 1% agarose gel containing 0.5× Tris-borate with EDTA (TBE) and ethidium bromide with a 100-bp DNA ladder (New England Biolabs). Electrophoresis was run for 50 min at 100 V. Gels were visualized by UV illumination.

Three-member synthetic community experiments

Experimental setup. Prior to initiating the synthetic community experiments, we characterized member growth curves to determine their compatibility in our experimental conditions. To perform the experiments, we diluted overnight cultures to concentrations that would allow the members to achieve stationary phase within 1 to 2 h of one another. Freezer stocks of *B. thailandensis*, *C. violaceum*, and *P. syringae* (**Table 2.1**) were plated on TSA50 at 28°C for 36 h. Isolated colonies were inoculated in 5 ml of M9–0.2% glucose medium and grown overnight at 28°C with gentle shaking. Overnight cultures of each strain were diluted 1:20 in fresh M9-glucose medium prior to inoculation in the filter plates (130 µl/well), and the medium reservoir was filled with 31 ml M9-glucose. Filter plates were prepared as described above. For each plate, a custom R script (RandomArray.R [see the GitHub repository]) was used to randomize community member placement in the wells so that each member occupied a total of 31 wells per plate. For each of four replicate time courses (where each time course included

five points assessed every 5 h over stationary phase), five replicate filter plates were prepared for destructive sampling. Filter plates were incubated at 28°C with gentle shaking (~0.32 rcf). The first plate was destructively sampled at 15 h, and each subsequent plate was destructively sampled every 5 h thereafter until 35 h. Spent medium (~31 ml) from the shared reservoir was flash-frozen in liquid nitrogen and stored at −80 °C prior to metabolite extraction.

Flow cytometry. Prior to analysis, live/dead gates were established using overnight cultures grown in in M9-glucose. Fifteen microliters of log-phase cells was placed in either 135 µl Tris-buffered saline (TBS; 20 mM Tris, 0.8% NaCl [pH 7.4]) (live) or 135 µl 70% isopropanol (dead) and incubated at room temperature for 10 min. Live and dead cells were then diluted an additional 100-fold (1,000-fold total dilution) and stained with the Thermo Scientific LIVE/DEAD BacLight bacterial viability kit at final concentrations of 1.5 µM Syto9 (live stain) and 2.5 µM propidium iodide (dead stain). Two hundred microliters of stained cultures was transferred to a 96-well microtiter U-bottom microplate (Thermo Scientific). Twenty microliters of sample was analyzed on a BD Accuri C6 flow cytometer (BD Biosciences) at a fluidics rate of 66 µl/min and a threshold of 500 on an FL2 gate. The instrument contained the following optical filters: FL1-533, 30 nm; FL2-585, 40 nm; and FL3, 670-nm longpass. Data were analyzed using BD Accuri C6 software version 1.0.264.21 (BD Biosciences). Live/dead gates are provided for each member (**Appendix B Figure 6**). Reproducibility in cell counts was assessed using the coefficient of variation (CV) in R.

After gates were established, we used live/dead staining of cells with flow cytometry to determine member population size from cells collected at each time point. For each member, five replicate wells containing spent culture were prepared for flow cytometry analysis. From

each well, 20 µl of culture was placed in 180 µl TSB. In plate arrangements where *P. syringae* was arrayed with *B. thailandensis*, *P. syringae* culture was diluted 70-fold in TBS. In plate arrangements where *P. syringae* was arrayed in monoculture or in coculture with *C. violaceum*, *P. syringae* was diluted 900-fold in TBS. Diluted cultures were stained and analyzed as described above. Flow cytometry analyses of both *B. thailandensis* and *C. violaceum* were prepared as described above, except that *B. thailandensis* was diluted 1,300-fold and *C. violaceum* was diluted 1,540-fold before staining.

Metabolite extraction and preparation. To prepare samples for nonpolar mass spectral analysis, 5-ml aliquots of spent medium from each filter plate medium reservoir and four M9-glucose medium controls were thawed on ice with 5 ml of 100% methanol. After thawing, solutions were transferred to glass separatory funnels that were initially washed with Liquinox (Alconox, Inc., New York, NY), rinsed with water, dried, and then rinsed three times with acetone. Three separate 5-ml liquid-liquid extractions were performed on each sample using dichloromethane, and then the combined volume of the organic layers from each extraction (15 ml) was pooled into a 50-ml canonical tube. The organic layer was dried under nitrogen (N2 evaporator system; Glas-Col). Samples were resuspended in 1.0 ml 65%:35% (vol/vol) acetonitrile–0.1% formic acid in water.

To prepare samples for polar mass spectral analysis, 2 ml of the aqueous layer from liquid-liquid extractions was evaporated using a Savant SVC 100H centrifugal evaporator. Dried samples were resuspended in 150 µl of methanol, sonicated (Branson M1800) for 30 min, further resuspended with the addition of 350 µl of acetonitrile, and centrifuged at 20,817 × *g* for 20 min, and the supernatant was filtered through a 0.22-µm-pore PVDF membrane.

Mass spectral analysis. Reverse-phase chromatography and mass detection of exometabolites were performed on a Waters Xevo G2-XS QTof UPLC–MS-MS instrument. For nonpolar UPLC analysis, 10 µl was injected into a C_{18} column (BEH Shield; 2.1 by 100 mm, 1.7-µm particle size; Waters, Milford, MA) maintained at 35°C. Samples were eluted at a flow rate of 0.3 ml/min under the following gradient conditions: 99% A–1% B for 1 min, followed by 1% to 99% B in 10 min, then hold at 99% B for 3 min before returning to the initial condition for 1 min. Mobile phase A consisted of 0.1% formic acid in water (pH 2.7), and mobile phase B consisted of acetonitrile. MS conditions were set as follows: mass range acquisition, 50 to 2,000 *m*/*z*; ionization mode, electrospray ionization negative (ESI^-) sensitivity mode; scan time, 0.5 s; collision energy, 6 eV; capillary voltage, 2.5 kV; sampling cone, 40 V; source temperature, 100°C; desolvation temperature, 350°C; cone gas flow, 50 liters/h; desolvation gas flow, 550 liters/h; and low mass (LM) resolution, 4.7. For accurate mass acquisition, a lock mass of leucine enkephalin ($[M - H]^-$ = 554.2615) was used. Twenty experimental samples (4 time series replicates and 5 time points/series) and 4 M9-glucose controls (1 for each time series) were analyzed twice as mass spectral replicates. All samples, including solvent blanks, were analyzed in a random order. In addition, a composite quality control (QC) sample was made by combining 50 µl from each experimental sample, including all biological replicates but excluding medium controls (45). A QC dilution series was prepared by diluting the QC sample 2-, 4-, and 8-fold. The QC sample was used to condition the column at the beginning of the mass spectral analysis (117) and to assess instrument stability at six time points over the course of the mass spectral analysis (117). The QC dilutions were analyzed at the end of the mass spectral analysis and were used to filter out noisy features as part of the data quality control prior to statistical

analysis (118). Raw Waters MS data files were converted to netCDF file format using MassLynx DataBridge software (Waters, Milford, MA).

Hydrophilic interaction liquid chromatography (HILIC) mass detection of exometabolites was performed on a Waters Xevo G2-XS quadrupole time of flight (QTOF) UPLC–MS-MS instrument. For polar UPLC analysis, 10 µl of each sample was injected into an HILIC column (Cortecs UPLC, 2.1 by 100 mm, 1.7-µm particle size; Waters, Milford, MA) maintained at 35°C. Samples were eluted at a flow rate of 0.3 ml/min under the following gradient conditions: 0% A–100% B for 1 min, 0% to 52.5% A in 13 min, hold at 52.5% A for 3 min before returning to the initial condition for 5 min. Mobile phase A consisted of 5 mM ammonium acetate in water (pH 3), and mobile phase B consisted of 95% acetonitrile–5% 5 mM ammonium acetate in water (pH 3). MS conditions were set as follows: mass range acquisition, 50 to 2,000 *m*/*z*; ionization mode, ESI^+ sensitivity mode; scan time, 0.1 s; collision energy, 6 eV; capillary voltage, 3.0 kV; sampling cone, 35 V; source temperature, 100°C; desolvation temperature, 350°C; cone gas flow, 25 liters/h; desolvation gas flow, 600 liters/h; and LM resolution, 4.7. For accurate mass acquisition, a lock mass of leucine enkephalin ($[M + H]^+ = 556.2771$) was used. Samples were analyzed in blocks of 4 time series replicates, starting with 35 h and decreasing sequentially to 15 h, followed by 4 medium control samples. A solvent blank was run between each block. Given the expectation of bactobolin accumulation through time (100), samples were analyzed in this order to ensure that there was no sample carryover in each subsequent block analyzed. The sample taken at 35 h from replicate 4 was chosen for MS-MS analysis to confirm the identification of bactobolin. For MS-MS analysis, similar UPLC conditions and MS conditions

were used with the following exceptions: MS set mass, 383.1; MS-MS range acquisition, 40 to 600 *m*/*z*; LM resolution, 17.0; and collision energy ramp, 20 to 80 eV.

Peak selection, quality control, and global analysis of nonpolar mass spectral data. mzMatch version 2.0-13 was used for metabolomics analysis (97). Fifty-seven mass spectral files were analyzed: 4 time series replicates, 5 time points/series, 2 mass spectral replicates/time point, 4 negative controls with 2 mass spectral replicates each, 6 QC samples, and 3 QC dilution series samples. First, XCMS version 1.48.0 was used within mzMatch for peak selection and retention time correction (96). Then, peak grouping, peak filling, and peak filtering steps were performed in mzMatch. Filtering steps included noise filtering, medium control removal, removal of features below and above the elution gradient (<0.5 min and >18 min of retention), and QC dilution series assessment. Pearson's correlation was used to assess congruence across dilutions for each feature and to determine if the experimental series for an undiluted feature was highly correlated with that of its 1:2, 1:4, and 1:8 dilutions (118). Features with a dilution series Pearson's *r* of <0.9 and/or *P* value of >0.05 had an irreproducible dilution trend and were removed (118). The resulting feature by sample matrix was converted from a .peakml file to a text file and was imported into R. The coefficient of variation (CV) was calculated in R to assess reproducibility of QC samples. Duplicate retention times were removed, features with a positive Pearson correlation coefficient from the QC dilution series were removed, and features with the greatest average abundances in the QC samples were removed. The three QC dilution series samples and medium control samples were omitted from the statistical analysis of differential patterns. Missing values were changed to half the minimum value, and labels were added to comply with the MetaboAnalyst data format (119).

The feature table was uploaded into MetaboAnalyst 3.0 (119). Raw feature intensity values from the quality-filtered data set were normalized using probabilistic quotient normalization (120) and $\log_2$ transformed (121). The resulting mass feature table was used for statistical analysis and visualization. We used principal-component analysis to explore global changes in metabolite profiles across samples. We tested for significant differences among time points using permutational multivariate analysis of variance (PERMANOVA) (122), implemented with the Adonis function in the vegan package (123). We first performed a global test with Adonis to determine as if there are any differences among any time points. If the global test was significant, *post hoc* pairwise tests between all time points were performed to determine which were different from each other (e.g., time 15 versus time 20). To correct for multiple comparisons, we used a false-discovery rate (FDR) adjustment to the *P* values for *post hoc* tests, using the p.adjust script from the base package in R (124). We used a Procrustes superimposition analysis to determine if replicate time series were coherent (98). This test was implemented with the PROTEST function in the vegan package (123). We used MetaboAnalyst to create a heat map to visualize feature changes over time. For the heat map, time point replicates were standardized with *Z* scores, and then features were averaged within a time point. A full heat map with each replicate as a separate column is provided in the supplemental material.

Bactobolin identification from polar mass spectral data. For MS analysis targeting bactobolin, polar mass spectral data from the HILIC analysis were used. Targeted peaks were detected in MZmine 2.17 with the following parameters: intensity tolerance, 10%; noise level, 50; *m*/*z* tolerance, 30 ppm; and retention time tolerance, 0.4 min. After peak detection, peak

extension was used with the following parameters: *m*/*z* tolerance, 30 ppm; and minimum height, 50. Selected peaks were joined into one data file using the join aligner function in MZmine, and peak areas were exported to a CSV file. The R package ggplot2 (125) was used to make a box plot tracking bactobolin accumulation through time.

For MS-MS analysis, the netCDF file was uploaded into MZmine to observe MS-MS fragments. Scan number 2405 was chosen to produce the fragment list provided in **Appendix A Table 1** because this MS-MS scan had the least parts per million errors for all fragments. Extracted ion chromatographic traces of bactobolin from the MS and MS-MS data files were generated in XCMS.

Availability of data.

Computing workflows (source code and input files) are available on GitHub (https://github.com/ShadeLab/PAPER_Chodkowski_mSystems_2017). Mass spectral data have been submitted to MetaboLights (http://www.ebi.ac.uk/metabolights/MTBLS525).

Results

Description of the synthetic community experimental system.

The apparatus of the experimental system is a sterile microtiter plate. In the plate, each well has a 0.22-µm-pore filter bottom and the plate fits into a shared medium reservoir. The pore size of the filters physically separates each member from its neighbors but permits resource and metabolite sharing through the reservoir. This allows for observation of outcomes

of chemical interactions between members. It is ready fabricated and commonly used for eukaryotic tissue culture. Any comparable product could be used for the synthetic community; we have used plates from Millipore (Darmstadt, Germany). Isolates from the habitat of interest are arrayed randomly into the plate, with a single member occupying each well at a known initial density or population size. The total number of wells occupied by an isolate can be used to calculate its proportional contribution to the total community. The plate, with its combination and arrangement of isolates, represents the level of the experimental unit and is replicated. The plates are incubated with gentle shaking to homogenize member access to media and exometabolites and to omit spatial effects (91). Because the filter bottom of one well is removed and used for transfer of media to the reservoir, as many as 95 unique members can be included in one consortium.

Observation of known microbial interactions in the system.

We demonstrate that relevant microbial molecules can pass through the filter membranes into the shared community reservoir. We asked if molecules made by bacteria arrayed into the plate could be produced in biologically relevant concentrations to impact other members. We paired *Chromobacterium violaceum* Cv017, a strain that produces acyl-homoserine lactone (AHL), with the AHL biosensor *C. violaceum* Cv026. Cv026 is a strain that lacks the ability to make AHLs but produces the purple pigment violacein when exogenous AHLs are sensed (95). The violacein gene cluster is regulated by quorum sensing. Controls showed that Cv026 did not produce violacein when grown alone, as no AHLs were produced to induce quorum sensing (**Figure 2.1A**). In triplicate, we arrayed each strain at opposite ends of a filter

plate, with several wells of uninoculated medium separating them. This was done to ensure that there was not spatial heterogeneity in molecule production or sensing, which was not expected given that the plates were incubated with gentle shaking. Cv026 produced violacein when arrayed in the filter plate system with Cv017, demonstrating that it could sense the AHLs produced by Cv017 (**Figure 2.1B**). After Cv026 produced violacein in the filter plates, wells containing Cv026 were serially diluted onto agar plates. All Cv026 colonies reverted to beige on the plate (**Figure 2.1C**). This showed that AHLs produced from Cv017 were necessary to induce violacein production in Cv026 in the filter plates and that there was no contamination of Cv017 or relevant mutations in Cv026. We confirmed this result by comparing endpoint reverse transcription (RT)-PCR of gene expression of *vioC* to that of the housekeeping gene *rpoB*. We compared gene expression in the filter plate coculture with the test tube monoculture for Cv026 and Cv017 (**Appendix B Figure 1**). This experiment showed that the synthetic community system reproduces microbial production and sensing of small molecules relevant for known microbial interactions.

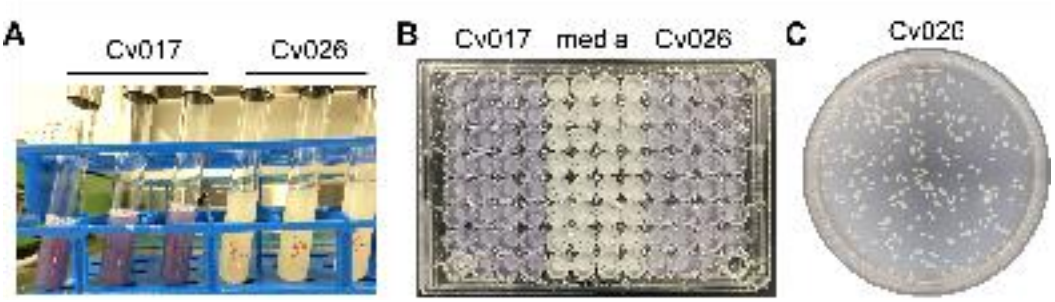

Figure 2.1. The filter plate system reproduces known microbial interactions facilitated by exometabolites.

A) Control. The *Chromobacterium violaceum* mutant strain Cv026 cannot produce acyl-homoserine lactones (AHLs), while strain Cv017 can. AHLs trigger production of the purple pigment violacein. **B)** AHLs from Cv017 diffused through wells to induce quorum sensing and violacein production in Cv026. **C)** Colonies of Cv026, diluted from the Transwells in panel B and plated, reverted color in the absence of exogenous AHLs.

System measurements.

Both community and member-specific parameters of the system can be measured to interpret the community outcomes. At the community level, the primary data collected are untargeted exometabolite profiles of molecules extracted from the shared medium reservoir. These profiles serve as readout of direct functional output and are relevant for member interactions. The exometabolite extraction protocol will depend on the molecules of interest (e.g., signaling molecules, small peptides, extracellular enzymes, antibiotics, etc.). Alternatively, a "global" approach could be used with multiple extraction solvents and mass spectral conditions to capture a breadth of molecules. Ecological and functional community properties can be quantified as appropriate for the scientific question.

Member-specific data can also be collected from the synthetic system. As a proxy for member success in the system, growth and viability can be determined using either live/dead staining with flow cytometry or dilution to extinction of plated well contents. As a measurement of member production, biomass can be assessed. At the end of the experiment, planktonic cells can be vacuumed onto the filters, and then the collection of filters for each member can be excised, dried, and weighed with a microbalance. Alternatively, total protein accumulation could be assayed per well. Growth and biomass are quantified relative to control conditions within the experimental design. To couple regulation with functional output, member transcript sequencing can be performed to explore linkages between gene regulation and exometabolite production. Transcript data also can inform the upregulation of cryptic pathways or help to identify exometabolites from the untargeted analysis. Biomass for each member can be removed from wells by pipetting and then combined and flash-frozen for RNA

extraction. Optimally, member genome sequences would be available to be used as references for transcript assembly and analysis.

Demonstration.

We demonstrated the use of the synthetic community system with a three-member community comprised of common environmental strains: *Burkholderia thailendensis* E264, *C. violaceum* SC11,368, and *Pseudomonas syringae* DC3000 (**Table 2.1**). The members were randomly arrayed in a filter plate and each occupied 31 wells so that the community was even. Over 15 to 35 h in stationary phase, we extracted shared community metabolites from the medium reservoir every 5 h and performed liquid-liquid extraction to separate the nonpolar and polar phases. Nonpolar metabolites were analyzed by ultraperformance liquid chromatography-mass spectrometry (UPLC-MS). Peak picking and retention time alignment from the UPLC-MS data set was performed in XCMS (96), and additional quality filtering steps were performed in mzMatch (97). After quality filtering, there were 977 features in the nonpolar profile. Mass spectral replicates were reproducible (**Figure 2.2**); median Pearson's r = 0.98; range, 0.96 to 0.99; all P values of <0.0001). As expected, our quality control (QC) samples had similar profiles even though they were analyzed at different times over the mass spectral operation (**Appendix B Figure 2**; median coefficient of variation [CV], 2.62%; range, 0.45 to 12.10%). QC samples represented an average of all other profiles (**Figure 2.2**). These data show that the synthetic community system offers experimental consistency in mass spectral results.

Table 2.1. Strains used in this study

Strains	*Genotype*	*Reference*
SC 11,378	Wild-type *Chromobacterium violaceum ATCC 31532 (WTCV)*	Wells, J. S. *et al.* 1982 (ref. (127))
Cv017	Sm^r mini-Tn*5* Hg^r Derivative of SC 11,378	Chernin, L. S. *et al.* 1998 (ref. (128))
Cv026	Sm^r mini-Tn*5* Hg^r *cviI*::Tn*5xylE* Km^r Derivative of Cv017	McClean K. H. *et al.* 1997 (ref. (95))
E264	Wild-type *Burkholderia thailandensis* ATCC 700388	Brett, P. J. *et al.* 1998 (ref. (129))
DC3000	Wild-type *Pseudomonas syringae* ATCC BAA-871	Buell, C. R. *et al.* 2003 (ref. (130))

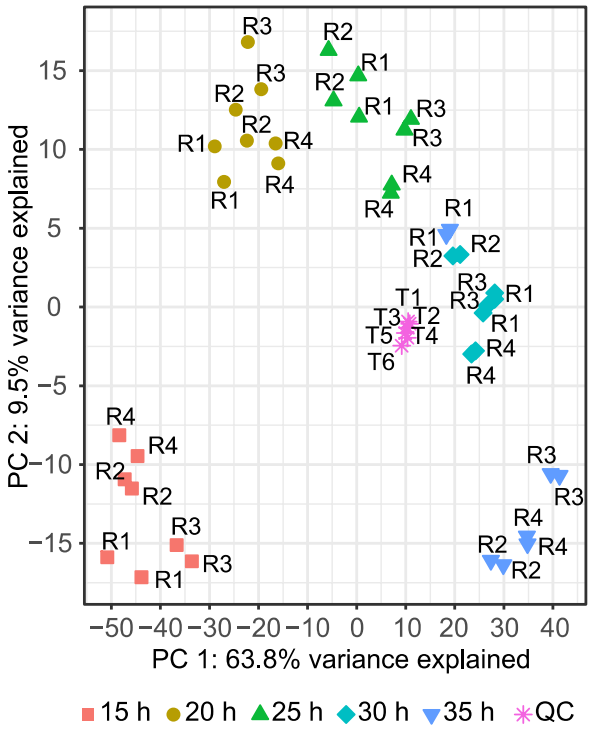

Figure 2.2. Global exometabolite changes in a three-member community compared across time and with mass spectral replication.

Shown are results from principal-component analysis (PCA) of normalized, $\log_2$-transformed mass spectral profiles. Profiles are colored by time and labeled by replicate (R1 to R4). Quality control series (QC), a composite of all experimental samples, are labeled by analysis order (T1 to T6). A total of 977 mass features were included after quality filtering.

We observed directional changes in the three-member community's nonpolar exometabolite profile over time, explained by axis 1 in the principal-component analysis (PCA) (**Figure 2.2**). There was high reproducibility in the metabolite profile changes with time across the four independent time series (PROTEST [98]; all pairwise r^2 values of ≥0.938, all P values of ≤0.025). Thus, our results show that replicate time series were synchronous. There also were clear differences in metabolite profiles with time, as each time point had distinct profiles (global Adonis $r^2 = 0.758$, $P \leq 0.01$, all pairwise false discovery rate [FDR]-adjusted P values of ≤0.05). An exception was the 30- and 35-h profiles, which were not statistically distinct (FDR-adjusted $P = 0.41$). These results generally show that the system is robust and can facilitate observations of biologically induced changes in community exometabolites.

To observe the common temporal patterns of features, a heat map was created using Ward's clustering algorithm with Euclidean distances from *Z*-scored data **(Figure 2.3**). We observed both decreases in existing features (clusters A and B) and production of new features over time (clusters D, E, and F). There were also some features that were enriched in early or mid-time points (i.e., in cluster C and in cluster E at 20 to 25 h, respectively). There were a few features that had variable dynamics, such as in cluster A. While it is outside the scope of this work to identify each of these features, these overarching patterns demonstrate that there are biological changes occurring in the three-member community's exometabolite profile over time that are attributable to member production as well as medium depletion. A heat map including all replicates is provided in **Appendix B Figure 3**.

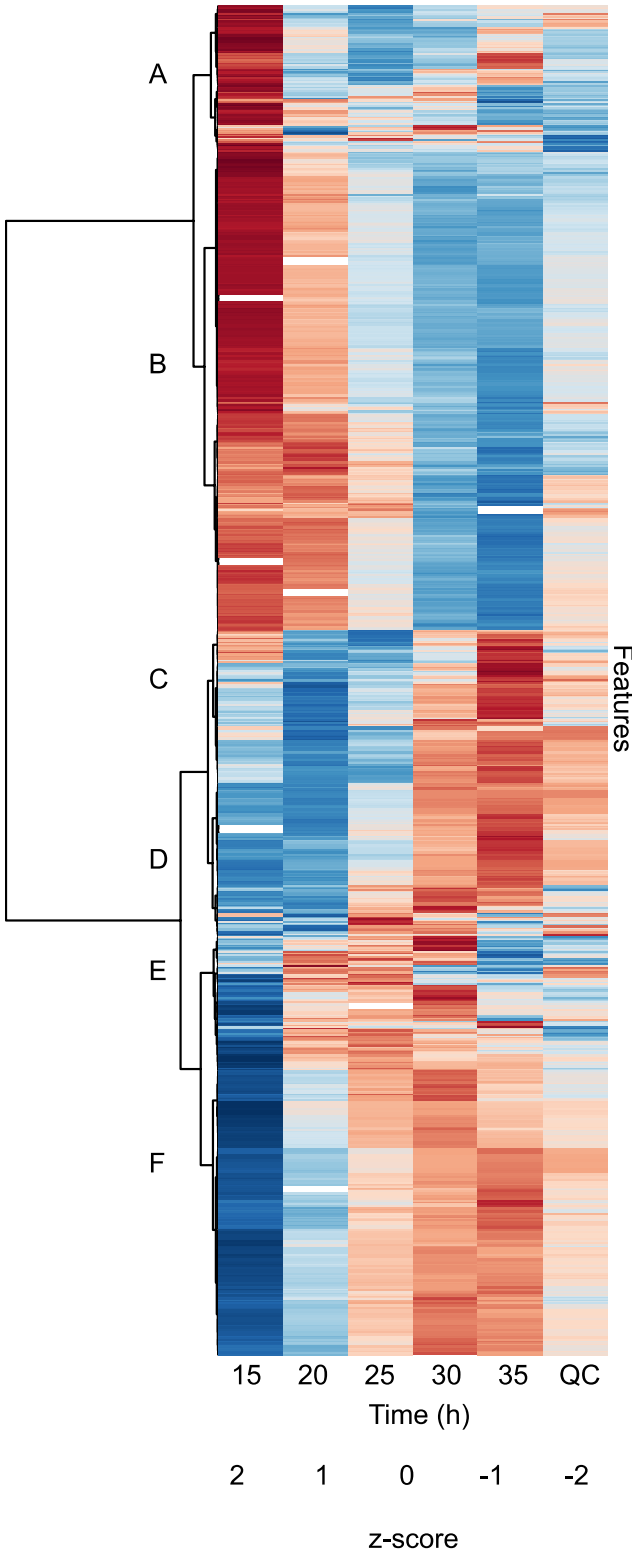

Figure 2.3. Exometabolites exhibit directional changes over stationary phase in a three-member synthetic microbial community.

Figure 2.3 (cont'd)

Shown is a heat map of 977 mass feature changes over time within a three-member community, where samples are columns and features are rows. Each sample is the average of four time point replicates, each started independently from new cultures. Euclidean distance was calculated from Z-scored mass spectral profiles. Features with similar dynamics were clustered by Ward's method. Letter designations for clusters were added post hoc to aid in discussion. "QC" is quality control series, an even composite of all experimental samples that was run at regular intervals on the mass spectrometer to assess instrument stability and feature consistency.

To further validate that the synthetic community system can produce the expected results in biologically complex situations, we also asked whether we could observe the expected dynamics of a known molecule within the system. We hypothesized that bactobolin, a characterized bacteriostatic molecule produced by *B. thailandensis* E264 (99), would accumulate in the medium reservoir of the three-member community over stationary phase, as previously reported for other *B. thailandensis* cultivation conditions (100). We identified a feature consistent with the mass of bactobolin using polar metabolite analysis (m/z = 383.075) (**Appendix B Figure 4A**). Tandem MS (MS-MS) fragments of the parent ion were consistent with those reported in the mass spectral molecule database METLIN (101) for bactobolin (**Appendix A Table 1** and **Appendix B Figure 4B**), confirming the identity of this feature as bactobolin. In addition, the feature identified as bactobolin accumulated in the media of the three-member community through time (**Appendix B Figure 4C**).

We also demonstrated member-specific measurements from the system. We measured cells recovered over time in a three-member experiment and also from monoculture and from coculture experiments conducted in filter plates. Cell count data using live/dead staining with flow cytometry had high reproducibility (median CV, 1.55%; range, 0.87 to 2.35%). These data revealed potential antagonism between *P. syringae* and *B. thailandensis*, as evidenced by the reduced *P. syringae* live cell counts when grown in the same consortium as *B. thailandensis* compared to its cell counts in monoculture or when grown only with the third community member, *C. violaceum* (**Figure 2.4**). To the best of our knowledge, this is the first time that antagonism between *B. thailandensis* E264 and *P. syringae* DC3000 has been observed, although previous studies have shown that *B. thailandensis* can produce antibacterials

(100, 102). This is relevant because *P. syringae* spp. are common plant pathovars, and we suggest subsequent work should explore this interaction with biocontrol applications in mind.

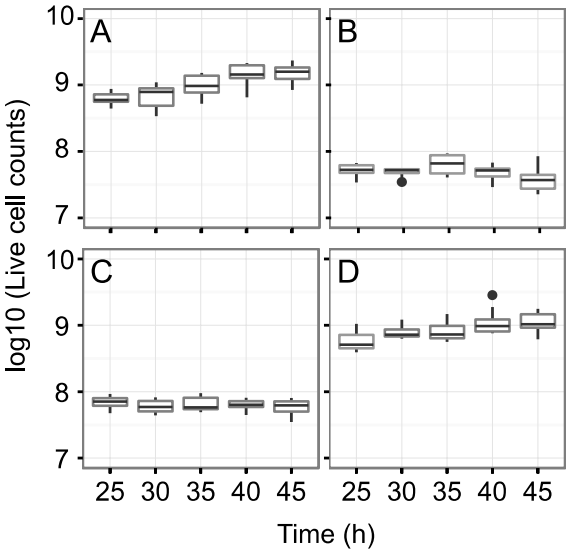

Figure 2.4. The filter plate system provides evidence of inhibition among members.

Shown are changes in live cell counts of *P. syringae* over stationary phase, measured using flow cytometry of Syto9-stained cells recovered from the filter plates. Five wells per plate and two replicate plates per time point were used to assess *P. syringae* cell counts when grown in monoculture (A), the three-member community (B), coculture with *B. thailandensis* (C), and coculture *with C. violaceum* (D). Reduced counts in coculture and the three-member community (compared to counts in monoculture or with *C. violaceum*) suggest an antagonistic interaction with *B. thailandensis.*

We observed consistent population sizes for each community member over stationary phase (**Appendix B Figure 5**), suggesting that, for this community, exometabolite interactions that occurred during stationary phase impacted functional output without impacting standing population sizes. Thus, outcomes of member exometabolite interactions did not drastically alter population sizes in this consortium. In contrast, the expectation in ecological compensatory dynamics is that population sizes of competitors are negatively correlated, such that an increase in the more fit population corresponds with a decrease in the less fit population. The observation of static population sizes in the synthetic system is important because it suggests that we can identify signatures of microbial interactions that are not necessarily indicated by changes in population size. Microbial interactions without obvious growth outcomes may be more cryptic and require more precise characterization than what total cell counts can provide, but would be observable in this system if driven by exometabolites.

Taken together, our synthetic community results demonstrate that this new system can reveal global exometabolite dynamics and interactions among microbial community members.

Discussion

The synthetic community system introduced here can be applied to address a variety of timely and compelling questions in systems and community microbiology. First, the synthetic system can be used to address fundamental questions about the consequences of community diversity. Membership manipulations can be performed to address the importance of community richness (total number of taxa) and structure (relative contributions of members)

on member interactions and emergent community properties. For example, it has been suggested that microbial community structure matters most for function in the production of exometabolites such as enzymes and polysaccharides, which have implications for biogeochemical processes like carbon cycling (84) and N fixation (85). The system could be used to interrogate these exometabolites directly. Similarly, the system can be used to investigate temporal changes in member interactions, to determine how member interactions change in response to perturbations, and to experimentally evolve microbial interactions within communities. These and similar lines of inquiry will allow researchers to ask how microbial interactions and products change as the result of controlled and specific environmental cues. Finally, the system can facilitate discovery of natural products. Member genomes can be mined for cryptic metabolic pathways from bioinformatic predictions, and this information could then be coupled to synthetic community manipulations to observe regulation. Novel or unknown exometabolites are likely to be discovered in an untargeted analysis of the community exometabolites, and their chemical structures and activities can be pursued subsequently.

This synthetic community system offers several experimental advantages. First, the synthetic system offers an opportunity to interrogate a relatively simple community within well-defined experimental conditions (45). It allows researchers to focus specifically on community outcomes driven by exometabolites and not by physical contact, as well as the causes and consequences of those outcomes. These interactions can be challenging to target in other mixed batch or bioreactor systems. The system also is versatile because it can be used with microbial consortia from any ecosystem and adjusted to simulate environmental conditions of interest. The system also is scalable, not only for increasing the overall community

diversity, but also for moving toward higher-throughput and high-content screens for molecules and community outcomes of interest. Finally, the system is accessible. The filter plates are available to any lab, and manual manipulation of the system without specialized equipment is feasible. We suggest that the most limiting factor is access to mass spectrometers and expertise in mass spectral analysis, which if not available locally is accessible via research support facilities.

As is true for any laboratory-scale experimental system, this synthetic community system also has several limitations. First, all possible types of microbial interactions are not observable using this system. Some exceptions include interactions that are contact dependent or in which chemical exchanges and physical contact are not clearly distinguishable or independent. The system instead allows for control of the influence of physical spatial structure on microbial interactions, which has been shown to be important for stabilizing some communities, especially for highly structured environments like biofilms or soil matrices (e.g., 89, 91, 103, 104). However, because members are spatially partitioned yet permitted to interact chemically, this system allows the researcher to control for spatial effects without a typical limitation of homogenous coculture: overgrowth of one member that prevents long-term observations of community interactions (89).

Not all relevant microbial exometabolites and community outcomes will be observable in this system. Specifically, exometabolites that have a rapid turnover or that are concentration dependent in ranges outside the system's physical constraints and imposed experimental conditions will be inaccessible (e.g., total medium volume or experiment duration, respectively). The ability to observe a molecule and its community outcomes also depends on

the sensitivity of the microbial sensing/signaling systems involved, which will depend on the members' capabilities. Also, this system may not be ideal for situations in which the local accumulation of an exometabolite inhibits the reaction generating the exometabolite, but this will depend on the duration of the experiment relative to the expected rate of exometabolite accumulation in the reservoir. Finally, interactions that are reliant on volatiles that may off-gas during plate shaking will not be observable.

Only cultivable organisms can be applied easily to the system, and so if the most functionally important or prevalent members of a community are yet uncultivable, their interactions will be difficult to observe with this system. However, cultivation methods are improving, in part because cultivation conditions can be informed by metagenome and (meta)transcriptome data (105), and there is evidence that growing microbial community members in cohorts from the environment can improve isolate recovery (106). Thus, this synthetic community system could be used to provide insights into the precise memberships and molecules required to bring new isolates into laboratory culture.

A general limitation of any system used to observe exometabolites is that many microbial exometabolites are unknown and difficult to identify. We anticipate that this limitation will be overcome as technology and infrastructure for exometabolite identification advances. Analysis pipelines to integrate exometabolite data with other microbial omics approaches, such as transcripts and metabolic flux analysis, are also in active development (107, 108). Therefore, the first experiments using the synthetic community system will face necessary challenges in spearheading analysis and integration approaches.

There are general criticisms offered for using model or laboratory-scale systems in microbial ecology, and a common concern is that any model cannot mimic natural conditions and therefore is not biologically relevant. The synthetic community system described here is an artificial, simplified model. However, it is a model that offers many advantages specifically for understanding the chemical feedbacks on community ecology driven by microbial interactions, which is a key goal of synthetic microbial ecology (45). These interactions have the potential to occur in nature, especially when thoughtful experimental designs are employed to (i) include organisms that are naturally cooccurring or have evidence of interactions and (ii) manipulate the pertinent primary drivers of natural ecosystems. Furthermore, important advances in ecology and evolution have been made using model systems (109–112). Microbial synthetic systems especially have offered insights because of their malleable communities and molecular tools for understanding population dynamics (42, 113–115). Thus, researchers continue to use model systems because they can inform as to both biological potential and constraints in nature. When complemented with careful studies *in situ*, the synthetic community system described here can serve to discover and interrogate microbial interactions, the signatures of which may otherwise be unobservable within the complexity of natural systems.

CHAPTER 3 : Exometabolite Dynamics over Stationary Phase Reveal Strain-Specific Responses

Work presented in this chapter has been published as Chodkowski JL, Shade A. 2020. Exometabolite Dynamics over Stationary Phase Reveal Strain-Specific Responses. *mSystems* 5:e00493-20.

Abstract

Microbial exponential growth is expected to occur infrequently in environments that have long periods of nutrient starvation punctuated by short periods of high nutrient flux. These conditions likely impose non-growth states for microbes. However, non-growth states are uncharacterized for the majority of environmental bacteria, especially in regard to exometabolite production. We compared exometabolites produced over stationary phase across three environmental bacteria: *Burkholderia thailandensis* E264 (ATCC 700388), *Chromobacterium violaceum* ATCC 31532, and *Pseudomonas syringae* pathovar tomato DC3000 (ATCC BAA-871). We grew each strain in monoculture and investigated exometabolite dynamics from mid-exponential to stationary phase. We focused on exometabolites that were released into the media and accumulated over 45 hours, including approximately 20 hours of stationary phase. We also analyzed transcripts (RNA-seq) to interpret exometabolite output. We found that a majority of exometabolites released were strain-specific, with a subset of identified exometabolites involved in both central and secondary metabolism. Transcript analysis supported that exometabolites were released from intact cells, as various transporters had either increased or consistent transcripts through time. Interestingly, we found that succinate was one of the most abundant identifiable exometabolites for all strains, and that each strain re-routed their metabolic pathways involved in succinate production during stationary phase. These results show that non-growth states can be metabolically dynamic, and that environmental bacteria can enrich a minimal environment with diverse chemical compounds as a consequence of growth and post-growth maintenance in stationary phase. This work provides

insights into microbial community interactions via exometabolites in conditions of growth cessation or limitation.

Introduction

Much of microbiology research in the laboratory is conducted with bacterial or archaeal populations that are growing exponentially. However, it is estimated that 60% of microbial biomass in the environment is in a non-growing state (131, 132). Non-growing states can arise by virtue of being dormant (e.g. low metabolic activity) or entering stationary phase (e.g. maintenance-levels of metabolic activity) (133), where the latter refers to a population-level phenomenon that occurs after exponential growth. Various abiotic and biotic stressors at carrying capacity are known to induce stationary phase including nutrient exhaustion/inaccessibility and the accumulation of waste products. Particular environments impose conditions where microbial populations are in stationary phase for a better part of their existence. For example, dry soils with intermittent periods of rewetting (54, 134, 135), activated sludge operating in a sequencing batch reactor (SBR) (56, 136), and in the human gut (55, 137). Thus, unlike most cultivated laboratory strains, microbes experience stationary phase in environments where short periods of high nutrient flux is followed by long periods of famine (138, 139).

Bacteria survive in stationary phase by employing various stress response adaptations (53, 58, 140). Stress response adaptations include changes to cell morphology, transcription, translation, and metabolism. Furthermore, in stationary phase, microbes can re-route

metabolic pathways to maintain essential components of the cell and the proton motive force (52). While these adaptations are thought to serve as survival mechanisms, the levels and types of metabolic activities in stationary phase are not well understood for most environmental microbes.

It is known, however, that microbes can exhibit appreciable metabolic activity in stationary phase (141). For example, entry into stationary phase resulted in prolonged protein production in Escherichia coli despite a decrease in overall protein levels (59). Metabolomic studies of E. coli in stationary phase support that there are unique metabolite production profiles associated with metabolic responses to growth arrest (60, 142, 143). These studies have provided valuable insights into stationary phase physiology. However, metabolome studies of microorganisms have generally focused on the dynamics of intracellular metabolites. It is expected that understanding metabolite dynamics in the extracellular environment can provide insights into metabolic responses that are relevant for microbial communities and interactions amongst coexisting community members.

Exometabolomics is the characterization of small, extracellular molecules either released by a microbe through means of lysis or diffusion, passive or active (5). Characterizing exometabolites can provide insights into the potential for microbes to engage locally with other microbes and the environment via release of small molecules (2). The effect of these small molecules on neighboring microbes can range from cooperative (e.g. signaling molecules) to antagonistic (e.g. antibiotics) (1). Some exometabolites, such as antibiotics, are known to increase in production upon entry into stationary phase (53). In addition, computational models have predicted that costless exometabolite production, such intermediates of central carbon

metabolism, may be common among bacteria (144), which could provide an overall benefit in a microbial community setting. Untargeted exometabolomic profiling has benefited from recent advances in the sensitivity and throughput of mass spectrometers (39). This approach provides an experimental basis to observe the breadth of exometabolites produced by microbial strains and strain-specific contributions to the exometabolite pool. Characterizing the exometabolite profile of a microbial population over time can be applied to understand the dynamic interplay between cell metabolism and the environment. Integrating untargeted exometabolomic approaches with other 'omic technologies (e.g. transcriptomics, genomics) informs comparisons across microbial populations of their metabolic responses in stationary phase.

We present an investigation of three environmental bacterial strains that are commonly associated with terrestrial environments (soils or plants) (**Table 3.1**). These strains were chosen because of reported (145) and observed interspecies exometabolite interactions in the lab. This current study evaluated exometabolite production for each strain in monoculture to first establish typical single-strain responses over stationary phase, with goals to next proceed to understand exometabolite-mediated interactions among strains. Our previous work established a robust and flexible approach to investigate microbial exometabolite production in either monoculture or co-culture (146). Our approach uses filter plates that allow for the separation of cells from an exometabolite reservoir. Here, we examined the detailed exometabolite and transcript dynamics, defined as compositional changes through time, for each of these three environmental strains in monoculture over stationary phase after growth in minimal glucose (3.7 mM) medium. We asked: What is the diversity of unique exometabolites that accumulate over stationary phase? What is a likely explanation (e.g. transport from viable cells or lysis) for

the accumulation of exometabolites? How does exometabolite composition and production compare across strains and time, and what general insights could these provide for understanding microbial metabolism and ecology of stationary phase?

Table 3.1. Bacterial strains used in this study.

	Family	Genome size (Mb)	ORFs[a]
Burkholderia thailandensis E264 (129)	Burkholderiaceae	6.72	5,641
Chromobacterium violaceum ATCC 31532 (127)	Neisseriaceae	4.75	4,371
Pseudomonas syringae pathovar *tomato* DC3000 (130)	Pseudomonadaceae	6.53	5,853

[a]ORFs, open reading frames.

We found that exometabolite composition is dynamic through stationary phase, and that accumulated exometabolites were likely released from intact cells. We also found that a majority of released exometabolites were strain-specific, suggesting that different bacterial strains have individualized responses to stationary phase. Finally, we found that all three strains re-routed metabolism in stationary phase.

Materials and Methods

Bacterial strains and culture conditions

Glycerol stocks of *B. thailandensis*, *C. violaceum*, and *P. syringae* (**Table 3.1**) were plated on half-concentration Trypticase soy agar (TSA50) at 27°C for at least 24 h. Strains were inoculated in 7 ml of M9–0.2% glucose medium and grown for 16 h at 27°C, 200 rpm. Cultures were then back-diluted into 50 ml M9-0.2% glucose medium such that exponential growth phase was achieved after 10 h of incubation at 27°C, 200 rpm. Strains were back-diluted in 50 ml M9–0.067% glucose medium to target ODs (*B. thailandensis* 0.3 OD, *C. violaceum*: 0.035 OD, *P. syringae* 0.035 OD) such that stationary phase was achieved after approximately 24 h of incubation in filter plates.

Filter plate experiments

We used the filter plate system to study each strain in monoculture over the course of stationary phase. Filter plate preparation was performed as previously described (146). Briefly, we used sterile filter plates with 0.22-µm-pore polyvinylidene difluoride (PVDF) filter bottoms

(MultiScreen GV Filter Plate, 0.22 µm, MSGVS2210, Millipore). Prior to use, filter plates were washed three times with sterile water using a vacuum apparatus (NucleoVac 96 vacuum manifold; Clontech Laboratories). The filter of well H12 was removed with a sterile pipette tip and forceps, and 31 ml of M9–0.067% glucose medium was added to the reservoir through well H12. Each well was then filled with 130 µl of back-diluted culture in M9–0.067% glucose medium or medium only. For a given time series replicate, a custom R script (RandomArray.R [see the GitHub repository]) was used to randomize the placement of a strain in the wells so that a strain occupied a total of 31 wells per plate and the remaining 64 wells were filled with medium. Each monoculture time course was independently replicated four times for a total of 12 experiments. The time course included 6 time points: an exponential phase point (12.5 h) and 5 points assessed every 5 h over stationary phase (25 h – 45 h). Plates were destructively sampled, comprising a total of 72 plates for the entire experimental design of 3 strains x 6 timepoints x 4 replicates.

Filter plates were incubated at 27°C with gentle shaking (~0.32 rcf). We again used our RandomArray.R script to randomize wells used for RNA extraction (16 wells, pooled per plate) and flow cytometry (5 wells, pooled per plate). During destructive sampling, first, the wells containing spent culture assigned to RNA-seq were pooled into a 1.5 mL microcentrifuge tube, flash frozen in liquid nitrogen, and stored at -80 ^{o}C for RNA extraction. Next, wells containing spent culture assigned to flow cytometry were pooled, and then 20 µL was initially diluted in 180 µL Tris-buffered saline (TBS; 20 mM Tris, 0.8% NaCl [pH 7.4]), and then, after checking concentrations needed for accurate flow cytometry counts, diluted further in TBS to reach final dilutions of 1,300-fold, 1,540-fold, and 900-fold for *B. thailandensis*, *C. violaceum*, *P. syringae*,

respectively. Finally, spent medium (~31 ml) from the shared reservoir was transferred into 50 mL conical tubes, flash-frozen in liquid nitrogen and stored at −80 °C for subsequent exometabolite extraction.

Flow cytometry

Diluted cultures were stained with the Thermo Scientific LIVE/DEAD BacLight bacterial viability kit at final concentrations of 1.5 µM Syto9 (live stain) and 2.5 µM propidium iodide (dead stain). Two hundred microliters of stained cultures were transferred to a 96-well microtiter U-bottom microplate (Thermo Scientific). Twenty microliters were analyzed on a BD Accuri C6 flow cytometer (BD Biosciences) at a fluidics rate of 66 µl/min and a threshold of 500 on an FL2 gate. The instrument contained the following optical filters: FL1-533, 30 nm; FL2-585, 40 nm; and FL3, 670-nm longpass. The counting accuracy of the flow cytometer was periodically checked with GFP beads. Data were analyzed using BD Accuri C6 software version 1.0.264.21 (BD Biosciences).

LCMS sample preparation and data acquisition

The following methods were according to the Department of Energy Joint Genome Institute (DOE JGI) standard operating protocols performed at the DOE JGI facility. Spent medium samples from the monocultures were shipped from Michigan State to the DOE JGI overnight on dry ice. Spent medium (ranging from 2.5 to 8 mL) were lyophilized in a Labconoco FreeZone 2.5 lyophilizer (Labconco, Kansas City, MO). Dried samples were resuspended in 700

µL methanol, vortexed, sonicated for 10 minutes in a water bath (VWR Scientific Aquasonic Water Bath, Model 150HT), and then centrifuged for 2 minutes at 1200 g. Supernatant was transferred to 96 deep-well plate (1.1 mL) and then dried in a speed-vac (SPD111V, Thermo Scientific). Samples were stored at -80 ^{o}C until LC-MS analysis. Four extraction blanks were also prepared using the same protocol.

Dried samples were resuspended in methanol containing internal standards (ITSD). ITSD used for polar analysis were 13C,15N amino acid mixture (30 µM, 767964, Sigma, Inc). ITSD for nonpolar analysis was 2-Amino-3-bromo-5-methylbenzoic acid (ABMBA, 1 µg/mL). Additionally, a quality control (QC) sample containing ~20 common biomolecules was prepared. ITSD are used to check for injection errors, mass accuracy, and RT shifts within a sample. The m/z accuracy and retention time shifts in QC samples were assessed to check for instrument consistency and column performance. Samples were analyzed for both polar and non-polar exometabolites. Resuspended samples containing ITSD were vortexed, sonicated in a water bath for 2 minutes, transferred to transwell plates (MultiScreen GV Filter Plate, 0.22 µm, MSGVS2210, Millipore) and centrifuged for 2 min at ~1200 g into a 96-well plate, and then transferred into an LC-MS glass vial.

UHPLC chromatography was performed using and Agilent 1290 LC stack, with MS and tandem mass spectrometry (MS2) data collected in both positive and negative ion mode using a Thermo QExactive (for HILIC) or Thermo QExactive HF (for C18) mass spectrometer (Thermo Scientific, San Jose, CA). Full MS spectra was collected for m/z 80-1,200 at 60,000 resolution for C18, and m/z 70-1,050 at 70,000 resolution for HILIC. MS/MS fragmentation data was acquired using stepped collision energies between 10−40 eV at 17,500 resolution. Specifically, 1 MS1

scan was followed by 2 MS2 scans of the 2 most intense ions, then another MS1 scan followed by another 2 MS2 scans of the 2 most intense ions. If the 2 most intense ions were already fragmented in the previous 10 seconds of analysis, the next 2 most intense ions were fragmented. For MS2, 10,20 and 30eV collision energies were collected and averaged with the exception of one biological replicate per condition, where 10, 20 and 40eV collision energies were collected and averaged.

For detection of nonpolar metabolites, reverse phase chromatography was performed using a C18 column (Agilent ZORBAX Eclipse Plus C18, Rapid Resolution HD, 2.1 x 50 mm, 1.8 µm) at a flow rate of 0.4 mL/min. Samples were run on the C18 column held at 60 ºC equilibrated with 100% buffer A (100% LC-MS water with 0.1 % formic acid) for 1 minute, followed by a linear gradient to 100% buffer B (100% acetonitrile with 0.1% formic acid) over 7 minutes, and then an isocratic elution in 100% buffer B for 1.5 minutes. A final re-equilibration to 100% buffer A over 1 minute and isocratic hold for 1 minute was performed prior to the next sample injection. For detection of polar metabolites, normal phase chromatography was performed using a ZICHydrophilic Interaction Liquid Chromatography (HILIC) column (SeQuant ZIC-HILIC 3.5-µm particle size, 200 Å porosity, 150 mm x 2.1 mm, Millipore Sigma). Samples were run on the ZIC-HILIC column held at 40 ^{o}C equilibrated with 100% buffer B (95:5 acetonitrile:water with 5mM ammonium acetate) at a flow rate of 0.45 mL/min for 1.5 minutes, diluting buffer B down to 65% with buffer A (100% water with 5mM ammonium acetate) over 13.5 minutes, followed by a linear increase in flowrate to 0.6 mL/min as buffer B approached 0% over 3 minutes, and then an isocratic elution in 100% A for 5 minutes. This was followed by

a 2 minute linear gradient back to 100% B and decrease in flowrate to 0.45 mL/min, and then a final 5 minute column re-equilibration at 100% B prior to the next sample injection.

Sample injection order on the mass spectrometer was randomized and an injection blank (2 uL of methanol) was run between each sample. For all samples, resuspension volume (70 to 120 µL) and injection volume (2 µL to 8 µL) varied to normalize by initial sample volume prior to extraction. A total of 257 samples were successfully analyzed (See Dataset 4 at https://github.com/ShadeLab/Paper_Chodkowski_MonocultureExometabolites_2020/tree/master/Datasets). Samples not included in downstream analyses were removed either because they failed quality standards during mass spectrometry analysis or the sample had low intragroup reproducibility.

Mass spectrometry analysis

Both MS and MS/MS data were used for untargeted metabolomics analysis. A total of 257/288 metabolomic samples were used for analysis (See Dataset 4 at https://github.com/ShadeLab/Paper_Chodkowski_MonocultureExometabolites_2020/tree/master/Datasets); 30 samples were removed due to failed injection and 1 sample was removed due to low intragroup reproducibility in polar analysis (Pearson's $r \leq 0.14$). MZmine (version 2.42) (167) was used for peak picking, aligning features across samples, and peak integration for both nonpolar and polar analyses and in both negative and positive ion mode. MZmine XML parameter files for all analyses can be viewed and downloaded from GitHub (See Dataset 7 at https://github.com/ShadeLab/Paper_Chodkowski_MonocultureExometabolites_2020/tree/mas

ter/Datasets). For MS data, a feature by sample matrix was exported for additional feature filtering steps. For MS/MS data, the GNPS feature was used to export data in addition to performing a local spectra database search within MZmine (see Compound identification section, below).

We used filter featuring steps to identify exometabolites released from each strain in stationary phase. The feature filtering steps were performed as follows on a per-strain basis: 1) Features were removed if the max peak area was found in one of the replicates for the external control sample. 2) A noise filter: the minimum peak area of a feature from a replicate at the last time point (45 hr) needed to be 3X the maximum peak area of the same feature in one of the external control replicates. 3) Coefficient of variation (CV) values for each feature calculated between replicates at each time point needed to be less than 20% across the time series. 4) The minimum value of the average peak area needed to be observed in the first, exponential phase time point (12.5 h). 5) The log2 fold change of the average peak areas observed between the last (45 h) and first (12.5 h) timepoints needed to be greater than 1. 6) The time series abundance of a feature needed to have a Pearson correlation greater than or equal to 0.7.

Four final feature datasets from polar and nonpolar analysis in both ionization modes were analyzed in MetaboAnalyst 4.0 (168). Features were normalized by an internal standard (ITSD) reference feature (See Dataset 5 at https://github.com/ShadeLab/Paper_Chodkowski_MonocultureExometabolites_2020/tree/master/Datasets) and cube root transformed. Reference features for polar analysis in positive (13C-15N-proline) and negative (13C-15N-alanine) was determined by the ITSD with the lowest CV value across all samples. The reference feature for nonpolar datasets was the ITSD 2-Amino-3-

bromo-5-methylbenzoic acid (ABMBA). Heatmaps were generated in MetaboAnalyst using Ward's clustering algorithm with Euclidean distances from Z-scored data. Normalized and transformed datasets were exported from MetaboAnalyst to generate principal coordinate analysis (PCoA) plots in R. Abundances for exometabolites that did not pass release criteria in each strain were replaced with NAs prior to distance matrix computation.

Compound identification

A three step process was used to identify compounds or characterize chemical ontologies (162). Identification confidence was assigned according to the Metabolomics Standards Initiative (MSI) (169). First, compounds were identified by an in-house reference library at the Joint Genome Institute (JGI). This reference library was curated to identify compounds based on m/z, retention time, and MS/MS spectra of standards. A compound passing the first two criteria were denoted MSI level 1. A compound passing all three criteria exceeded MSI level 1. All compounds at or exceeding MSI level 1 were identified using the reference library. This reference library was only available for polar analysis. Ranges for m/z and retention time values for compounds in the reference library were used to identify exometabolites from the MZmine analysis (See Dataset 6 at https://github.com/ShadeLab/Paper_Chodkowski_MonocultureExometabolites_2020/tree/master/Datasets).

We made an effort to identify as many of the remaining compounds from both polar and nonpolar analyses that had MS/MS data. MS/MS data acquired during mass spec analysis

were used to putatively identify compounds that matched to fragmentation patterns from libraries outside of JGI; these were assigned MSI level 2. First, MS/MS data was exported to GNPS format and analyzed in GNPS (170) to match fragmentation patterns against the NIST17 commercial library. Second, a local spectra database search was performed within MZmine using the entire compound library from MassBank of North American (MoNA-https://mona.fiehnlab.ucdavis.edu). For both approaches, compounds were putatively identified if cosine scores were 0.7 or above. A subset of the final feature datasets was created from compounds identified at MSI level 1 and level 2 (See Dataset 2 at https://github.com/ShadeLab/Paper_Chodkowski_MonocultureExometabolites_2020/tree/master/Datasets). These datasets were processed in MetaboAnalyst (see Mass spectrometry analysis section, above) to generate heat maps, perform pathway analysis (see Pathway analysis section, below), and perform ANOVA analysis between strains exometabolite abundances.

All remaining unidentified compounds with MS/MS data were analyzed with CSI:Finger ID and assigned MSI level 3. This method provides the putative chemical ontology of a compound. The top CSI:Finger ID match was used for each compound. Then, lnChl keys from all MSI levels were used to perform a chemical ontology analysis using ClassyFire version 1.0. SDF files from ClassfyFire were exported from each analysis to extract both Class level and Direct Parent level ontologies. These data were then exported to R for data visualization.

RNA sample prep, sequencing, and QC

At Michigan State, RNA was extracted using the E.Z.N.A. Bacterial RNA kit (Omega Bio-tek, Inc.). An in-tube DNase I (Ambion, Inc AM2222, 2U) digestion was performed to remove DNA from RNA samples. RNA samples were purified and concentrated using the Qiagen RNAeasy MinElute Clean up Kit (Qiagen, Inc). Ten random samples were chosen to assess RNA integrity on an Agilent 2100 Bioanalyzer.

The following methods were according to DOE JGI standard operating protocols and performed at the DOE JGI facility. RNA samples were shipped from Michigan State to DOE JGI overnight on dry ice. RNA samples were placed into 4, 96-well plates- 1 plate for each species containing all stationary phase time points and 1 plate containing exponential phase time points. Plate-based RNA sample prep, including the Ribo-Zero rRNA Removal Kit (Illumina, for Bacteria) and the TruSeq Stranded Total RNA HT sample prep kit, was performed on the PerkinElmer Sciclone NGS robotic liquid handling system with the following conditions: total RNA starting material of 100 ng per sample and 10 cycles of PCR for library amplification. The prepared libraries were quantified using KAPA Biosystem's next-generation sequencing library qPCR kit and run on a Roche LightCycler 480 real-time PCR instrument. The quantified libraries were then prepared for sequencing on the Illumina HiSeq sequencing platform utilizing a TruSeq Rapid paired-end cluster kit, v4. Sequencing of the flowcell was performed on the Illumina HiSeq2500 sequencer using HiSeq TruSeq SBS sequencing kits, v4, following a 2x100nt indexed run.

Read preprocessing and filtering

BBDuk (171) was used on raw fastq files to filter contaminants and trim both adaptor sequence and right quality trim reads where quality dropped to 0. Using BBDuk, raw reads were evaluated for artifact sequences by kmer matching (kmer=25), allowing 1 mismatch and detected artifacts were trimmed from the 3' end of the reads. BBDuk was used to remove reads that contained 1 or more 'N' bases, had an average quality score across the read less than 10 or had a minimum length <= 51 bp or 33% of the full read length. Reads mapped with BBMap (171) to masked human, cat, dog and mouse references at 93% identity were removed. Reads aligned to common microbial contaminants were also removed. Ribosomal RNA reads were also removed.

Pseudo-alignment and counting

The reads from each library were pseudo-aligned to the transcriptome of each strain with kallisto (172). Raw counts from each library were combined into gene count matrix for each strain. The gene count matrix was used for downstream analyses.

RNA quality filtering and differential gene expression (DGE) analysis

Count matrices for each strain were quality filtered in two steps prior to DGE: genes containing 0 counts in all samples were removed and genes with a count < 10 in more than 90% of samples were removed. DGE was performed in DESeq2 version 1.22.1 (173). We tested for differential gene expression by evaluating genes that changed at any time point (FDR < 0.01).

Genes with differential expression were then evaluated for log2 fold changes >1. Specifically, we focused on genes involved in transport (see Transporter analysis section, below).Defining expression minimums

A cumulative abundance plot was generated for each strain by organizing locus IDs from low transcript counts to high transcript counts and plotting the % of total transcripts against the % of total read counts (174, 175). The 25th quantile was calculated to obtain the transcript count value that defined a low expression minimum. That is, all genes with transcript counts above this minimum were considered to be expressed in the cell, regardless of longitudinal differential expression.

Transporter analysis

TransportDB 2.0 (http://www.membranetransport.org/transportDB2/index.html) was used to annotate transporters in each strain (176). Annotated transporters were then evaluated to determine differential expression or expression above the low expression minimum.

KEGG pathway analysis

We extracted log2 fold change (LFC) values from transcripts in each strain from DESeq analysis. Log2 fold change were obtained by comparing each stationary phase time point to the exponential time point 1 (12.5 h). We then mapped longitudinal LFCs onto KEGG pathways for each strain using the pathview package in R. First, K numbers were assigned to genes for both *C. violaceum* and *P. syringae* using BlastKOALA (version 2.2). K numbers were not assigned to *B.*

thailandensis because KEGG identifiers were available. KEGG identifiers for *B. thailandensis* and K numbers assigned to *C. violaceum* and *P. syringae* were used to map longitudinal LFCs onto KEGG pathways. Pathways of interest were curated and manually edited in Inkscape (verision 0.92.4) using a colorblind palette.

Annotation of biosynthetic gene clusters (BSGC)

BSGC were annotated using antismash bacterial version 5.0 (177). Annotated genome files for each strain were submitted to the online server. Default parameters included a relaxed detection strictness and extra features such as KnownClusterBlast, SubClusterBlast, and ActiveSiteFinder.

Code availability

Computing code and workflows and datasets are available at https://github.com/ShadeLab/Paper_Chodkowski_MonocultureExometabolites_2020. R packages used during computing analyses included vegan (178), ggplot2 (125), VennDiagram (179), RVAideMemoire (180), patchwork (181), DESeq2 (173), pathview (182), KEGGREST (183), and helper functions (184–187).

Data availability

Genomes for *B. thailandensis*, *C. violaceum*, and *P. syringae* are available at JGI Genome Portal under project IDs 1133672, 1133669, and 1133674, respectively. An improved annotated draft genome of *C. violaceum* is available under NCBI BioProject number PRJNA402426 (Genbank Accession ID: PKBZ00000000). Re-sequencing efforts for *B. thailandensis* and *P. syringae* are under NCBI BioProject numbers PRJNA402425 and PRJNA402424, respectively. Metabolomics data and transcriptomics data are also available at JGI Genome Portal (188) under JGI Proposal ID 502921. MZmine XML parameter files for all analyses can be viewed and downloaded from GitHub (See Dataset 7 at https://github.com/ShadeLab/Paper_Chodkowski_MonocultureExometabolites_2020/tree/master/Datasets). Large data files (e.g. MZmine project files) are available upon request. Other datasets are also available on GitHub (See Datasets at https://github.com/ShadeLab/Paper_Chodkowski_MonocultureExometabolites_2020/tree/master/Datasets).

Results

Each strain had a distinct exometabolite profile in stationary phase

In total, 10,352 features were detected by mass spectral analysis (**Figure 3.1**, Table 2) across the three strains. These features represent what we defined as released exometabolites (see Methods: Mass spectrometry analysis section). Briefly, released exometabolites were defined as those that had temporal accumulation (assessed via peak area) in stationary phase. Most features detected were strain-specific, and the number of unique features from any one

strain outnumbered the total number of features shared by at least two strains (1494 features, ~16.9%). Of the 1494 shared features, ~12.7% were shared among all three strains. Specifically, *B. thailandensis* had the most unique detected features (~41.8%), followed by *P. syringae* (~25.2%) and *C. violaceum* (~18.6%) compared to all detected features. These data suggest that, despite monoculture growth in minimal medium initially containing one carbon source, an abundance of strain-specific exometabolites are produced during stationary phase.

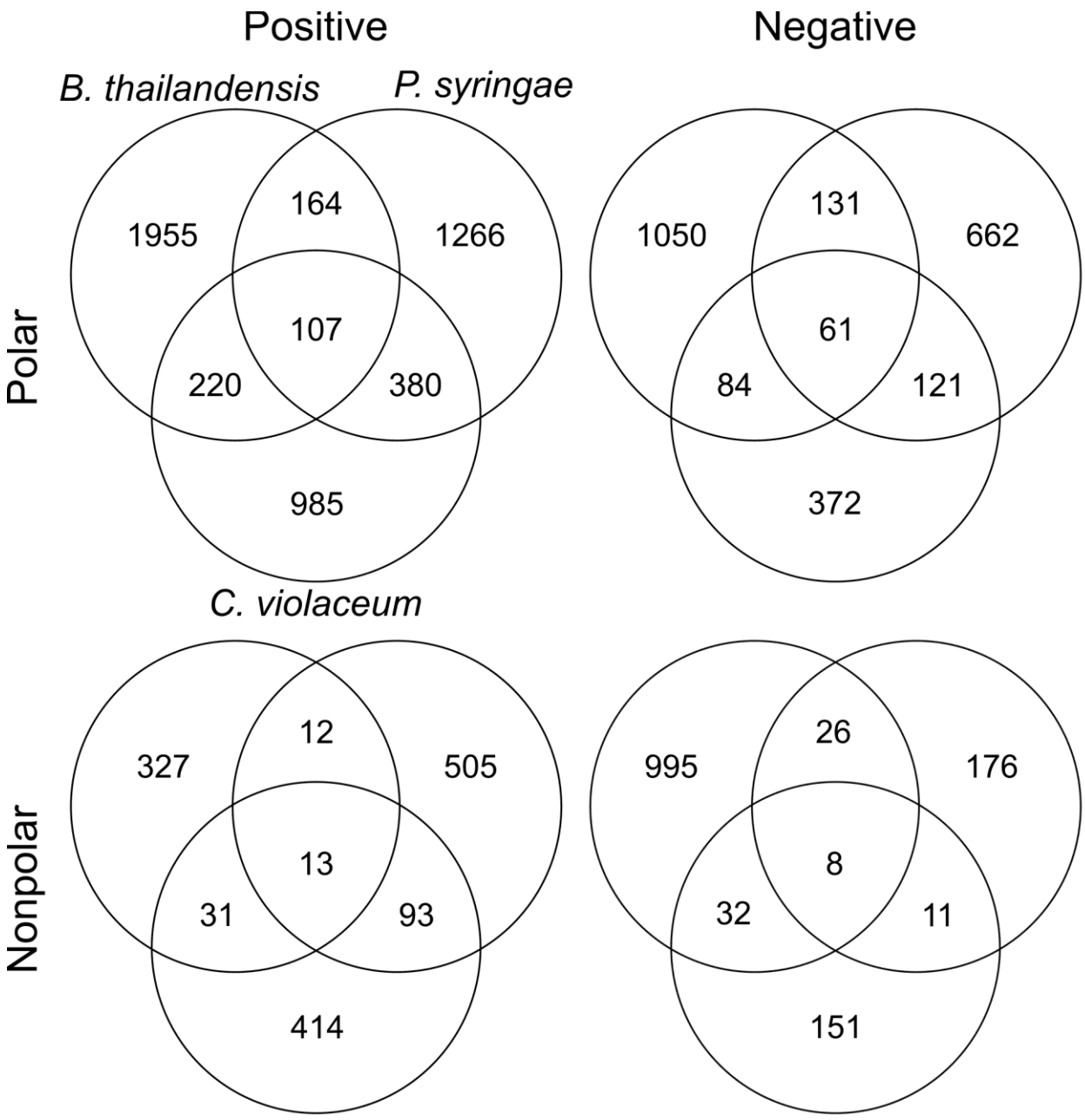

Figure 3.1. Quantification of all features that fit criteria for released in all strains across all polarity/ionization modes.

Table 3.2. Summary of released exometabolites for each strain

	B. thailandensis	*C. violaceum*	*P. syringae*
Total no. of features	5216	3083	3736
No. of unique features	4327	1922	2609
No. Features in common with *B. thailandensis*	-	367	333
No. Features in common with *C. violaceum*	367	-	605
No. of features in common with *P. syringae*	333	605	-
No. of features detected in all strains	189	189	189

We were interested in understanding differences in exometabolite composition and exometabolite temporal dynamics over stationary phase (**Figure 3.2**). Comparing across strains (**Figure 3.2A-D**), each strain had strain-specific exometabolite profiles (Adonis $0.590 \leq r^2 \leq 0.808$, P value ≤ 0.001, all pair-wise FDR-adjusted P values ≤ 0.001). For each strain, exometabolite profiles from exponential growth phase were distinct from stationary phase profiles (Fig 2). Strain differences in released exometabolites were more important than time in explaining variation in exometabolite composition on both PCoA axes. As expected, strain identity explained ≥ 57% of the variation while time explained ≤ 6% of the variation across all polarity/ionization modes (**Appendix A Table 3**). However, the most variation was explained by the interaction effect of strain x time (**Appendix A Table 3**). Thus, exometabolite compositional differences were mainly driven by the different released exometabolites by the different strains. This was expected given the large number of unique features detected for each strain (**Table 3.2**).

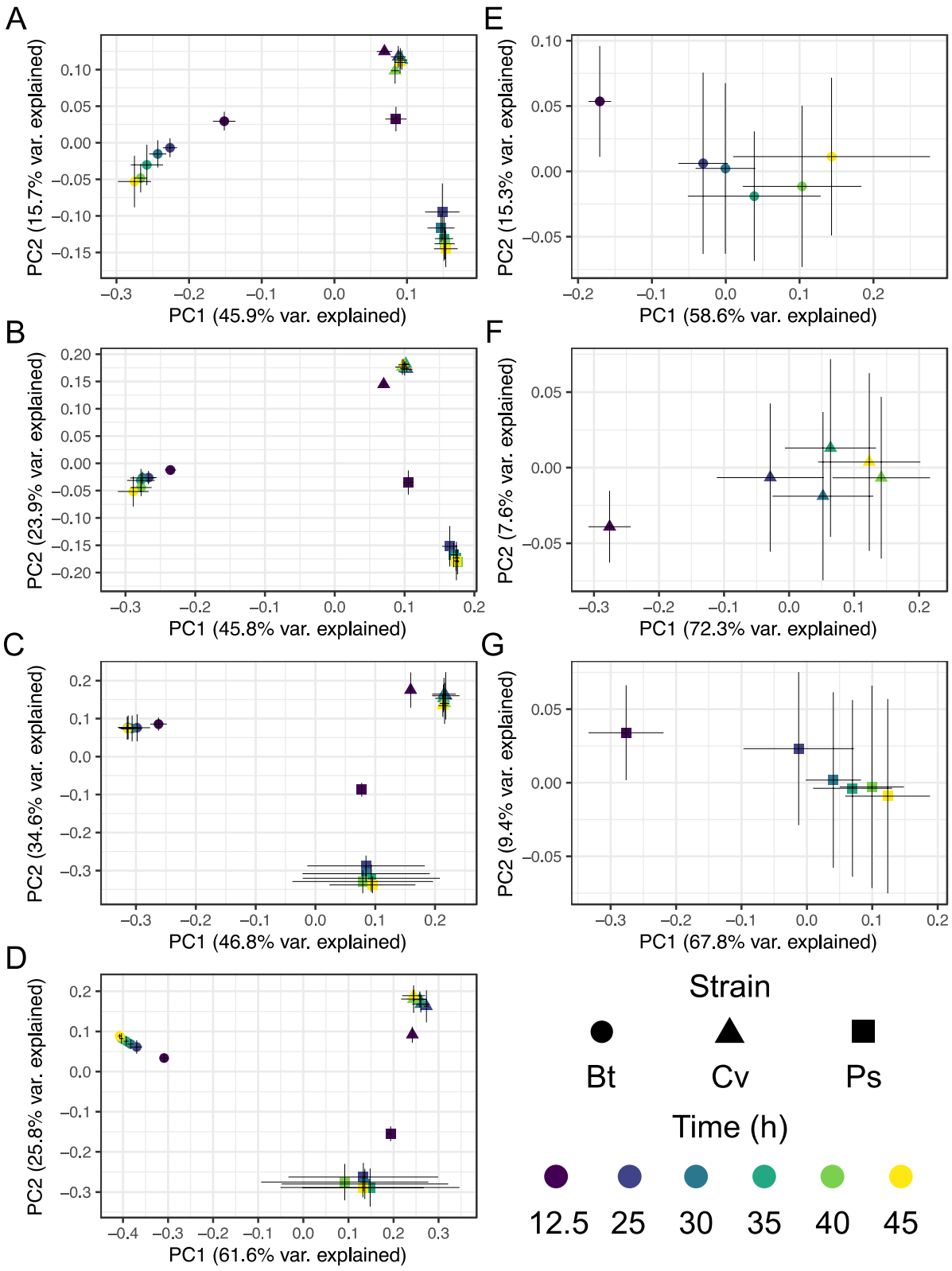

Figure 3.2. Exometabolite profiles differ by strain and time.

Figure 3.2 (cont'd)

PCoA plots for polar positive (**A**), polar negative (**B**), nonpolar positive (**C**), nonpolar negative (**D**), and combined polar positive + polar negative exometabolites (accounting for 72-77% of released exometabolites per strain) for *B. thailandensis* (**E**), *C. violaceum* (**F**), and *P. syringae* (**G**). Each point represents the exometabolite profile (relative contributions assessed by peak area) for a particular strain at a particular time point. Features were normalized by an internal standard (ITSD) reference feature and cube root transformed. Bray-Curtis distance metric was used to calculate dissimilarities between exometabolite profiles. Strain is indicated by shape (*B. thailandensis* (●), *C. violaceum* (▲), *P. syringae* (■)) and timepoint is indicated by a color gradient. Error bars are 1 standard deviation around the mean axis scores of n = 2 to 4 replicates destructively sampled from the same strain/time point condition.

Alternatively, we further looked at the influence of time on exometabolite profiles by observing exometabolites released by each strain, separately. We considered only those exometabolites that met our stringent criteria for release and accumulation over time (see Methods). Notably, with these criteria, some of the same exometabolites were classified as released for some strains but not for others. In these cases, exometabolites were excluded from the temporal analysis of any strains for which the release criteria were not met. Directional temporal dynamics was observed for each strain (**Figure 3.2E-G**), though continued directionality was not observed in some of the latest time points (e.g. **Figure 3.2F**). We define directional as a progressive, step-wise trajectory between time points, where each time point is distinguished from any of the previous time points, and even more distinct from previous time points in PCoA space. This ultimately reflects temporal changes in exometabolite composition. Temporal trajectories in exometabolite profiles were highly reproducible for each strain across biological replicates (Protest analyses, **Appendix A Table 4**). For all strains, the difference between exometabolite profiles progressively increased when comparing each stationary phase time point to the initial, exponential phase time point (**Appendix A Table 5**). But, comparing successive time points revealed that the greatest differences occurred between the first stationary phase time point and the exponential phase time point. Notably, dissimilarity decreased between successive time points in stationary phase such that the latest time points were more similar to each other than the earliest time points (**Appendix A Table 6**). For each strain, the exometabolite profile changed over time (**Appendix A Table 7**). However, this was primarily due to differences in exometabolite profiles when comparing the exponential phase time point to each of the stationary phase time points (**Appendix A Table 8**). We note that

hundreds to thousands of features were detected in late stationary phase but were excluded (see Methods: Mass spectrometry analysis section) from the final dataset of released exometabolites. We maintained strict criteria for the detection of and accumulation of released exometabolites over stationary phase. Taken together, these data suggest that differences in exometabolite composition are largely driven by strain- specific production of exometabolites. Accounting for all released exometabolites within each strain, similar temporal patterns emerge, with the largest differences observed between exponential phase and stationary phase and more subtle differences observed over consecutive time points within stationary phase.

Hierarchal clustering analysis also revealed strain-specific features and their dynamics (**Figure 3.3**). Most features across all strains reached maximum accumulation in late stationary phase. Notably, exometabolites accumulated despite generally steady strain population levels (**Appendix B Figure 7**). We did observe ~1 generation in *B. thailandensis* and *P. syringae* over the course of stationary phase but the doubling took 20 h to complete. Dead cells across the time series remained consistent for both *B. thailandensis* and *C. violaceum* but increased for *P. syringae* (**Appendix B Figure 7**). However, the quantity of live cells remained higher than the quantity of dead cells across the time series for all strains. Largely consistent counts of viable cells and a lack of death phase suggest that many exometabolites were released by intact cells rather than by lysis. To add support to this hypothesis, transcriptomics data indicate multiple organic molecule transporters were either consistently expressed throughout the time series or differentially expressed (**Table 3.3**, See Dataset 1 at https://github.com/ShadeLab/Paper_Chodkowski_MonocultureExometabolites_2020/tree/master/Datasets). Notable examples for all strains include various transporters related to dipeptide

and C-4 dicarboxylate transport. In summary, despite growth arrest, each bacterial strain continued to produce (and the media accumulated) a distinctive and dynamic profile of exometabolites into stationary phase.

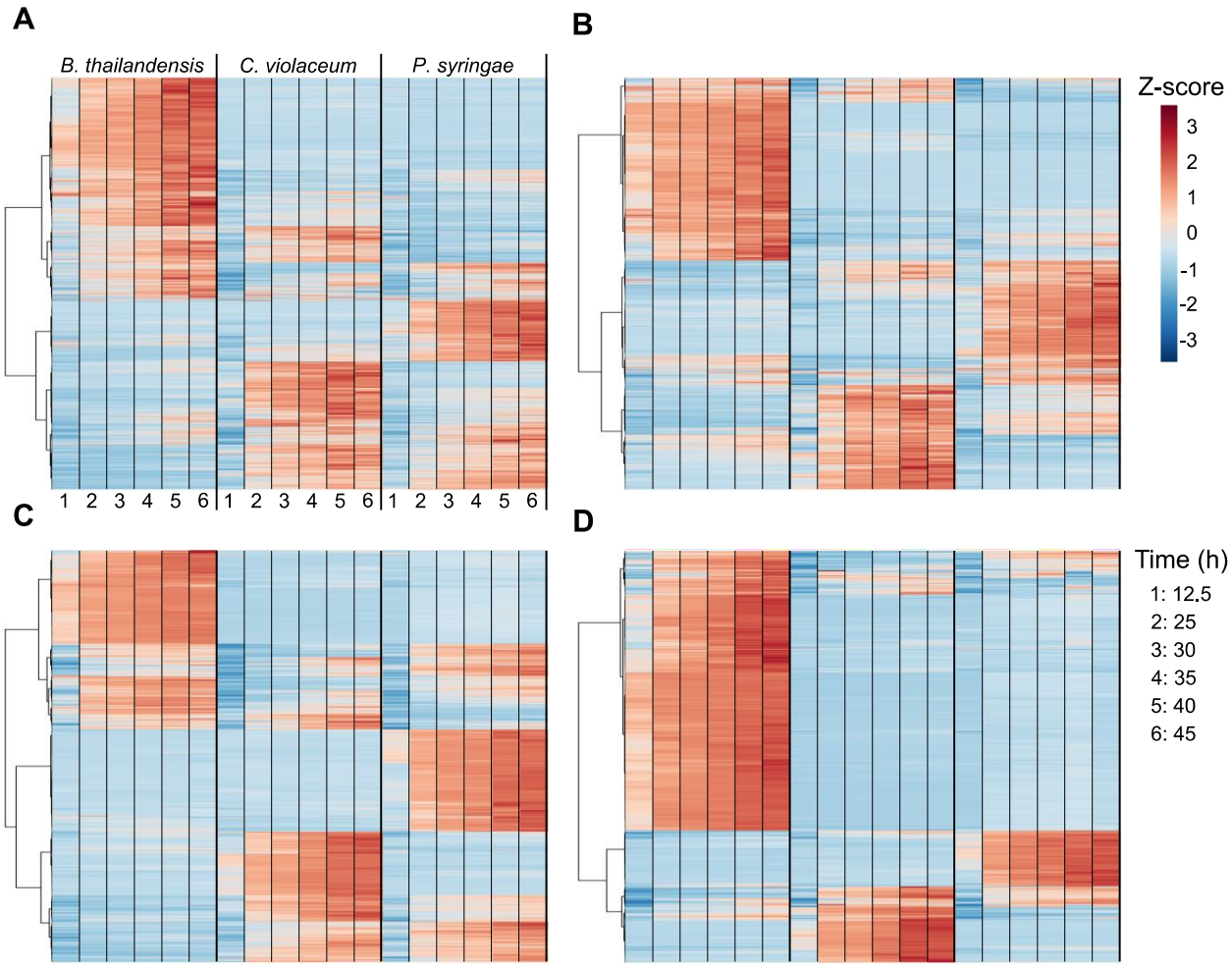

Figure 3.3. Released exometabolites and their temporal dynamics.

A heat map of all released exometabolites is shown for **A**) polar positive, **B**) polar negative, **C**) nonpolar positive, and **D**) nonpolar negative modes, where samples are columns are exometabolites are in rows. Each sample is the average of independent time point replicates (n = 2 to 4). Euclidean distance was calculated from Z-scored mass spectral profiles (containing peak areas). Prior to Z-scoring, features were normalized by an internal standard (ITSD) reference feature and cube root transformed. Features were clustered by Ward's method.

Table 3.3. Summary of RNA-Seq results with focus on genes annotated as transporters[d].

	B. thailandensis			*C. violaceum*			*P. syringae*		
Genes involved in transport	669			465			689		
	447[a]	103[a,b]	20[a,b,c]	354[a]	169[a,b]	53[a,b,c]	461[a]	136[a,b]	12[a,b,c]
Genes annotated as transporters related to dipeptide/C4-dicarboxylate transport	26			22			43		
	17[a]	4[a,b]	0[a,b,c]	22[a]	7[a,b]	1[a,b,c]	20[a]	10[a,b]	0[a,b,c]
Genes annotated as transporters related to dipeptide/C4-dicarboxylate transport (transcripts below LEM)	9			0			23		

[a]Above LEM

[b]Differentially expressed (Q-value < 0.01)

[c]LFC > 1

Table 3.3 (cont'd)

[d]Criteria included genes that were a) above the low expression minimum (LEM), b) genes that were differentially expressed, and c) genes with a stationary phase time point that had a $\log_2$ fold change (LFC) > 1 compared to the exponential phase time point.

Identity of stationary phase exometabolites

Of the total set of exometabolite features, only 188 (~1.8%) could be identified (**Figure 3.4**, **Appendix B Figures 8-10**, See Dataset 2 at https://github.com/ShadeLab/Paper_Chodkowski_MonocultureExometabolites_2020/tree/master/Datasets). These were classified according to the Metabolomics Standards Initiative (MSI): MSI level 1 (Identified compounds) and MSI level 2 (putatively identified compounds). Most of the identified exometabolites were uniquely produced by one strain under our experimental conditions, though there were some exometabolites shared across strains, especially between *C. violaceum* and *P. syringae* (See Dataset 2 at https://github.com/ShadeLab/Paper_Chodkowski_MonocultureExometabolites_2020/tree/master/Datasets). Many of the identified exometabolites, particularly those molecules involved in central metabolism, such as amino acids, nucleotides/nucleosides, and carboxylic acids, were classified using an in-house standard in accordance with MSI level 1. In addition, MSI level 1 exometabolites such as ectoine, proline, trehalose, and glutamate likely indicated a cellular stress (e.g. osmotic stress).

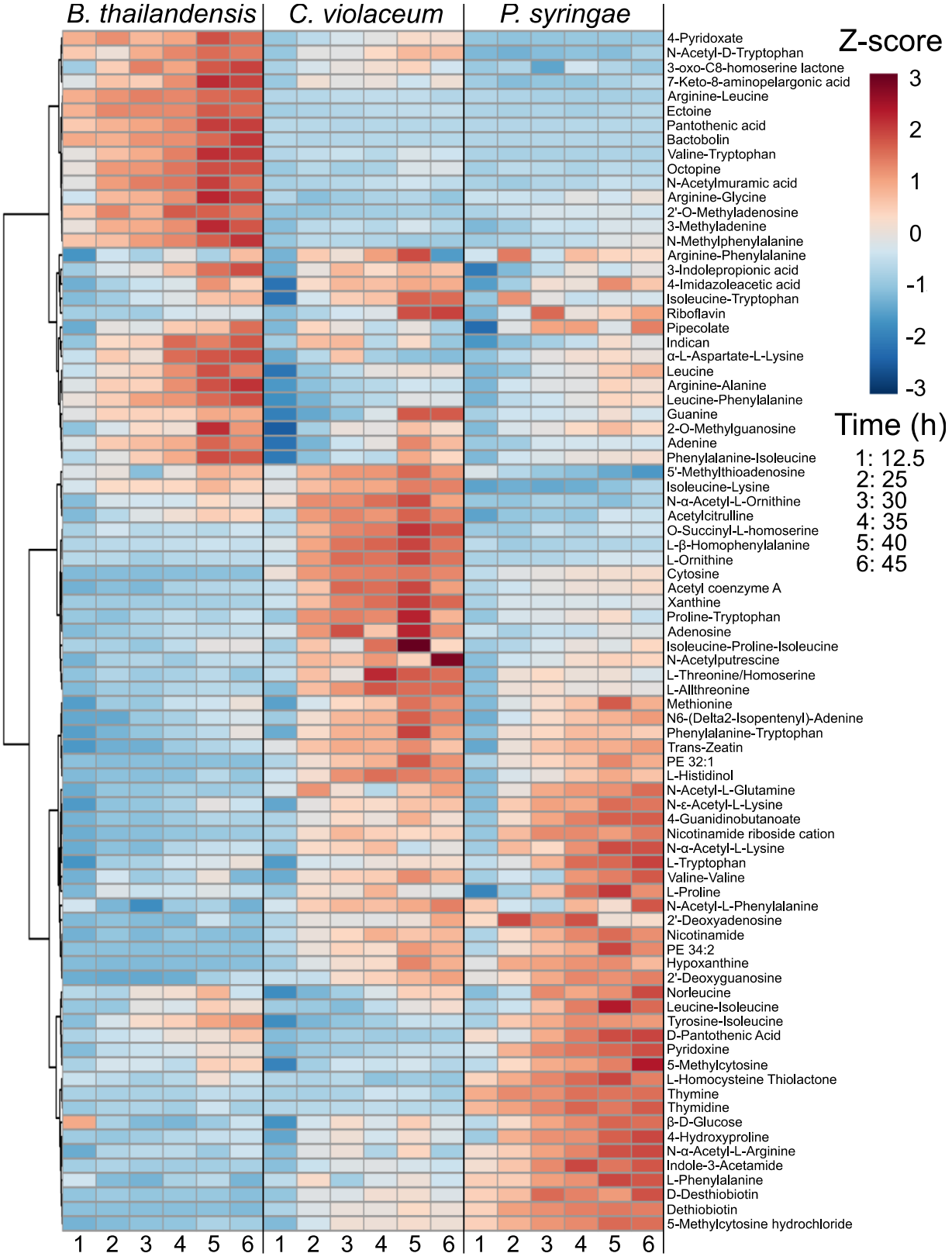

Figure 3.4. Released and identified exometabolites and their temporal dynamics.

Figure 3.4 (cont'd)

A heat map of identified exometabolites in polar positive mode is shown, where samples are columns are exometabolites are in rows. Each sample is the average of independent time point replicates (n = 3 or 4). Euclidean distance was calculated from Z-scored mass spectral profiles (containing peak areas). Prior to Z-scoring, features were normalized by an internal standard (ITSD) reference feature and cube root transformed. Features were clustered by Ward's method.

Exometabolites putatively identified at MSI level 2 were annotated by matching MS/MS fragmentation to a reference database. MSI level 2 exometabolites included secondary metabolites such as bactobolin, yersiniabactin, and acyl homoserine lactones (AHLs) produced by *B. thailandensis, P. syringae*, and *C. violaceum*, respectively. Bactobolin and yersiniabactin are bioactive molecules, previously characterized as a bacteriostatic antibiotic (100) and a siderophore/virulence factor (147), respectively. AHLs induce quorum sensing in *C. violaceum*, and are linked to the production of hydrogen cyanide, antibiotics, and proteases (95, 148). These putatively identified secondary exometabolites suggest that stationary phase is coordinated with shifts in metabolism, priming strains for competition via chemical warfare or nutrient scavenging. These data also suggest that a competitive phenotype may be standard among bacteria even in the absence of non-kin competitors, suggesting either priming for interspecific competition or engagement in intraspecific competition. This competitive priming is also supported by the observation of increased transcripts for transport systems involved in competition. For example, competitive transport systems included the type III secretion system in *B. thailandensis* and multidrug efflux systems for both *C. violaceum* and *P. syringae*. When comparing transcripts between times 45h to 12.5h, the aforementioned transport systems had a $\log_2$-fold change (LFC) in expression > 1. (See Dataset 1 at https://github.com/ShadeLab/Paper_Chodkowski_MonocultureExometabolites_2020/tree/master/Datasets). Finally, a large proportion of MSI level 2 exometabolites were dipeptides, suggesting either the degradation of proteins (58) or the formation of dipeptides by non-ribosomal peptide synthetases (NRPS), found in biosynthetic gene clusters (See Dataset 3 at https://github.com/ShadeLab/Paper_Chodkowski_MonocultureExometabolites_2020/tree/mas

ter/Datasets). In summary, there was a consistent accumulation of a diversity of exometabolites in stationary phase, including exometabolites that were intermediates in central carbon metabolism as well as secondary metabolites implicated in competition.

To maximize annotation of remaining unidentified MS/MS data, we performed chemical ontology analysis to determine chemical classes of exometabolites produced in stationary phase. Using *in silico* prediction of exometabolites by MS/MS fragmentation patterns, we putatively characterized compound classes (MSI level 3 designation). Broadly, carboxylic acids and derivatives were the most abundant type of exometabolite produced in stationary phase for all strains (**Figure 3.5A**). This is expected because carboxylic acid derivatives are prominent in cellular constituents and molecules involved in primary metabolism (e.g. TCA cycle). Their excess production, and release to relieve internal accumulation, may be due to stoichiometric constraints in metabolic network topology (149). However, MSI level 3 exometabolites revealed considerable quantification of exometabolites related to fatty acyls, organonitrogen compounds, organooxygen compounds, and benzene and substituted derivatives, suggesting additional classes of exometabolites contributing to the exometabolite pool that are unable to be identified by MSI level 1 and level 2 standards. These chemical ontologies were resolved further to the direct parent level (**Figure 3.5B**). Amino acids and peptides were the most abundant and common exometabolites across all identification levels. In particular, dipeptides were the most abundant exometabolite. Transcriptomics data also indicated that dipeptide transporters for each strain were either consistently expressed or differentially expressed over time (**Table 3.3**, See Dataset 1 at https://github.com/ShadeLab/Paper_Chodkowski_MonocultureExometabolites_2020/tree/mas

ter/Datasets). In summary, chemical ontology analysis revealed chemical classes represented in the exometabolite dataset but lacking identification and, revealed that dipeptides were a common exometabolite released by all strains.

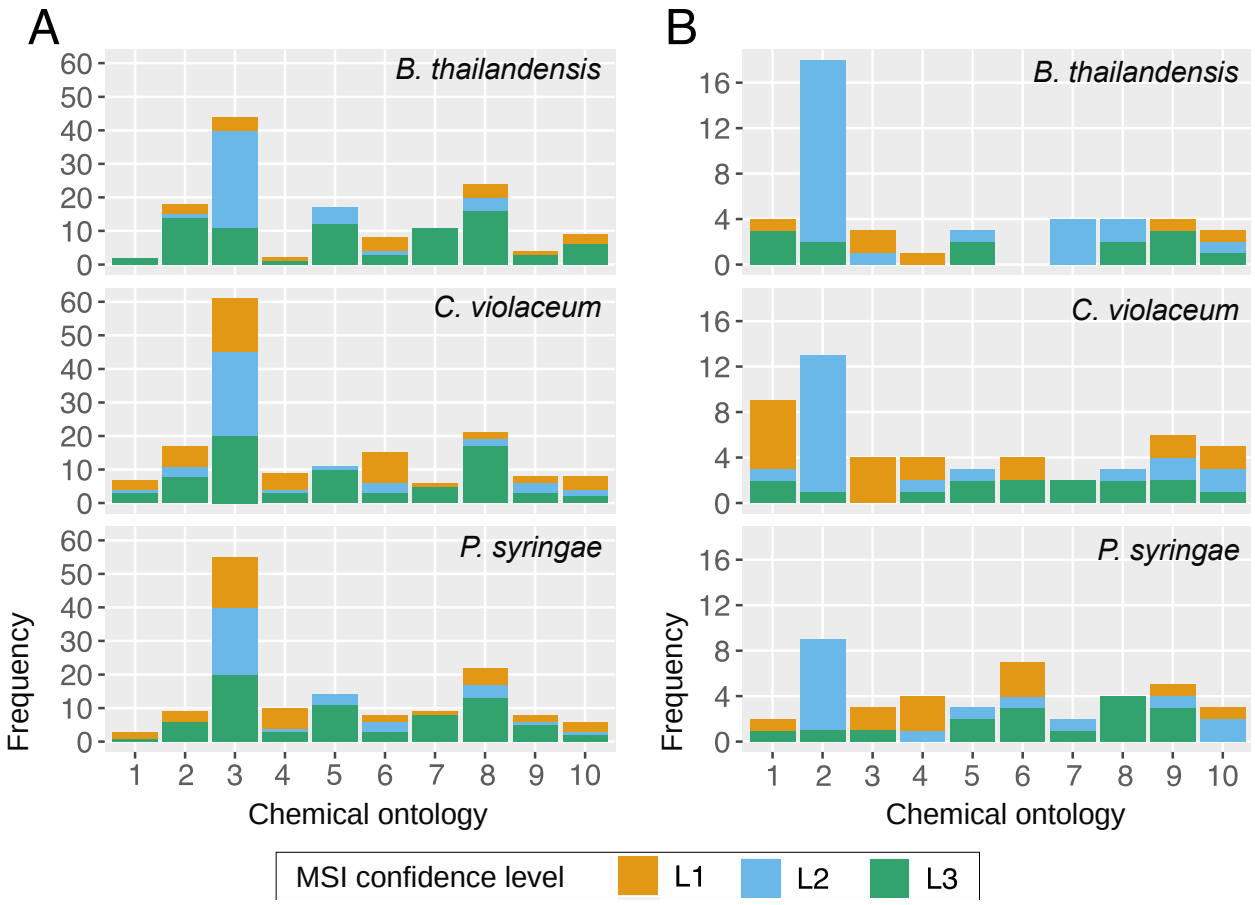

Figure 3.5. Chemical ontologies at different MSI levels.

ClassyFire was used to categorize identified (MSI level 1 and level 2) and in silico predicted MS/MS data (MSI level 3) at the **A**) class and **B**) direct parent levels. Identification confidence 1,2, and 3 refers to Metabolomics Standards Initiative (MSI) identification levels 1, 2, and 3, respectively. The top ten chemical ontologies are provided for each classification level. Chemical ontologies for panel A: 1) Azoles, 2) Benzene and substituted derivatives, 3) Carboxylic acids and derivatives, 4) Diazines, 5) Fatty Acyls, 6) Imidazopyrimidines, 7) Organonitrogen compounds, 8) Organooxygen compounds, 9) Purine nucleosides, 10) Pyridines and derivatives. Chemical ontologies for panel B: 1) Alpha amino acids, 2) Dipeptides, 3) Hydroxybenzoic acid derivatives, 4) Hydroxypyrimidines, 5) Medium-chain fatty acids, 6) N-acyl-alpha amino acids, 7)

Figure 3.5 (cont'd)

N-acyl-alpha amino acids and derivatives, 8) Peptides, 9) Purine nucleosides, 10) 6-alkylaminopurines.

Insights into stationary phase metabolic re-routing

We then aimed to interpret strain metabolism in stationary phase by focusing on exometabolites most confidently identified (MSI level 1). For each strain, we examined the 10 most abundant exometabolites that accumulated and were detected at the last time point (45 h) for positive and negative polar exometabolites. We included all MSI level 1 exometabolites in this analysis. Generally, the abundant, accumulated exometabolites that were distinct for each strain were also uniquely detected in those strains (**Figure 3.6**, ANOVA, all Q-values ≤ 0.01), with two exceptions: 5'-methylthioadenosine and hypoxanthine were also abundant in *Chromobacterium violaceum* media but not within its top 10 accumulated exometabolites. Transporters that had a $\log_2$-fold change (LFC) in expression (comparing times 45h to 12.5h) > 1 could be linked with their substrates for both *C. violaceum* and *P. syringae* (See Dataset 1 at https://github.com/ShadeLab/Paper_Chodkowski_MonocultureExometabolites_2020/tree/master/Datasets). This included substrates such as succinate and cytosine for *C. violaceum* and *P. syringae*, respectively. None of the most abundant exometabolites in *B. thailandensis* could be linked to a transporter with a large LFC. The majority of strain-specific abundant exometabolites suggest that each strain released a set of unique metabolic intermediates into the extracellular environment. This finding could have implications for how bacterial populations maintain viability through interspecies interactions in periods of nutrient exhaustion. Perhaps a simple explanation for differences in the types of exometabolites released could result from differences in the alteration of stationary phase metabolism.

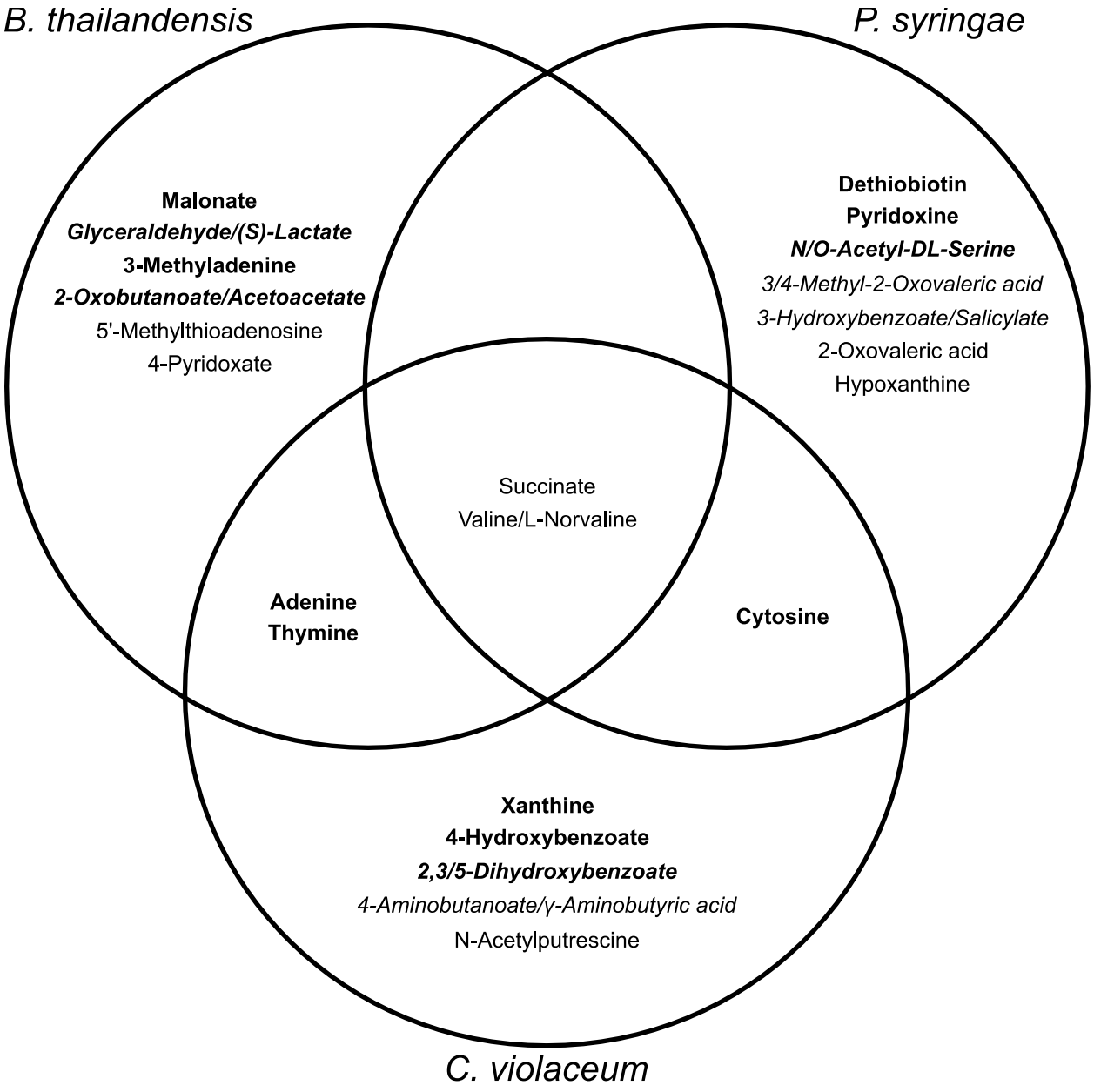

Figure 3.6. Distinctions and overlaps between the most abundant exometabolites in each strain.

Exometabolites in bold passed criteria for released. Exometabolites in italics are isomers and could not be resolved to determine the exact identification.

Of the most accumulated exometabolites, succinate was a common exometabolite detected in all strains, and this is unsurprising as it is directly involved in central metabolism. Notably, succinate did not meet our stringent definition of released and accumulating over stationary phase (**Figure 3.6**). However, its abundance and accumulation for all strains and its important role in central metabolism warranted further investigation. We overlaid temporal log fold changes in gene expression onto KEGG pathways involved in succinate production (**Figure 3.7**). These data suggest that all strains re-routed metabolism during stationary phase. For the most part, transcripts involved in glycolysis and the TCA were decreased in all strains (KEGG Pathways). With regard to succinate production, both *B. thailandensis* and *C. violaceum* appear to have re-routed metabolism to use the glyoxylate cycle, as supported by the increase in transcripts for isocitrate lyase and increase in transcripts involved in the ß-oxidation of fatty acids. *P. syringae* appears to have re-routed metabolism to use the methylcitrate cycle to generate succinate, as evidenced by the increase in transcripts for 2-methylisocitrate lyase. Other potential sources of succinate production include the GABA shunt and succinyl-CoA:acetate CoA-transferase in both *B. thailandensis* and *P. syringae*. In all strains, stationary phase results in exometabolite production that appears to coincide with alterations in metabolism.

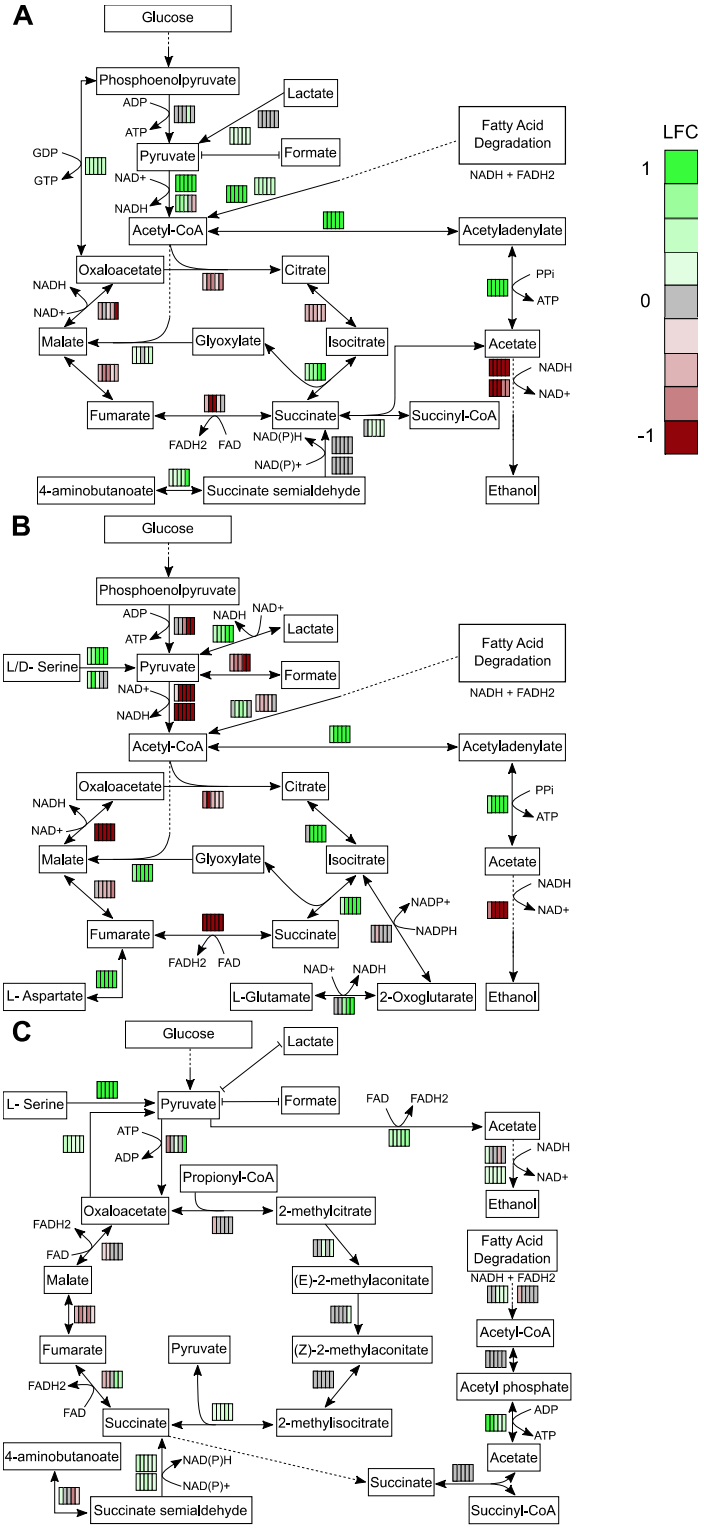

Figure 3.7. Temporal changes in transcriptomics reveal re-routing of metabolism towards succinate production.

Figure 3.7 (cont'd)

Log2-fold change (LFC) values were mapped onto pathways involved in succinate production for a) *B. thailandensis*, b) *C. violaceum*, and c) *P. syringae*. LFC values are represented by rectangles alongside each reaction in the pathway map. Each column represents the 5 stationary phase time points. Colors within each rectangle represent LFC (green-increased transcripts, red-decreased transcripts) compared to the exponential phase time point.

Discussion

Microbes can experience a feast-or-famine lifestyle in environments (e.g. soil, activated sludge, in the gut) where long periods of starvation are punctuated by short periods of nutrient flux (54-56, 134-137). Thus, microbes in particular environments predominantly exist in stationary phase. Understanding the metabolic response to stationary phase can reveal generalities as well as strain-specific strategies to maintain viability in nutrient-exhausted environments.

We studied exometabolite production in stationary phase across three bacterial strains. We specifically focused our analyses on released exometabolites, metabolites that accumulated in the medium over time. Even though we applied a very conservative definition to identify features that accumulated over time, we detected and characterized thousands of features that met our criteria. However, in the end, only a subset of these features could be identified using standards, MS/MS databases, and computational predictions based on chemical characteristics (**Figure 3.4**, **Appendix B Figures 8-10**, See Dataset 2 at https://github.com/ShadeLab/Paper_Chodkowski_MonocultureExometabolites_2020/tree/master/Datasets).

Exometabolites could accumulate over stationary phase by two mechanisms. First, exometabolites could be transported passively or actively across viable cells' membranes. Second, cells could lyse and spill primary metabolites and other debris into extracellular environment (150). Our results suggest that a major contributing factor to exometabolite accumulation for all three strains investigated here was exometabolite release from intact cells.

In fact, we did not observe a death phase over stationary phase (**Appendix B Figure 7**). Live cells generally remained at consistent levels throughout stationary phase. One generation during stationary phase was observed for both *B. thailandensis* and *P. syringae*. Given the decrease in transcripts observed for multiple genes in central metabolism (KEGG Pathways), this generation was likely the result of reductive cell division (151–153). Dead cells were present and in particular, increased for *P. syringae* throughout the time course. While dead cells could leak exometabolites, the accumulation of certain exometabolites (e.g. secondary metabolites) were identified and have been previously associated with production from viable cells in stationary phase cultures from each strain (100, 147, 148) Furthermore, our results are consistent with a previous study in *E. coli* that observed the extracellular accumulation of nucleobases upon entry into stationary phase (142). Ribosome degradation is initiated in growth-limiting environments and is a likely source of nucleobase accumulation due to the degradation of rRNA (154). We also observed the accumulation of various nucleobases in the extracellular environment across all strains, consistent with the concept of some common stationary phase phenomenon among bacteria. Additional evidence of exometabolite release from intact cells was provided by RNA-seq analysis. Transcriptomics results indicated the increase in transcripts for or consistent expression of transporters (See Dataset 1 at https://github.com/ShadeLab/Paper_Chodkowski_MonocultureExometabolites_2020/tree/master/Datasets). In a previous study, Paczia *et al.* also observed similar patterns of exometabolite accumulation in stationary phase in various strains (155). They were able to rule out lysis and determine that passive or active diffusion could explain exometabolite production in growth limited conditions. In integrating transcriptomics with exometabolomics, our study builds on

the findings of Paczia *et al.* to identify transporters likely involved in exometabolite accumulation and to provide insights into alterations in stationary phase metabolism. Findings from our work and from Paczia *et al.* in agreement with metabolic models that suggest that the extracellular accumulation of central metabolites could be attributed to costless metabolic secretions in resource poor environments (144). Unintuitively, the release of exometabolites by viable cells, and, particularly, release of central carbon intermediates, may be a common adaptation of bacteria in stationary phase. An interesting explanation is that the stoichiometry of metabolites is constrained by evolved metabolic network topology: some metabolites could be produced in excess to meet all metabolite requirements for a bacterium. Fitness tradeoffs of metabolite overproduction (e.g. toxic accumulation) could be alleviated through metabolite efflux (149).

In addition to the characterization of exometabolites implicated in cooperative interactions (e.g. central carbon intermediates or quorum sensing molecules), we also identified exometabolites implicated in competition. An antibiotic (bactobolin), with previously described bioactivity (145, 100, 156), was produced by *B. thailandensis* and a siderophore/virulence factor (yersiniabactin) was produced by *P. syringae* (147), representing interference (direct harm to neighbors) and exploitative (indirect negative interaction) competition strategies, respectively (157, 158). These exometabolites are involved in interspecies competition but, here, were produced in monoculture. While we did not identify an exometabolite in *C. violaceum* involved in competition, we did identify quorum sensing molecules, which are linked to the production of competitive exometabolites in this strain (95, 148). Taken together, the metabolic profile in each strain was altered in stationary phase and

resulted in production of both cooperative and competitive exometabolites. Simultaneous production of both cooperative and competitive exometabolites may be an advantageous strategy to sustain kin while maintaining competition for scarce resources (23, 144). Additional studies that include co-coculturing experiments are needed to understand the impact that these exometabolites may have on ecological dynamics and these interplay of biotic factors under changing environmental conditions.

Putative (MSI level 2) exometabolite identifications provided evidence for the release of dipeptides (**Figure 3.5B**) and transcriptomics provided evidence for differentially regulated or consistent expression of dipeptide transporters (See Dataset 1 at https://github.com/ShadeLab/Paper_Chodkowski_MonocultureExometabolites_2020/tree/master/Datasets). Hydrolysis by dipeptidyl peptidases of ribosomal proteins or degradation of other polypeptide chains can be one source of dipeptide production. Estimates in *E. coli* have shown that 50-80% of ribosomes were degraded upon transition from exponential phase to stationary phase (154). Interestingly, another source of dipeptides may be active production. Recent studies have examined dipeptide formation by adenylation domains in nonribosomal peptide synthetases (NRPS) (159, 160). All strains in our study have numerous NRPS that could contribute to the production of dipeptides (See Dataset 3 at https://github.com/ShadeLab/Paper_Chodkowski_MonocultureExometabolites_2020/tree/master/Datasets). Furthermore, one dipeptide was characterized as a cyclic dipeptide. Cyclic dipeptides can be involved in cell communication (161). Thus, the diverse chemical ecology that can be facilitated by dipeptides points to the importance of understanding how dipeptides are formed and of characterizing the environments that induce their production.

A clear limitation to our study is in the incomplete exometabolite annotations. Only 1.8% of released exometabolites could be identified. While exact molecule identifications are lagging behind the identification of new features, efforts have been put forth to chemically classify all MS/MS data (162). We used the same approach to computationally predict and classify the chemical ontology of MS/MS data not identified at MSI level 1 or level 2 (**Figure 3.5**). Differences between *in silico* predictions of MS/MS data (MSI level 3) and MSI levels 1 and 2 was most apparent at the class level (**Figure 3.5A**). This knowledge can be used to direct research efforts and analytical techniques to identify underrepresented classes of compounds. Targeted identification efforts of exometabolites will reveal uncharacterized biological phenomena occurring in experimental systems.

Microbes in growth-arrested states can re-route metabolism to maintain the proton motive force (PMF) and stabilize ATP levels (52). We used a combination of exometabolomics and transcriptomics to shed light on metabolic re-routing in each strain investigated. Notably, all three strains accumulated high levels of succinate, and this was further supported by RNA-seq data that showed an increase in transcripts in genes involved in succinate production (**Figure 3.7**). We found that the major metabolic re-routing in stationary phase included transitioning to the glyoxylate cycle in *B. thailandensis* and *C. violaceum* and to the methylcitrate cycle in *P. syringae*. This finding, specifically for *B. thailandensis*, agrees with previous studies in *B. thailandensis* and closely related strains. Previous studies found quorum-sensing mediated metabolic re-routing to the glyoxylate cycle during stationary phase in *B. thailandensis and Burkholderia glumae* as a mechanism to combat alkalinity toxicity (163, 164). Furthermore, the greatest increase in isocitrate lyase was observed in *Burkholderia cenocepacia*

during stationary phase compared to other abiotic stressors (165). This supports the notion that a re-routing metabolism to the glyoxylate cycle in stationary phase may be a shared feature among members of the genus *Burkholderia*. Prior evidence for stationary phase metabolic re-routing in both *C. violaceum* and *P. syringae* is lacking. However, a metabolic model in *C. violaceum* ATCC 12472 suggested metabolic re-routing to the glyoxylate cycle occurred in response to antibiotics in a streptomycin-resistant population (166). In support of succinate extracellular accumulation, we found that C4-dicarboxylic acid transporters were transcriptionally active in all three strains (See Dataset 1 at https://github.com/ShadeLab/Paper_Chodkowski_MonocultureExometabolites_2020/tree/master/Datasets). It could be that succinate export is facilitated by a succinate/proton symporter for maintenance of the PMF. However, both cycles involved in succinate production do not generate ATP, and the generation of ATP is are also necessary to maintain cell viability. While ATP could be generated through the production of acetate (**Figure 3.7**), we note that we did not quantify acetate and therefore are unable to confirm this scenario. Additional studies are needed to confirm the mechanisms of maintaining cell viability during stationary phase. Regardless, combining exometabolomic and transcriptomic approaches provided increased biological interpretation that could not have been achieved by either approach in isolation. The characterization of exometabolite production and metabolic response to stationary phase in monocultures sets the stage for understanding exometabolite-mediated interspecies interactions within a microbial community.

CHAPTER 4 : Bioactive exometabolites involved in competition strategies drive community member dynamics over stationary phase

Abstract

Some environments (e.g. soils) impose a stationary phase lifestyle, where microbes experience long periods of non-growth because of nutrient inaccessibility or short periods of nutrient flux. However, microbes can produce a diverse array of exometabolites in stationary phase that can shape the response and behaviors of surrounding neighbors in a microbial community. Knowledge gaps remain regarding the role of interspecies interactions in microbial communities, specifically the influence of exometabolite-mediated interactions during stationary phase. We evaluated the consequences of exometabolite interactions over stationary phase among three environmental bacteria: *Burkholderia thailandensis* E264 (ATCC 700388), *Chromobacterium violaceum* ATCC 31532, and *Pseudomonas syringae pv. tomato DC3000* (ATCC BAA-871). We grew each strain in monoculture and all coculture arrangements (3 pairwise cocultures and the 3-member community) in synthetic communities to investigate the responses (transcripts) and behaviors (exometabolites) of each member resulting from coculturing. We found that members' transcriptional dynamics were altered due to coculturing. These alterations could be attributed to the production and response to bioactive exometabolites involved in competition strategies. *B. thailandensis* had the largest influence on other synthetic community members, as it proactively responded to coculturing by upregulating biosynthetic gene clusters involved in the production of bioactive exometabolites. We also found that members' outcomes in the 3-member community were not always a simple summation of pairwise outcomes. These results reflect the importance of understanding how the maintenance of competitive strategies over stationary phase may contribute to community member dynamics during long periods of non-growth. These results also imply that bacterial

responses and behaviors in more complex communities may not always be the sum of individual effects.

Introduction

Bacteria interact with other bacteria and their environment within complex, multi-species communities. Bacterial interactions rely on the ability to sense and respond to both biotic and abiotic stimuli (189, 190). These stimuli can alter bacterial behaviors (191, 192), and ultimately, can also alter community functioning (193, 194). There is much evidence that bacterial taxa interact in the environment, as inferred from relatively strong co-occurrences (195, 196). And, it is expected that interspecies interactions play an important role in shaping microbial community dynamics (197). However, multiple stimuli in the environment make it difficult to disentangle influences for microbial community dynamics (198). Efforts to characterize interspecies interactions are important to understand how they shape microbial communities (76).

Interspecies interactions can be facilitated through small molecules (1). Extracellular small molecules are collectively referred to as exometabolites (2, 3, 5). Depending on the exometabolite produced, these molecules can mediate interspecies interactions that range from competitive to cooperative (86). Of these interaction types, competition has been shown to have a major influence in structuring microbial communities (23, 199, 200). Thus, competitive interactions that are mediated by exometabolites are also expected to influence to microbial community dynamics. In addition, different types of exometabolites can be employed

by bacteria to gain advantage in both exploitative (e.g. nutrient scavenging) and interference (direct cell damage) categories of competition.

Traditionally, competition has been viewed through the lens of resource acquisition (201). In these studies, competitiveness is modeled with respect to yield given resource consumption and growth (202, 203). However, competition for *survival* or *maintenance* may be just as important as competition for yield, especially during periods of resource limitation (204, 205). Competition for maintenance is likely prevalent in environments, such as soils, sequencing batch reactors, and the human gut, that experience long periods of nutrient famine punctuated by short periods of nutrient influx (55, 89, 136, 206). The stationary phase of a bacterial growth curve falls within this context of growth cessation, and pulses of nutrients may be transiently available as cells die and lyse (necromass), while the total population size remains stagnant. Stationary phase is often coordinated with a metabolic shift to secondary metabolism (53, 207). Therefore, an effective "maintenance" competitor may produce bioactive exometabolites, like antibiotics, which are often produced as a result of secondary metabolism. In particular, bacteria can activate biosynthetic gene clusters (BSGCs) to produce bioactive exometabolites (6). The activation of BSGCs is closely tied to stress responses, suggesting that bacteria can sense the stress of competition (24, 208). While it is known that certain exometabolites can trigger BSGC upregulation and, more generally alter transcription (209), there is much to understand about the outcomes of interspecies interactions for BSGCs in multi-member microbial communities.

Here, we build on our previous research to understand how exometabolite-mediated interactions among bacterial neighbors contribute to community outcomes in a simple, three-

member community (**Table 4.1**). These three members are commonly associated with terrestrial environments (soils or plants) and were chosen because of reported (145) and observed interspecies exometabolite interactions in the laboratory. We used a synthetic community approach (42) by applying our previously described transwell system (146), which allows for evaluation of "community goods" within a media reservoir that is shared among members. The members' populations are physically isolated by membrane filters at the bottom of each transwell, but can interact chemically via the reservoir. In our prior work, we investigated each member's exometabolites and transcription over stationary phase, and the objective was to understand monoculture responses (in minimal glucose media) before assembling the more complex 2- and 3- member communities. We found that each member in monoculture produced a variety of exometabolites in stationary phase, including bioactive molecules involved in competition (210). In this work, we build to 2- and 3- member arrangements to ask: How do members interact via exometabolites in simple communities during maintenance (stationary phase), and what are the competitive strategies and outcomes of those interactions? What particular genetic pathways, molecules, and members drive the responses? Which outcomes in 3-member community are predicted by the 2-member communities, and which are "greater than the sum of its parts"?

We found that *B. thailandensis* had a major influence on the transcriptional responses of both *C. violaceum* and *P. syringae*. This influence could be attributed to competition, which we defined as the enhancement of both interference and exploitative competition strategies. Furthermore, this resulted in non-additive transcriptional responses and exometabolite production, particularly for *B. thailandensis* with respect to BSGCs. These findings show that

diverse competitive strategies can be deployed even when bacterial neighbors are surviving rather than exponentially growing. Therefore, we suggest that contact-independent, exometabolite-mediated interference and exploitation are important competitive strategies in resource-limited environments and also support the non-yield outcome of maintenance.

Table 4.1.Bacterial members used in the SynCom system.

Member	*Burkholderia thailandensis* E264	*Chromobacterium violaceum* ATCC 31532	*Pseudomonas syringae* pv. tomato DC3000
Genome size (Mb)	*6.72*	4.76	6.54
Family	*Burkholderiaceae*	*Neisseriaceae*	*Pseudomonadaceae*
No. of CDSs[a]	*5639*	*4393*	*5576*
Chromosomes	*2*	*1*	*1*
Plasmids	*0*	*0*	*2*

[a]CDSs, Coding sequences.

Materials and Methods

Bacterial strains and culture conditions

Freezer stocks of *B. thailandensis*, *C. violaceum*, and *P. syringae* were plated on half-concentration Trypticase soy agar (TSA50) at 27°C for at least 24 h. Strains were inoculated in 7 ml of M9–0.2% glucose medium and grown for 16 h at 27°C, 200 rpm. Cultures were then diluted into 50 ml M9-0.2% glucose medium such that exponential growth phase was achieved after 10 h of incubation at 27°C, 200 rpm. Strains were then diluted in 50 ml M9 glucose medium to target ODs (*B. thailandensis* 0.3 OD, *C. violaceum*: 0.035 OD, *P. syringae* 0.035 OD) such that stationary phase growth would be achieved by all members within a 2 h time frame after 24 h incubation in the transwell plate. The glucose concentration in the final back-dilution varied upon community arrangement- 0.067% for monocultures, 0.13% for pairwise cocultures, and 0.2% for the 3-member community. For each strain, 48 ml of back-diluted culture was transferred as 4 mL aliquots in 12, 5 mL Falcon tubes prior to transferring them into the transwell plate.

Synthetic community experiments

Transwell plate preparation was performed as previously described (146). Briefly, we used sterile filter plates with 0.22-µm-pore polyvinylidene difluoride (PVDF) filter bottoms (Millipore MAGVS2210). Prior to use, filter plates were washed three times with sterile water using a vacuum apparatus (NucleoVac 96 vacuum manifold; Clontech Laboratories). The filter of well H12 was removed with a sterile pipette tip and tweezer, and 31 ml of M9 glucose medium was added to the reservoir through well H12. The glucose concentration in the reservoir varied

upon community arrangement- 0.067% for monocultures, 0.13% for pairwise cocultures, and 0.2% for the 3-member community. Each well was then filled with 130 µL of culture or medium. For each plate, a custom R script (RandomArray.R [see the GitHub repository]) was used to randomize community member placement in the wells so that each member occupied a total of 31 wells per plate. In total, there were 7 community conditions- 3 monocultures, 3 pairwise cocultures, and the 3-member community. A time course was performed for each replicate. The time course included an exponential phase time point (12.5 h) and 5 time points assessed every 5 h over stationary phase (25 h – 45 h). Four biological replicates were performed for each community condition for a total of 28 experiments. For each experiment, 6 replicate filter plates were prepared for destructive sampling for a total of 168 transwell plates.

Filter plates were incubated at 27°C with gentle shaking (~0.32 rcf). For each plate, a custom R script (RandomArray.R [see the GitHub repository]) was used to randomize wells for each organism assigned to RNA extraction (16 wells) and flow cytometry (5 wells). The following procedure was performed for each organism when a transwell plate was destructively sampled: i) wells containing spent culture assigned to RNA extraction were pooled into a 1.5 mL microcentrifuge tube and flash frozen in liquid nitrogen and stored at -80 until further processing. ii) 20 µL from wells assigned for flow cytometry were diluted into 180 µL Tris-buffered saline (TBS; 20 mM Tris, 0.8% NaCl [pH 7.4]). In plate arrangements where *P. syringae* was arrayed with *B. thailandensis*, *P. syringae* had a final dilution of 70-fold in TBS. In plate arrangements where *P. syringae* was arrayed in monoculture or in coculture with *C. violaceum*, *P. syringae* had a final dilution of 900-fold in TBS. Final dilutions for *B. thailandensis* and *C. violaceum* were 1,300-fold and 1,540-fold, respectively. iii) Spent medium (~31 ml) from the

shared reservoir was transferred to 50 mL conical tubes, flash-frozen in liquid nitrogen and stored at −80 °C prior to metabolite extraction.

Flow cytometry

Diluted cultures were stained with the Thermo Scientific LIVE/DEAD BacLight bacterial viability kit at final concentrations of 1.5 µM Syto9 (live stain) and 2.5 µM propidium iodide (dead stain). Two hundred microliters of stained cultures were transferred to a 96-well microtiter U-bottom microplate (Thermo Scientific). Twenty microliters of sample were analyzed on a BD Accuri C6 flow cytometer (BD Biosciences) at a fluidics rate of 66 µl/min and a threshold of 500 on an FL2 gate. The instrument contained the following optical filters: FL1-533, 30 nm; FL2-585, 40 nm; and FL3, 670-nm longpass. Data were analyzed using BD Accuri C6 software version 1.0.264.21 (BD Biosciences).

RNA extraction

RNA was extracted using the E.Z.N.A. Bacterial RNA kit (Omega Bio-tek, Inc.). An in-tube DNase I (Ambion, Inc AM2222, 2U) digestion was performed to remove DNA from RNA samples. RNA samples were purified and concentrated using the Qiagen RNAeasy MinElute Clean up Kit (Qiagen, Inc). Ten random samples were chosen to assess RNA integrity on an Agilent 2100 Bioanalyzer.

RNA sample prep, sequencing, QC, read preprocessing, and filtering

Standard operating protocols were performed at the Department of Energy Joint Genome Institute as previously described (210).

Pseudoalignment and counting

Reads from each library with pseudoaligned to the transcriptome of each strain with kallisto (172). Raw counts from each library were combined into a gene count matrix for each strain. The gene count matrix was used for downstream analyses.

Quality filtering and differential gene expression analysis

Count matrices for each member were quality filtered in two steps: genes containing 0 counts in all samples were removed, and genes with a transcript count of ≤10 in more than 90% of samples were removed. DESeq2 (173) was used to extract size factor and dispersion estimates. These estimates were used as external input into ImpulseDE2 for the analysis of differentially regulated genes (211). Case-control (Cocultures-monoculture control) analyses were analyzed to identify both permanent and transient regulated genes at an FDR-corrected threshold of 0.01. For each member, differences in gene regulation between the three coculture conditions was visualized with venn diagrams using the VennDiagram package.

The initial differential gene expression analysis compared each coculture to the monoculture control, separately. It was revealed that were was a subset of genes that were only differentially expressed in the 3-member community. These genes were parsed from the dataset and used to perform two additional analyses in ImpulseDE2. Case-control analyses

were performed to analyze differential expression between the 3-member community to each of the pairwise cocultures as controls. Functional enrichment analysis was performed on the collection of genes determined to have unique differential expression in the 3-member community using the BiNGO package (212) in Cytoscape.

COG analysis

Protein fasta files were downloaded from NCBI and uploaded to eggNOG-mapper v2 (http://eggnog-mapper.embl.de/) to obtain Clusters of Orthologous Groups (COG) categories. Genes corresponding to COGs were categorized as upregulated or downregulated based on their temporal expression patterns and plotted using ggplot2.

RNA-seq principal coordinates analysis and statistics

We extracted genes that were differentially expressed with an FDR-corrected threshold of < 0.01 and a log2 fold-change >1 or < -1. A variance-stabilizing transformation was performed on normalized gene matrices using the rlog function in DESeq2. A distance matrix based on the Bray-Curtis dissimilarity metric was then calculated on the variance-stabilized gene matrices and principal coordinates analysis was performed using the R package vegan. Principal coordinates were plotted using ggplot2. Coordinates of the first two PCoA axes were used to perform Protest analysis using the protest function in vegan. Dissimilarity matrices were used to perform PERMANOVA and variation partitioning and using the adonis and varpart functions in vegan, respectively. The RVAideMemoire package was used to perform a post-hoc pairwise PERMANOVAs.

Circos plots

A subset of the top ~500 of differentially regulated genes was determined for each member by assessing differential expression in the 3-member community. A log2 fold-change (LFC) cutoff of at least > 1.5 or < -1.5 was used to capture both upregulated and downregulated genes. The LFC threshold needed to be met in at least one timepoint. We then filtered these genes by those that had differential expression with a significance cutoff of < 0.01 (FDR corrected). *P. syringae* genes encoded on plasmids were an exception. We extracted all coding sequence genes from both plasmids because the entirety of each plasmid could be visualized on a Circos plot with high resolution. From these genes of interest, a variance-stabilizing transformation was performed on normalized gene matrices using the rlog function in DESeq2 and Z-scored on a per gene basis. Circular genome plots were generated in Circos version 0.69-5. Pseudo-genes composed of the minimum and maximum Z-scores were added to each of four tracks to make the Z-score color scale comparable across all community arrangements. Functional enrichment analysis was performed on the collection of genes within each *P. syringae* plasmid using the BiNGO package in Cytoscape.

Biosynthetic gene cluster (BSGC) analysis

NCBI accession numbers were uploaded to antiSMASH 6 beta bacterial version (213) to identify genes involved in BSGCs using default parameters. Where possible, literature-based evidence and BSGCs uploaded to MIBiG (214) were used to better inform antiSMASH predictions. Log2 fold-changes (LFCs) were calculated for all predicted biosynthetic genes within each predicted cluster by comparing coculture expression to monoculture expression at

each time point. Average LFCs were calculated from all predicted biosynthetic genes within a predicted BSGC at each time point. Temporal LFC trends were plotted using ggplot2. An upregulated BSGC was defined as a BSGC that had at least two consecutive time points in stationary phase with a LFC > 1.

Network analysis

Unweighted co-expression networks were created from quality filtered and normalized expression data. Networks were generated for pairwise cocultures containing *B. thailandensis*. First, data were quality filtered as previously described (See section: *Quality filtering and differential gene expression analysis*). Then, normalized expression data was extracted from DESeq2. Biological replicates for each member within each timepoint were averaged by mean. Interspecies networks were then inferred from the expression data using the context likelihood of relatedness (215) algorithm within the R package Minet (216). Gene matrices for each coculture pair were concatenated to perform the following analysis. Briefly, the mutual information coefficient was determined for each gene-pair. To ensure robust detection of co-expressed genes, a resampling approach was used as previously described (217). Then, a Z-score was computed on the mutual information matrix. A Z-score threshold of 4.5 was used to determine an edge in the interspecies network. Interspecies networks were uploaded into Cytoscape version 3.7.1. for visualization, topological analysis, and enrichment analysis (218).

Gene annotation and gene ontology files were obtained for *B. thailandensis*, *P. syringae,* and *C. violaceum* for enrichment analyses. For *B. thailandensis,* annotation and ontology files

were downloaded from the Burkholderia Genome Database (https://www.burkholderia.com). For *P. syringae*, annotation and ontology files were downloaded from the Pseudomonas Genome Database (http://www.pseudomonas.com/strain/download). Annotation and ontology files for *C. violaceum* were generated using Blast2GO version 5.2.5 (219). InterProScan (220) with default parameters were used to complement gene annotations from *C. violaceum*. GO terms were assigned using Blast2GO with default parameters. In addition, genes involved in secondary metabolism were manually curated and added to these files as individual GO terms. These genes were also used to update the GO term GO:0017000 (antibiotic biosynthetic process), composed of a collection of all the biosynthetic genes. (See section: *Biosynthetic gene cluster analysis*).

Topological analysis was performed as follows: Nodes were filtered from each coculture network to only select genes from one member. The GLay community cluster function in Cytoscape was used to determine intra-member modules. Functional enrichment analysis was then performed on the modules using the BiNGO package in Cytoscape.

To determine interspecies co-regulation patterns, we filtered network nodes that contained an interspecies edge. Functional enrichment analysis was performed on the collection of genes containing interspecies edges for each member using the BiNGO package in Cytoscape. Modules of interest (e.g. thailandamide and malleilactone) were filtered in Cytoscape for visualization. The biosynthetic gene cluster organization of thailandamide and malleilactone were obtained from MIbig and drawn in InkScape.

Protein sequences from an interspecies gene of interest from the thailandamide module cluster (CLV_2968) and an interspecies gene of interest from the malleilactone module cluster

(PSPTO_1206) were obtained. A protein blast for each protein was run against *B. thailandensis* protein sequences. *B. thailandensis* locus tags were extracted from the top blast hit from each run. Normalized transcript counts for these 4 genes of interest were plotted in R. Time course gene trajectories were determined using a loess smoothing function.

Non-additive gene expression

The quality filtered and normalized expression matrix from each community member was used to extract log2 fold-change (LFC) values within DESeq2. LFCs were calculated by comparing transcript counts from each time point to its respective time point in the monoculture condition. LFCs were converted to fold-changes (FC). Non-additive outcomes were determined based on the null expectation that FCs in the 3-member community should reflect a summation of FCs from the pairwise cocultures. The thresholds for assigning a gene as non-additive upregulation was as follows:

$$(TM/MC)/(PWC1/MC+PWC2/MC) > 1.2$$

Where TM are the gene counts in the 3-member community, MC are the gene counts in the monoculture condition, and PWC1/PWC2 are the gene counts in the pairwise coculture conditions 1 & 2, respectively. Non-additive gene expression patterns were determined at each time point and plotted using ggplot2. Venn diagrams were also created to analyze the patterns of non-additivity across the time series and between the exponential phase time point and

stationary phase times points. Functional enrichment analysis was performed on the collection of genes determined to have non-additive upregulation using the BiNGO package in Cytoscape.

LCMS sample preparation and data acquisition

Standard operating protocols were performed at the Department of Energy Joint Genome Institute as previously described (210).

Feature detection

MZmine2 (167) was used for feature detection and peak area integration as previously described (210). Select exometabolites were identified in MZmine2 by manual observation of both MS and MS/MS data. We extracted quantities of these identified exometabolites for ANOVA and Tukey HSD post-hoc analysis in R.

Feature filtering and HM visualization

We filtered features in three steps to identify coculture-accumulated exometabolites. The feature-filtering steps were performed as follows on a per-member basis: (i) retain features where the maximum peak area abundance occurred in a coculture community arrangement ; (ii) a noise filter, the minimum peak area of a feature from a replicate at any time point needed to be 3 times the maximum peak area of the same feature in one of the external control replicates, was applied; (iii) coefficient of variation (CV) values for each feature calculated between replicates at each time point needed to be less than 20% across the time series.

Four final feature data sets from polar and nonpolar analyses in both ionization modes were analyzed in MetaboAnalyst 5.0 (221). Features were normalized by an ITSD reference feature (see Dataset 5 at https://github.com/ShadeLab/Paper_Chodkowski_MonocultureExometabolites_2020/tree/master/Datasets) and cube root transformed. Reference features for polar analyses in positive ([13C,15N]proline) and negative ([13C,15N]alanine) modes were determined by the ITSD with the lowest CV value across all samples. The reference feature for nonpolar data sets was the ITSD ABMBA. Heat maps were generated in MetaboAnalyst using Ward's clustering algorithm with Euclidean distances from Z-scored data. Data for each sample are the averages from independent time point replicates (n = 2 to 4). Normalized and transformed data sets were exported from MetaboAnalyst to generate principal-coordinate analysis (PCoA) plots in R.

Mass spectrometry principal coordinates analysis and statistics

A distance matrix based on the Bray-Curtis dissimilarity metric was used to calculate dissimilarities between exometabolite profiles. Principal coordinates analysis was performed using the R package vegan. Principal coordinates were plotted using ggplot2. Coordinates of the first two PCoA axes were used to perform Protest analysis using the protest function in vegan. Dissimilarity matrices were used to perform PERMANOVA and variation partitioning and using the adonis and varpart functions in vegan, respectively. The RVAideMemoire package was used to perform a post-hoc pairwise PERMANOVAs. Monoculture community arrangements were removed to focus on coculture trends.

Non-additive metabolomics production

All reference standard normalized, filtered features (across both polarities and ionization modes) were combined. Non-additive outcomes were determined based on the null expectation that fold-changes (FC) in the 3-member community should reflect a summation of FCs from the pairwise cocultures. The thresholds for assigning a metabolomic feature as non-additive production was as follows:

$$(TM)/(PWC1 + PWC2 + PWC3) > 1.5$$

Where TM is the peak area abundance in the 3-member community, and PWC1/PWC2/PWC2 are the peak area abundance in the pairwise coculture conditions 1,2, and 3, respectively. FCs were determined at each time point. A feature was determined to be produced in the 3-member community in a non-additive manner if it was above the FC threshold at least 3 times during stationary phase. At each time point, a Z-scored distribution of FCs was plotted in R. Z-scores were extracted from exometabolite of interest (thailandamide, pyochelin, and capistruin) to plot as vertical ablines on the Z-scored distributions. In addition, the non-additive features were extracted from the dataset to generate a heat map in MetaboAnalyst. Ward's clustering algorithm was used with Euclidean distances from Z-scored data. Data for each sample are the averages from independent time point replicates (n = 2 to 4).

To find statistical support for non-additive exometabolite production in the 3-member community, we created an "expected" time course abundance for identified exometabolites

that had non-additive upregulation (thailandamide, pyochelin, and capistruin). The "expected" time course abundance was determined by calculating the summation of peak abundances across pairwise cocultures with *B. thailandensis*. Due to the issue of replicate independence for each time course, the standard deviation would vary depending on what replicates were combined. As a conservative approach, we permuted all possible pairwise coculture combinations and used the replicate combination that resulted in the highest standard deviation. The time course peak abundance of thailandamide, pyochelin, and capistruin from pairwise cocultures with *B. thailandensis*, from the 3-member community, and from the "expected" 3-member community were plotted in ggplot2. We then ran a repeated measures permutation ANOVA to compare the time course peak abundance of thailandamide, pyochelin, and capistruin observed in the 3-member community to the "expected" 3-member community. A post-hoc pairwise t-test was performed to observe which time points were statistically significant. We note each iteration of repeated measures ANOVA would result in different statistical result. This was because the replicate identifiers for the "expected" time course were arbitrarily assigned. For this reason, we only considered a test significant if it was consistently below a *p* threshold of 0.05 across 10 iterations of the code.

Code availability

Computing code, workflows, and data sets are available at [insert GitHub link]. R packages used during computing analyses included DEseq2 (173), ImpulseDE2 (211), Minet (216), vegan 2.5-4 (178), ggplot2 (222), VennDiagram (179), RVAideMemoire (180), rtracklayer (223), viridis (224), and helper functions (184, 185, 187, 225).

Data availability

Genomes for *B. thailandensis*, *C. violaceum*, and *P. syringae* are available at the National Center for Biotechnology Information (NCBI) under accession numbers NC_007651 (Chromosome I)/NC_007650 (Chromosome II), NZ_PKBZ01000001, and NC_004578 (Chromosome)/NC_004633 (Plasmid A)/NC_004632 (Plasmid B), respectively. An improved annotated draft genome of *C. violaceum* is available under NCBI BioProject accession number PRJNA402426 (GenBank accession number PKBZ00000000). Data for resequencing efforts for *B. thailandensis* and *P. syringae* are under NCBI BioProject accession numbers PRJNA402425 and PRJNA402424, respectively. Metabolomics data and transcriptomics data are also available at the JGI Genome Portal (226) under JGI proposal identifier 502921. MZmine XML parameter files for all analyses can be viewed at and downloaded from GitHub (see Dataset 7 at https://github.com/ShadeLab/Paper_Chodkowski_MonocultureExometabolites_2020/tree/master/Datasets). Large data files (e.g., MZmine project files) are available upon request. Other data sets are also available on GitHub [Insert GitHub link for supplementary files].

Results

Stationary phase dynamics of microbial communities: transcriptional responses

We had four replicate, independent timeseries of each of seven community arrangements (three monocultures plus four cocultures of every pair and the 3-member arrangement), and here focus on the coculture analyses to gain insights into community outcomes. A range of 518 to 1204 genes were differentially expressed by each member in

coculture, irrespective of the identity of neighbors (**Appendix B Figure 11**, FDR< 0.05). In addition, each member also had differential gene expression that was unique to particular neighbor(s). Summarizing across all coculture arrangements, 2,712/5639 (48.1%), coding sequences (CDSs), 3267/4393 CDSs (74.4%), and 4974/5576 CDSs (89.2%) genes in *B. thailandensis*, *C. violaceum*, and *P. syringae* were differentially expressed, respectively. Both community membership and time contributed to the transcriptional response of each member (**Figure 4.1**, **Appendix A Table 9**). Together, these data suggest that there are both general and specific consequences of neighbors for the transcriptional responses of these bacterial community members.

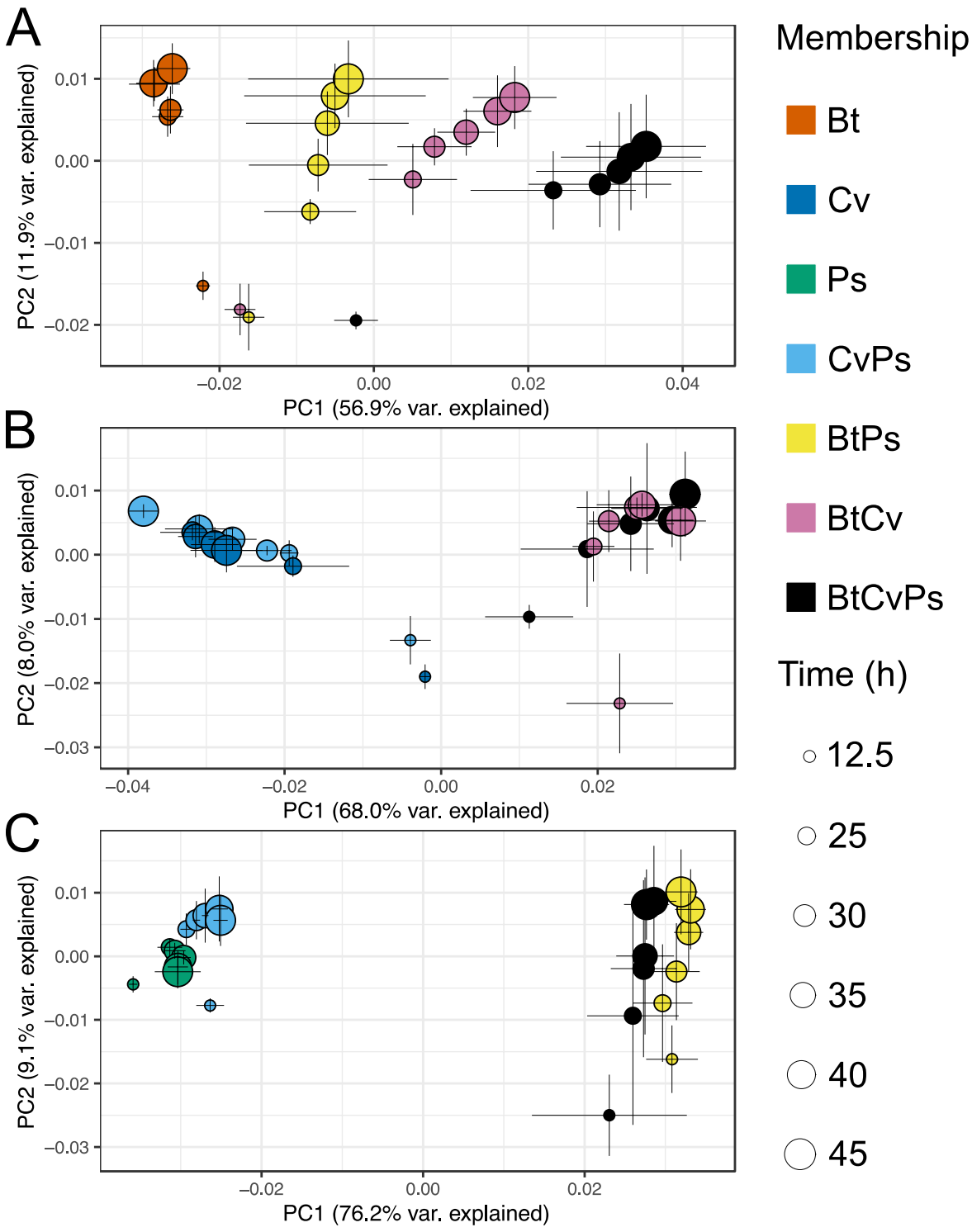

Figure 4.1. Transcriptional responses are driven by community membership and time.

Figure 4.1 (cont'd)

Shown are principal coordinates analysis (PCoA) plots for *B. thailandensis* (Bt, A), *C. violaceum* (Cv, B), and *P. syringae* (Ps, C). Each point represents a mean transcript profile for a community member given a particular community arrangement (neighbor(s) included, indicated by symbol color) and sampled at a given time point over exponential and stationary growth phases (in hours since inoculation, h, indicated by symbol size, n=3 to 4 replicates per timepoint/community arrangement). The Bray-Curtis distance metric was used to calculate dissimilarities between transcript profiles. Error bars are 1 standard deviation around the mean axis scores.

Temporal trajectories in transcript profiles were generally reproducible across replicates for each member given a particular community arrangement (PROTEST analyses, **Appendix A Table 10**). Each member had a distinct transcript profiles ($0.480 \leq r2 \leq 0.778$ by Adonis; P value, 0.001; all pairwise false discovery rate [FDR]-adjusted P values, ≤0.068 except for the *C. violaceum* coculture with *B. thailandensis* vs 3-member comparison, **Appendix A Table 11**). For all ordinations, the major contribution to the variation was community membership (Axis 1) followed by time (Axis 2), with the most variation was explained by the interaction between time and membership (**Appendix A Table 9**). Membership alone accounted for 60.6% and 77.0% of the variation explained in *C. violaceum* and *P. syringae* analyses, respectively and 46.3% in the *B. thailandensis* analysis (**Appendix A Table 11**).

When included in the community, *B. thailandensis* strongly determined the transcript profiles of the other two members. For example, the inclusion of *B. thailandensis* in a coculture differentiated transcript profiles for both *C. violaceum* and *P. syringae* (**Figure 4.1B** and **Figure 4.1C**). Thus, *B. thailandensis* appears to have a dominating influence on the transcriptional response of neighbors, and these responses were dynamic with respect to time.

We analyzed clusters of orthologous groups of proteins (COGs) to infer the responses of members to their neighbors. Differentially expressed genes were categorized as upregulated or downregulated based on temporal patterns and representation in COG groups (**Appendix B Figure 12**). We focused on the largest discrepancies between upregulated and downregulated within COG groups, which provide insights into broad biological processes affected by exometabolite interactions. COG groups trending towards upregulation in *B. thailandensis* included secondary metabolites biosynthesis, transport, and catabolism [Q], signal transduction

mechanisms [T], and cell motility [N] while COG categories trending towards downregulation included cell cycle control, cell division, chromosome partitioning [D], translation, ribosomal structure and biogenesis [J], and defense mechanisms [V]. These results suggest that *B. thailandensis* responds to neighbors via downregulation of growth and reproduction and upregulation of secondary metabolism. We therefore hypothesized that *B. thailandensis* was producing bioactive exometabolites against *C. violaceum* and *P. syringae* to competitively inhibit their growth.

Because of the strong transcript response of *C. violaceum* and *P. syringae* when neighbored with *B. thailandensis* (**Figure 4.1B & 4.1C**), we first focused on COG group trends within community arrangements with *B. thailandensis* (**Appendix B Figure 12B** & **Appendix B Figure 12C**, rows 2 & 3). COG groups tending towards upregulation in *C. violaceum* and *P. syringae* were translation, ribosomal structure and biogenesis [J] and replication, recombination, and repair [L], respectively. COG groups tending towards downregulation in *C. violaceum* and *P. syringae* were signal transduction mechanisms [T] and secondary metabolites biosynthesis, transport, and catabolism [Q], respectively. These results suggest that presence of *B. thailandensis* alters its neighbors ability to respond to the environment and inhibits secondary metabolism.

We were interested in understanding patterns of differential gene regulation and how individual genes contribute to the observed dynamics in **Figure 4.1**. The top ~500 differentially expressed genes (see methods: *Circos plots*) were visualized by genomic location and temporal dynamics (**Appendix B Figure 13**-**Appendix B Figure 15**). These results show that the gene dynamics for *C. violaceum* and *P. syringae* when grown in the 3-member community are

consistent with each neighbor's gene dynamics when grown only with *B. thailandensis* (**Appendix B Figure 14 and Appendix B Figure 15**, heatmap, outer two tracks vs. inner two tracks). Interestingly, 68.4% (340 genes) of the top differentially regulated genes in *B. thailandensis* were located on chromosome II despite chromosome II only accounting for 44.0% of all coding sequences (2365 coding sequences). In addition, nearly all *P. syringae* plasmid genes were upregulated when *P. syringae* was neighbored with *B. thailandensis*. These plasmids were significantly enriched for processes related to DNA recombination, recombinase activity, and DNA binding/integration (GO enrichment, **Appendix A Table 12**).

Stationary phase dynamics of microbial communities: exometabolomic responses

Because member populations are physically separated in the SynCom transwell system but allowed to interact chemically, observed transcript responses in different community arrangements are inferred to result from exometabolite interactions. Spent medium from the shared medium reservoir was collected from each transwell plate and analyzed using mass spectrometry to detect exometabolites. We focused our analysis on those exometabolites that had maximum accumulation in a coculture community arrangement (either in pairs or in 3-member community). Consistent with the transcript analysis, we found that both community membership and time explained the exometabolite dynamics, and that the explanatory value of membership and time was maintained across all polarities and ionization modes (**Figure 4.2** and **Appendix A Table 13**).

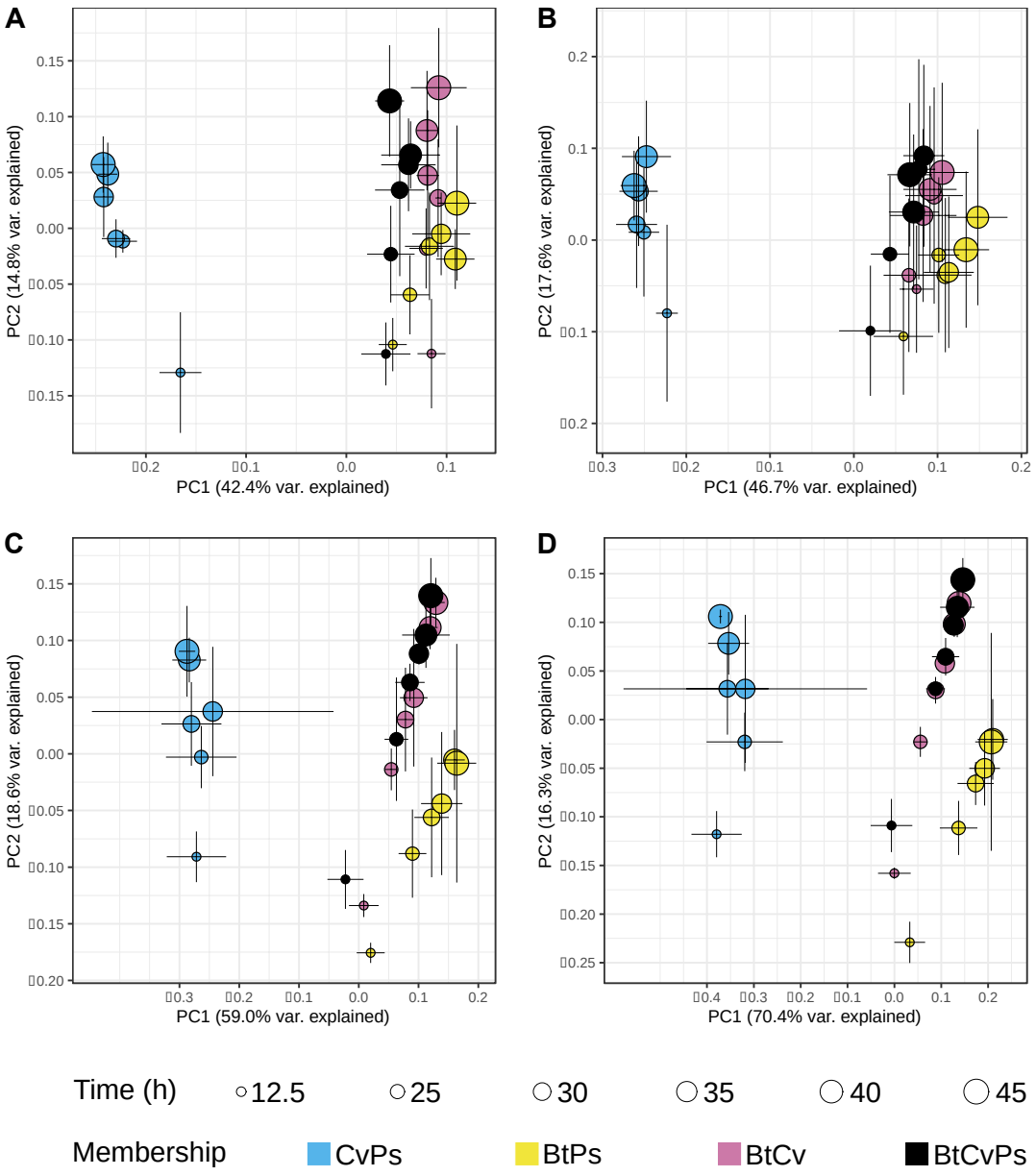

Figure 4.2. Bacterial community exometabolite profiles differ by community membership and time.

Shown are PCoA plots for exometabolite profiles from the following mass spectrometry modes: polar positive (A), polar negative (B), nonpolar positive (C), and nonpolar negative (D). Each

Figure 4.2 (cont'd)

point represents the mean exometabolite profile (relative contributions by peak area) given a particular community membership (indicated by symbol color) at a particular time point (indicated by symbol shape). The Bray-Curtis distance metric was used to calculate dissimilarities between exometabolite profiles. Error bars are 1 standard deviation around the mean axis scores (n= 2 to 4 replicates). Bt is *B. thailandensis*, Cv is *C. violaceum*, and Ps is *P. syringae*.

Temporal trajectories in exometabolite profiles were generally reproducible across replicates with some exceptions (Protest analyses, **Appendix A Table 14**, Supplemental File 2.1). Exometabolite profiles were distinct by community membership ($0.475 \leq r2 \leq 0.662$ by Adonis; P value, 0.001; all pairwise false discovery rate [FDR]-adjusted P values, ≤0.025, **Appendix A Table 15**), and also dynamic over time. As observed for the member transcript profiles, and the interaction between membership and time had the highest explanatory value for the exometabolite data (**Appendix A Table 13**).

We found that the *C. violaceum-P. syringae* coculture exometabolite profiles were consistently the most distinct from the other coculture memberships (**Figure 4.2**), supporting, again, that the inclusion of *B. thailandensis* was a major driver of exometabolite dynamics, possibly because it provided the largest or most distinctive contributions to the community exometabolite pool. Indeed, we observed that a majority of the most abundant exometabolites were either detected uniquely in the *B. thailandensis* monoculture or accumulated substantially in its included community arrangements (**Appendix B Figure 16**). Some exometabolites detected in *B. thailandensis*-inclusive communities were not detected in its monocultures (**Appendix B Figure 16D**), suggesting that the inclusion of neighbors contributed to the accumulation of these particular exometabolites (e.g. upregulation of biosynthetic gene clusters or lysis products). *C. violaceum* and *P. syringae* contributed less to the 3-member community exometabolite profile, as exometabolites detected in the *C. violaceum-P. syringae* coculture arrangement were less abundant and had lower accumulation over time in the 3-member community arrangement (**Appendix B Figure 16A**). Together, these results suggest that *B. thailandensis* can suppress or overwhelm expected outputs from neighbors.

In summary, we observed both increased accumulation and unique production of exometabolites in pairwise cocultures and in the 3-member community arrangements, with *B. thailandensis* contributing the most to the shared exometabolite pool as determined by comparisons with its monoculture exometabolite profile. Related, the transcriptional responses of *C. violaceum* and *P. syringae* in the 3-member community arrangement is most similar to their respective transcriptional response when neighbored with *B. thailandensis* alone, despite the presence of the third neighbor.

B. thailandensis increases competition strategies in the presence of neighbors

We observed relatively unchanged viability in *B. thailandensis* (**Appendix B Figure 17**). On the contrary, we observed a slight reduction (~2.1 log2 fold change) in *C. violaceum* live cell counts, and a drastic reduction (~4.7 log2 fold change) in *P. syringae* live cell counts, when either was cocultured with *B. thailandensis* (**Appendix B Figure 18** and **Appendix B Figure 19**). Given this reduction in viability and that there have been competitive interactions between *B. thailandensis* and *C. violaceum* previously reported (Chandler et al., 2012), we hypothesized that *B thailandensis* was using competition strategies to influence its neighbors via production of bioactive exometabolites. If true, we would expect an upregulation in *B. thailandensis* biosynthetic gene clusters (BSGC) that encode bioactive exometabolites. Indeed, we found evidence of this when *B. thailandensis* had neighbors (**Figure 4.3**, **Appendix A Table 16**).

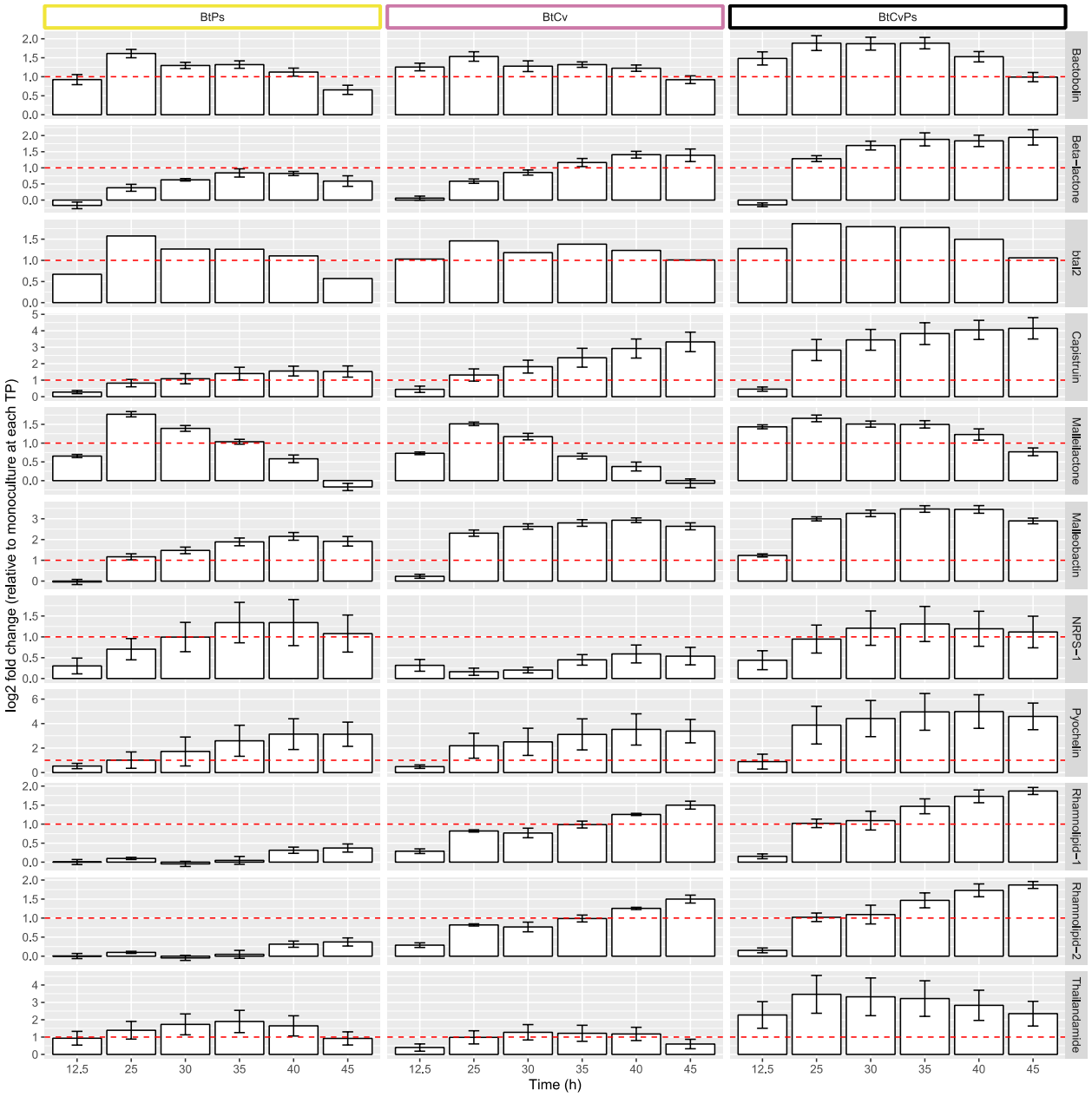

Figure 4.3. *B. thailandensis* upregulates biosynthetic gene clusters (BSGC) in cocultures. Columns represent community membership where Bt: *B. thailandensis*, Cv: *C. violaceum*, and Ps: *P. syringae* and rows represent BSCC in *B. thailandensis*. Genes part of a BSGC were curated from antiSMASH predictions and literature-based evidence. Within each BSGC, log2 fold-changes (LFC) were calculated by comparing gene counts from a coculture to the monoculture

Figure 4.3 (cont'd)

control at each time point. LFC were then averaged from all biosynthetic genes in the BSGC at each time point. We defined an upregulated BSGC as a BSGC that had at least two consecutive stationary phase time points with a LFC > 1 (indicated by the horizontal line). Note that plots for each BSGC have separate scales for the Y-axis.

This suggests that *B. thailandensis* responded to neighbors by upregulating genes involved in the production of bioactive compounds, likely to gain a competitive advantage. However, not all BSGCs in *B. thailandensis* were upregulated. Some BSGCs were unaltered or downregulated (**Appendix B Figure 20**). *C. violaceum* upregulated only 1 BSGC in coculture with *B. thailandensis,* while *P. syringae* did not upregulate any BSGC in any coculture (**Appendix B Figure 21** and **Appendix B Figure 22**). Interestingly, coculturing with *C. violaceum* and *P. syringae* resulted in the upregulation of an unidentified beta-lactone and an unidentified non-ribosomal peptide synthetase (NRPS) in *B. thailandensis*, respectively. Similarly, coculturing with *B. thailandensis* resulted in the upregulation on an unidentified NRPS- Type I polyketide synthase in *C. violaceum*. We also note that two additional unidentified NRPS passed the LFC threshold of 1 in *C. violaceum*. However, these were only upregulated at the exponential phase time point and subsequently downregulated or below the LFC threshold in all stationary phase time points. Interspecies interactions led to the upregulation of BSGC in both *B. thailandensis* and *C. violaceum* and three of these BSGC encode potentially novel bioactive exometabolites.

We were able to identify 6 of the 11 products from the upregulated *B. thailandensis* BSGC and quantify their abundances from mass spectrometry data (**Appendix B Figure 23** and **Appendix A Table 17**). For any given identified exometabolite, it differentially accumulated between community arrangements containing *B. thailandensis* (**Appendix A Table 18**), particularly when comparing the *B. thailandensis* monoculture compared to each coculture arrangement (**Appendix A Table 19**). As expected, these identified exometabolites were not detected in community arrangements that did not include *B. thailandensis*. Bactobolin was the only identified exometabolite that accumulated in monoculture to equivalent levels of

accumulation in to all coculture conditions. Thus, *B. thailandensis* increased competition strategies with neighbors through the upregulation and production of many bioactive exometabolites. Of these bioactive exometabolites, three are documented antimicrobials (227, 228, 229), two are siderophores (230, 231), and one is a biosurfactant (232). We conclude that *B. thailandensis* produced bioactive exometabolites to competitively interact using both interference and exploitative competition strategies (233). Given that *B. thailandensis* proactively upregulated competition strategies, and responded more broadly in producing competition-supportive exometabolites when grown with neighbors, we hypothesized that these bioactive exometabolites are responsible for the altered transcriptional responses in *C. violaceum* and *P. syringae*.

Interspecies co-transcriptional networks reveal coordinated gene expression related to competition

We performed interspecies coexpression network analysis to infer interspecies interactions. We used temporal profiles to generate 23 and 24 coexpression networks for *B. thailandensis-C. violaceum* and *B. thailandensis-P. syringae* cocultures, respectively (**Appendix A Table 20**). As expected, the majority of nodes network had intraspecies edges only, with interspecies edges composing 1.85% and 1.90% of the total edges in the *B. thailandensis-C. violaceum* and *B. thailandensis-P. syringae* networks, respectively. We explored interspecies edges for evidence of interspecies transcriptional co-regulation.

We performed two analyses (module analysis and GO enrichment) to validate networks and infer interspecies interactions (**Appendix B Figure 24**). Module analysis validated networks as intraspecies modules enriched for biologically relevant processes (Supplemental File 4.1). To infer interspecies interactions, we filtered genes with interspecies edges and performed enrichment analysis (Supplemental File 4.2). The top enriched Gene Ontology (GO) term for *B. thailandensis* when paired with *C. violaceum* was antibiotic synthesis of thailandamide, supporting interference competition. Though the top enriched GO term in *B. thailandensis* when paired with *P. syringae* was bacterial-type flagellum-dependent cell motility, antibiotic synthesis of malleilactone was also enriched. Both thailandamide genes from the *B. thailandensis-C. violaceum* network (**Figure 4.4**) and malleilactone genes from the *B. thailandensis-P. syringae* network (**Appendix B Figure 25**) formed near-complete modules within their respective BSGCs.

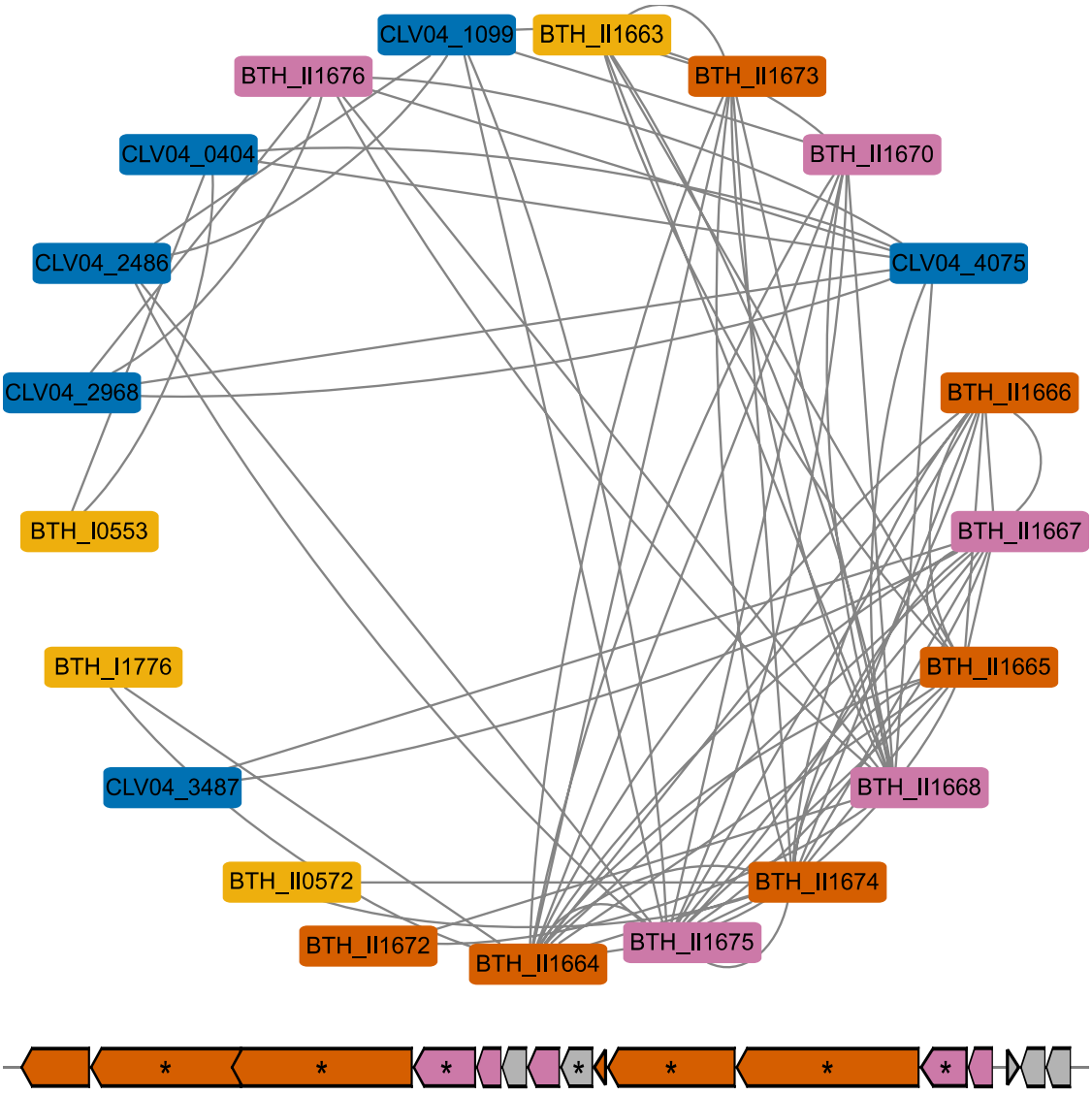

	B. thailandensis-C. violaceum interspecies network	*B. thailandensis-P. syringae* interspecies network
Bactobolin	✓	✓
Beta-lactone	✓	×
Capistruin	✓	✓
Malleilactone	✓	✓
Malleobactin	✓	✓
NRPS-1	×	✓
Pyochelin	✓	✓
Rhamnolipid	×	×
Thailandamide	✓	✓

Figure 4.4. *B. thailandensis* genes involved in thailandamide production are detected as interspecies edges in the *B. thailandensis-C. violaceum* coexpression network and biosynthetic genes organize into network modules.

Figure 4.4 (cont'd)

A network module containing the thailandamide BSGC is shown. The network module nodes are color coded by *B. thailandensis* gene type (BSGC or not) and type of connections (interspecies or not): thailandamide biosynthetic genes that had interspecies edges (magenta), thailandamide biosynthetic genes that did not have interspecies edges (orange), or other genes that were not part of the BSGC (yellow); as well as genes that were from *C. violaceum* (blue). The chromosomal organization of the thailandamide BSGC is shown below the network module. The same colors are applied to the BSGC operon. The operons also depict genes that were not detected within the interspecies network, shown in gray. Asterisks indicate core biosynthetic genes in the BSGCs, as predicted from antiSMASH. The table shows upregulated *B. thailandensis* BSGCs (**Figure 4.3**) and whether there were interspecies edges detected (check is yes, x is no).

At least one gene from each of *B. thailandensis's* upregulated BSGCs (**Figure 4.3**, **Table**) had an interspecies edge, except for rhamnolipid. The top GO term for both *C. violaceum* and *P. syringae* genes that had edges shared *B. thailandensis* was bacterial-type flagellum-dependent motility. Other notable enriched GO processes were efflux activity for *C. violaceum* and signal transduction for *P. syringae*. Specifically, a DNA starvation/stationary phase gene (CLV04_2968, **Figure 4.4**), *dspA*, was connected within the thailandamide module of the *B. thailandensis*-*C. violaceum* network and a TonB-dependent siderophore receptor gene (PSPTO_1206, **Appendix B Figure 25**) was connected within the malleilactone module of the *B. thailandensis*-*P. syringae* network (Supplementary File 4.3). Interestingly, both CLV04_2968 and PSPTO_1206 were differentially downregulated when cocultured with *B. thailandensis* (**Appendix B Figure 26A** and **Appendix B Figure 27A**, respectively). Additionally, the closest homolog for *dspA* in *B. thailandensis* was unaltered (BTH_I1284, Supplementary File 4.4) when cocultured with *C. violaceum* (**Appendix B Figure 26B**) and the closest homolog to the TonB-dependent receptor in *B. thailandensis* (BTH_I2415, Supplementary File 4.4) was differentially upregulated when cocultured with *P. syrinage* (**Appendix B Figure 27B**). Taken together, these interspecies networks revealed that *B. thailandensis* BSGC have coordinated expression patterns to biological process in both *C. violaceum* and *P. syringae*, suggesting that bioactive exometabolites were driving their transcriptional responses.

Distinctive member responses when assembled together

Within a complex community, there can be outcomes that are not expected based on interactions that are observed in simpler situations of member pairs (234-236). A typical

predictive approach uses the additivity assumption, where the null expectation is that a members' outcome in more complex communities is a summation of its outcomes in simpler communities (237). Patterns that deviate from the assumption arise from biological phenomena that are deemed non-additive. Much emphasis has been placed on predictions on the additive (or non-additive deviation) nature of growth outcomes in more complex environments (199, 238, 239). Here, we evaluated non-additive responses (e.g. transcriptomics) and behaviors (e.g. exometabolite production). We identified genes with non-additive upregulation in the 3-member community (**Appendix B Figure 28**, Supplemental File 5.1, see methods: *Non-additive gene expression*). For *B. thailandensis*, most of these genes consistently had nonadditive upregulation throughout stationary phase. Both *P. syringae* and *C. violaceum* trended towards transient dynamics of non-additive upregulation, which tended to occur at a specific timepoint. For each member, there was a stark contrast in genes with non-additivity between the exponential phase timepoint and all stationary phase time points. Notably, the top GO enrichments included antibiotic biosynthesis for *B. thailandensis* and structural constituents of the ribosome for both *C. violaceum* and *P. syringae* (Supplemental file 5.2). Of the BSGC in *B. thailandensis*, multiple genes involved in the production of thailandamide, pyochelin, capistruin, and malleobactin had non-additive upregulation. Since we were able to identify some of these compounds as features within the mass spectral data, we asked if non-additive transcriptional activity corresponded to non-additive exometabolite production.

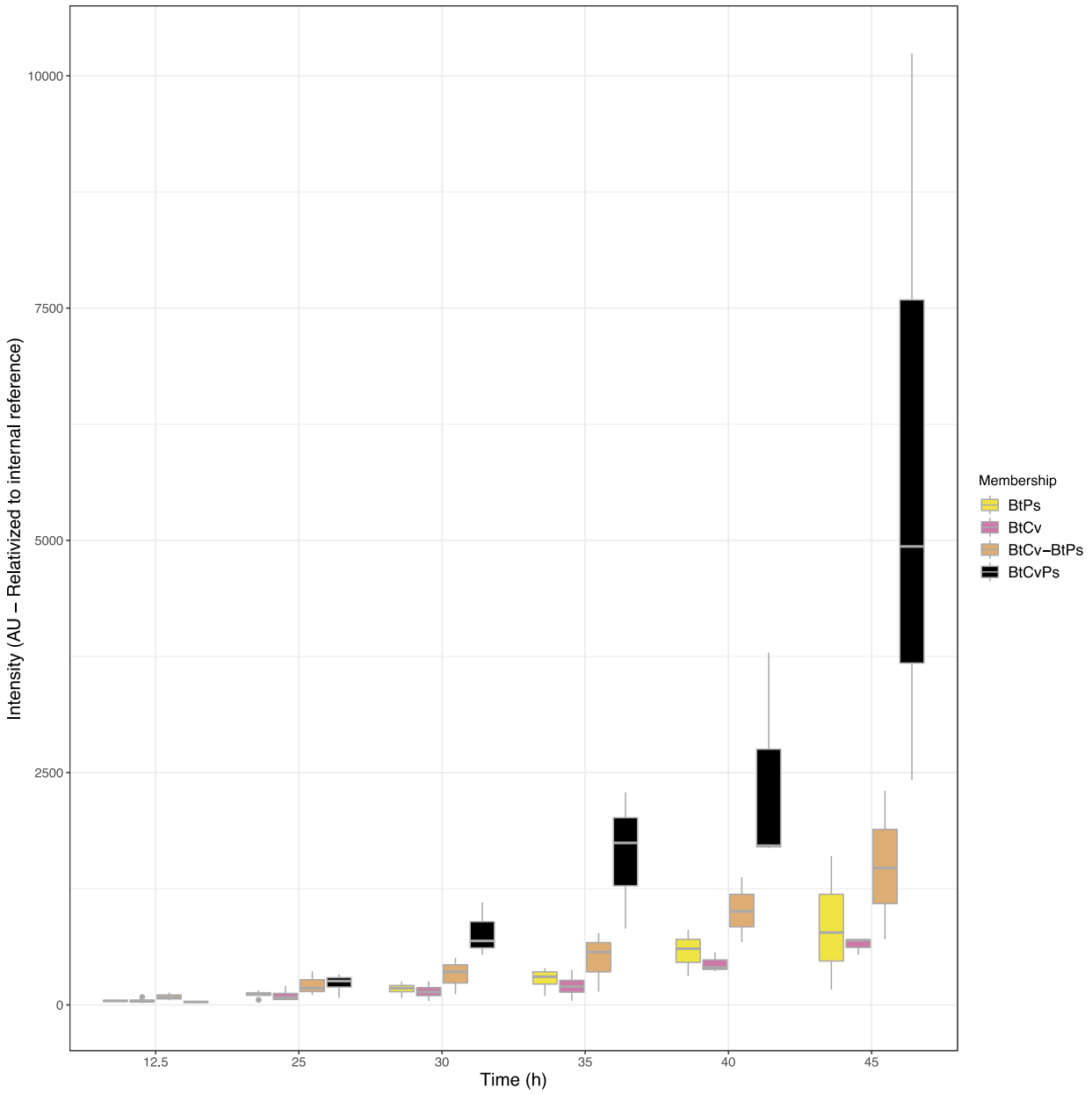

Figure 4.5. Thailandamide accumulates in a non-additive manner.

The accumulation of thailandamide was quantified through time (n = 3-4 integrated peak areas per time point). The bottom and top of the box are the first and third quartiles, respectively, and the line inside the box is the median. The whiskers extend from their respective hinges to the largest value (top), and smallest value (bottom) was no further away than 1.5× the interquartile range. Colors correspond to the community membership for the *B.thailandensis-P.*

Figure 4.5 (cont'd)

syringae coculture (yellow, BtPs), the *B. thailandensis-C. violaceum* coculture (magenta, BtCv), the "expected" exometabolite abundance in the 3-member community obtained from additive peak areas from the *B.thailandensis-P. syringae* and *B.thailandensis-C. violaceum* cocultures (orange, BtCv+BtPs), and the 3-member community (black, BtCvPs).

Most exometabolite features did not exceed expectations, as the average fold change across all time points was ~0.6 (**Appendix B Figure 29**). However, we did find that 858 exometabolomic features accumulated in the 3-member community in a non-additive manner (**Appendix B Figure 30**), including thailandamide (**Figure 4.5**) and pyochelin (**Appendix B Figure 31**), but not capistruin (**Appendix B Figure 32**). At the final stationary phase time point (45 h), thailandamide accumulated ~4-fold more and pyochelin accumulated ~3-fold more than the additive expectation. Thailandamide and pyochelin were consistently above 1σ of the average additive fold change for all coculture filtered exometabolites throughout stationary phase (**Appendix B Figure 29**, ablines). We combined peak areas from pairwise cocultures to create an "expected" exometabolite abundance over the time course for thailandamide, pyochelin, and capistruin (**Figure 4.5**, **Appendix B Figure 31**, and **Appendix B Figure 32**, orange). The experimental exometabolite abundance over the time course was significantly different from the "expected" exometabolite abundance for thailandamide, but not for pyochelin and capistruin (repeated measures ANOVA, **Appendix A Table 21**). When comparing each time point separately for thailandamide, significance was obtained only for the initial time point, and later time points were trending toward significance (**Appendix A Table 22**).

Discussion

Here, we used a synthetic community system to understand how exometabolomic interactions determine members responses and behaviors. Our experiment used a bottom-up approach to compare the seven possible community arrangements of three members, and their dynamics in member transcripts and community exometabolites over stationary phase.

Differential gene expression across community arrangements and over time show that the exometabolites released by a member were sensed and responded to by its neighbors. Furthermore, members' behaviors in monocultures changed because of coculturing, as evidenced by differential exometabolite production. *B. thailandensis* evoked the largest transcriptional changes in *C. violaceum* and *P. syringae*, and these changes were driven largely by several enhancements in *B. thailandensis* competitive strategies. Numerous transcripts and exometabolite were non-additive in the 3-member community, suggesting that predictions of members outcomes in more complex communities will not always be a simple summation of pairwise outcomes. That interactions within a relatively simple community altered the behavior of each member is important because these kinds of behavioral changes could, in turn, drive changes in community structure and/or function in an environmental setting. For example, it was shown that interspecies interactions more strongly influenced the assembly of *C. elegans* gut communities than host-associated factors (240). Therefore, mechanistic and ecological characterization of interspecies interactions will inform as to the principles that govern emergent properties of microbial communities.

Overall, competitive interactions predominated in this synthetic community. Our previous study found that, over stationary phase in monocultures, each member released and accumulated at least one exometabolite documented to be involved in either interference or exploitative competition (210). This suggests that entry into stationary phase primed members for competitive interactions, whether or not there were heterospecific neighbors present. We interpret this strategy of preemptive aggression to be especially advantageous to *B. thailandensis,* as it successfully used competitive strategies against both *C. violaceum* and *P.*

syringae. *B. thailandensis's* success was supported by decreased viable *P. syringae* cells when cocultured with *B. thailandensis*. Though *C. violaceum* viable cell counts were not as affected directly by the coculture with *B. thailandensis*, *B. thailandensis*-produced bactobolin (100) was detected in the shared medium reservoir. Bactobolin is a bacteriostatic antibiotic previously shown to be bioactive against *C. violaceum* (145). But, *C. violaceum* can resist bactobolin through upregulation of an RND-type efflux pump (241). This finding also is supported by our data, as all genes coding for the CdeAB-OprM RND-type efflux system and the TetR-family transcriptional regulator were upregulated in *C. violaceum* cocultures with *B. thailandensis* (CLV04_2412-CLV04_2415).

Coculturing can induce secondary metabolism (242-244) because an exometabolite produced by one microbe can prompt secondary metabolism in a neighbor (208). We found that coculturing led to the upregulation of numerous BSGCs in *B. thailandensis*. These exometabolites included bactobolin, malleilactone (230, 245; siderophore and cytotoxin), malleobactin (246, 247; siderophore), capistruin (102; lasso peptide), thailandamide (248; polyketide), pyochelin (231; siderophore), rhamnolipids (232; biosurfactants), and two uncharacterized BSGCs encoding nonribosomal peptide synthetases. Of these exometabolites, bactobolin, capistruin, and thailandamide have documented antimicrobial activities through translation inhibition (227), transcription inhibition (228), and inhibition of fatty acid synthesis (229), respectively. For those exometabolites we were able to identify with mass spectrometry, their accumulation in cocultures was correlated with the upregulation of their BSGCs. Furthermore, up/downregulated patterns across all *B. thailandensis* BSGCs is consistent with ScmR global regulatory patterns of secondary metabolism (249). Though we were not able to

pinpoint the exact inducers of BSGCs, exometabolites such as antibiotics (250) and primary metabolites (251) have been documented to induce secondary metabolism in *B. thailandensis*. *C. violaceum* can inhibit *B. thailandensis* (145) but we did not observe *B. thailandensis* inhibition based on cell counts. However, we did find that in stationary phase *C. violaceum-B. thailandensis* cocultures, *C. violaceum* upregulated an uncharacterized hybrid nonribosomal peptide synthetase-type I polyketide synthase. *P. syringae* was the least competitive of the three neighbors, as evidenced by a reduction in live cell counts when cocultured with *B. thailandensis*. Also, *P. syringae* did not enhance competitive strategies when cocultured, as no BSGCs were consistently upregulated across all coculture conditions. In summary, though all three neighbors used competitive strategies, *B. thailandensis* was most successful and displayed continued aggression in cocultures over stationary phase through enhanced production of exometabolites involved in interference and exploitative competition strategies.

Given the upregulation of BSGCs in *B. thailandensis* and the strong transcriptional responses of *C. violaceum* and *P. syringae* to the presence of *B. thailandensis*, we hypothesized that competitive exometabolites were contributing to their community dynamics. Thus, we used a coexpression network analysis with our longitudinal transcriptome series to infer interspecies interactions (252). This use of this approach was first demonstrated to infer coregulation between a phototroph-heterotroph commensal pair (253). Our network confirmed that *B. thailandensis* BSGCs had coordinated gene expression patterns with both *C. violaceum* and *P. syringae*. Interspecies nodes in both networks contained various genes involved in the aforementioned upregulated *B. thailandensis* BSGCs. In particular, we focused on interspecies edges within thailandamide nodes for the *B. thailandensis-C. violaceum* network and

interspecies edges within malleilactone nodes for the *B. thailandensis-P. syringae* network because these were significantly enriched as interspecies nodes. A *C. violaceum* gene of interest, CLV04_2968, was contained within the thailandamide cluster of interspecies nodes. This gene codes for a DNA starvation/stationary phase protection protein and had the highest homology to the Dps protein in *Escherichia coli* across all *C. violaceum* protein coding genes. Dps mediates tolerance to multiple stressors and *dps* knockouts are more susceptible to thermal, oxidative, antibiotic, iron toxicity, osmotic, and starvation stressors (254). Interestingly, CLV04_2968 was downregulated when cocultured with *B. thailandensis*, suggesting that *B. thailandensis* attenuates *C. violaceum* stress tolerance over stationary phase. While we observed a slight decrease in viable *C. violaceum* cells when cocultured with *B. thailandensis*, one may expect *C. violaceum* to have increased sensitivity to a subsequent stress (e.g. pH stress; 255) resulting from CLV04_2968 downregulation in the presence of *B. thailandensis*.

In the *B. thailandensis-P. syringae* coexpression network, a *P. syringae* gene of interest, PSPTO_1206, was contained within the malleilactone cluster of interspecies nodes. PSPTO_1206 is annotated as a TonB-dependent siderophore receptor. A *P. syringae* iron-acquistion receptor had coordinated expression with a malleilactone, which has been characterized as a siderophore with antimicrobial properties (230). Interestingly, this gene was downregulated when in coculture with *B. thailandensis*. In contrast, the closest TonB-dependent siderophore receptor homolog to PSPTO_1206 in *B.thailandensis*, BTH_I2415, was upregulated in coculture conditions with *P. syringae*.

To summarize, coexpression network analysis reveal coordinated gene expression patterns that helped to infer that BSGC upregulation likely explains the influence of *B. thailandensis* on both *C. violaceum* and *P. syringae*. *B. thailandensis*-enhanced competition strategies were coordinated with a potential decrease in competition strategies in *C. violaceum* via reduced stress tolerance and in *P. syringae* with reduced iron acquisition ability.

A major goal in microbial ecology is to predict community dynamics for purposes of modulating and/or maintaining ecosystem function (256, 257). At its core, microbial functional properties emerge, in part, from the concerted interactions of multi-species assemblages. Predictions can be complicated by non-additive phenomena that arise in more complex communities. For example, non-additive phenomena have been documented in gene expression (258, 259), growth (238), and fitness (260). Here, we also have documented non-additive responses and behaviors in our system when combinatorial stimuli was present in the 3-member community. *B. thailandensis* BSGCs displayed non-additive phenomena, as we are able show that the transcriptional response of certain BSGCs in the 3-member community was greater than the naive summation of transcriptional response in pairwise arrangements. Furthermore, non-additive transcriptional responses resulted in non-additive exometabolite accumulation (e.g. thailandamide & pyochelin) with exceptions (e.g. capistruin). However, we only quantified exometabolite accumulation in the shared medium reservoir. Differential release and uptake of bioactive molecules within the community can complicate tracking metabolite dynamics in the system. Thus, analyses that incorporate both intracellular and extracellular metabolomics can provide a more complete understanding of altered microbial metabolism under different conditions. Regardless, we documented non-additive accumulation

of secondary metabolites involved in both competition strategies. This finding may have implications for high-order interactions, meaning, the nature of the interaction between two members may be altered by the addition of a third member (261). For example, one member could produce sublethal antibiotics in the presence of an antibiotic-sensitive member. The addition of a third member could stimulate the antibiotic producer to increase antibiotic production, altering the nature of the initial interaction from sublethal to lethal for antibiotic-sensitive member (262). In other words, the nature of interactions may be altered depending on surrounding stimuli that can exacerbate bacterial behaviors not expected by studying the system as simpler parts (235). Therefore, characterizing transcriptome and metabolome dynamics in microbial communities is expected to inform how non-additive phenomena arise and how they contribute to deviations in predictive models of community outcomes.

Our results indicated that each member continued to maintain competitive strategies despite stagnant population growth. In particular, *B. thailandensis* upregulated various bioactive exometabolites involved in both interference and exploitative competition when with neighbors. Our idea of a competitor through maintenance and upregulation of exometabolites involved in competitive strategies is in contrast to the typical notion of being an efficient competitor- one that is defined as the ability to outcompete neighbors via growth advantage that stems from efficient nutrient uptake and biomass conversion rates (263, 264). However, some environments impose a stationary phase lifestyle, where long periods of nutrient depletion are punctuated with short periods of nutrient flux. In these scenarios, it warrants to understand how competitive strategies are deployed in the interim of growth and the extent to which these interactions contribute to long-term community dynamics. Though population

levels remain constant, sub-populations of growing cells have been observed in stationary phase (265), and continued production of competitive exometabolites may serve as an advantageous strategy to hinder growth of competitors. In addition, some antibiotics remain effective in non-replicating bacteria (266). The ability for continued upkeep of competition strategies during stationary phase may provide spatiotemporal maintenance of population levels before growth resumption. The long-term consequences of competition will be realized with the incorporation of both competition during periods of growth and continued aggression via upkeep of both interference and exploitative competition strategies during periods of non-growth (233).

In summary, we evaluated the consequences of exometabolite-mediated interactions over stationary phase using a synthetic microbial community approach. The emergence of complex community behaviors can be realized through the use of synthetic microbial ecology (267) using model synthetic community members (268). We demonstrated that members' transcriptional and exometabolite patterns are altered over stationary phase in cocultures compared to monocultures. These alterations could be attributed to the response of bioactive exometabolites involved in competition strategies. *B. thailandensis*, in particular, had a strong influence on the transcriptional responses of the other synthetic community members, as it proactively responded to coculturing by upregulating biosynthetic gene clusters that corresponded to increased production of bioactive exometabolites involved in competition strategies. In addition, all members had a subset of genes that were upregulated in a non-additive in the 3-member community. In some scenarios, non-additive transcriptional patterns resulted in non-additive exometabolomic production in the 3-member community. These

results implicate that bacterial responses and behaviors in more complex communities are not always a simple summation of pairwise outcomes. Furthermore, the ability to upkeep competitive strategies may be important to the maintenance of population levels during long periods of non-growth.

CHAPTER 5 : A coevolution experiment reveals genetic signatures of antibiotic resistance

Abstract

Bacteria can compete for survival through the production of antibiotics. Antibiotic-sensitive strains can counter antibiotics through tolerance mechanisms and through the evolution of antibiotic resistance. We grew an antibiotic-producing strain, *Burkholderia thailandensis* E264, and an antibiotic-sensitive strain, *Flavobacterium johnsoniae* UW101, together and separately on agar plates to examine the coevolutionary repercussions to long-term chemical interactions. The *F. johnsoniae* ancestor could tolerate the *B. thailandensis*-produced antibiotic through efflux mechanisms. After sequencing clonal isolates from *F. johnsoniae* coevolved and monoculture lines, we uncovered mutational ramifications to long-term exometabolite interactions (7.5 months, 5 plate passages). The coevolved genomes from *F. johnsoniae* revealed signatures of antibiotic resistance that were not observed in the evolved monoculture lines. One mutation was a 33 bp deletion in *tolC* that corresponded to the deletion of 11 amino acids that were part of an extracellular loop in TolC. TolC, along with AcrA/B form the tripartite multidrug efflux system. The other mutation was a G83R nonsynonymous mutation in acetyl-coA carboxylayse carboxyltransferase subunit alpha (AccA). Placing the *tolC* 33 bp deletion back into the *F. johnsoniae* ancestor conferred some degree of antibiotic resistance, but not to the degree of resistance observed in coevolved lines. Furthermore, the *accA* mutation matched a previously described mutation conferring resistance to *B. thailandensis*-produced thailandamide. Transposon mutants effecting thailandamide production revealed that this molecule was bioactive against *F. johnsoniae* but also suggested that more than one *B. thailandensis*-produced antibiotic was inhibiting *F. johnsoniae*. This study

reveals how long-term interspecies chemical interactions can result in a novel mutational mechanism that confers antibiotic resistance.

Introduction

Sequencing has revealed the prevalence of antibiotic resistance genes in pristine environments (26), indicating that antibiotics and their corresponding resistance mechanisms have long-evolved in natural environments that predate their use in medicine (269). In fact, glycopeptide antibiotics and resistance mechanisms have been present in bacterial genomes for at least 150 million years (270). Thus, there have been efforts to understand the evolution of antibiotic resistance in non-clinical settings to identify novel mechanisms of antibiotic resistance (271).

Microbial antibiotic production in environmental settings is typically viewed through the lens of competition (272). Bacteria produce these bioactive molecules that interact directly with competitors by inflicting cell damage (interference competition; 23). These antibiotics are organized in biosynthetic gene clusters (BSGC), where locally grouped genes encode the biosynthetic pathway to molecule production (6). The activation of BSGCs is typically tied to stress regulatory networks (273), suggesting antibiotic production is deployed as a survival strategy during unideal growth conditions (75).

While the bacterial production of antibiotics is for chemical warfare (274), the heterogeneous nature of certain environments (e.g. soil matrix) can result in sublethal levels of antibiotic exposure that provides the means for surrounding neighbors to induce antibiotic

resistance mechanisms (275). One general form of antibiotic resistance is multidrug efflux pumps (276). Low-levels of antibiotic exposure can upregulate intrinsic mechanisms of resistance, such as efflux pumps (277). The survival of bacteria to low levels of antibiotics can facilitate adaptive resistance (278). Therefore, studying multigenerational interactions between antibiotic-producing and antibiotic-sensitive environmental isolates may provide insight into evolutionary dynamics driving antibiotic resistance.

We performed an agar-based experimental coevolution with an antibiotic-producer (*B. thailandensis*) and an antibiotic-sensitive strain (*F. johnsoniae*). These strains were co-plated and plated in monocultures on M9 minimal medium agar plates containing 0.2% for 1.5 months. *B. thailandensis* and *F. johnsoniae* were co-plated such that *B. thailandensis* antibiotic inhibition of *F. johnsoniae* could occur but the colonies would not physically interact. After 1.5 months, these strains were transferred to the second plate passage for another 1.5 months of incubation. This continued for a total of 5 plate passages. By comparing outcomes of the coevolved lines to the evolved monoculture lines, we asked: What are the genetic and phenotypic repercussions of coevolution and how consistent are they across independent replicates?; What are the genetic signatures of *F. johnsoniae* antibiotic resistance?; and What is the antibiotic produced by *B. thailandensis* that inhibits *F. johnsoniae*. We found that coevolved *F. johnsoniae* lines gained resistance to the *B. thailandensis*-produced antibiotic while evolved monoculture lines remained susceptible. A 33 bp deletion in *tolC* and a nonsynonymous mutation in *accA* suggested two different paths to the evolution of antibiotic resistance in *F. johnsoniae.* Placing the *tolC* 33 bp deletion back in the ancestor resulted in antibiotic resistance, but not equivalent antibiotic resistance observed in the coevolved lines, suggesting that

multiple mutations may be involved in obtaining higher levels of antibiotic resistance. Lastly, thailandamide, an antibiotic that inhibits fatty acid synthesis, was evidenced as one of the bioactive compounds that inhibited *F. johnsoniae*, but our data suggests that more than one *B. thailandensis*-produced antibiotic may be inhibiting *F. johnsoniae*. These results have implications for the consequences of interspecies chemical interactions on the evolution of antibiotic resistance.

Materials and Methods

Extraction of B. thailandensis supernatant containing bioactivity

A freezer stock of *B. thailandensis* was plated on 50% trypticase soy agar (TSA50) and grown overnight at 27 ^{o}C. A collection of lawn growth was transferred to 7 mL of M9 minimal salts-glucose (M9-glucose) medium to achieve an initial OD of ~0.2. The culture was incubated over night at 27 ^{o}C, 200 rpm. The next day, 1 mL of culture was transferred to 50 mL fresh M9-glucose medium. The culture was incubated for 24 h at 27 ^{o}C, 200 rpm. The culture was transferred to a falcon tube and centrifuged at 4 ^{o}C, 5000 rpm for 20 min. The supernatant was removed, filtered with a 0.22 µM filter, and transferred to a separatory funnel. Ten mL of dichloromethane (DCM) was added to the separatory funnel. The separatory funnel was agitated three times and the DCM layer was removed. This process was repeated twice more in batches of 10 mL additions of DCM. The collected DCM layer was dried under nitrogen gas. The dried DCM extracts were reconstituted in 1 mL of a 50:50 methanol:water mixture. This mixture was used for the efflux pump inhibitor experiment.

Efflux pump inhibitor experiment

A freezer stock of *F. johnsoniae* was plated on TSA50 and grown over night at 27 °C. Five individual colonies were then inoculated in 5 mL 50% trypticase soy broth (TSB50) and grown overnight at 27 °C, 200 rpm. After ~16 hr growth, 50 μL of culture was back-diluted into 4.95 mL of fresh TSB50 for each independent replicate. Then, 650 μL aliquots were dispensed in each of seven tubes for each replicate. Seven conditions were prepared as follows: 1) *F. johnsoniae* culture control 2) *F. johnsoniae* with DMSO control 3) *F. johnsoniae* with 50:50 methanol:water control 4) *F. johnsoniae* with DMSO + 50:50 methanol:water control 5) *F. johnsoniae* with daidzein + 50:50 methanol:water 6) *F. johnsoniae* with DMSO + *B. thailandensis* bioactive supernatant and 7) *F. johnsoniae* with daidzein + *B. thailandensis* bioactive supernatant. A volume of 1.04 μL was added to tubes containing Daidzein (10 mg/ml) or DMSO and a volume of 16.25 μL was added to tubes containing *B. thailandensis* bioactive supernatant or 50:50 methanol:water. After additions of solvent or bioactive components, 200 μL aliquots from each tube was placed in a 96 well plate. The plate contained 5 independent replicates, 2 technical replicates/independent replicate for conditions 1-3 and 3 tech reps/independent replicate for conditions 4-7 (90 samples). For the remaining 6 wells, 200 μL TSB50 was added to each well as a negative control. An initial absorbance reading (590 nm) was taken on a Tecan Infinite® F500 Multimode Microplate Reader (Tecan Group Ltd., Männedorf, Switzerland). The plate was then incubated for 24 h at 27 °C, 200 rpm. A final absorbance reading (590 nm) was taken after 24 h of incubation. ANOVA was used to compare all the controls and results were insignificant (p = 0.544). For this reason, we only used the *F. johnsoniae* culture control (with no added solvents)

to serve as a control for a follow-up ANOVA that compared final OD across test conditions. TukeyHSD was performed for post-hoc analysis.

Experimental evolution

B. thailandensis E264 and *F. johnsoniae* UW101 were plated from freezer stocks onto TSA50. Plates were incubated over night at 27 ^{o}C. A single, isolated colony of *B. thailandensis* and of *F. johnsoniae* were inoculated as separate cultures in 7 mL of TSB50. Cultures were incubated over night at 27 ^{o}C, 200 rpm. The following day, the cultures were pelleted by centrifuged at 5000 rpm for 10 min, the supernatant was removed, and the cultures were resuspended in 1X phosphate buffered saline (PBS). This process was repeated once more. The cultures were resuspended in PBS at a final volume of 5 mL. Ancestral freezer stocks were prepared by adding 750 mL of each culture to 750 mL of 70% glycerol. All freezer stocks were stored at -80 ^{o}C. From the remaining cultures, the OD was measured and each culture was back-diluted to an OD of 0.1 in PBS to prepare the evolution experiments. Ten μL of a culture (OD 0.1) was spotted onto M9 minimal salts agar plates containing 0.2% glucose. Strains were plated both in isolation and co-plated together. When co-plated together, *B. thailandensis* and *F. johnsoniae* were spotted 14 mm apart. Five independent replicates were prepared, resulting in 15 plates total. The plates were wrapped with parafilm and incubated at 27 ^{o}C for 1.5 months.

After incubation, we performed a plate passage. Sterilized toothpicks were used to resuspend colonies into 1 mL of PBS. For *B. thailandensis*, we preferentially collected radial

colony growth that was growing toward *F. johnsoniae*. A section of radial colony growth was collected for *B. thailandensis* colonies in isolation. The entirety of the *F. johnsoniae* was removed from each plate. First plate passage freezer stocks were prepared by adding 500 mL of each resuspended culture to 500 mL of 70% glycerol. From the remaining cultures, the OD was measured and each culture was back-diluted to an OD of 0.1 in PBS. The plating scheme was repeated as previously described while preserving the replicate structure of co-evolving lines (e.g. *B. thailandensis* coevolved replicate 1 was re-plated with *F. johnsoniae* coevolved replicate 1). The plates were wrapped with parafilm and incubated at 27 ^{o}C for 1.5 months. This process was repeated for a total of 5 plate passages, resulting in a total experimentation time of 7.5 months.

Measurements of radial colony growth

Prior to a setting up another plate passage, plates were imaged using a scanner (at 1.5 months). A ruler was placed in the scanner to scale pixels to mm for measurements. Images were uploaded to ImageJ2 for analysis (279, 280). Radial growth was determined by measuring the distance from the center of the colony to the furthest point of radial growth. Measurements were uploaded to R for ggplot.

Whole genome sequencing

All *F. johnsoniae* replicates (monoculture and co-evolution experiments) from the 5th plate passage and the *F. johnsoniae* ancestor were plated from freezer stocks onto TSA50 (11

freezer stocks total). These were incubated overnight at 27 °C. The following night, isolated colonies were inoculated into TSB50 medium and incubated over night at 27 °C, 200 rpm. The following morning, DNA was extracted from all 10 cultures using the E.Z.N.A.® Bacterial DNA Kit (Omega Bio-tek, Norcross, GA) according to the manufacturer's instructions. DNA integrity was assessed from 260/280 and 260/230 ratios using a NanoDrop® ND-1000 UV-Vis Spectrophotometer (Thermo Fisher Scientific, Waltham, MA) and quantified using a qubit 2.0 fluorometer (Invitrogen, Carlsbad, CA, USA). DNA samples were sent to the Microbial Genome Sequencing Center (MiGS, Pittsburgh, PA) for whole genome sequencing. Illumina DNA library preparations were performed at the MiGS facility according to standard operating protocols. Sequencing (2x151bp) was performed on a NextSeq 2000 platform. A minimum of 200 Mbp of sequencing data was obtained with >Q30 reads. Mutations were identified using the breseq (0.33.2) pipeline (281).

TolC model prediction

The *F. johnsoniae* TolC protein sequence of interest (FJOH_RS06580) was downloaded from NCBI. The protein FASTA file was manually edited to remove 11 amino acids associated with the 33 bp deletion (amino acids 87-97). The protein FASTA file was also manually edited to create the nonsynonymous mutation (G83R). Then all three files were placed into SWISS-MODEL to model the protein structure of TolC (282). The template used for rendering all models was SMTL ID : 6wxi.1. The model from TolC wild-type was downloaded and uploaded into Swiss-PdbViewer to highlight amino acids associated with the 33 bp deletion (283).

Construction of mutants in F. johnsoniae ancestral strain

Single mutations of interest observed in the coevolved lines were engineered into the ancestral strain. These mutants were constructed following the previously described method (284), with the exception a nested PCR step. All primers used in this study are listed in **Appendix A Table 23**.

Nested PCR

DNA extracted from coevolved lines for whole genome sequencing was used as templates for PCR. Coevolved line 1 (JCCE01) was used to amplify the 33 bp deletion in *tolC* (*F. johnsoniae* locus FJOH_RS06580; 261-293 in coding sequence), coevolved line 3 (JCCE03) was used to amplify the nonsynonymous mutation in *tolC* (*F. johnsoniae* locus FJOH_RS06580; G247A in coding sequence), and coevolved line 4 (JCCE04) was used to amplify the base insertion sequence in *ragB*/*susD* (*F. johnsoniae* locus FJOH_RS24865; G at 794 in coding sequence). Nested PCR was performed to obtain enough DNA for restriction digestion and plasmid ligation. For the first round of nested PCR, a 3.3-kbp fragment containing *tolC*Δ33 or *tolC* (G247A) was amplified using primers 1001 and 1002. A 3.5-kbp fragment containing *ragB*794_795insG was amplified using primers 1010 and 1011. The PCR reactions contained reagents and volumes outlined in **Appendix A Table 24**. PCR conditions were as follows: 98 °C for 30 s, 98 °C for 10 s, 56 °C for 15 s, and 72°C for 70 s, repeated 29 times from step 2, followed by 72°C for 10 min and hold at 4 °C. PCR products were run on a 0.8% agarose gel at 100V for 60 min. PCR bands at the correct fragment sizes were excised from the gel and extracted using

Wizard® SV Gel and PCR Clean-Up System (Promega Corporation, Madison WI). PCR products were quantified using a qubit 2.0 fluorometer (Invitrogen, Carlsbad, CA, USA).

For the second round of PCR, a 3.2-kbp fragment containing *tolC*Δ33 or *tolC* (G247A) was amplified using primers 1003 (engineered XbaI site) and 1004 (engineered BamHI site). A 3.1-kbp fragment containing *ragB*794_795insG was amplified using primers 1012 (engineered XbaI site) and 1013 (engineered BamHI site). The PCR reactions contained reagents and volumes outlined in **Appendix A Table 25**. PCR conditions were as follows: 98 °C for 30 s, 98 °C for 10 s, 56 °C for 15 s, and 72°C for 70 s, repeated 29 times from step 2, followed by 72°C for 10 min and hold at 4 °C. PCR products were run on a 0.8% agarose gel at 100V for 60 min. PCR bands at the correct fragment sizes were excised from the gel and extracted using Wizard® SV Gel and PCR Clean-Up System (Promega Corporation, Madison WI). PCR products were quantified using a qubit 2.0 fluorometer (Invitrogen, Carlsbad, CA, USA).

Plasmid isolation and purification

A *E. coli* DH5αmcr_pYT354 freezer stock was plated on lysogeny broth (LB) agar with ampicillin (100 µg/mL) and incubated overnight at 37 °C. A single colony was inoculated into 5 mL LB with ampicillin (100 µg/mL) and incubated at 37 °C, 200 rpm overnight. Plasmid was extracted and purified the following morning using the E.Z.N.A.® Plasmid DNA Mini Kit I Q-spin (Omega Bio-tek, Norcross, GA) according to the manufacturer's instructions.

Restriction enzyme digestion and ligation

Separately prepared restriction enzyme double digestions were performed on purified PCR products from nested PCR round 2 and pYT354. The reaction reagents and volumes are outlined in **Appendix A Table 26**. Reactions were incubated at 37 °C for 15 min. Reactions were then run on a 0.8% agarose gel at 100V for 60 min. Bands at the correct fragment sizes were excised from the gel and extracted using Wizard® SV Gel and PCR Clean-Up System (Promega Corporation, Madison WI). PCR products were quantified using a qubit 2.0 fluorometer (Invitrogen, Carlsbad, CA, USA).

The PCR fragment containing *tolC*Δ33 was ligated to pYT354 to form pJC101, the PCR fragment containing *tolC* (G247A) was ligated to pYT354 to form pJC102, and the PCR fragment containing *ragB*794_795insG was ligated to pYT354 to form pJC103. Ligation reagents are outlined in **Appendix A Table 27**. The reactions were incubated at room temperature for 10 min and then heat inactivated for 10 min at 65 °C.

Preparation of heat shock competent cells

A *E. coli* DH5αmcr freezer stock was plated on lysogeny broth (LB) agar and incubated overnight at 37 °C. A single colony was inoculated into 5 mL LB and incubated at 37 °C, 200 rpm overnight. One mL of the overnight cultured was diluted into 100 mL LB and incubated at 37 °C, 200 rpm until the OD reached 0.3 (~ 2 h). The culture was placed on ice for 15 min. Two 45 mL aliquots were placed into 2, 50 mL falcon tubes and centrifuged at 4 °C, 4000 rpm for 10 min. Supernatant was decanted, and the pellets were resuspended in 45 mL ice-cold 0.1 M $CaCl_2$. The

resuspended cultures were placed on ice for 30 min. Cultures were then centrifuged at 4 °C, 4000 rpm for 10 min. Supernatant was decanted, and the pellets were resuspended in 4.5 mL ice-cold 0.1 M $CaCl_2$ with 15% glycerol. The cultures were then distributed as 50 µL aliquots into microcentrifuge tubes. Competent cells were stored as freezer stocks at -80 °C until ready for use.

Heat shock transformation

Heat shock competent cells (50 µL) were removed from the freezer and placed on ice for 20 min (4 tubes, 1 for each ligation product and 1 pYT354 plasmid control). Two µL of ligation products (and 1 µL of 10 ng/µL pYT354 plasmid) were added to each tube and placed on ice for an additional 20 min. Cells were then heat shocked for 45 s at 42 °C. Heat shocked cells were placed on ice for 2 min. One mL of super optimal broth (SOC) medium was added to each tube and the tubes were incubated at 37 °C, 200 rpm for 1 h. Cells were pelleted by centrifugation at 4000 g for 2 min at 4 °C. The supernatant was removed (950 µL) and the remaining culture was plated on LB agar containing ampicillin (100 µg/mL). Plates were incubated over night at 37 °C. Successful transformants were inoculated into LB containing ampicillin (100 µg/mL) and incubated overnight. Freezer stocks were made the following morning for triparental conjugation.

Triparental conjugation and recombinant confirmation

pJC101, pJC103, and pJC104 in recombinant *E. coli* DH5αMCR needed to be transferred to the *F. johnsoniae* ancestral strain. This was introduced into *F. johnsoniae* by triparental conjugation as previously described (285) using recombinant *E. coli* DH5αMCR, *F. johnsoniae* ancestor, and *E. coli* HB101 (carrying the helper plasmid pRK2013), except that the *sacB* and *ermF*-containing suicide vector was used to select for successful *F. johnsoniae* recombinants (284). *F. johnsoniae* recombinants (JCAC01, JCAC02, JCAC03) were confirmed by sanger sequencing at the Michigan State Genomics Core using primers 1005 and 1006 for *tolC*Δ33 or *tolC* (G247A) recombinants and primers 1014 and 1014 for the *ragB*794_795insG recombinant.

Acetyl-CoA carboxylase carboxyl transferase subunit alpha (AccA) protein alignment

AccA sequences were download from *F. johnsoniae* UW101 (protein ID: WP_011921560.1) and from *Salmonella enterica* serovar Typhimurium strain LT2 (protein ID: NP_459237.1) on NCBI and concatenated as a text file. The text file was uploaded to T-Coffee (Version_11.00) for protein alignment using default parameters (286). The FASTA alignment file from T-Coffee output was download and used as input for BoxShade (version 3.21) using default parameters. The protein alignment was then uploaded to Inkscape for final edits.

Re-plating experiments

Strains of interest were plated from freezer stocks onto TSA50. Plates were incubated over night at 27 ^{o}C. Single isolated colonies were inoculated as separate cultures in 7 mL TSB50.

Cultures were incubated over night at 27 °C, 200 rpm. The following day, the cultures were pelleted by centrifuged at 5000 rpm for 10 min, the supernatant was removed, and the cultures were resuspended in 1X PBS. This process was repeated once more. The cultures were resuspended in PBS at a final volume of 5 mL. The OD was measured and each culture was back-diluted to an OD of 0.1 in PBS. Ten μL of a culture (OD 0.1) was spotted onto M9 minimal salts agar plates containing 0.2% glucose. Strains were either plated in isolation or co-plated together. When co-plated together, strains were spotted 14 mm apart. Plates were incubated at 27 °C for various amounts of time (see figure legends for details). *B. thailandensis* transposon mutants were acquired from the Manoil lab (287).

Data availability

Supplemental files, sanger sequencing files, and our breseq pipeline are available at [https://github.com/ShadeLab/Paper_Chodkowski_Coevolution_2021]. *F. johnsoniae* whole genome sequences files are available on NCBI's Seqence Read Archive (SRA; https://www.ncbi.nlm.nih.gov/biosample/?term=(Ashley%20Shade)%20AND%20biosample_sra[filter]%20AND%20public[filter]).

Results

B. thailandensis produces a bioactive compound that inhibits F. johnsoniae

B. thailandensis inhibits *F. johnsoniae* when co-plated on M9-agar plates (**Figure 5.1**). *B. thailandensis* exhibits radial growth on all edges along the circumference of the colony while *F. johnsoniae* proximal to *B. thailandensis* is inhibited. However, the distal end of the *F. johnsoniae*

can grow away from *B. thailandensis*, suggesting that *F. johnsoniae* can still grow in the presence of an antibiotic.

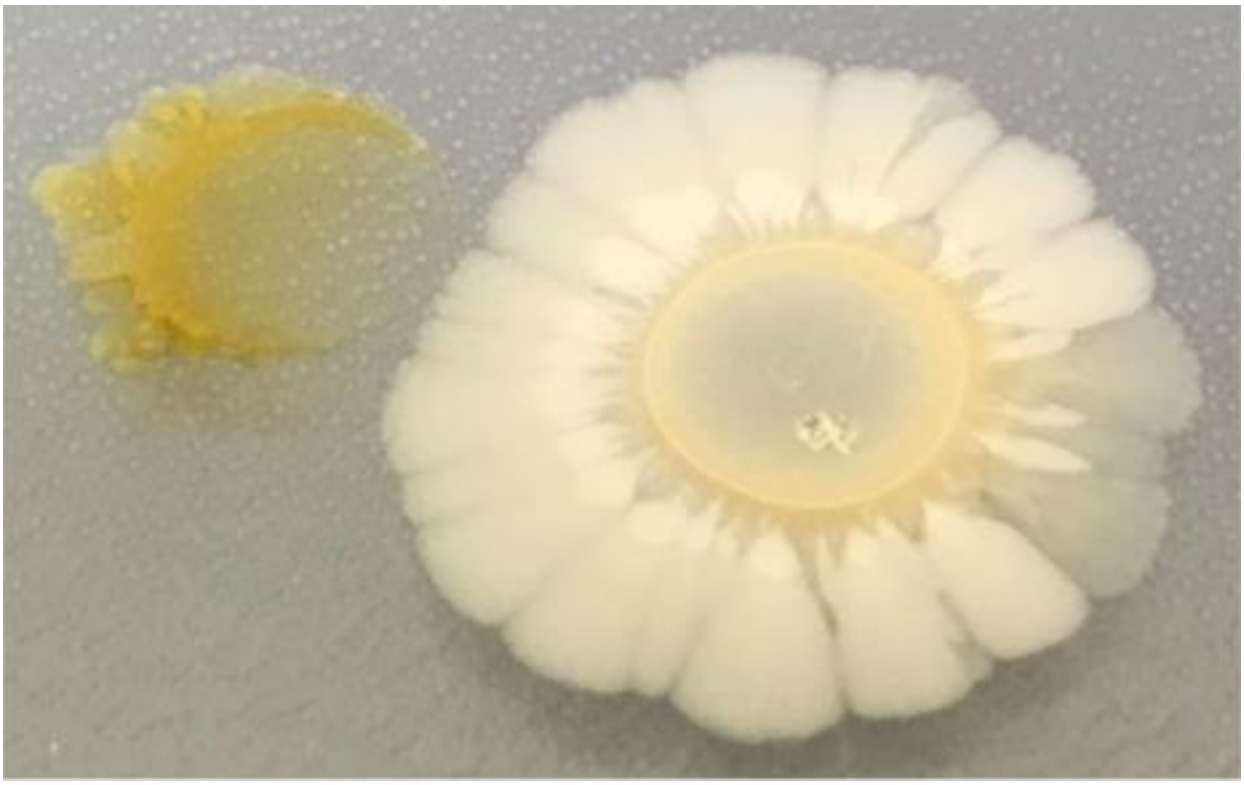

Figure 5.1. *B. thailandensis*-produced antibiotic inhibits *F. johnsoniae.*

B. thailandensis (right) and *F. johnsoniae* (left) were co-plated on M9-glucose agar at a distance that allowed for chemical interactions. An unidentified antibiotic(s) inhibited the growth of *F. johnsoniae*.

Efflux allows F. johnsoniae to grow in the presence of a B. thailandensis-produced antibiotic

Given the growth pattern of *F. johnsoniae* when co-plated with *B. thailandensis*, we hypothesized that efflux contributed to *F. johnsoniae* growth under antibiotic exposure. We extracted bioactive supernatant from *B. thailandensis* grown in monoculture. We treated *F. johnsoniae* cultures with the bioactive supernatant alone and in combination with daidzein, an efflux pump inhibitor (288). The bioactive supernatant inhibited *F. johnsoniae* growth, daidzein did not, and the bioactive supernatant + daidzein synergistically inhibited *F. johnsoniae* (**Figure 5.2**). This suggests that *F. johnsoniae* growth is still permitted in the presence of an antibiotic because of efflux-mediated antibiotic extrusion.

The bioactive supernatant was obtained from *B. thailandensis* grown in monoculture, suggesting that its antibiotic production is not induced by the presence of *F. johnsoniae*. Bactobolin is well-characterized antibiotic produced by *B. thailandensis* in stationary phase monocultures (100, 227). Thus, we hypothesized that bactobolin was the bioactive compound inhibiting *F. johnsoniae* growth. We used a *btaK*::T23 transposon mutant to test for *F. johnsoniae* inhibition. *btaK* (BTH_II1233) is directly involved in the biosynthesis of bactobolin and *btaK* mutants do not produce bactobolin (100). The *B. thailandensis btaK*::T23 transposon mutant still inhibited *F. johnsoniae* despite the inability to produce bactobolin (**Appendix B Figure 33**), suggesting that bactobolin was not the bioactive compound or that multiple bioactive compounds inhibit *F. johnsoniae*.

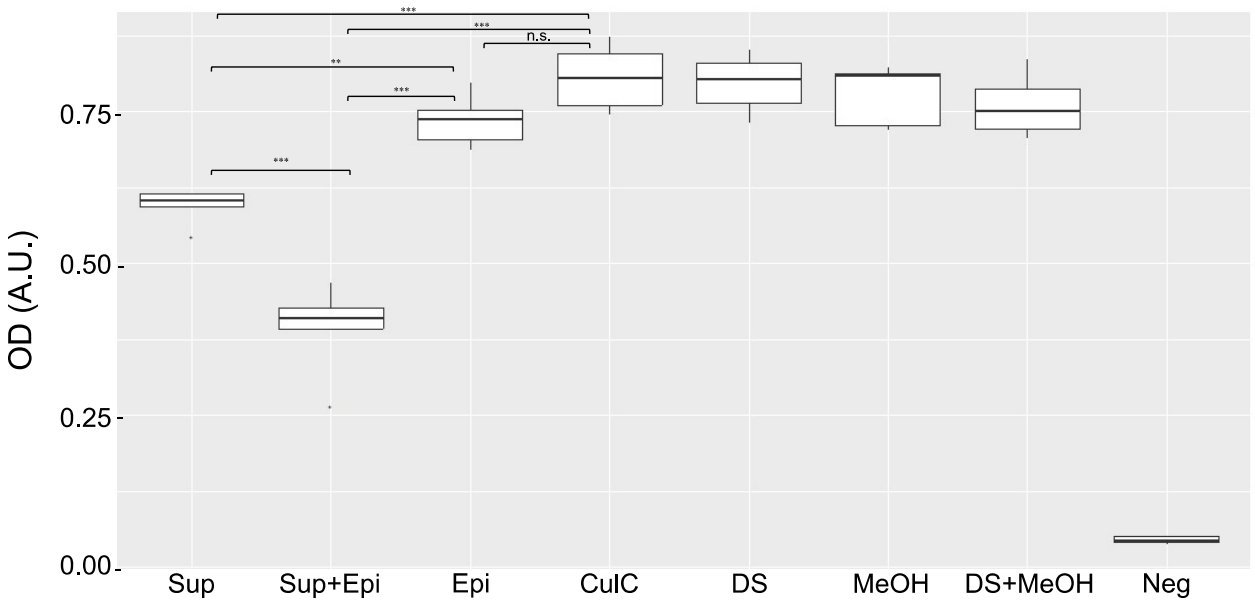

Figure 5.2. *F. johnsoniae* efflux system contributes to the extrusion of a *B. thailandensis*-produced antibiotic.

An end-point growth measurement was taken after *F. johnsoniae* incubation with bioactive supernatant (Sup), daidzein efflux pump inhibitor (Epi), or a combination of the bioactive supernatant and daidzein (Sup+Epi). An untreated culture (CulC), culture with DMSO (DS), culture with methanol (MeOH), culture with combined solvents (DS+MeOH), and blank medium (Neg) served as controls. An ANOVA was performed comparing all treatments to the culture control. A Tukey HSD post-hoc analysis was performed for pairwise comparisons. Data shown are representative of 5 independent experiments; * $p<0.05$, ** $p<0.001$, ***$p<0.0001$, ns: not significant.

Coevolutionary outcomes of B. thailandensis-F. johnsoniae interactions

F. johnsoniae displayed intrinsic mechanisms to remove the *B. thailandensis*-produced antibiotic, but we were also interested in the evolutionary outcomes from long-term exometabolite interactions between these strains. Specifically, we asked if and how *F. johnsoniae* could increase antibiotic resistance if coevolved with *B. thailandensis*. We performed an agar-based coevolution experiment with monoculture controls (**Appendix B Figure 34**). Strains were placed 14 mm apart to allow for exometabolite exchange and passaged onto another plate before intergrowth of the colonies could occur. It was observed that *B. thailandensis* attenuated *F. johnsoniae* growth during the first plate passage (**Appendix B Figure 35**). We observed that the growth, as measured by radial growth, of *F. johnsoniae* generally increased with each successive plate passage (**Figure 3** and **Appendix B Figure 35**), suggesting that *F. johnsoniae* obtained increased resistance to the antibiotic.

We found that antibiotic resistance did increase because of co-plating, as coevolved *F. johnsoniae* grew more successfully than the evolved monoculture when plated with the *B. thailandensis* ancestor (**Appendix B Figure 36**). Interestingly, coevolved *F. johnsoniae* was also able to resist colony invasion by *B. thailandensis* while evolved monoculture could not (**Appendix B Figure 37).** Overall, these results suggest evolved outcomes of long-term exometabolite interactions, specifically increased resistance to antibiotics.

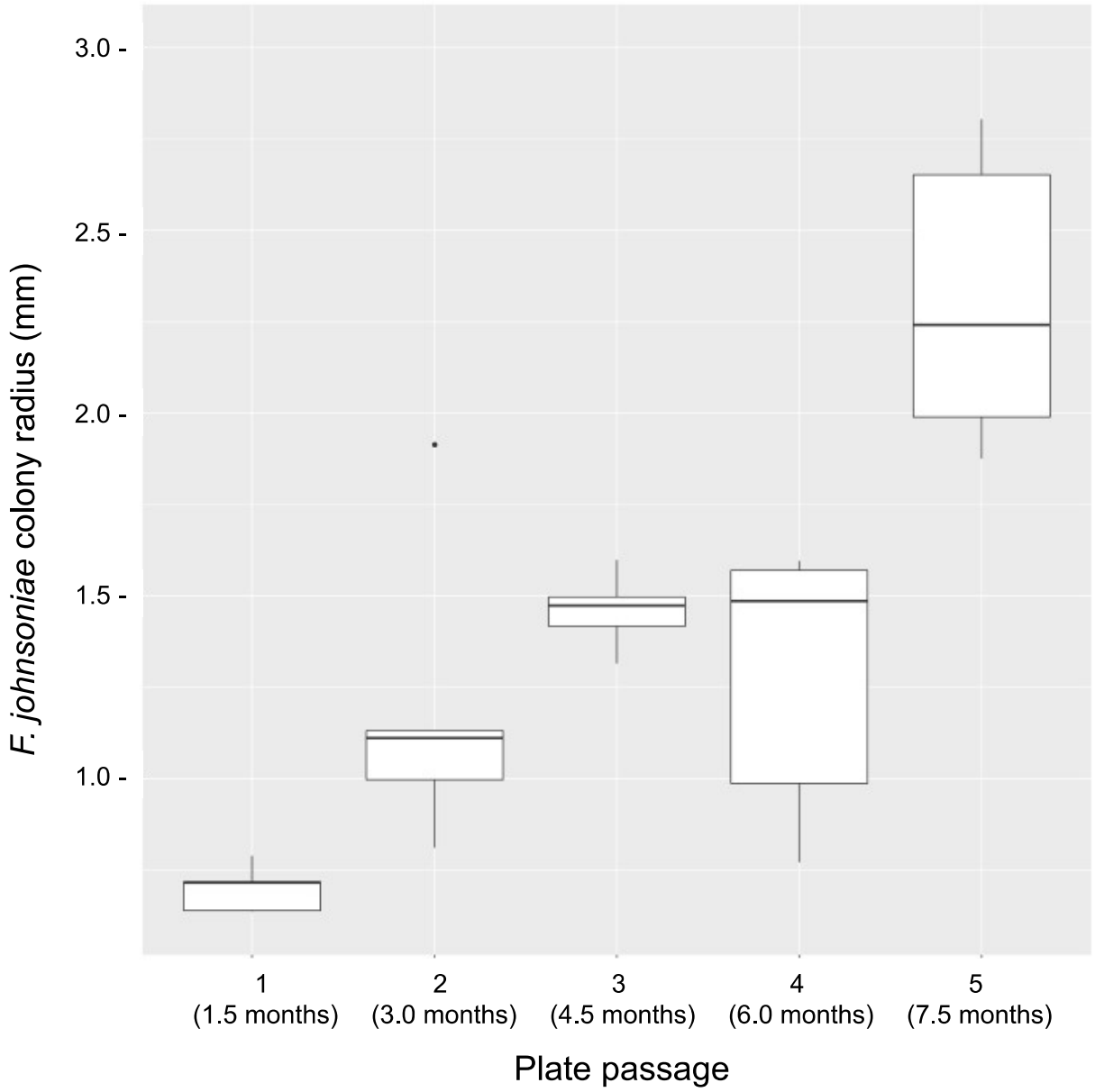

Figure 5.3. *F. johnsoniae* trends toward increased growth success with each plate passage in the presence of *B. thailandensis*.

Radial colony growth of coevolved *F. johnsoniae* was measured from the center of the colony to point of furthest growth on the agar plate. Measurements were taken at the end of each plate passage.

Whole genome sequencing reveals genetic signatures of antibiotic resistance

We performed whole genome sequencing to look for mutations that may have contributed to increased antibiotic resistance in *F. johnsoniae* coevolved lines. Clonal isolates from the *F. johnsoniae* ancestor and from all 5 independent replicates, both from coevolved and monocultures from the fifth plate passage, were sequenced. Mutations were observed in all isolates (**Table 5.1, Supplemental File 1**). Most mutations were unique when comparing genes with mutations observed in monocultures to coevolved lines (**Appendix B Figure 38**). This suggests that there were evolved outcomes to exometabolite interspecies interactions.

Mutations in an efflux outer membrane protein suggested antibiotic resistance (**Table 5.2**). A *tolC* mutation was observed in 4 out of the 5 coevolved lines. While *F. johnsoniae* contains 16 *tolC* genes (**Appendix A Table 28**), the same gene was mutated in 4 independent replicates. Furthermore, parallel evolution was found at the nucleotide level, as 3/4 coevolved lines with mutations in *tolC* had the same 33 bp deletion (**Supplemental File 1**). This deletion occurred from nucleotides 261-293 in the FJOH_RS06580 coding sequence, resulting in a deletion that was not aligned with the codon sequence but did not disrupt the normal sequence of codons (**Figure 5.4**). This deletion appears to have occurred in one of the extracellular loops of TolC. An 11 bp direct repeat was observed just before the start of the deletion and represented the last 11 bp of the 33 bp deletion, suggesting a replication deletion event. The other mutation in FJOH_RS06580 (coevolved line 3) was a single nucleotide polymorphism (G247A in the coding sequence) that resulted in a nonsynonymous mutation (G83R). Protein modeling suggested that this mutation narrowed the diameter of the efflux channel (**Appendix B Figure 39**). Coevolved line 4 did not harbor a mutation in FJOH_RS06580

but had a unique bp insertion in a *ragB*/*susD* nutrient uptake outer membrane protein (FJOH_RS24865). Guanine was inserted at nucleotide position 794 in the coding sequence for FJOH_RS24865. This frameshift mutation resulted in a premature termination codon 6 bp downstream of the insertion, rendering the protein nonfunctional.

Table 5.1. Summary of mutation types observed in *F. johnsoniae* from the (co)evolution experiment.

Mutations are representative of clonal isolates at plate passage 5.

F. johnsoniae isolate	Total	Insertion	Deletion	Nonsynonymous	Synonymous	Nonsense
Coevolved rep 1	6	2	1	3	0	0
Coevolved rep 2	5	0	2	3	0	0
Coevolved rep 3	6	0	0	5	1	0
Coevolved rep 4	5	1	1	3	0	0
Coevolved rep 5	5	1	2	2	0	0
Evolved monoculture rep 1	6	1	3	2	0	0
Evolved monoculture rep 2	7	1	3	2	0	1
Evolved monoculture rep 3	6	0	4	2	0	0
Evolved monoculture rep 4	6	2	1	3	0	0
Evolved monoculture rep 5	3	0	2	0	0	1
Ancestor[a]	2	0	1	1	0	0

[a]Ancestor mutations are not counted toward total mutations in the evolved lines.

Table 5.2. Distinctions and overlaps of loci with mutations unique to the coevolved lines.

These mutations were present (✓, mutation present; ×, mutation not present) in at least one coevolved line and not present in any of the evolved monocultures.

***F. johnsoniae* Locus**	**Annotation**	**Rep 1**	**Rep 2**	**Rep 3**	**Rep 4**	**Rep 5**
FJOH_RS00255	acetyl-CoA carboxylase carboxyltransferase subunit alpha	×	×	✓	×	×
FJOH_RS02320	aminomethyl-transferring glycine dehydrogenase	×	×	×	×	✓
FJOH_RS04780	hypothetical protein	✓	×	×	×	×
FJOH_RS06580	TolC family protein	✓	✓	✓	×	✓
FJOH_RS07830	NAD(P)/FAD-dependent oxidoreductase	×	✓	×	×	×
FJOH_RS09515	response regulator transcription factor	×	✓	×	×	✓
FJOH_RS09520	GHKL domain-containing protein	✓	×	✓	✓	×
FJOH_RS11170	Gfo/Idh/MocA family oxidoreductase	×	×	✓	×	×
FJOH_RS12240	phosphoribosylformylglycinamidine cyclo-ligase	×	×	✓	×	×
FJOH_RS14175	response regulator transcription factor	×	✓	×	×	×
FJOH_RS20510	TetR/AcrR family transcriptional regulator	✓	×	×	×	×
FJOH_RS21875	glycoside hydrolase	✓	×	×	×	×
FJOH_RS24865	RagB/SusD family nutrient uptake outer membrane protein	×	×	×	✓	×
FJOH_RS25290	phosphoribosylanthranilate isomerase	×	×	×	✓	×

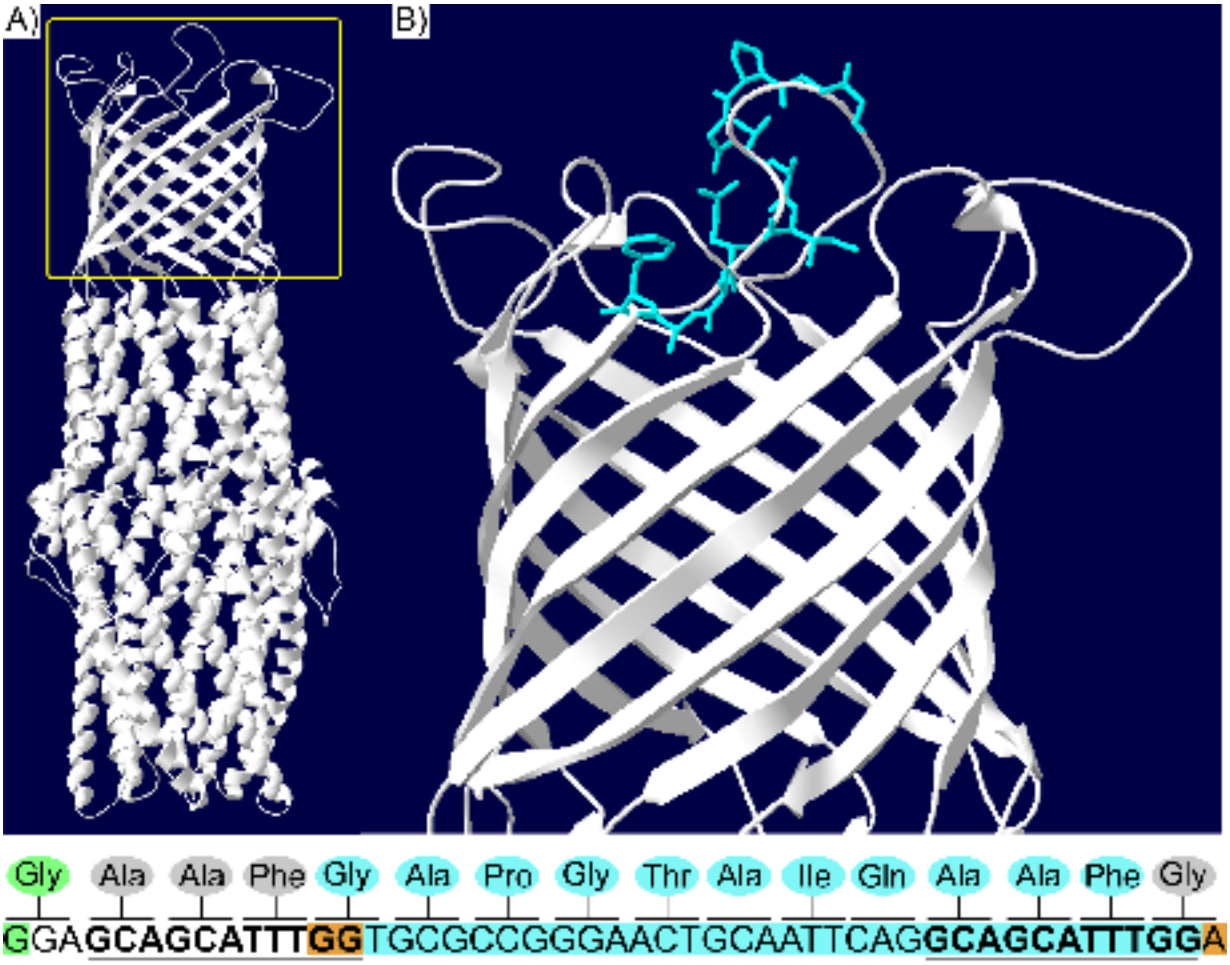

Figure 5.4. A *tolC* 33 bp deletion is located on a TolC extracellular loop.

The TolC protein (**A**) contains a α-helical trans-periplasmic tunnel, a β-barrel channel embedded in the outer membrane**,** and extracellular loops at the cell surface. The yellow box represents the inset in (**B**), where the 11 amino acids corresponding to the 33 bp deletion are highlighted in blue. These amino acids are part of one of the extracellular loops. The nucleotide sequence is shown below the image, representing bps 247-294 in the FJOH_RS06580 coding sequence. The corresponding amino acids are shown above each codon. Nucleotides highlighted in blue represent the 33 bp deletion. Nucleotides highlighted in orange show how the 33 bp deletion

Figure 5.4 (cont'd)

does not disrupt the normal sequence of codons. The 11 bp direct repeats are in bold and underlined. The nucleotide highlighted in green is associated with the nonsynonymous mutation (G247A in the coding sequence, G83R in TolC).

The FJOH_RS06580 tolC 33 bp deletion confers antibiotic resistance

We asked whether the mutations in *tolC* or the mutation in *ragB/susD* would provide resistance to the *B. thailandensis*-produced antibiotic. These mutations were amplified from the coevolved lines and recombined into the *F. johnsoniae* ancestor so that the ancestor would only harbor one of these mutations without the additional mutations observed in the coevolved lines. Strains and plasmids used to make recombinant *F. johnsoniae* are outlined in **Table 5.3**. Uniform colony growth was observed in recombinant strain JCAC01 when plated with *B. thailandensis*, suggesting that the 33 bp deletion confers some degree of antibiotic resistance (**Figure 5.5**). In contrast, the ancestor and strains JCAC03/JCAC04 displayed sparse colony growth in the presence of *B. thailandensis*. In fact, JCAC03 appeared to have less growth success than the ancestor, suggesting that a narrower opening to the TolC efflux channel is detrimental to fitness. However, the 33 bp deletion in *tolC* alone was not enough to confer equivalent resistance observed in the coevolved lines (**Appendix B Figure 40**). Recombinant strains with the 33 bp deletion in *tolC* grew better than the ancestor but not as well at the coevolved lines when plated with *B. thailandensis*. This suggests that coevolved lines harboring the *tolC* 33 bp mutation contain additional antibiotic resistance-conferring mutations.

Table 5.3. Strains and plasmids used in this study.

Strain or plasmid	Description[a]	Source or reference
Escherichia coli strains		
DH5αmcr	Strain used for general cloning	Life Technologies (Grand Island, NY)
HB101	Strain used with pRK2013 for triparental conjugation	289; 290
DH5amcr_pYT354	pYT354 in DH5amcr; sacB-containing suicide vector	284
B. thailandensis strain		
E264 (ATCC 700388)	Wild type	129
F. johnsoniae strains		
UW101 (ATCC 17061)	Wild type	291
JCCE01	Coevolved strain containing a 33 bp (261-293) deletion in tolC (FJOH_RS06580)	This study
JCCE03	Coevolved strain containing a nonsynonymous mutation (G247A) in tolC (FJOH_RS06580)	This study
JCCE04	Coevolved strain containing an insertion (G) at position 794 in ragB/susD (FJOH_RS24865)	This study
JCAC01	tolC 33 bp deletion placed in ancestor	This study
JCAC02	tolC G247A mutation placed in ancestor	This study
JCAC03	ragB/susD bp (G) insertion at position 794 placed in ancestor	This study
Plasmids		
pYT354	sacB-containing suicide vector; Ap^r (Em^r). pYT354 is modified from pYT313 with different multiple cloning site	284
pJC101	Construct used to replace ancestral native tolC with tolC 33 bp deletion	This study
pJC102	Construct used to replace ancestral native tolC with tolC G247A	This study
pJC103	Construct used to replace ancestral native ragB/susD with ragB/susD 794G inseration	This study
pRK2013	Helper plasmid for triparental conjugation; Km^r	290

[a]Abbreviations: Ap^r-ampicillin resistance, 100 micrograms per ml; Km^r kanamycin resistance 30

Table 5.3 (cont'd)

micrograms per ml; (Em^r-erythromycin resistance, 100 micrograms per ml for *F. johnsoniae*). Antibiotics resistance phenotypes listed in parentheses (Em) are those expressed in *F. johnsoniae* but not in *E. coli*. Antibiotics resistance phenotypes listed not in parentheses (Ap, Km) are those expressed in *E. coli* but not in *F. johnsoniae*.

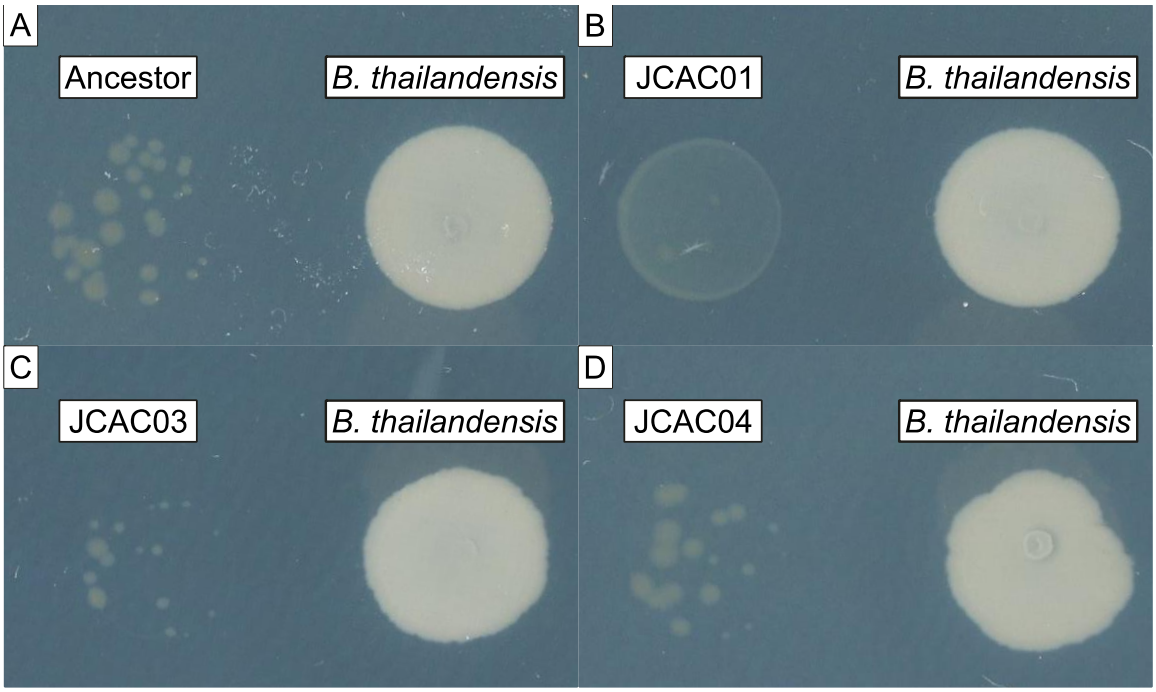

Figure 5.5. The *tolC* 33 bp deletion confers antibiotic resistance.

The ancestor (**A**) and recombinant strains of *F. johnsoniae* ancestor (**C-D**) were co-plated with *B. thailandensis*. The recombinant strain with the *tolC* 33 bp deletion (**B**) displays uniform colony growth while the ancestor and other recombinant strains display sparse colony growth. Plates were imaged after a week of incubation.

Thailandamide is one of the bioactive molecule produced by B. thailandensis

The nonsynonymous mutation in *tolC* did not confer resistance to the *B. thailandensis*-produced antibiotic. But, *F. johnsoniae* coevolved line 3 still developed resistance to the antibiotic despite harboring this mutation (**Figure 5.6A**). We observed that coevolved line 3 also contained a unique nonsynonymous mutation in acetyl-CoA carboxylase carboxyltransferase subunit alpha (*accA*, **Table 5.2**). This was a C479A nonsynonymous mutation in the coding sequence of *accA* that resulted in a P160Q alteration in AccA. This mutation was reminiscent to a P164Q mutation in AccA from *Salmonella enterica* serovar Typhimurium strain LT2 that conferred resistance to thailandamide from *B. thailandensis* (229). Thailandamide is a characterized antibiotic that inhibits fatty acid synthesis (292). The P164Q mutation from *S. enterica* aligned with the P160Q mutation observed in our coevolved line (**Figure 5.6**). Thus, we hypothesized that thailandamide was also the antibiotic responsible for inhibition of *F. johnsoniae*.

We plated the *F. johnsoniae* ancestor with *B. thailandensis thaF* (BTH_II1675), *thaA* (BTH_II1681), and *atsR* (BTH_I0633) transposon mutants. *thaF* encodes a polyketide synthetase trans-AT domain directly involved in the biosynthesis of thailandamide, *thaA* encodes a LuxR-type regulator in the thailandamide biosynthetic gene cluster, and *astR* encodes a global regulator. ThaA positively regulates the thailandamide biosynthetic gene cluster while AtsR negatively regulates the thailandamide biosynthetic gene cluster. We found that *thaF*::T23 and *thaA*::T23 mutants decreased inhibition of *F. johnsoniae* (**Figure 5.6B** and **Figure 5.6C**) while the *atsR*::T23 mutant increased inhibition of *F. johnsoniae* (**Figure 5.6D**). This suggests that thailandamide is bioactive against *F. johnsoniae*. However, *F. johnsoniae* was still slightly

inhibited when plated with *thaF*::T23 and *thaA*::T23 mutants, which also suggests that in addition to thailandamide, there may be another *B. thailandensis*-produced antibiotic that is inhibiting *F. johnsoniae*. However, we were unable to determine this molecule.

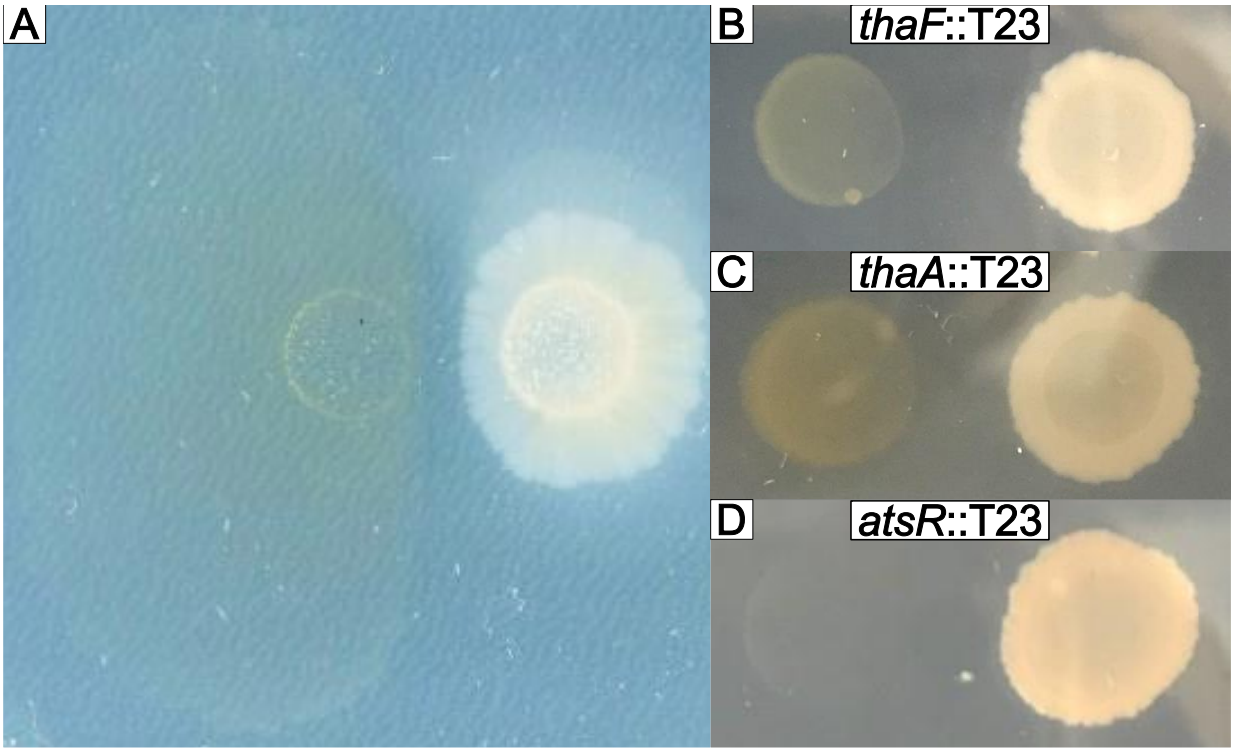


```
UW101_ACC-alpha     1 M--EYLDFELPIKELEEQLEKCVIIGKE---SDVDVTPTCKEINKKLEQT
LT2_ACC-alpha       1 MSLNFLDFEQPIAELEAKIDSLTAVSRQDEKLDINIDEEVHRLREKSVEL
consensus           1 *.. .**** ** ***  ..    . . ... *. .    . .  *

UW101_ACC-alpha    46 KKDIYKNLTAWQRVQLSRHPNRPYTLDYIKAICGDTFLELHGDRGFKDDK
LT2_ACC-alpha      51 TRKIFADLGAWQVAQLARHPQRPYTLDYVR-LAFDEFDELAGDRAYADDK
consensus          51  . *.  * ***  ** ***.*******....  * * ** ***.. ***

UW101_ACC-alpha    96 AMVGGLGKINGQSFMIVGQQKGYNTKTRQYRNFGMANPEGYRKALRLMKM
LT2_ACC-alpha     100 AIVGGIARLEGRPVMIIGHQKGRETKEKIRRNFGMPAPEGYRKALRLMEM
consensus         101 *.***.... *   **.* ***  ** .  *****  ********** *

UW101_ACC-alpha   146 AEKFGIPVLTLVDTPGAYPGLEAEERGQGEAIARNIFEMVRLQVPIITII
LT2_ACC-alpha     150 AERFNMPIITFIDTPGAYPGVGAEERGQSEAIARNLREMSRLNVPVICTV
consensus         151 **.* .*..* .**.***** ****** ******. ** **.**.*  .

UW101_ACC-alpha   196 VGEGASGGALGIGVGDRVYMLENTWYSVISPESCSSILWKSWEYKERAAE
LT2_ACC-alpha     200 IGEGGSGGALAIGVGDKVNMLQYSTYSVISPEGCASILWKSADKAPLAAE
consensus         201 .***.*****.*****.* **  . ******* * ****** .    ***

UW101_ACC-alpha   246 ALKLTSSDMKKQKLVDDVIPEPLGGAHYDREITTFKTVADYITKGYNELKD
LT2_ACC-alpha     250 AMGIIAPRLKELKLIDSIIPEPLGGAHRNPEAMAASLKAQLLEDLADLDV
consensus         251 *. .    .*  **.* .********    *    ..   .     .*

UW101_ACC-alpha   296 LSTADLIAQRMDKYSNMGEYKE
LT2_ACC-alpha     300 LSTDDLKNRRYQRLMSYGYA--
consensus         301 *** **   *  .    *  ..
```

Figure 5.6. Thailandamide is bioactive against *F. johnsoniae*.

Figure 5.6 (cont'd)

While the nonsynonymous mutation in *tolC* did not confer antibiotic resistance (present in *F. johnsoniae* coevolved line 3), *F. johnsoniae* coevolved line 3 still displayed antibiotic resistance at the end of plate passage five (**A**). *B. thailandensis* transposon mutants in *thaF* (**B**) and *thaA* (**C**) have decreased inhibition toward *F. johnsoniae* while an *atsR* transposon mutant has increased inhibition of *F. johnsoniae* (**D**). Below the panels is an amino acid sequence alignment between the *F. johnsoniae* AccA and *S. enterica* AccA. The asterisks indicate positions within the proteins that were identical. The blue box highlights the alignment of P160 in *F. johnsoniae* and P164 in *S. enterica.*

Discussion

We performed an experimental coevolution study between a strain capable of antibiotic production (*B. thailandensis*) and an antibiotic-sensitive strain (*F. johnsoniae*). Our findings show how long-term interspecies interactions, facilitated through chemical exchange via diffusion in agar, can lead to the evolution of antibiotic resistance. Mutational analysis revealed that antibiotic resistance was conferred via efflux. Specifically, a 33 bp deletion in *tolC*. This deletion corresponded to the elimination of 11 amino acids that were part of an extracellular loop in TolC. Placing this mutation in the ancestor provided antibiotic resistance but this strain did not achieve resistance levels observed in the coevolved lines, suggesting additional mutations can confer even greater antibiotic resistance. A different path to resistance was achieved through a nonsynonymous mutation in *accA*. Furthermore, this mutation provided insight that the *B. thailandensis*-produced antibiotic was thailandamide, given this mutation was first described in a Salmonella strain that gained resistance to thailandamide (229). *B. thailandensis* transposon mutants with abrogated thailandamide production confirmed that thailandamide was bioactive against *F. johnsoniae*, but slight inhibition persisted, suggesting more than one antibiotic may be bioactive against *F. johnsoniae.*

Performing the experimental coevolution on agar plates created a heterogenous environment that set the stage for the evolution of antibiotic resistance. *F. johnsoniae* growth at the distal end of the colony was permitted because of an antibiotic concentration gradient that was established via diffusion. Low-dose antibiotics likely upregulated intrinsic mechanisms of resistance (e.g. efflux pumps) that conferred low-levels of resistance (293). The ability to persists in the presence of antibiotics can provide the opportunity for mutational acquisition of

resistance (278, 294). This was demonstrated experimentally in a seminal study that found that a heterogenous environment increased the rate of adaptation to antibiotics with as few at 100 bacteria in the initial inoculum (295). This approach has been expanded to show how the initial adaptation to low levels of antibiotics facilitate adaptations to high levels of resistance (296). Thus, evolutionary adaptations to antibiotic resistance can be fostered in heterogenous environments that would otherwise not be achieved in a uniform environment (297, 298).

F. johnsoniae antibiotic resistance was conferred through a 33 bp deletion in *tolC*. The occurrence of the 11 bp directed repeats may support a replication misalignment event that led to the 33 bp deletion (299, 300). TolC forms the outmembrane channel part of the tripartite AcrAB-TolC drug efflux pump (301). *tolC* (FJOH_RS06580) is located in an operon that includes the remaining components necessary for a functional efflux pump. This includes a TetR/AcrR family transcriptional regulator (FJOH_RS06575), a membrane fusion protein (FJOH_RS06585), and an inner membrane transporter (FJOH_RS0690). Elimination of 11 amino acids from an extracellular loop in TolC may result in TolC more frequently adopting an open conformation, which could increase the rate of antibiotic extrusion. “Leaky” TolC mutants have been characterized, but these mutations occurred at the periplasmic end of TolC (302, 303). In fact, mutational studies of the TolC extracellular loops appear uncommon but may present a novel mechanism for antibiotic resistance (304).

The *F. johnsoniae* recombinant strain harboring the 33 bp deletion in *tolC* was resistant, but not as resistant as the *F. johnsoniae* coevolved lines to the *B. thailandensis*-produced antibiotic. Additional mutations in the coevolved lines are likely to provide increased antibiotic resistance. For example, coevolved line 1 also harbored a 1 bp insertion (T) at position 4734734

in FJOH_RS20510, annotated as a TetR/AcrR family transcriptional regulator. This results in a nonsense mutation that would render the protein nonfunctional. TetR regulators are typically negative regulators, so a nonfunctional TetR regulator would lead to increased expression of efflux pump systems (305). We note that this occurred in FJOH_RS20510 and not FJOH_RS06575, but some TetR regulators have multiple targets and TetR from FJOH_RS20510 could also be negatively regulating the FJOH_RS06580-FJOH_RS06585-FJOH_RS06590 efflux system (306). The remaining coevolved lines with the 33 bp deletion in *tolC* (line 2 and line 5) also had mutations in transcriptional regulators (OmpR and LytTR) but their potential contributions to increased antibiotic resistance is unclear.

A nonsynonymous mutation in *accA* in coevolved line 3 also provided resistance to the *B. thailandensis*-produced antibiotic. In addition, this mutation guided our efforts to uncover that thailandamide was the antibiotic produced in *B. thailandensis* that inhibited *F. johnsoniae*. Thailandamide resistance was first characterized in spontaneous mutants from *S. enterica* (229). Wozniak and colleagues found 6 unique mutations for 3 different amino acid positions in AccA that provided thailandamide resistance. One of these mutations was also spontaneously generated in our study (P160Q in *F. johnsoniae*, P164Q in *S. enterica*). *B. thailandensis* transposon mutants with abrogated thailandamide production effectively reduced inhibition of *F. johnsoniae*. But, noticeable inhibition still persisted. *B. thailandensis* can produce numerous antibiotics (100, 102, 250). It is likely that *F. johnsoniae* was subjected to multiple antibiotics but other mutations observed in the coevolved lines did not provide insight into antibiotic resistance to other *B. thailandensis*-produced antibiotics.

F. johnsoniae coevolved line 4 did not harbor a mutation in *tolC* or *accA*. However, the *ragB/susD* mutation was unique to coevolved line 4 and we hypothesized that this may provide an alternative mechanism for antibiotic resistance. Some antibiotics enter bacterial cells via nutrient transporters (307, 308). Since the *ragB/susD,* rendered the protein nonfunctional, antibiotic resistance could have been conferred to coevolved line 4 by prevention of antibiotic uptake. We did not find this to be the case, as the *F. johnsoniae* recombinant strains with the *ragB/susD* nonsynonymous mutation had equivalent susceptibility to the *B. thailandensis*-produced antibiotic as the *F. johnsoniae* ancestor. The other mutations in coevolved line 4 may confer antibiotic resistance or, it is possible that mutations for antibiotic resistance did not fixate in the population, and we chose an isolate for sequencing that did not acquire a mutation conferring antibiotic resistance. Bacterial population sequencing could shed light on this discrepancy.

Our experiment demonstrates how interspecies chemical interactions can have evolutionary consequences for antibiotic resistance. Coevolution on an agar plate created a structured environment that allowed for interspecies chemical exchange via diffusion. Structured environments also occur in natural settings, such as soil, where antibiotic concentration gradients can be established (309). The exposure to low levels of antibiotics in heterogeneous environments can select for resistance mutations (310). The diversity of antibiotics (311) and corresponding resistance mechanisms (312) highlight the genetic novelties that have arisen from millions of years of bacterial competition. Studying these competitive interspecies interactions may shed light on coevolutionary arms race for antibiotic upkeep and antibiotic resistance (313).

CHAPTER 6 : Conclusions and Future Directions

Summary

This dissertation examined the consequences of exometabolite-mediated interactions regarding responses and behaviors of members within a synthetic microbial community and the genetic mechanisms of adaptive evolution. In Chapter 2, a new synthetic community system (transwell system) was established that facilitates and focuses on exometabolite-mediated interspecies interactions. The transwell system consists of two main parts- a 96-well plate where each well contains a 0.22-µm filter bottom, and shared medium reservoir fitted below the 96 well plate. The transwell system was biologically verified using an AHL producer-AHL receiver combination. It was demonstrated that AHLs were able to be produced in individual wells, diffuse into the shared medium reservoir, and be received by the AHL-sensing population. This is a versatile, scalable system that is readily available to the scientific community. For example, the transwell plates are compatible with liquid handling robots, which permits scalable, functional screens. Establishing the transwell system facilitated further studies in Chapters 3 and 4.

In Chapter 3, we investigated the dynamics of exometabolite production in monocultures of 3 environmental isolates over stationary phase. We defined dynamic as compositional changes through time. Broadly, we observed directional dynamics of exometabolite production for each strain, meaning, there was a stepwise trajectory between time points where each time point was distinguished from any of the previous time points and even more distinct from previous time points in PCoA space. This revealed that these microbial strains were metabolically active in stationary phase and continuing to transform their environment. Exometabolite production coincided with increased or consistent transcripts

related to transporters, and consistent population levels, suggesting that live cells were either actively or passively releasing exometabolites into the shared medium reservoir. Each strain produced exometabolites involved in either interference or exploitative competition strategies (e.g. antibiotics or siderophores), suggesting that entry into stationary phase primes bacteria for competition even in the absence of heterospecifics. But, each strain also released a diverse array of primary metabolites as well, suggesting strains are primed for both positive and negative interaction within a microbial community context.

In Chapter 4, we placed these environment isolates in cocultures to observe their responses and behaviors to interspecies interactions over stationary phase. As observed in Chapter 3, we also observed directional dynamics, both in transcript and exometabolomic profiles. Exometabolite interspecies interactions led to differential responses of synthetic community members. *C. violaceum* and *P. syringae* transcriptional responses appeared to be largely driven by the presence of *B. thailandensis*, even in the 3-member community. With reductions in cell populations in both *C. violaceum* and *P. syringae*, we hypothesized that these transcriptional alterations may be due to the responses of bioactive compounds produced by *B. thailandensis*. We found that *B. thailandensis* upregulated numerous biosynthetic genes clusters (BSGCs) in coculture, encoding bioactive exometabolites involved in both interference and competitive strategies. Transcriptional upregulation of these BSGCs also resulted in increased exometabolite abundance of these bioactive compounds in cocultures. Coexpression network analysis revealed that the expression patterns of *B. thailandensis* BSGCs were coregulated to expression patterns of transcripts in both *C. violaceum* and *P. syringae*, suggesting that the influence of *B. thailandensis* on the transcriptional responses of *C.*

violaceum and *P. syringae* can be attributed to the exometabolites involved in competition strategies. Furthermore, we found that not all transcriptional responses and exometabolomic abundances in the 3-member community were additive outcomes observed in pairwise community arrangements. Lastly, these dynamics occurred over stationary phase, shedding light on the importance of upkeeping competition strategies during periods of non-growth.

Finally, in Chapter 5, we performed an agar-based coevolution experiment to observe the genomic signatures of adaptive evolution to antibiotic resistance. *B. thailandensis* was able to inhibit *F. johnsoniae* but, when spotted on agar at a distance that allowed for exometabolite exchange, *F. johnsoniae* could grow in the presence of the *B. thailandensis*-produced antibiotic. We attributed this growth success to efflux systems and continued to coevolve these strains through successive plate passages and observed that *F. johnsoniae* acquired increased resistance. Genome sequencing revealed two signature of antibiotic resistance- a 33 bp deletion in *tolC* and a nonsynonmous mutation in *accA*. The contribution of the *tolC* 33 bp deletion to antibiotic resistance was confirmed by creating a recombinant *F. johnsoniae* ancestor, but the deletion alone was not enough to confer equivalent resistance observed in the coevolved lines. The *accA* mutation guided bioactive molecule discovery given its match to a previously described spontaneous thailandamide-resistant Salmonella mutant. Thailandamide was found to be responsible for the inhibition *F. johnsoniae* but inhibition was still observed when co-plated with a *B. thailandensis* transposon mutant with abrogated thailandamide, suggesting *F. johnsoniae* is inhibited by more than one *B. thailandensis*-produced antibiotic.

Overall, this work provides a new synthetic community system available to microbial ecologists interested in studying exometabolite-mediated interspecies interactions (Chapter 2).

We've contributed to knowledge gaps concerning the transcriptional and exometabolomic dynamics during stationary phase (Chapter 3 and 4). This work also provides insights into the maintenance of competition strategies during periods of non-growth, which may have implications to survival strategies in environments with pulsed-nutrient resources (e.g. soil). And, we found that behaviors and responses in more complex communities may not always be a summation of pairwise outcomes, highlighting outcomes in the microbial communities can be "greater than the sum of its parts" (Chapter 4). Lastly, long-term exometabolomic interspecies interactions have implications for the emergence of antibiotic resistance (Chapter 5).

Future Directions

I will discuss each project highlighting future studies using a reductionist approach and then expand future directions to test ecological and evolutionary relationships more broadly. For the synthetic community, I would like to identify the uncharacterized bioactive molecules (BSGCs) that were upregulated in cocultures- two from *B. thailandensis* and one from *C. violaceum*. Bacterial coculturing has been a feasible way to discover new bioactive molecules given the ecological context of upregulated BSGCs when in the presence of competitors (314). More broadly, a fluorescent reporter system could be established to explore coculture combinations that upregulate BSGCs (315). I would also like to explore the regulatory landscape regarding the non-additivity of transcript upregulation and exometabolite production. Low-dose antibiotics, primary metabolites (e.g. homoserine), and inhibition of pyrimidine biosynthesis are linked to upregulation of BSGCs in *B. thailandensis* (250, 251, 315). How do

individual stimuli affect the regulatory and metabolic networks in *B. thailandensis* and, how do combinations of stimuli synergistically amplify behaviors?

More broadly, the transwell system can be used to test an array of ecological theories. Diversity-function relationships have been of interest to ecologists for purposes of defining how microbial community properties scale with output (316). The synthetic community system allows for a simple bottom-up or top-down approach to tease apart this relationship. For example, a fluorometric assay can be performed from the shared medium reservoir for functional enzyme activities (317). This could serve as proxy for nutrient cycling. Diversity can be defined phylogenetically (16S rRNA) or by functional traits (318) to understand how diversity scales with functional output. The impact of other community properties, such as evenness can easily be controlled in the system by the proportions of inoculated wells per member. This is can also be scaled to a 384 transwell plate to increase community richness (# of members). The synthetic community system can also be subjected to a disturbance to uncover emergent properties (319) derived from microbial interactions. Complex interaction networks that emerge from interspecies interactions likely contribute to microbial community resistance (the ability to withstand change) and resilience (the rate of recovery after disturbance), collectively referred to as microbial community stability (320). A microbial community can be subjected to a disturbance (e.g. thermal or pH stress) and community stability can be temporally tracked via a functional metric. This baseline disturbance response can then be compared to community stability subjected to disturbance with member additions or subtractions from the community. Major deviations of community stability from the baseline treatment could be subject to inquiry to understand the microbial interactions contributing to gain or loss of stability.

For the coevolution project, I would be interested in uncovering the additional antibiotic(s) produced by *B. thailandensis* that inhibited *F. johnsoniae*. Using an analytical approach, I could grow cultures of the thailandamide transposon mutant, collect spent supernatant, and using chromatograph techniques to isolate the compound. Mass spectrometry and NMR could then be used for compound identification. I could also use a biological approach by performing transposon mutagenesis on the thailandamide transposon mutant to screen for *B. thailandensis* colonies that no longer inhibit *F. johnsoniae*. These mutants of interest can be sent for whole genome sequencing to reveal the additional BSGC responsible for *F. johnsoniae* inhibition. I would also like to understand the fitness effects of antibiotic resistance associated with multiple mutations. Does placing both the 33 bp *tolC* deletion and the nonsense mutation in TetR/AcrR family transcriptional regulator confer greater antibiotic resistance? Sequencing coevolved lines at each plate passage may also reveal this by looking for the emergence of each of these mutations with time.

I would also like to test the evolutionary outcomes of *B. thailandensis*. While most focus in this dissertation was placed on *F. johnsoniae*, *B. thailandensis* did coevolve with *F. johnsoniae*. This contrasts with another coevolution experiment where the coevolution of *Pseudomonas aeruginosa* was monitored with *Staphylococcus aureus* (321). While *P. aeruginosa* was evolved through daily transfers, ancestral *S. aureus* was grown daily for *P. aeruginosa* transfers. Here, this agar-based experiment has the potential to track a coevolutionary arms race for antibiotic resistance and antibiotic production (313). Are *B. thailandensis* coevolved strains more inhibitory toward *F. johnsoniae* compared to the ancestor? We have some evidence to suggest that *B. thailandensis* morphotypes develop

without the presence of *F. johnsoniae*. Compared to the ancestor, some of these morphotypes have increased or decreased inhibition toward *F. johnsoniae*. What are the genetic determinants of increased inhibition? These increased inhibitory morphotypes could be selectively transferred to achieve an coevolutionary arms race.

Lastly, the methods performed for each dissertation chapter could be combined to study eco-evolutionary outcomes resulting from microbial interspecies interactions. Ghoul and Mitri describe consequences of competition that have been understudied (233). One of these is the concept of continued aggression, where ecological stability is predicted to remain low under scenarios where competitive phenotypes persist. From our synthetic community member experiments, we demonstrated the upregulation of competitive strategies in stationary phase. We could perform an experiment that involves continual serial transfers of the microbial community into new transwell plates that mimic nutrient pulses. The timing of these pulses could determine the longevity of competitive strategies, where frequent transfers would limit the effect of competition strategies and infrequent transfers would increase the effect of competition strategies. Functional outputs and ecological stability could be tested on these communities across different nutrient pulse regimes at selected time points. Communities can then be sequenced to understand how coevolutionary processes are tied to alterations in community members' competition strategies and overall community stability (322).

APPENDICES

APPENDIX A

Supplementary Tables

Appendix A Table 1. Fragments observed from MS/MS analysis of bactobolin.

MS/MS Fragments	Observed[a]	Calculated	PPM	Intensity (a.u.)
1	**366.053**	**366.051**	**5.46**	**7E2**
2	**365.064**	**365.067**	**8.22**	**4.3E2**
3	**322.026**	**322.025**	**3.11**	**1.8E3**
4	**312.039**	**312.041**	**6.41**	**1.6E4**
5	**294.026**	**294.030**	**13.60**	**3.1E3**
6	**286.050**	**286.048**	**6.99**	**6.6E2**
7	**276.021**	**276.019**	**7.25**	**1.6E3**

[a]MS/MS data were acquired under positive ionization mode. Bactobolin, (M+H)obs=383.075, (M+H)calc=383.077

Appendix A Table 2. *C. violaceum* primer sets designed for reverse transcription and end-point PCR.

Primer[a]	Primer (5’ – 3’)	Reference GenBank accession and location	Expected amplicon size (base pairs)	Citation
vioC_Cv Forward	GTCGATCTGGAAGGCAAGTC	LC000628.1:4401-5690	240	This study
vioC_Cv Reverse	CATGCCGAAGAAGTACAGCA			
rpoB_Cv Forward	GCTATGCCAAGCTGGACTTC	LKIW01000107.1:4687-8862	190	This study
rpoB_Cv Reverse	ATCTCGCCCATGTACACCTC			

[a]Primers were designed using the genome of *C. violaceum* Cv017 (58).

Appendix A Table 3. Percent variation explained on the effect of strain, time, and their interaction on exometabolite profiles.

Permanova revealed strain-specific differences in exometabolite composition (all $P \leq 0.001$).

	Strain	Time	Strain x Time
Polar Positive	0.578	0.061	0.685
Polar Negative	0.670	0.026	0.749
Nonpolar Positive	0.762	0.024	0.858
Nonpolar Negative	0.800	0.000	0.865

Appendix A Table 4. Summary of Protest analyses comparing exometabolite composition through time across independent replicates.

Coordinates of the first two PCoA axes were used to perform Protest analyses. Ranges reflect separate Protest analyses performed for each polarity (polar/nonpolar) and ionization mode (positive/negative).

	m12	R	*P*
B. thailandensis	0.019 – 0.389	0.782 – 0.990	0.001 – 0.040
C. violaceum	0.008 – 0.190	0.900 – 0.996	0.001 – 0.035
P. syringae	0.016 – 0.300	0.837 – 0.992	0.001 – 0.075

Appendix A Table 5. Average Bray-Curtis dissimilarity between group centroids when comparing each stationary phase time point to the initial, exponential phase time point (12.5 h).

Ranges reflect separate analyses performed for each polarity (polar/nonpolar) and ionization mode (positive/negative).

Time (h)	*B. thailandensis*	*C. violaceum*	*P. syringae*
25	0.132 - 0.181	0.232 – 0.378	0.233 – 0.374
30	0.148 - 0.215	0.298 – 0.382	0.303 – 0.436
35	0.179 - 0.265	0.326 – 0.442	0.339 – 0.458
40	0.218 - 0.323	0.381 – 0.521	0.370 – 0.506
45	0.242 - 0.333	0.361 – 0.526	0.391 – 0.519

Appendix A Table 6. Average Bray-Curtis dissimilarity between group centroids when comparing time points in a step-wise manner. Ranges reflect separate analyses performed for each polarity (polar/nonpolar) and ionization mode (positive/negative).

Time comparisons (h)	*B. thailandensis*	*C. violaceum*	*P. syringae*
25 to 12.5	0.132 - 0.181	0.232 – 0.378	0.233 – 0.374
30 to 25	0.036 – 0.056	0.035 – 0.112	0.070 – 0.096
35 to 30	0.041 – 0.064	0.042 – 0.078	0.032 – 0.058
40 to 35	0.029- 0.083	0.066 – 0.097	0.049 – 0.075
45 to 40	0.023 - 0.052	0.023 – 0.052	0.036 – 0.057

Appendix A Table 7. Repeated measures permanova performed on independently replicated time series within each strain.

P values are listed followed by R2 values in parenthesis.

	B. thailandensis	*C. violaceum*	*P. syringae*
Polar Positive	0.001 (0.553)	0.001 (0.644)	0.001 (0.626)
Polar Negative	0.068 (0.363)	0.001 (0.650)	0.002 (0.630)
Nonpolar Positive	0.003 (0.744)	0.002 (0.746)	0.001 (0.892)
Nonpolar Negative	0.001 (0.849)	0.001 (0.877)	0.001 (0.893)

Appendix A Table 8. Q-values from pairwise adonis tests comparing all time points within a strain.

Ranges reflect separate analyses performed for each polarity (polar/nonpolar) and ionization mode (positive/negative).

Time comparisons (h)	*B. thailandensis*	*C. violaceum*	*P. syringae*
25 to 12.5	0.093 – 0.21	0.088 – 0.15	0.075 – 0.17
30 to 12.5	0.093 – 0.21	0.088 – 0.13	0.075 – 0.17
35 to 12.5	0.093 – 0.21	0.088 – 0.13	0.075 – 0.17
40 to 12.5	0.093 – 0.21	0.088 – 0.15	0.075 – 0.17
45 to 12.5	0.093 – 0.21	0.088 – 0.15	0.075 – 0.17
30 to 25	0.75 – 0.89	0.38 – 1.0	0.15 – 0.79
35 to 25	0.15 – 0.86	0.16 – 0.28	0.15 – 0.72
40 to 25	0.098 – 0.69	0.088 – 0.2	0.075 – 0.59
45 to 25	0.12 – 0.69	0.088 – 0.2	0.086 – 0.40
35 to 30	0.75 – 0.89	0.49 – 0.98	0.64 – 1.0
40 to 30	0.15 – 0.75	0.13 – 0.45	0.15 – 0.79
45 to 30	0.15 – 0.75	0.11 – 0.59	0.15 – 0.60
40 to 35	0.38 – 0.96	0.16 – 0.56	0.46 – 0.97
45 to 35	0.27 – 0.96	0.15 – 0.88	0.38 – 0.83
45 to 40	0.90 – 0.96	0.87 – 1.0	0.94 – 1.0

Appendix A Table 9. Percent variation explained on the effect of membership, time, and their interaction on transcriptomic profiles.

	Membership	Time	Membership x Time
B. thailandensis	46.26	13.24	63.11
C. violaceum	60.60	3.88	68.29
P. syringae	77.03	0.00	81.40

Appendix A Table 10. Summary of Protest analyses comparing transcriptional profiles through time across independent replicates.

Coordinates of the first two PCA axes were used to perform Protest analyses. Ranges reflect separate Protest analyses performed between all replicates in a community arrangement. Values in parenthesis represent the median P value.

	m12	R	*P*
B. thailandensis			
Monoculture	0.048 – 0.820	0.424 – 0.976	0.010 – 0.867 (0.200)
P. syringae coculture	0.018 – 0.049	0.975 – 0.991	0.001 – 0.001 (0.001)
C. violaceum coculture	0.010 – 0.112	0.943 – 0.995	0.001 – 0.003 (0.001)
3-member	0.013 – 0.162	0.916 – 0.994	0.001 – 0.006 (0.001)
C. violaceum			
Monoculture	0.011 – 0.140	0.927 – 0.995	0.004 – 0.067 (0.039)
P. syringae coculture	0.045 – 0.206	0.891 – 0.977	0.003 – 0.042 (0.008)
B. thailandensis coculture	0.091 – 0.182	0.905 – 0.954	0.001 – 0.108 (0.019)
3-member	0.190 – 0.543	0.676 – 0.900	0.001 – 0.208 (0.013)
P. syringae			
Monoculture	0.178 – 0.538	0.680 – 0.907	0.008 – 0.136 (0.054)
C. violaceum coculture	0.035 – 0.251	0.865 – 0.982	0.001 – 0.083 (0.021)
B. thailandensis coculture	0.021 – 0.290	0.843 – 0.990	0.001 – 0.001 (0.001)
3-member	0.034 – 0.687	0.560 – 0.983	0.007 – 0.317 (0.038)

Appendix A Table 11. PERMANOVA results calculated on independently replicated time series within members across all community arrangements.

PERMANOVA results are presented as *P* values followed by R2 values in parenthesis in the first row. Post-hoc pairwise PERMANOVA results are presented below the first row.

	B. thailandensis	*C. violaceum*	*P. syringae*
adonis	0.001 (0.480)	0.001 (0.619)	0.001 (0.778)
Monoculture vs *B. thailandensis* coculture	-	0.002	0.001
Monoculture vs *C. violaceum* coculture	0.001	-	0.001
Monoculture vs *P. syringae* coculture	0.001	0.010	-
Monoculture vs 3-member	0.001	0.002	0.001
B. thailandensis coculture vs *C. violaceum* coculture	-	-	0.001
B. thailandensis coculture vs *P. syringae* coculture	-	0.002	-
C. violaceum coculture vs *P. syringae* coculture	0.001	-	-
B. thailandensis coculture vs 3-member	-	0.248	0.068
C. violaceum coculture vs 3-member	0.001	-	0.001
P. syringae coculture vs 3-member	0.001	0.002	-

Appendix A Table 12. GO enrichment for plasmid genes in *P. syringae*.

Enrichment was performed in Cytoscape using the BiNGO package.

GO-ID	Description	p-val	q-val	Cluster frequency	Total frequency
6310	DNA recombination	5.69E-06	1.42E-04	7/33 21.2%	76/3397 2.2%
150	Recombinase activity	1.06E-05	1.42E-04	5/33 15.1%	32/3397 0.9%
3677	DNA binding	4.19E-05	3.77E-04	13/33 39.3%	399/3397 11.7%
15074	DNA integration	3.11E-03	2.10E-02	4/33 12.1%	64/3397 1.8%

Appendix A Table 13. Percent variation explained on the effect of membership, time, and their interaction on exometabolite profiles.

	Membership	Time	Membership x Time
Polar Positive	45.76	7.26	55.89
Polar Negative	51.61	4.12	58.83
Nonpolar Positive	56.92	9.49	71.88
Nonpolar Negative	64.77	7.94	79.38

Appendix A Table 14. Summary of Protest analyses comparing exometabolite composition through time across independent replicates.

Coordinates of the first two PCoA axes were used to perform Protest analyses. Ranges reflect separate Protest analyses performed for each polarity (polar/nonpolar) and ionization mode (positive/negative).

	m12	R	*P*
C. violaceum-P. syringae coculture	0.022 – 0.906	0.307 – 0.989	0.001 – 0.849 (0.025)
B. thailandensis-P. syringae coculture	0.015 – 0.592	0.638 – 0.992	0.001 – 0.667 (0.050)
B. thailandensis-C. violaceum coculture	0.003 – 0.456	0.738 – 0.995	0.001 – 0.250 (0.003)
3-member community	0.021 – 0.556	0.667 – 0.990	0.001 – 0.133 (0.003)

Appendix A Table 15. PERMANOVA results calculated on independently replicated time series across coculture community arrangements.

PERMANOVA results are presented as *P* values followed by R2 values in parenthesis in the first row. Post-hoc pairwise PERMANOVA results are presented below the first row.

	Polar Positive	Polar Negative	Nonpolar Positive	Nonpolar Negative
adonis	0.001 (0.475)	0.001 (0.531)	0.001 (0.585)	0.001 (0.662)
B. thailandensis-*C. violaceum* coculture vs *C. violaceum*-*P. syringae* coculture	0.001	0.001	0.001	0.001
B. thailandensis-*C. violaceum* coculture vs *B. thailandensis*- *P. syringae* coculture	0.001	0.001	0.001	0.001
B. thailandensis- *P. syringae* coculture vs *C. violaceum*-*P. syringae* coculture	0.001	0.001	0.001	0.001
3-member community vs *C. violaceum*-*P. syringae* coculture	0.001	0.001	0.001	0.001
3-member community vs *B. thailandensis*- *P. syringae* coculture	0.001	0.001	0.001	0.001
3-member community vs *B. thailandensis*-*C. violaceum* coculture	0.002	0.008	0.019	0.025

Appendix A Table 16. Number of predicted biosynthetic gene clusters (BSGCs, first row) followed by the quantity of upregulated BSGCs in cocultures.

	B. thailandensis	*C. violaceum*	*P. syringae*
Predicted BSGCs	28	14	10
C. violaceum-P. syringae coculture	-	0	0
B. thailandensis-P. syringae coculture	8	-	0
B. thailandensis-C. violaceum coculture	10	1	-
3-member community	11	1	0

Appendix A Table 17. Identification of *B. thailandensis*-derived bioactive metabolites from mass spectral data.

	Molecular species	Observed	Calculated	PPM	RT	Scan	File
Bactobolin	Parent	383.0778	383.0769	2.34939773	4.22	1440	ZHILIC5um_POS-MSMS_3mem-45hr_Run76.mzML
	MS/MS Fragment	365.0674	365.067	1.09568928	4.22	1441	ZHILIC5um_POS-MSMS_3mem-45hr_Run76.mzML
	MS/MS Fragment	322.0248	322.025	0.62106979	4.22	1441	ZHILIC5um_POS-MSMS_3mem-45hr_Run76.mzML
	MS/MS Fragment	312.0406	312.041	1.28188283	4.22	1441	ZHILIC5um_POS-MSMS_3mem-45hr_Run76.mzML
	MS/MS Fragment	294.0301	294.03	0.34010135	4.22	1441	ZHILIC5um_POS-MSMS_3mem-45hr_Run76.mzML
	MS/MS Fragment	286.0491	286.048	3.84550845	4.22	1441	ZHILIC5um_POS-MSMS_3mem-45hr_Run76.mzML
	MS/MS Fragment	276.0192	276.019	0.7245878	4.22	1441	ZHILIC5um_POS-MSMS_3mem-45hr_Run76.mzML
Capistruin	Parent	1025.0189	1025.0191	0.195118315	11.09	3750	ZHILIC5um_POS-MSMS_3mem-45hr_Run76.mzML
	MS Adduct	1036.011	1036.01	0.965241648	11.09	3750	ZHILIC5um_POS-MSMS_3mem-45hr_Run76.mzML
Melleilactone	Parent	305.1752	305.1748	1.310724	7.15	2534	C18_NEG-MSMS_3mem-45hr_Run77.mzXL
	MS/MS Fragment	277.1807	277.1799	2.886212	7.15	2536	C18_NEG-MSMS_3mem-45hr_Run77.mzXL

Appendix A Table 17 (cont'd)

	MS/MS Fragment	249.1489	249.1486	1.204101	7.15	2536	C18_NEG-MSMS_3mem-45hr_Run77.mzXL
	MS/MS Fragment	221.154	221.1537	1.356523	7.15	2536	C18_NEG-MSMS_3mem-45hr_Run77.mzXL
	MS/MS Fragment	139.04	139.039	7.192227	7.15	2536	C18_NEG-MSMS_3mem-45hr_Run77.mzXL
Rhamnolipid	Parent	761.5052	761.5046	0.787914	8.48	4036	C18_NEG-MSMS_3mem-45hr_Run77.mzXL
	MS/MS Fragment	535.3125	535.3113	2.241686	8.48	4037	C18_NEG-MSMS_3mem-45hr_Run77.mzXL
	MS/MS Fragment	225.1858	225.185	3.552635	8.48	4037	C18_NEG-MSMS_3mem-45hr_Run77.mzXL
Thailandamide	Parent	718.4279	718.4314	4.871725	5.07	2547	C18_POS-MSMS_3mem-45hr_Run76.mzXL
	MS-Adduct	735.4571	735.4579	1.087758	5.07	2547	C18_POS-MSMS_3mem-45hr_Run76.mzXL
	Parent	716.4163	716.4157	0.837503	5.03	2429	C18_NEG-MSMS_3mem-45hr_Run77.mzXL
Pyochelin	Parent	325.0667	325.068	3.999163	4.77	2379	C18_POS-MSMS_3mem-45hr_Run76.mzXL
	MS/MS Fragment	178.0317	178.0325	4.493562	4.77	2381	C18_POS-MSMS_3mem-45hr_Run76.mzXL
	MS/MS Fragment	146.0267	146.0267	0	4.77	2381	C18_POS-MSMS_3mem-45hr_Run76.mzXL

Appendix A Table 18. One-way ANOVA[a] comparing the quantitation of identified secondary metabolites between community arrangements with *B. thailandensis* membership.

	Df (between)	Df (within)	*F* value	*p*
Bactobolin	6	160	392.10	<2e-16
Capistruin	6	160	77.83	<2e-16
Melleilactone	6	121	150.10	<2e-16
Rhamnolipid[b]	6	136	39.34	<2e-16
Thailandamide	6	121	61.02	<2e-16
Pyochelin	6	136	105.20	<2e-16

[a]Formula: aov(formula = log(Value) ~ Membership, data = .)

[b]Rhamnolipid congener Rha-Rha-C14-C14

Appendix A Table 19. TukeyHSD post-hoc results comparing quantitation of identified secondary metabolites between community arrangements with *B. thailandensis* membership. Values represent the adjusted P-value.

	Bactobolin	Capistruin	Melleilactone	Rhamnolipid[a]	Thailandamide	Pyochelin
Monoculture vs *P. syringae* coculture	8.41E-01	8.00E-07	4.00E-07	2.26E-01	1.25E-04	4.85E-01
Monoculture vs *C. violaceum* coculture	3.54E-01	8.45E-02	< 1.00E-07	2.53E-02	< 1.00E-07	8.55E-01
Monoculture vs 3-member	8.27E-01	5.00E-07	< 1.00E-07	1.00E-05	< 1.00E-07	7.13E-04
***C. violaceum* coculture vs *P. syringae* coculture**	8.38E-01	6.48E-03	5.45E-02	7.68E-01	9.27E-03	9.11E-01
***P. syringae* coculture vs 3-member**	3.28E-01	9.99E-01	1.00E-07	6.50E-03	4.32E-03	4.24E-02
***C. violaceum* coculture vs 3-member**	6.08E-02	4.20E-03	1.76E-03	7.76E-02	9.97E-1	6.20E-03

[a]Rhamnolipid congener Rha-Rha-C14-C14

Appendix A Table 20. Network summary results from interspecies coexpression networks.

Network	***B. thailandensis*-*C. violaceum***		***B. thailandensis*-*P. syringae***	
Member	*B. thailandensis*	*C. violaceum*	*B. thailandensis*	*P. syringae*
Total nodes	2701	2043	3254	3478
Nodes with only intraspecies edges	2418	1814	2749	2996
Nodes with interspecies edges	283	229	505	482
Total edges	9382	7240	15801	23319
Intraspecies edges	9074	6932	15056	22574
Interspecies edges	308		745	

Appendix A Table 21. Repeated measures ANOVA results comparing the "expected" exometabolite abundance over the time course of select identified exometabolites to the experimentally detected abundance.

The "expected" abundance was determined by adding the peak areas from the pairwise cocultures with *B. thailandensis* at each time point.

Effect	DFn	DFd	F	P[a]
Thailandamide				
Membership	1	2	5.755	1.39E-01
Time	5	10	51.698	8.02E-07
Membership:Time	5	10	3.9	3.20E-02
Pyochelin				
Membership	1	2	13.877	6.50E-02
Time	5	10	10.116	1.00E-03
Membership:Time	5	10	2.043	1.57E-01
Capistruin				
Membership	1	3	0.53	5.19E-01
Time	5	15	2.7	6.20E-02
Membership:Time	5	15	1.413	2.75E-01

[a]Note: One representative test is displayed. See caveat in methods section: *Non-additive metabolomics production*.

Appendix A Table 22. Post-hoc pairwise analyses comparing the "expected" exometabolite abundance to the experimental exometabolite abundance at each time point.

BtCv+BtPs represents the "expected" additive sum of pairwise cocultures with *B. thailandensis* and BtCvPs represents the experimental 3-member community.

Time	Group 1	Group 2	N1	N2	P.adj
Thailandamide					
12.5	BtCv+BtPs	BtCvPs	3	3	0.025
25	"	"	"	"	0.365
30	"	"	"	"	0.115
35	"	"	"	"	0.0944
40	"	"	"	"	0.0715
45	"	"	"	"	0.0723
Pyochelin					
12.5	BtCv+BtPs	BtCvPs	3	3	0.248
25	"	"	"	"	0.108
30	"	"	"	"	0.0897
35	"	"	"	"	0.0943
40	"	"	"	"	0.146
45	"	"	"	"	0.124
Capistruin					
12.5	BtCv+BtPs	BtCvPs	4	4	0.0673
25	"	"	"	"	0.0721
30	"	"	"	"	0.914
35	"	"	"	"	0.628
40	"	"	"	"	0.779
45	"	"	"	"	0.739

Appendix A Table 23. Primers used in this study

Primer	Sequence (5’ > 3’)	Description
1001	TTGCTTATTTGGGAGGAACAACA	Used to amplify tolC for nested PCR round 1
1002	CATCTGCTTTTGCAGCGATGA	Used to amplify tolC for nested PCR round 1
1003	GCTAGTCTAGAGCATCAGTTGAGTTTTCACTGGA	Used for nested PCR round 2 to construct pJC101 and pJC102; XbaI site underlined
1004	GCTAGGGATCCAAGCTTGCAACCTGGCTTTC	Used for nested PCR round 2 to construct pJC101 and pJC102; BamHI site underlined
1005	AAATGACGGTCCCATCTCAAA	Used to amplify tolC to confirm successful mutant construction
1006	CCCATGTAAAACTTCAATGCGT	Used to amplify tolC to confirm successful mutant construction
1010	TGAGAACCAAAGGCTGGGAA	Used to amplify ragB/susD for nested PCR round 1
1011	GGTACATTGTTTTCGGCGCA	Used to amplify ragB/susD for nested PCR round 1
1012	GCTAGTCTAGATGGGGATTAACCAGCGACAG	Used for nested PCR round 2 to construct pJC103; XbaI site underlined
1013	GCTAGGGATCCTTCACCTGCATCGGCAGTTC	Used for nested PCR round 2 to construct pJC103; BamHI site underlined
1014	ATGCTCCCGCAAAACCAAGA	Used to amplify ragB/susD to confirm successful mutant construction
1015	ATCAGGACCAGTTGTTGCCG	Used to amplify ragB/susD to confirm successful mutant construction

Appendix A Table 24. PCR conditions for nested PCR round 1

Reagent	Volume (µL)
Template (6.25 ng/µL)	10
Forward/Reverse primers (10 µM)	2.5
10 mM dNTPs (Sigma-Aldrich, St. Louis, MO)	1
Phusion DNA polymerase (New England BioLabs, Ipswich, MA)	0.5
Phusion 5X buffer (HF buffer for *tolC* and GC buffer for *ragB/susD*)	9.5
Nuclease-free water	24

Appendix A Table 25. PCR conditions for nested PCR round 2

Reagent	Volume (µL)
Template (1 ng/µL; PCR product from R1)	0.5
Forward/Reverse primers (10 µM)	2.5
10 mM dNTPs	1
Phusion DNA polymerase	0.5
Phusion 5X buffer (HF buffer for *tolC* and GC buffer for *ragB/susD*)	9.5
Nuclease-free water	33.5

Appendix A Table 26. Reagents and reaction volumes for restriction enzyme digestion

Reagent	Volume (µL)
Nested PCR R2 products or pYT354 (1 µg/µL)	1
10X cutsmart buffer (New England BioLabs, Ipswich, MA)	5
BamHI-HF (New England BioLabs, Ipswich, MA)	1 (20 units)
XbaI (New England BioLabs, Ipswich, MA)	1 (20 units)
Nuclease-free water	42

Appendix A Table 27. Reagents and reaction volumes/mass for ligation reactions

Reagent	Volume/Mass
Insert (~3.2 for *tolC*, ~3.1 kbp for *ragB/susD*)	Varied[a]
Vector (~7.7 kbp)	50 ng
T4 DNA ligase (New England BioLabs, Ipswich, MA)	1 µL
10 X T4 DNA ligase buffer (New England BioLabs, Ipswich, MA)	2 µL
Nuclease-free water	Up to 20 µL

[a]To achieve a 1:3 vector:insert molar ratio, 61.49 ng was used from *tolC*-containing PCR products and 59.37 ng used from *ragB/susD*-containing PCR products.

Appendix A Table 28. Summary of *tolC* loci in *F. johnsoniae*

Locus	Protein ID	Top blastp hit	AA length
FJOH_RS06580	WP_012023347.1	TolC family protein	444
FJOH_RS07030	WP_012023433.1	"	451
FJOH_RS08665	WP_012023747.1	"	461
FJOH_RS14165	WP_012024794.1	"	415
FJOH_RS15250	WP_012025000.1	"	436
FJOH_RS15955	WP_008463753.1	"	415
FJOH_RS16725	WP_012025212.1	"	469
FJOH_RS16800	WP_012025225.1	"	484
FJOH_RS17335	WP_044047818.1	"	426
FJOH_RS20485	WP_012025935.1	"	472
FJOH_RS22150	WP_044048008.1	"	461
FJOH_RS22200	WP_012026267.1	"	412
FJOH_RS22240	WP_012026275.1	"	472
FJOH_RS23175	WP_012026451.1	"	417
FJOH_RS25120	WP_012026826.1	"	479
FJOH_RS25325	WP_012026867.1	"	439

APPENDIX B

Supplementary Figures

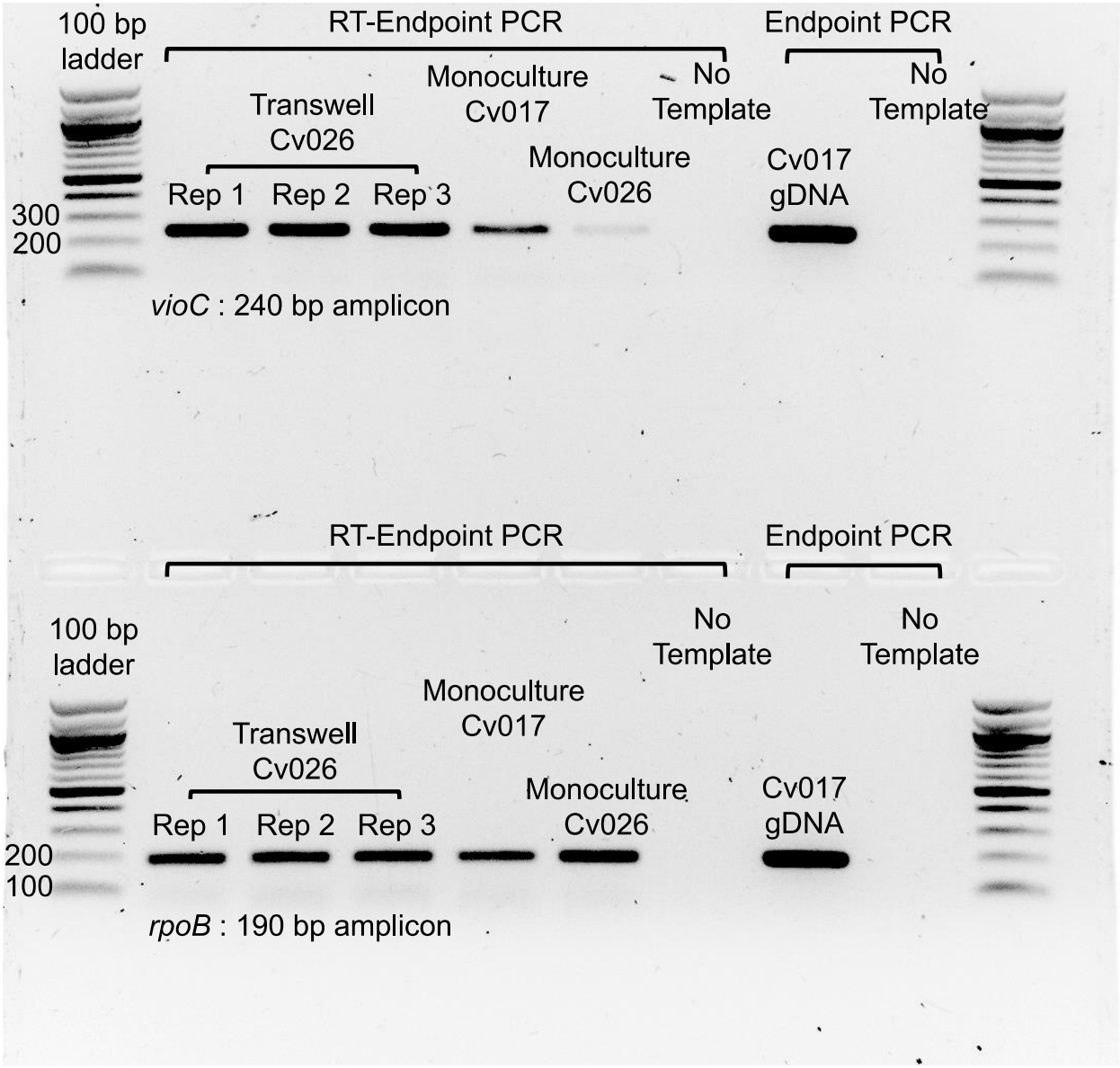

Appendix B Figure 1. Endpoint RT-PCR on *vioC* and *rpoB* genes.

A) When arrayed with Cv017 in the filter plate system, Cv026 had relatively higher yield of *vioC* transcripts (replicates [Reps] 1 to 3), providing evidence that AHLs produced by Cv017 accumulated in the medium reservoir at concentrations required for Cv026 to upregulate its violacein gene cluster. B) As a control, the constitutively expressed housekeeping gene *rpoB* had comparable transcript levels across all conditions.

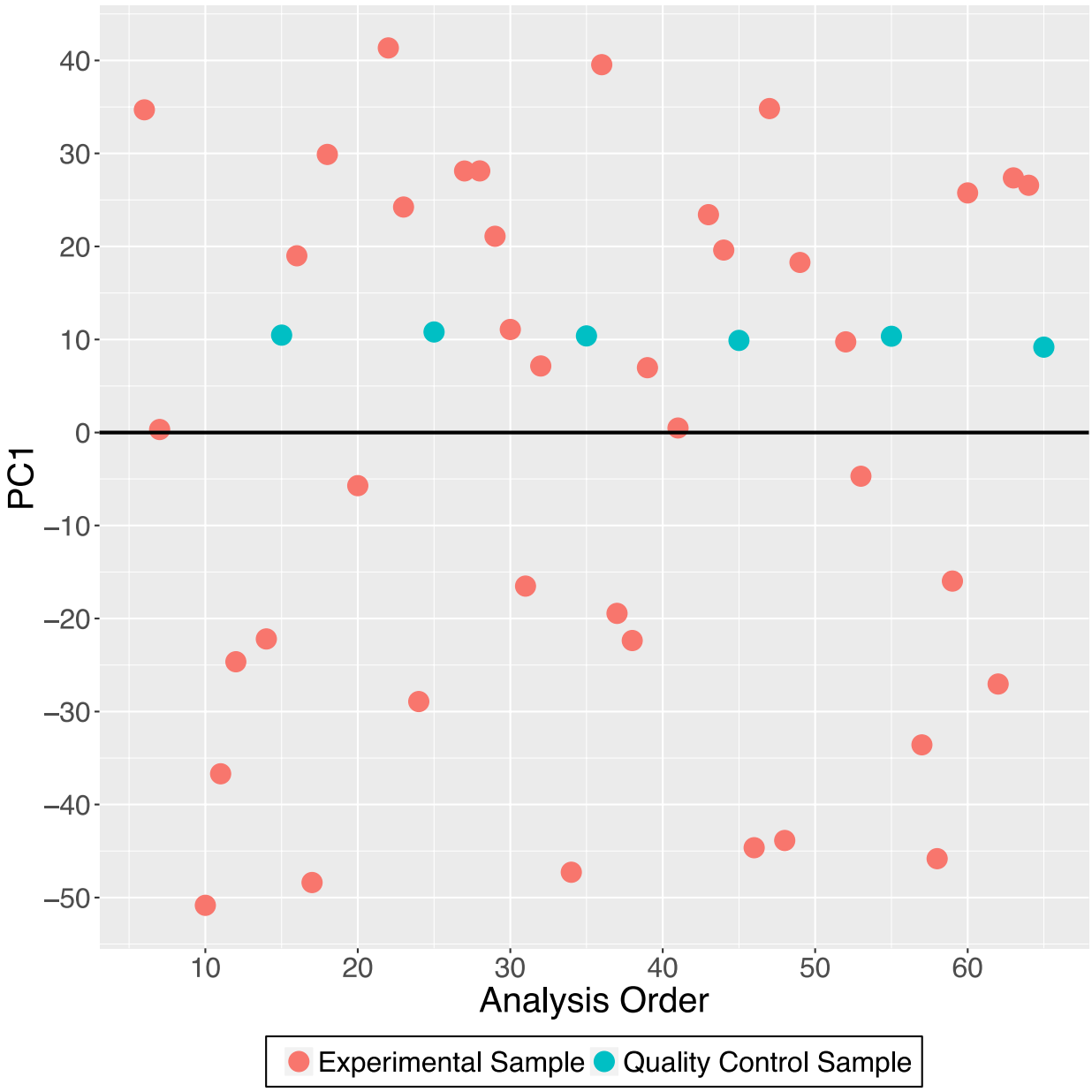

Appendix B Figure 2. Assessment of mass spectrometer stability using the quality control (QC) series.

Principal-component analysis axis 1 scores (from **Figure 2.2**) are plotted against analysis order and colored by sample type (experimental or QC). QC samples were an even composite of all

Appendix B Figure 2 (cont'd)

experimental samples, run at regular intervals on the mass spectrometer to assess instrument stability and feature consistency. QC samples do not vary along axis 1, despite the fact that they are not analyzed consecutively, demonstrating that the instrument was stable over the analyses that generated this data set (54).

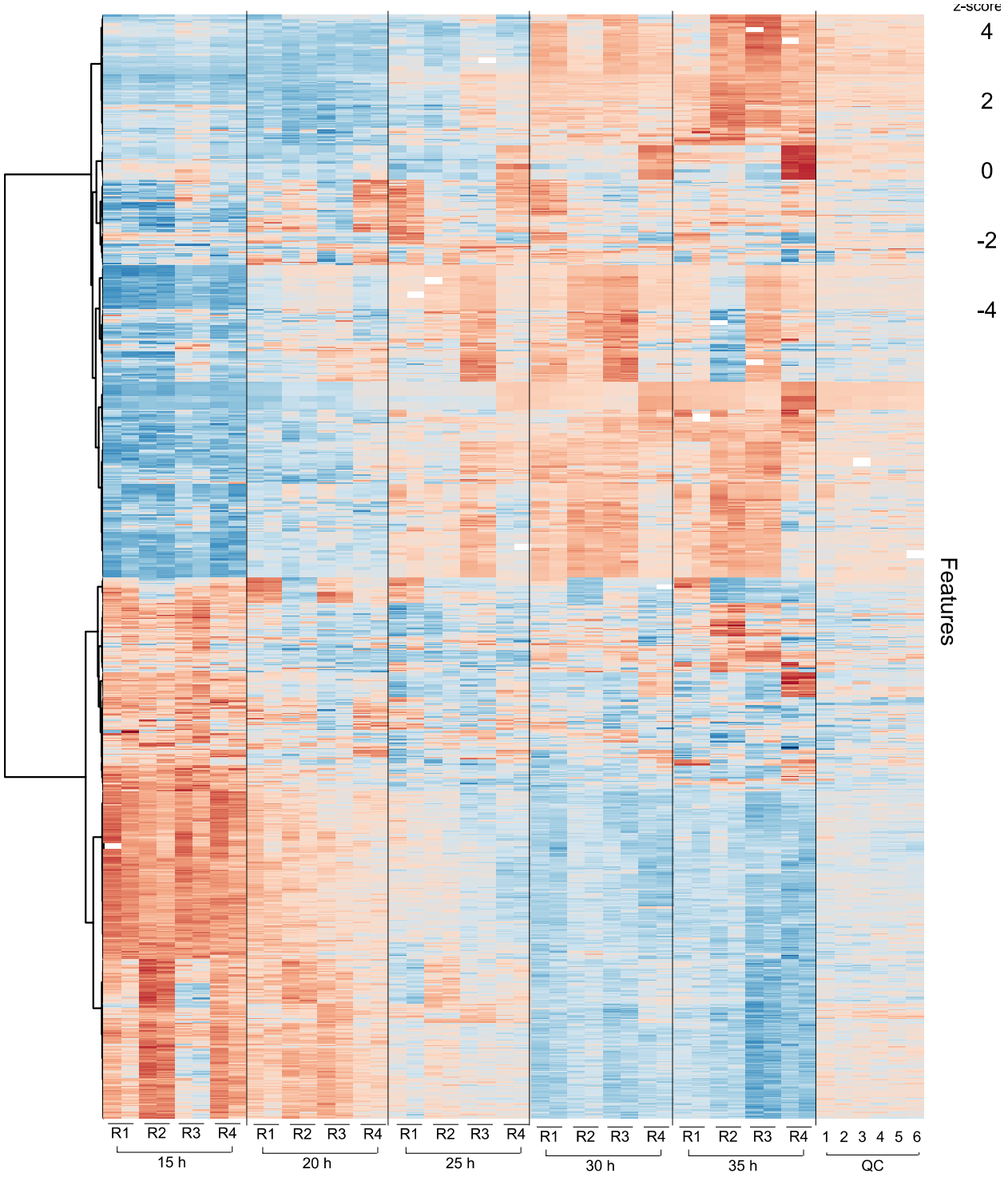

Appendix B Figure 3. Exometabolites exhibit directional changes over stationary phase in a three-member synthetic microbial community.

Appendix B Figure 3 (cont'd)

Shown is a heat map of 977 mass feature changes over time within a three-member community, where samples are columns and features are rows (Z score range, −4.37 to 3.94). All profiles are included as samples, including two mass spectral replicates from each of four time point replicates. Each time series also included a medium control (NC). A quality control sample (QC), an even composite of all experimental samples, was run at regular intervals on the mass spectrometer to assess instrument stability and feature consistency. Euclidean distance was calculated from Z-scored mass spectral profiles. Features with similar dynamics were clustered using Ward's method. Letter designations for clusters were added post hoc to aid in discussion.

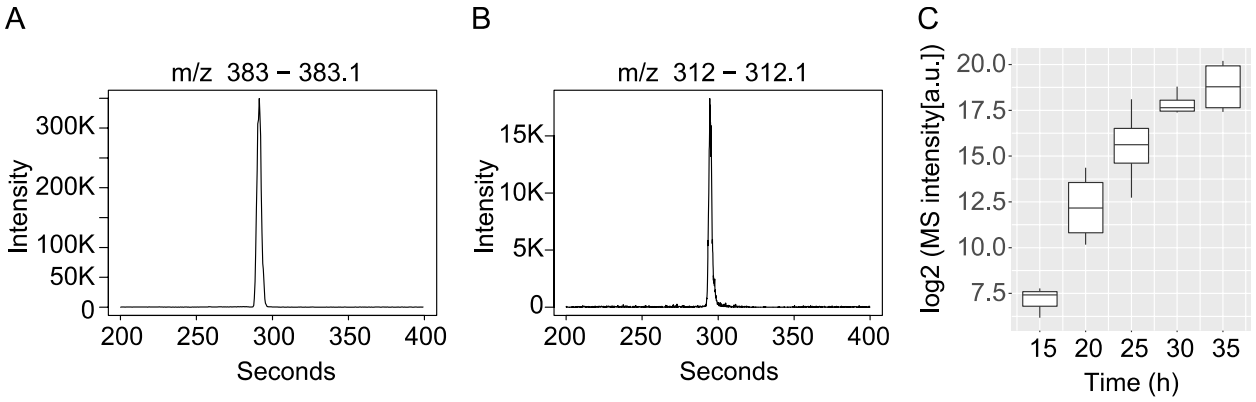

Appendix B Figure 4. Identification and accumulation of bactobolin.

Chromatographic traces of bactobolin from MS **(A)** and MS-MS **(B)** analyses. **C)** Bactobolin accumulation in the shared medium reservoir through time (n = 4 integrated peak areas per time point). The bottom and top of the box are the first and third quartiles, respectively, and the line inside the box is the median. The whiskers extend from their respective hinges to the largest value (top), and smallest value (bottom) was no further away than 1.5× the interquartile range.

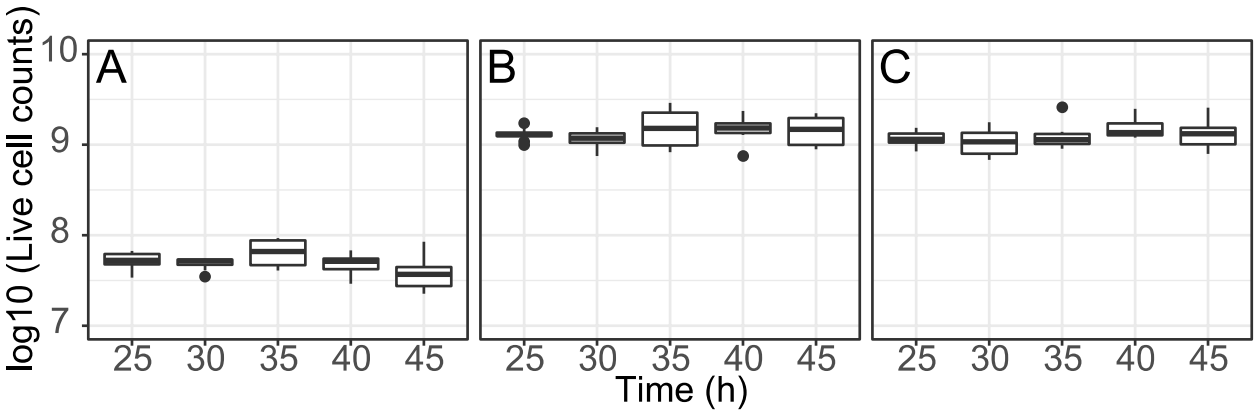

Appendix B Figure 5. Changes in live cell counts over stationary phase measured using flow cytometry of Syto9-stained cells that were recovered from the filter plates.

Five wells per plate and two replicate plates per time point were used to assess cell counts in the three-member community. **A)** *P. syringae*. **B)** *C. violaceum*. **C)** *B. thailandensis*.

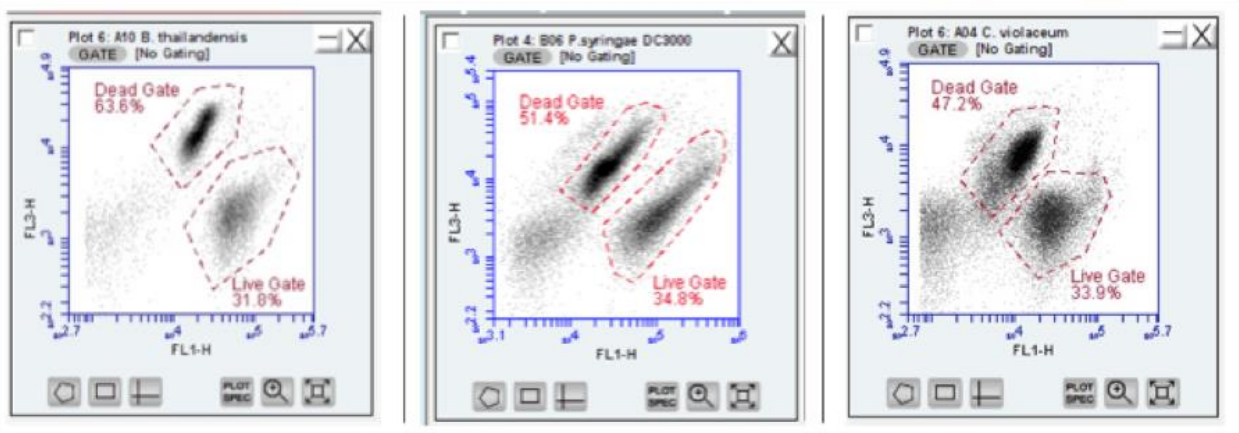

Appendix B Figure 6. Fluorescence scatter plot of live/dead cells.

Flow cytometry gates for community members show how live and dead cell events are captured predominantly on the FL1 channel and FL3 channel, respectively.

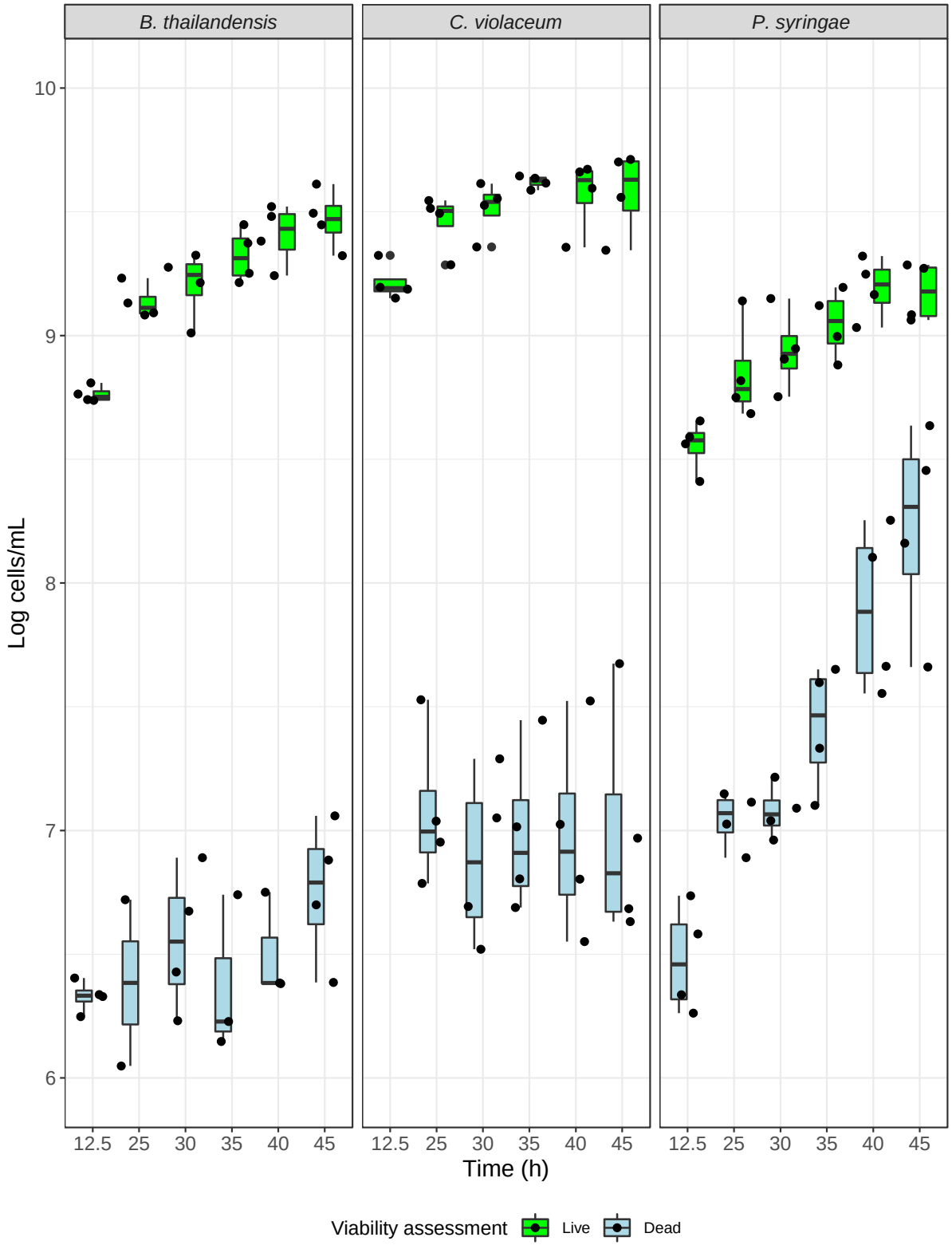

Appendix B Figure 7. Counts of live (green) and dead (blue) cells throughout the time course.

Appendix B Figure 7 (cont'd)

Cells were obtained from 5 wells in the transwell plate for 5 technical replicates/independent replicate at each time point. Syto9 and propidium iodide-stained cells were counted using flow cytometry.

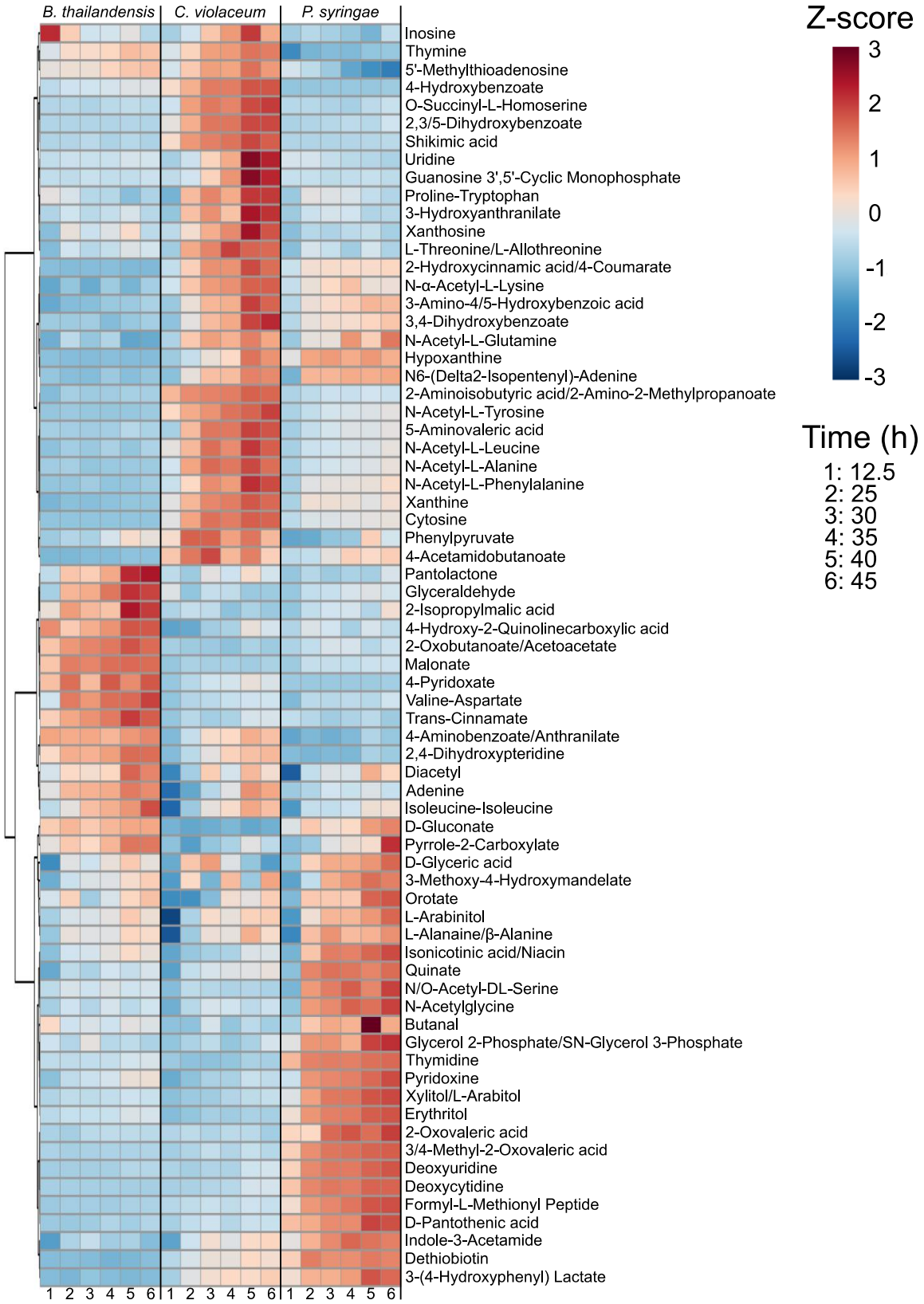

Appendix B Figure 8. Released and identified exometabolites and their temporal dynamics.

Appendix B Figure 8 (cont'd)

A heat map of identified exometabolites in polar negative mode is shown, where samples are columns and exometabolites are in rows. Each sample is the average of independent time point replicates (n = 3 or 4). Euclidean distance was calculated from Z-scored mass spectral profiles (containing peak areas). Prior to Z-scoring, features were normalized by an internal standard (ITSD) reference feature and cube root transformed. Features were clustered by Ward's method.

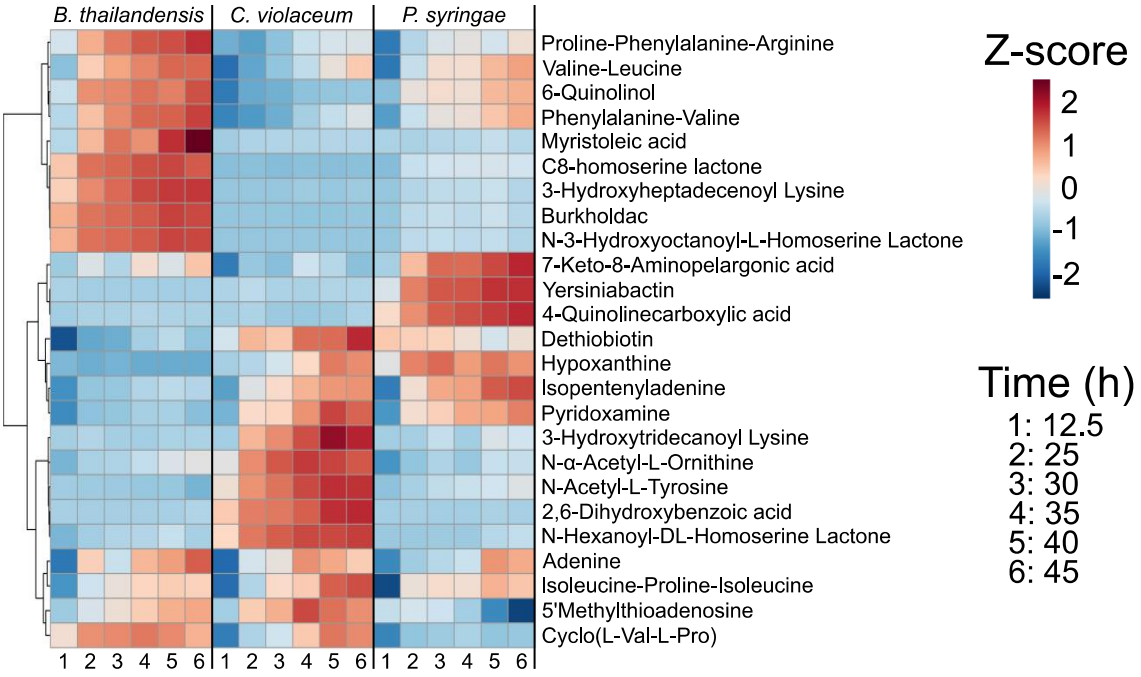

Appendix B Figure 9. Released and identified exometabolites and their temporal dynamics.

A heat map of identified exometabolites in nonpolar positive mode is shown, where samples are columns and exometabolites are in rows. Each sample is the average of independent time point replicates (n = 2 to 4). Euclidean distance was calculated from Z-scored mass spectral profiles (containing peak areas). Prior to Z-scoring, features were normalized by an internal standard (ITSD) reference feature and cube root transformed. Features were clustered by Ward's method.

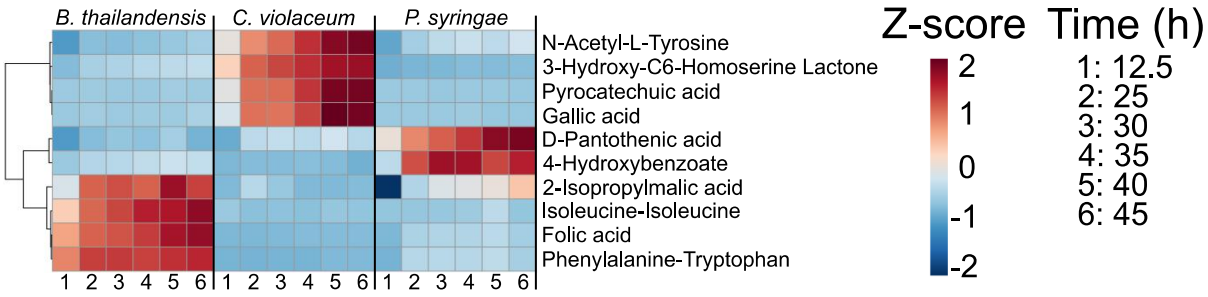

Appendix B Figure 10. Released and identified exometabolites and their temporal dynamics.

A heat map of identified exometabolites in nonpolar negative mode is shown, where samples are columns and exometabolites are in rows. Each sample is the average of independent time point replicates (n = 2 to 4). Euclidean distance was calculated from Z-scored mass spectral profiles (containing peak areas). Prior to Z-scoring, features were normalized by an internal standard (ITSD) reference feature and cube root transformed. Features were clustered by Ward's method.

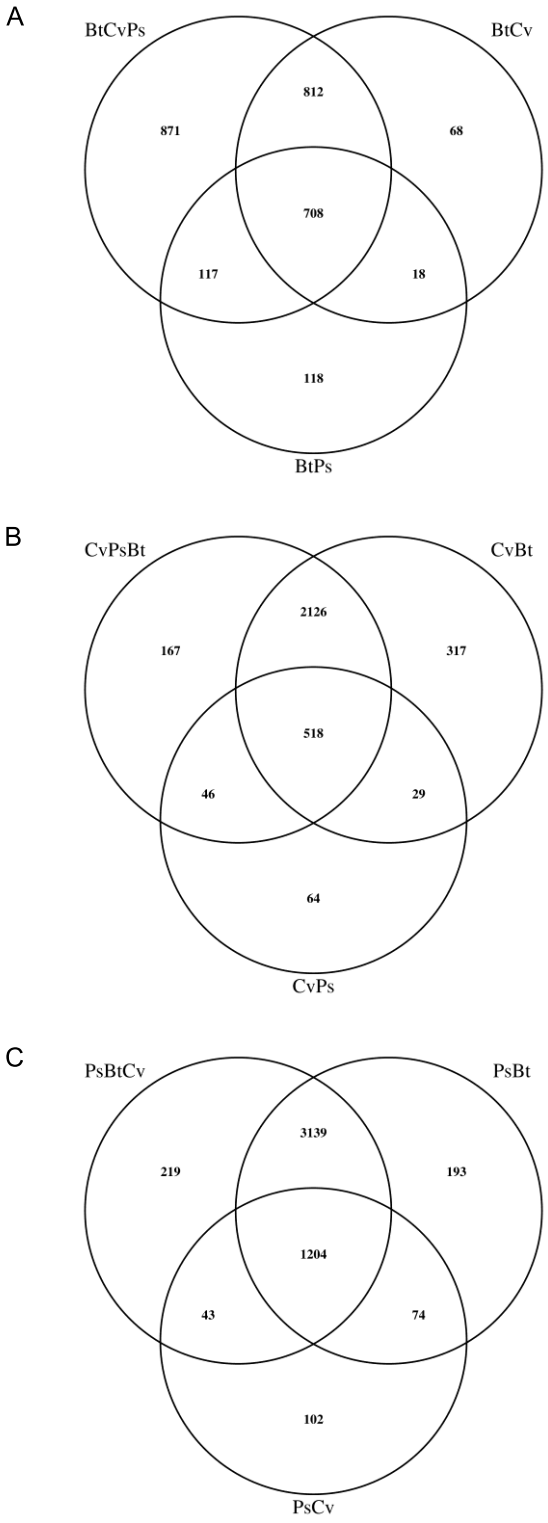

Appendix B Figure 11. Differential gene expression patterns across community memberships.

Appendix B Figure 11 (cont'd)

Venn diagram plots of differentially expressed genes in A) *B. thailandensis* B) *C. violaceum* and C) *P. syringae*. Differential gene expression was determined using ImpulseDE2 comparing longitudinal gene expression to a monoculture control (FDR-corrected cutoff of 0.01). Bt- *B. thailandensis*, Cv- *C.violaceum*, and Ps – *P. syringae*.

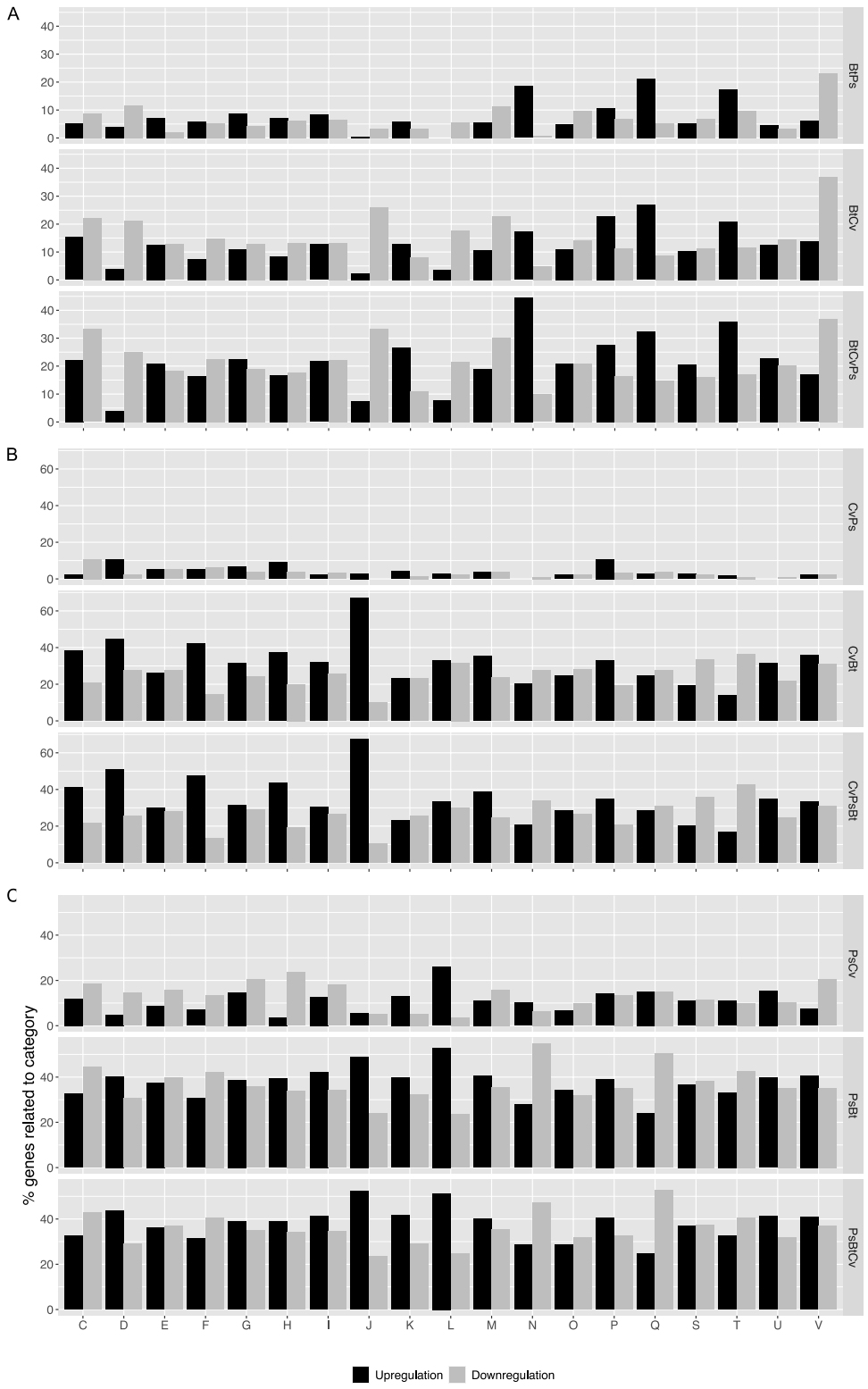

Appendix B Figure 12. Patterns of transcriptional regulation reveal biological responses to coculture.

Appendix B Figure 12 (cont'd)

Differentially expressed genes categorized by COG categories in A) *B. thailandensis* B) *C. violaceum* and C) *P. syringae*. COG categories include: **[C]** Energy production and conversion, **[D]** Cell cycle control, cell division, chromosome partitioning, **[E]** Amino acid transport and metabolism, **[F]** Nucleotide transport and metabolism, **[G]** Carbohydrate transport and metabolism, **[H]** Coenzyme transport and metabolism, **[I]** Lipid transport and metabolism, **[J]** Translation, ribosomal structure and biogenesis, **[K]** Transcription, **[L]** Replication, recombination and repair, **[M]** Cell wall/membrane/envelope biogenesis, **[N]** Cell motility, **[O]** Post-translational modification, protein turnover, and chaperones, **[P]** Inorganic ion transport and metabolism, **[Q]** Secondary metabolites biosynthesis, transport, and catabolism, **[S]** Function unknown, [**T]** Signal transduction mechanisms, **[U]** Intracellular trafficking, secretion, and vesicular transport, and **[V]** Defense mechanisms. Community arrangements are as follows: *B. thailandensis-P. syringae* coculture (BtPs/PsBt), *B. thailandensis-C. violcaeum* coculture (BtCv/CvBt), *C. violcaeum-P. syringae* coculture (CvPs/PsCv), and the 3-member community (BtCvPs/CvPsBt/PsBtCv).

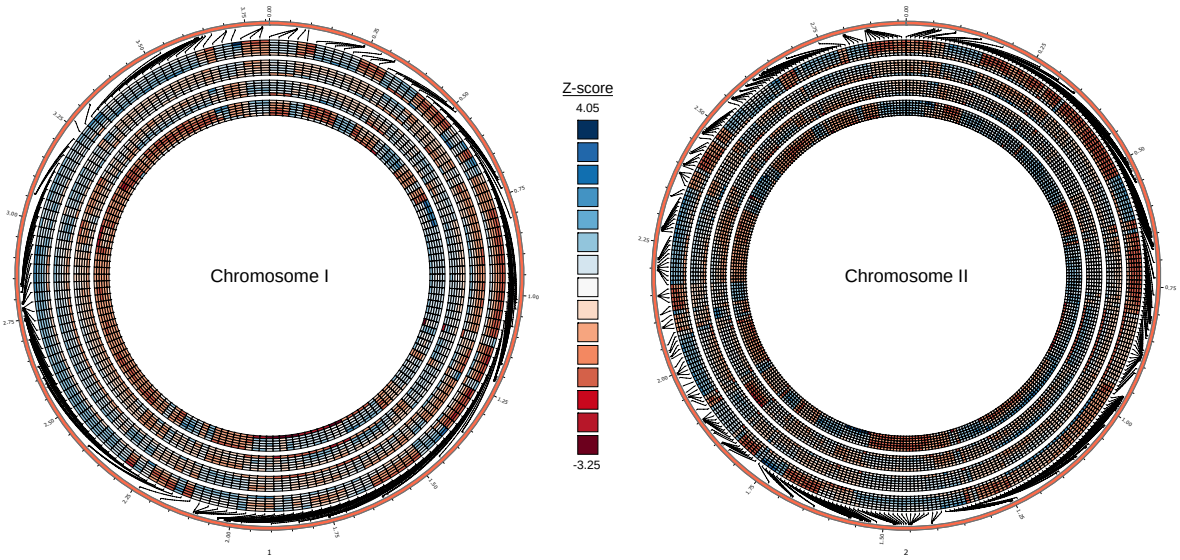

Appendix B Figure 13. Changes in gene expression as determined by time, community membership, and chromosome location for *B. thailandensis*.

Circos plot depicting gene expression pattern in *B. thailandensis* plotting the top differentially expressed genes (see methods: *Circos plots*). Normalzied gene counts of filtered genes were averaged across biological replicates, rlog-transformed and then Z-scored. Starting from the innermost track: *B. thailandensis* gene expression in monoculture, *B. thailandensis* gene expression in coculture with *P. syringae*, *B. thailandensis* gene expression in coculture with *C. violcaeum*, *B. thailandensis* gene expression in the 3-member community, gene location, and chromosome coordinates.

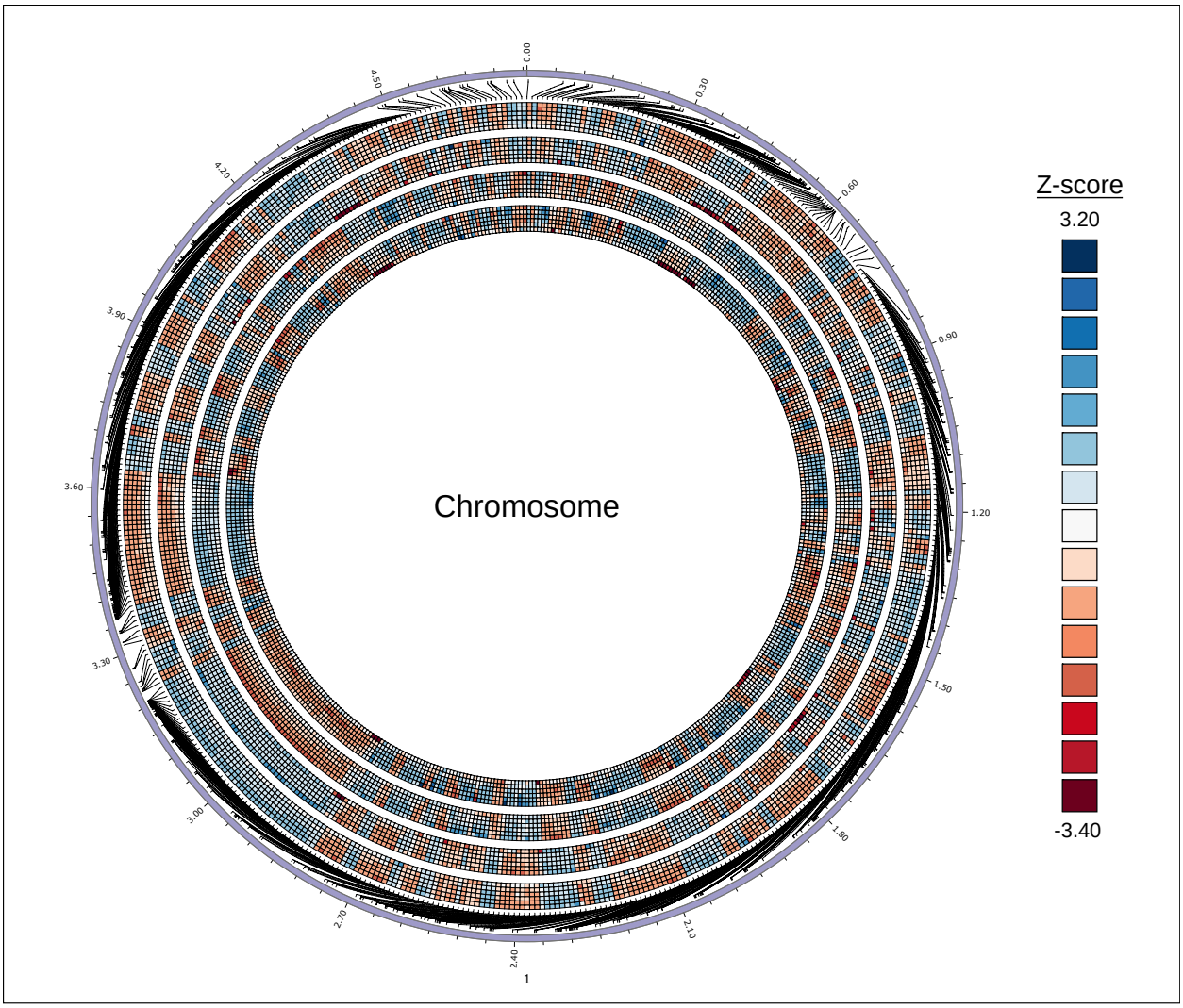

Appendix B Figure 14. Changes in gene expression as determined by time, community membership, and chromosome location for *C. violaceum*.

Circos plot depicting gene expression pattern in *C. violaceum* plotting the top differentially expressed genes (see methods: *Circos plots*). Normalzied gene counts of filtered genes were averaged across biological replicates, rlog-transformed and then Z-scored. Starting from the innermost track: *C. violaceum* gene expression in monoculture, *C. violaceum* gene expression in coculture with *P. syringae*, *C. violaceum* gene expression in coculture with *B. thailandensis*, *C.*

Appendix B Figure 14 (cont'd)

violaceum gene expression in the 3-member community, gene location, and chromosome coordinates.

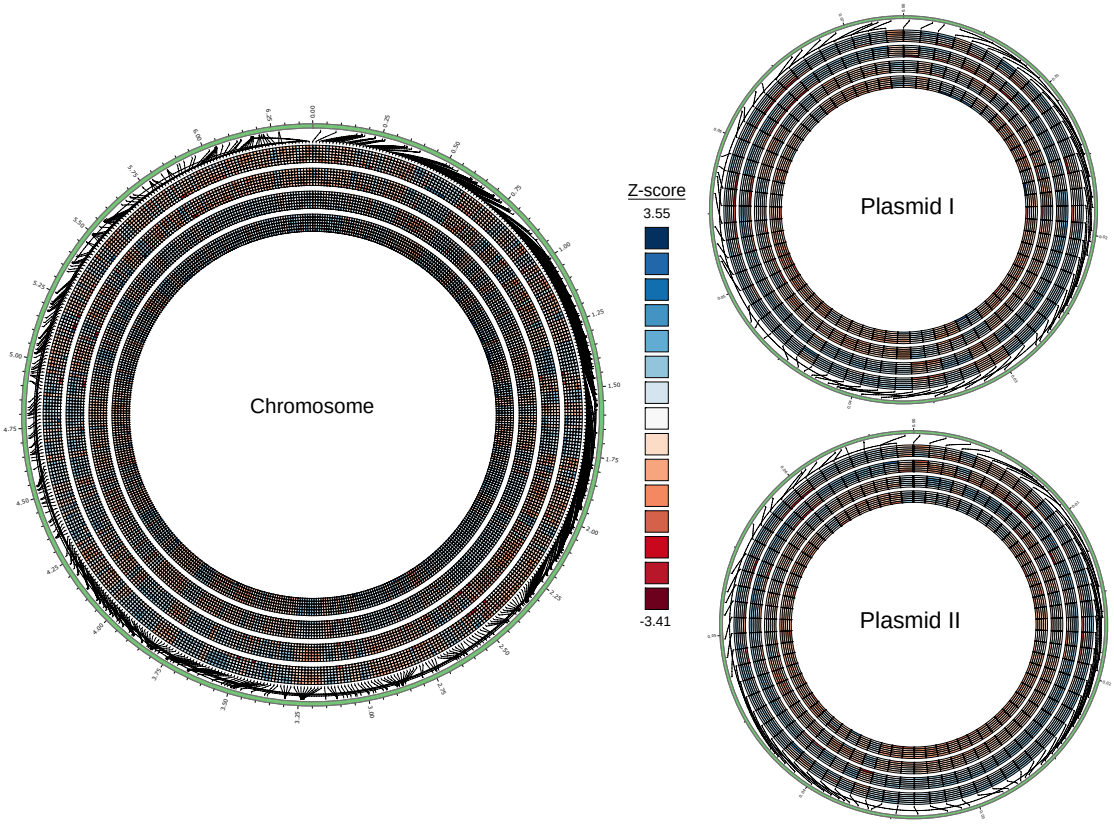

Appendix B Figure 15. Changes in gene expression as determined by time, community membership, and chromosome location for *P. syringae*.

Circos plot depicting gene expression pattern in *P. syringae* plotting the top differentially expressed genes (see methods: *Circos plots*). Normalzied gene counts of filtered genes were averaged across biological replicates, rlog-transformed and then Z-scored. Starting from the innermost track: *P. syringae* gene expression in monoculture, *P. syringae* gene expression in coculture with *C. violaceum*, *P. syringae* gene expression in coculture with *B. thailandensis*, *P.*

Appendix B Figure 15 (cont'd)

syringae gene expression in the 3-member community, gene location, and chromosome/plasmid coordinates.

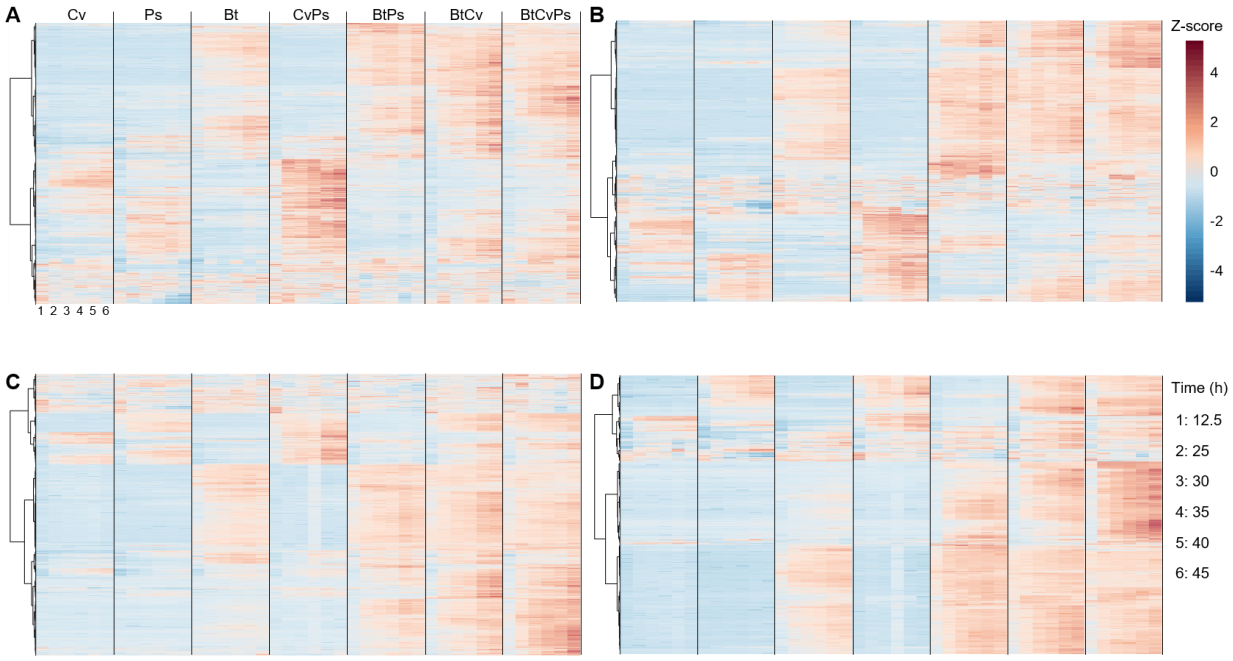

Appendix B Figure 16. Exometabolites have membership-specific production and temporal accumulation.

A heat map of coculture accumlated exometabolites is shown for polar positive (A), polar negative (B), nonpolar positive (C), and nonpolar negative (D) modes, for *C. violaceum* monoculture (Cv), *P. syringae* monoculture (Ps), *B. thailandensis* monoculture (Bt), *C. violaceum-P. syringae* coculture (CvPs), *B. thailandensis-P. syringae* coculture (BtPs), *B. thailandensis-C. violaceum* coculture (BtCv), and the 3-member community (BtCvPs), where samples are in columns and exometabolites are in rows. Data for each sample are the averages from independent time point replicates (n = 2 to 4).

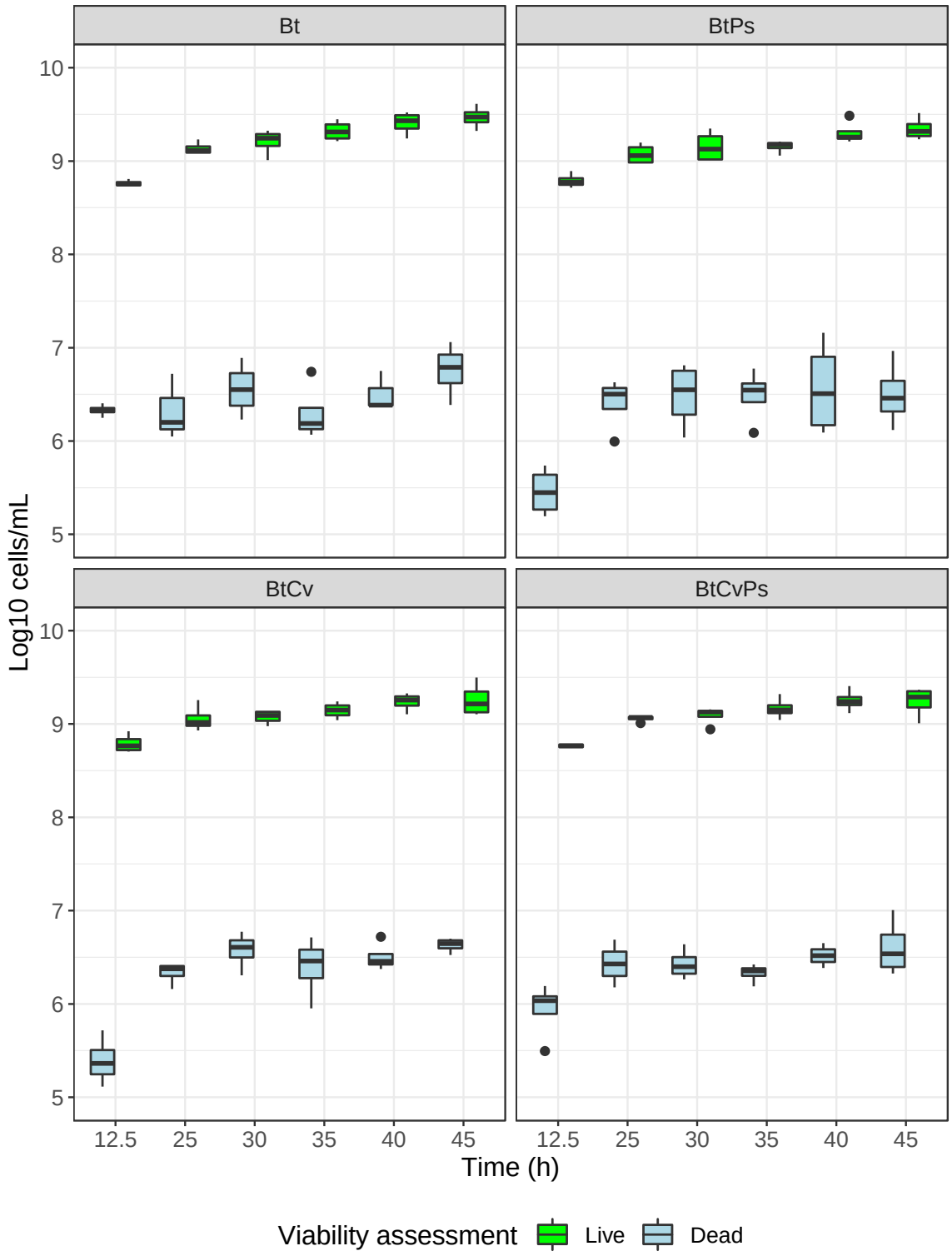

Appendix B Figure 17. *B. thailandensis* cell viability.

Appendix B Figure 17 (cont'd)

Counts of live (green) and dead (blue) cells throughout the time course. Cells were obtained from 5 wells in the transwell plate for 5 technical replicates/independent replicate at each time point. *B. thailandensis* monoculture (Bt), *B. thailandensis-P. syringae* coculture (BtPs), *B. thailandensis-C. violaceum* coculture (BtCv), and the 3-member community (BtCvPs).

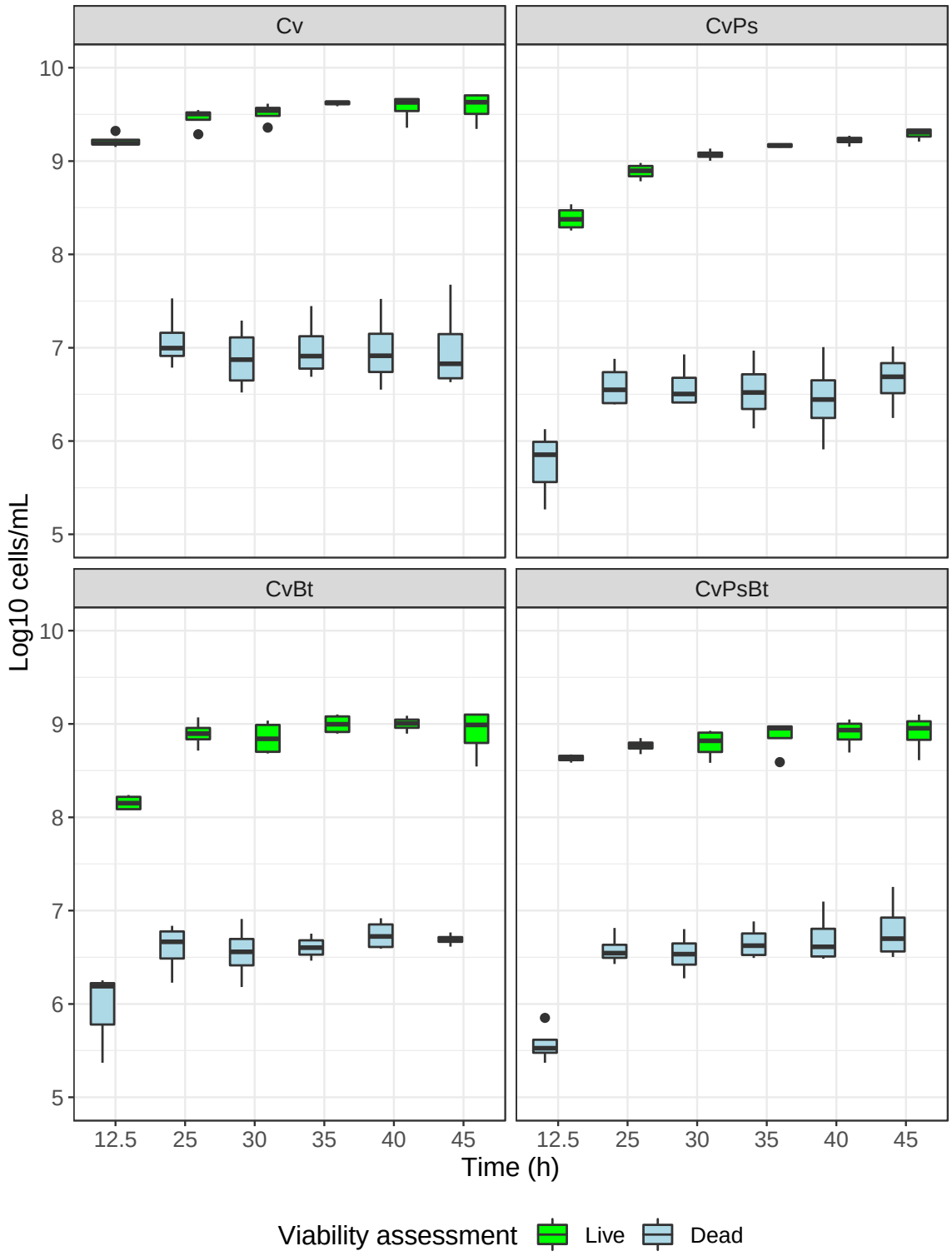

Appendix B Figure 18. *C. violaceum* cell viability.

Appendix B Figure 18 (cont'd)

Counts of live (green) and dead (blue) cells throughout the time course. Cells were obtained from 5 wells in the transwell plate for 5 technical replicates/independent replicate at each time point. *C. violaceum* monoculture (Cv), *C. violaceum*-*P. syringae* coculture (CvPs)*, C. violaceum*-*B. thailandensis* coculture (CvBt), and the 3-member community (CvPsBt).

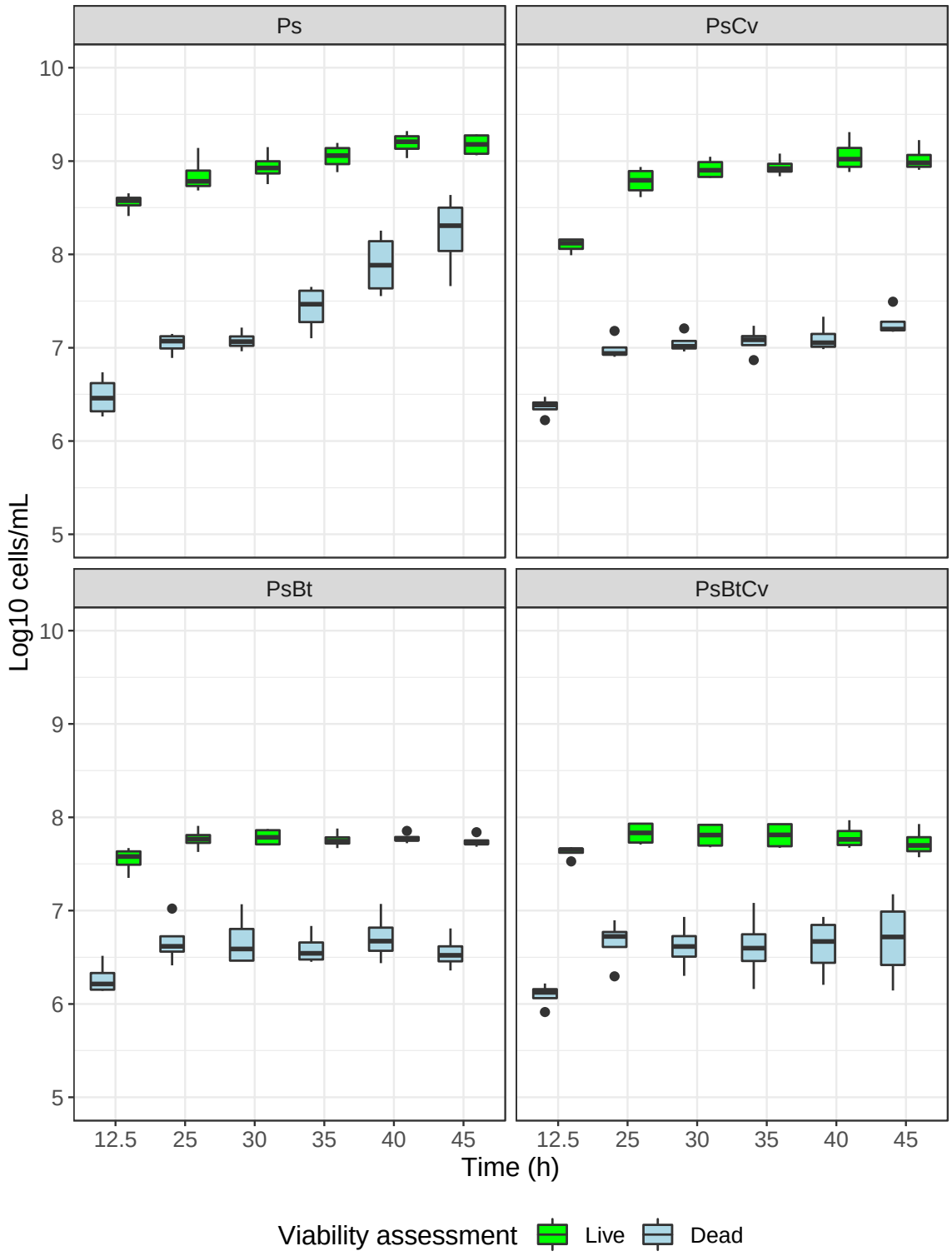

Appendix B Figure 19. *P. syringae* cell viability.

Appendix B Figure 19 (cont'd)

Counts of live (green) and dead (blue) cells throughout the time course. Cells were obtained from 5 wells in the transwell plate for 5 technical replicates/independent replicate at each time point. *P. syringae* monoculture (Ps), *P. syringae-C. violaceum* coculture (PsCv)*, P. syringae-B. thailandensis* coculture (PsBt), and the 3-member community (PsBtCv).

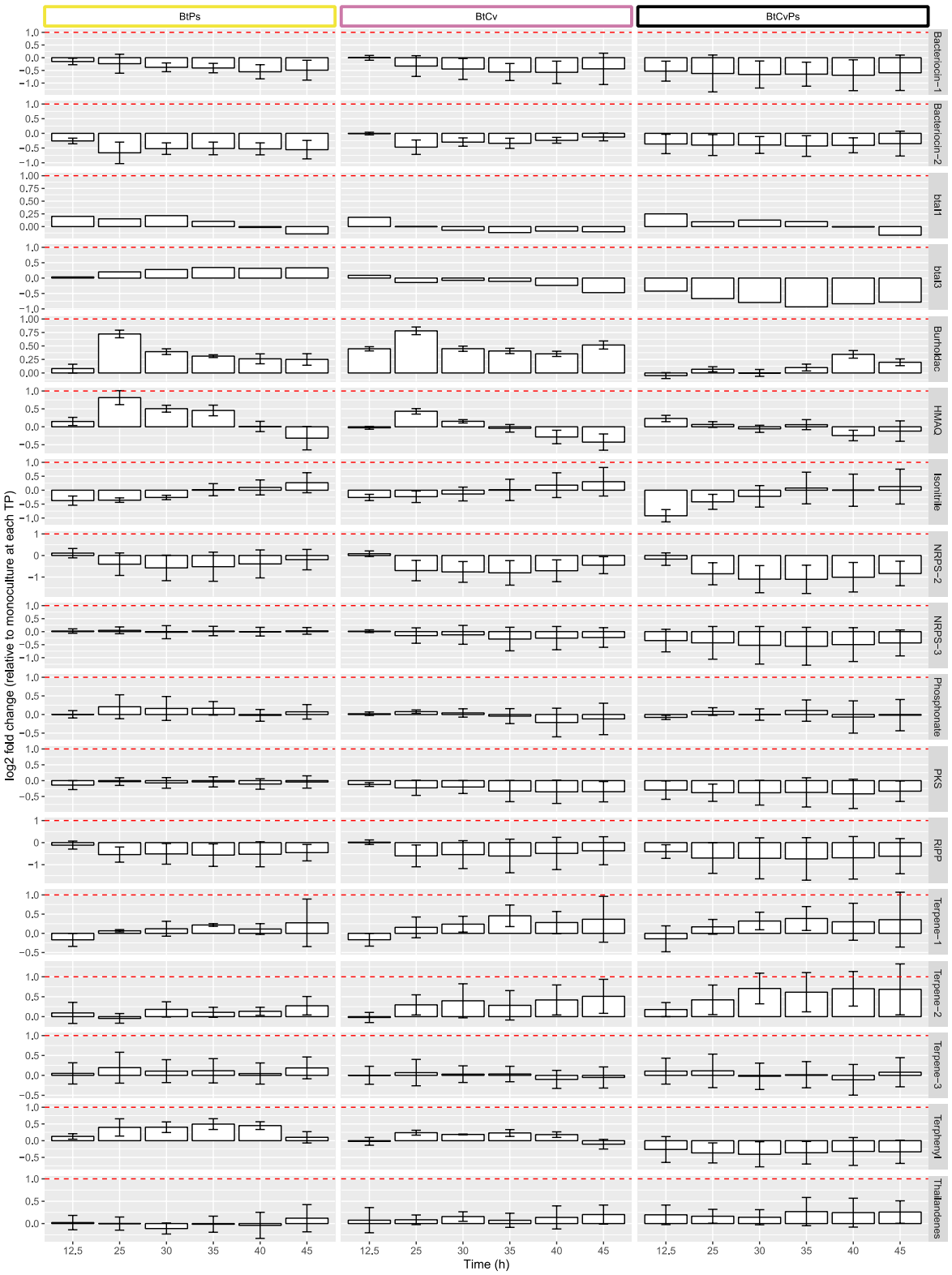

Appendix B Figure 20. BSGC downregulated or unaltered in *B. thailandensis*.

Appendix B Figure 20 (cont'd)

Biosynthetic genes involved in each BSGC were determined with antiSMASH and evidence from literature. At each timepoint, the average log2 fold-change (LFC) was determined across all biosynthetic genes for each BSGC. The horizontal line represents a LFC threshold of 1. Note that plots for each BSGC have separate scales for the Y-axis.

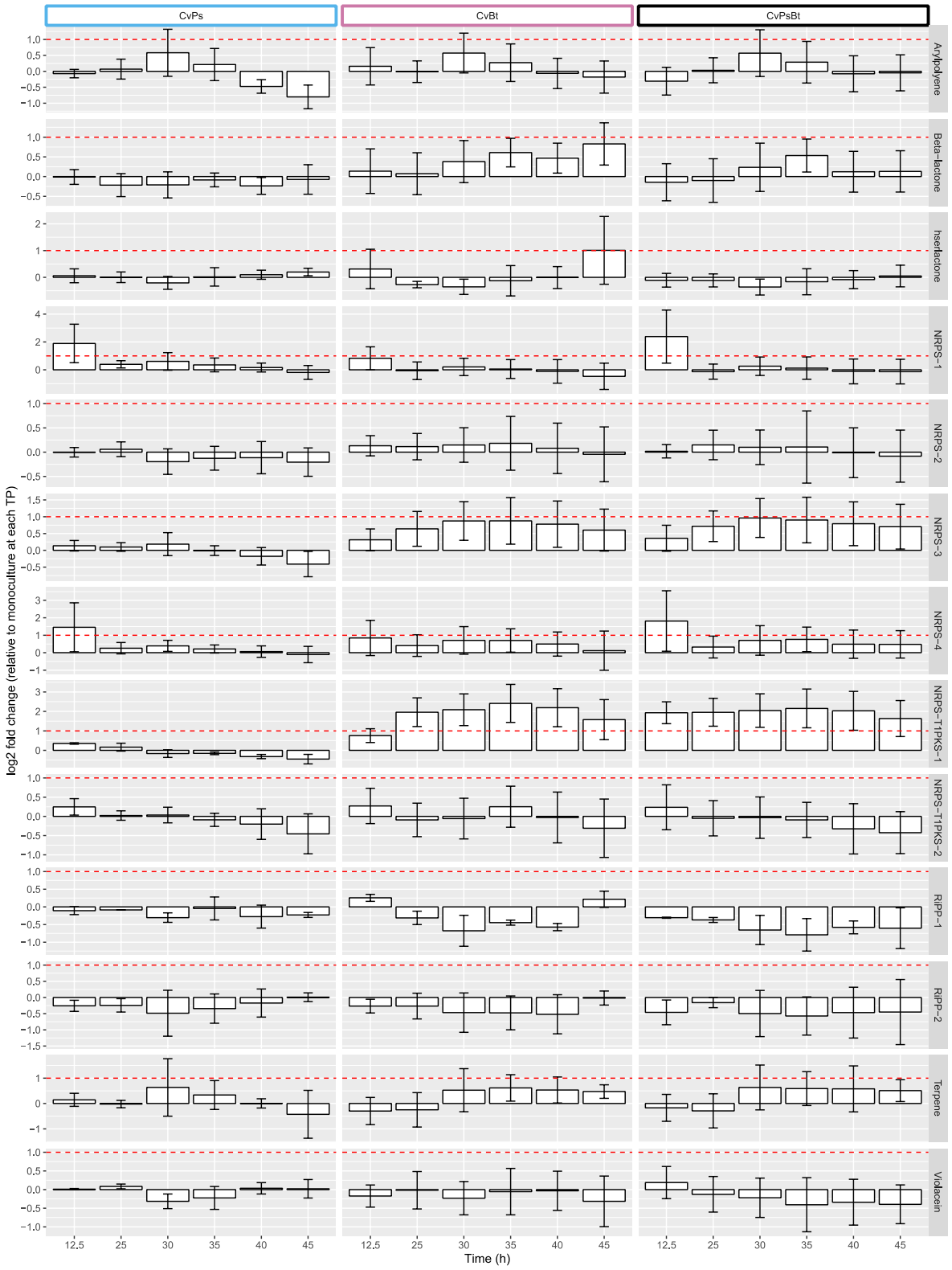

Appendix B Figure 21. Patterns of transcriptional regulation for BSGC in *C. violaceum*.

Appendix B Figure 21 (cont'd)

Biosynthetic genes involved in each BSGC were determined with antiSMASH and evidence from literature. At each timepoint, the average log2 fold-change (LFC) was determined across all biosynthetic genes for each BSGC. The horizontal line represents a LFC threshold of 1. Note that plots for each BSGC have separate scales for the Y-axis.

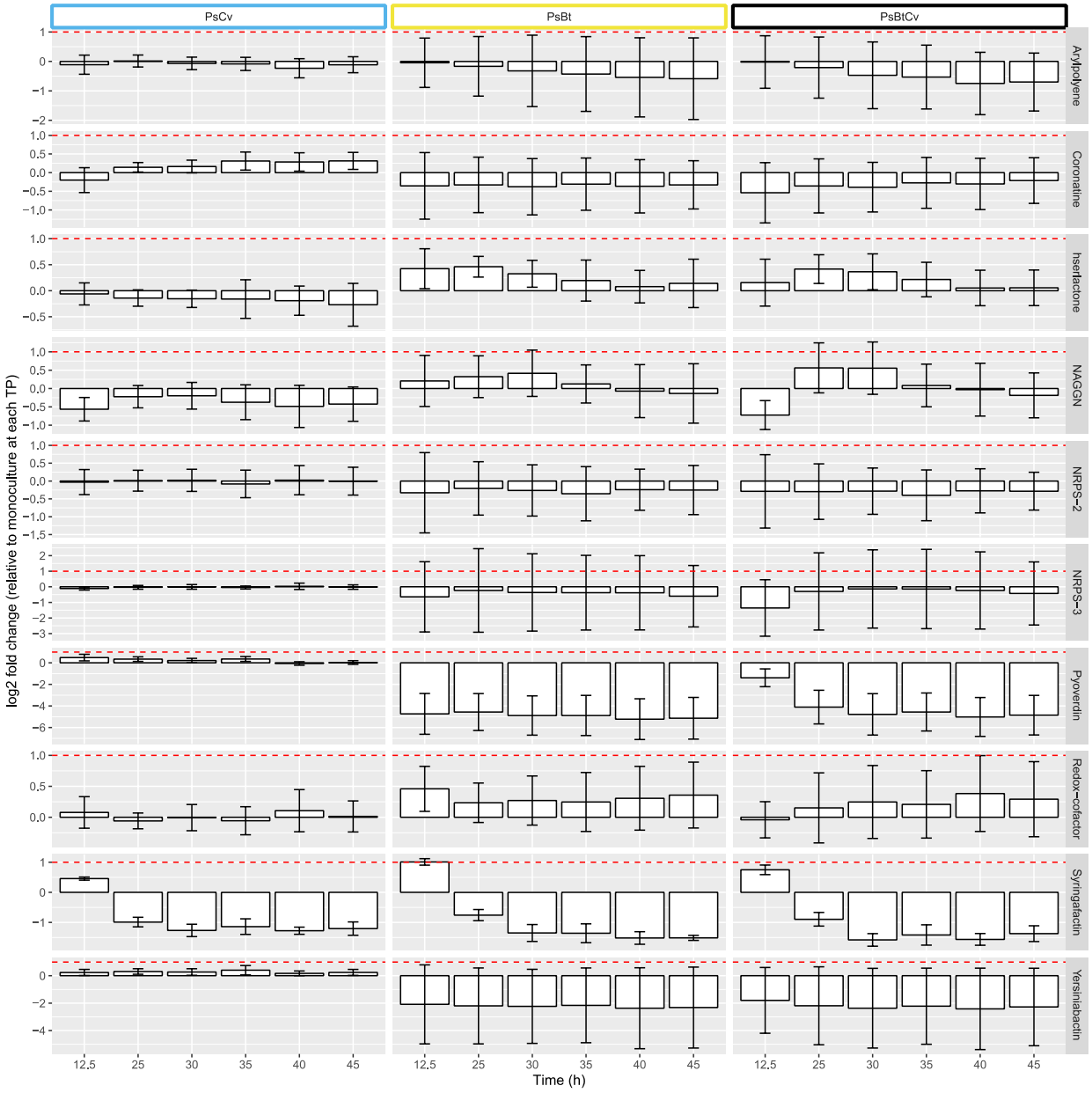

Appendix B Figure 22. Patterns of transcriptional regulation for BSGC in *P. syringae*.

Biosynthetic genes involved in each BSGC were determined with antiSMASH and evidence from literature. At each timepoint, the average log2 fold-change (LFC) was determined across all biosynthetic genes for each BSGC. The horizontal line represents a LFC threshold of 1. Note that plots for each BSGC have separate scales for the Y-axis.

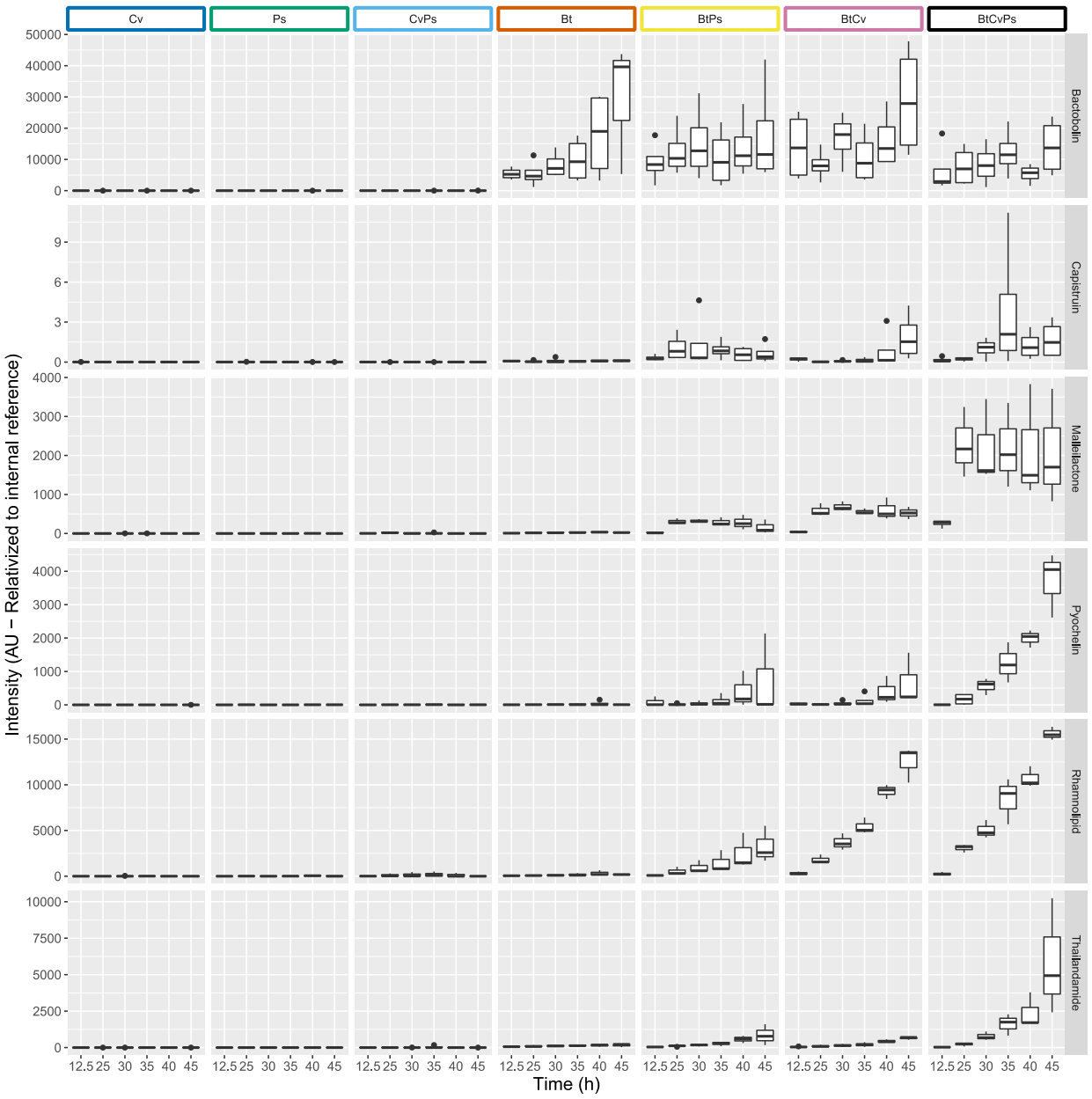

Appendix B Figure 23. Identified exometabolites from *B. thailandensis* BSGC temporally accumulate in cocultures.

Known bioactive secondary metabolites produced by *B. thailandensis* were identified in mzMine2 through the observation of MS and MS/MS data. The accumulation of each exometabolite was quantified through time (n = 2-4 integrated peak areas per time point). The

Appendix B Figure 23 (cont'd)

bottom and top of the box are the first and third quartiles, respectively, and the line inside the box is the median. The whiskers extend from their respective hinges to the largest value (top), and smallest value (bottom) was no further away than 1.5× the interquartile range.

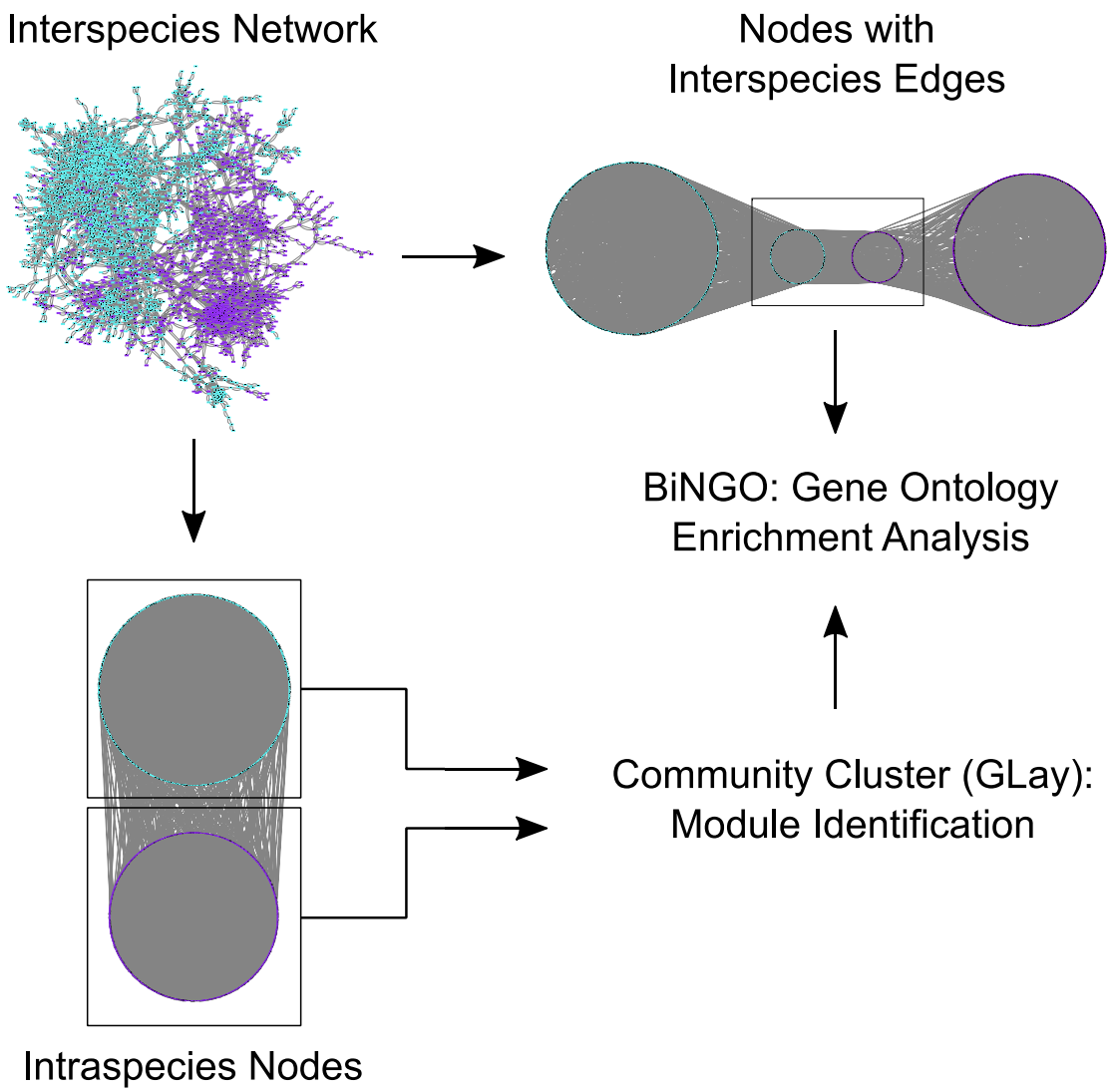

Appendix B Figure 24. Flow diagram for interspecies co-expression network analysis.

An interspecies coexpression network was created based on transcript counts from *B. thailandensis-C. violaceum* and *B. thailandensis-P. syringae* cocultures. All genes that passed initial quality filtering were included in the analysis to generate networks. Unweighted gene coexpression networks were generated with a Z-score cutoff of 4.5. Intraspecies genes were used to identify network modules. Gene ontology enrichment analysis was performed on nodes with interspecies edges.

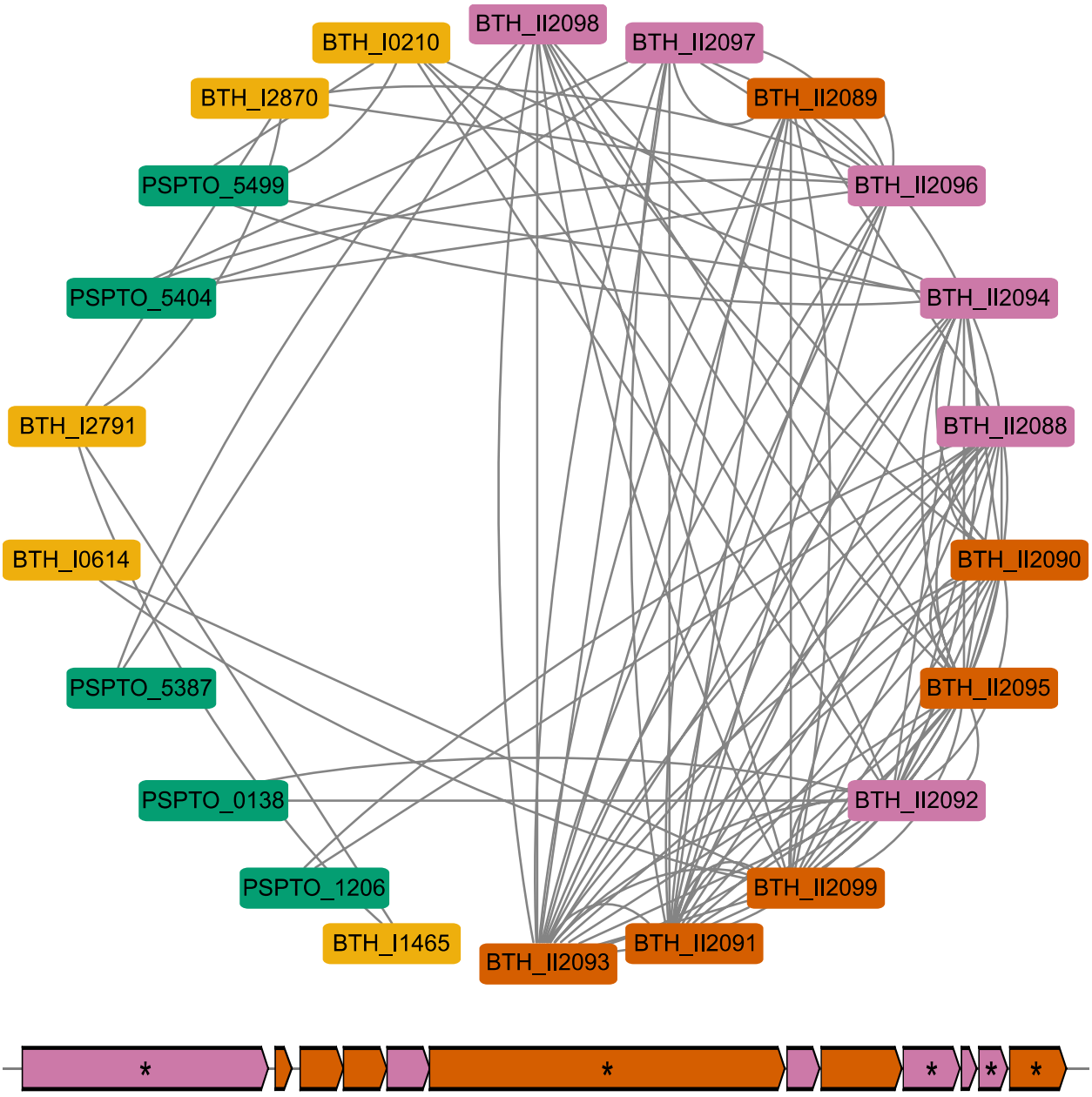

Appendix B Figure 25. *B. thailandensis* genes involved in malleilactone production are detected as interspecies edges in the *B. thailandensis-P. syringae* coexpression network and biosynthetic genes organize into network modules.

A network module containing the malleilactone BSGC is shown. The network module nodes are color coded by *B. thailandensis* gene type (BSGC or not) and type of connections (interspecies

Appendix B Figure 25 (cont'd)

or not): malleilactone biosynthetic genes that had interspecies edges (magenta), malleilactone biosynthetic genes that did not have interspecies edges (orange), or other genes that were not part of the BSGC (yellow); as well as genes that were from *P. syringae* (green). The chromosomal organization of the malleilactone BSGC is shown below the network module. The same colors are applied to the BSGC operons. Asterisks indicate core biosynthetic genes in the BSGCs, as predicted from antiSMASH.

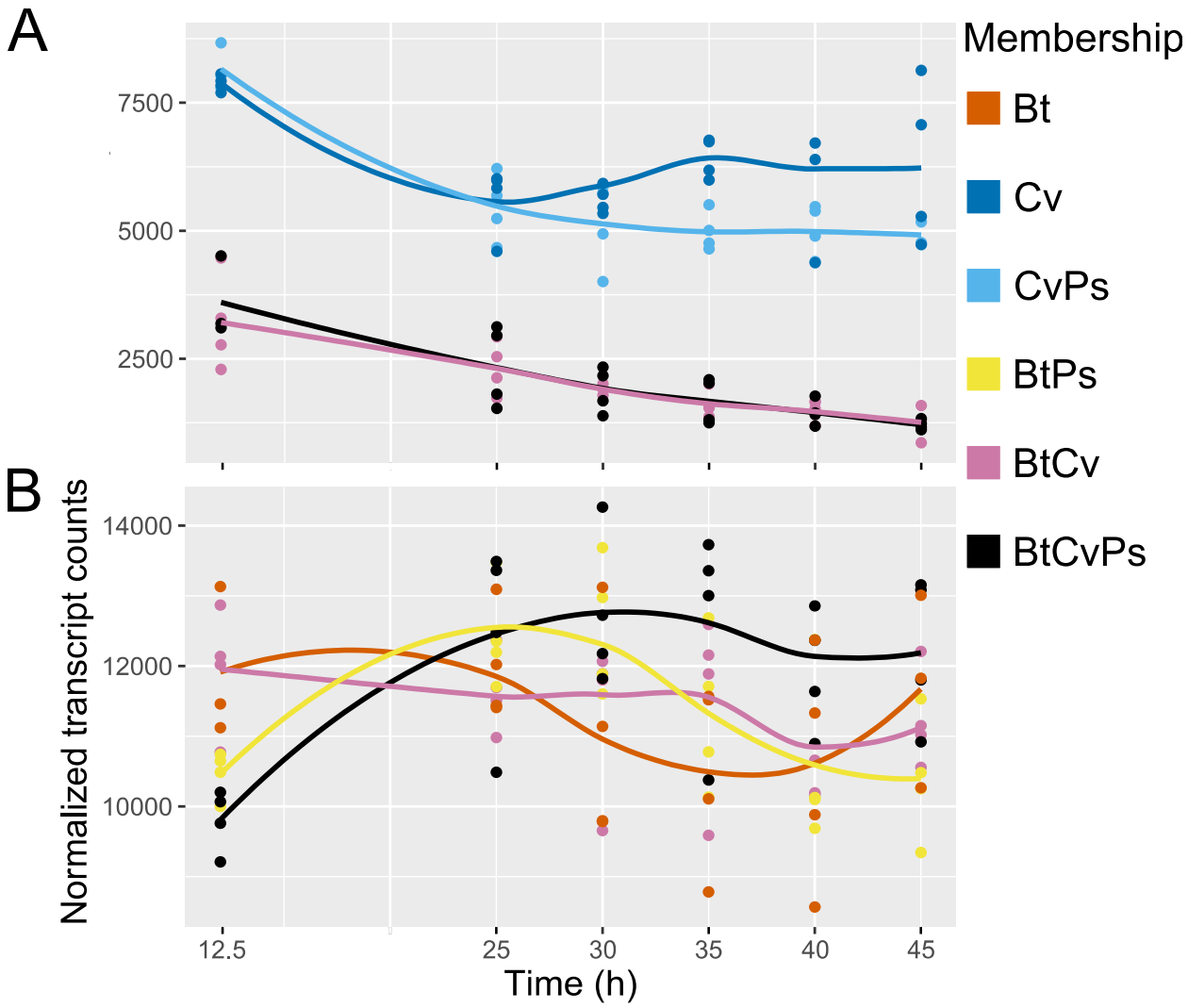

Appendix B Figure 26. The DNA starvation/stationary phase protection gene, dpsA, in downregulated in *C. violaceum* when cocultured with *B. thailandensis* while unaltered in *B. thailandensis*.

Transcript abundance trajectories of *dpsA* are plotted for *C. violaceum* (A) and *B. thailandensis* (B). Time course scatter plots were smooth curve fitted by loess. Community arrangements are as follows: *B. thailandensis* monoculture (Bt), *C. violaceum* monoculture (Cv), *C. violaceum-P. syringae* coculture (CvPs), *B. thailandensis-P. syringae* coculture (BtPs), *B. thailandensis-C. violaceum* coculture (BtCv), and the 3-member community (BtCvPs).

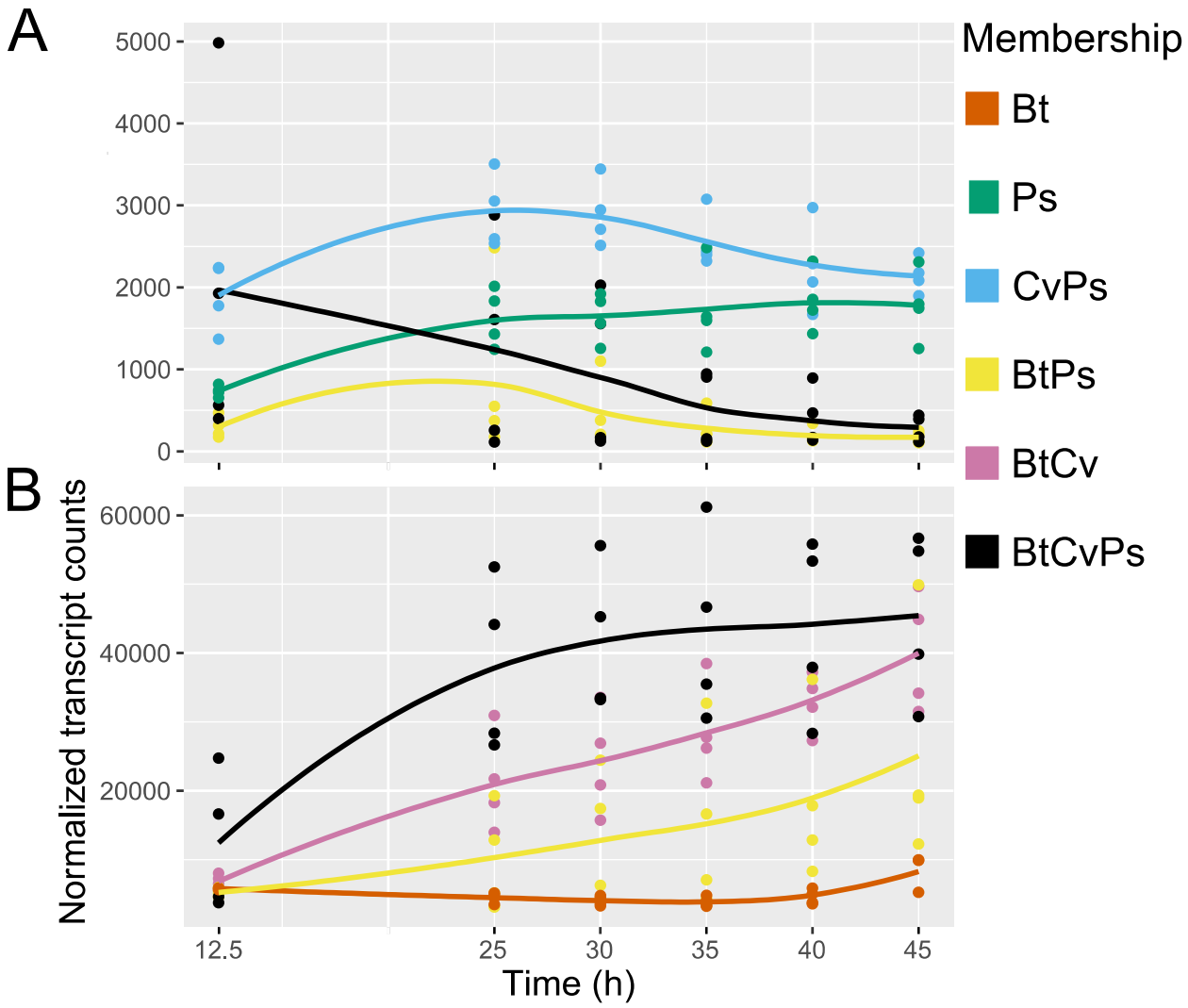

Appendix B Figure 27. The gene encoding a TonB-dependent siderophore receptor is downregulated in *P. syringae* when cocultured with *B. thailandensis* while upregulated in *B. thailandensis*.

Transcript abundance trajectories of *tonB* are plotted for *P. syringae* (A) and *B. thailandensis* (B). Time course scatter plots were smooth curve fitted by loess. Community arrangements are as follows: *B. thailandensis* monoculture (Bt), *P. syringae* monoculture (Ps), *C. violaceum-P. syringae* coculture (CvPs), *B. thailandensis-P. syringae* coculture (BtPs), *B. thailandensis-C. violaceum* coculture (BtCv), and the 3-member community (BtCvPs).

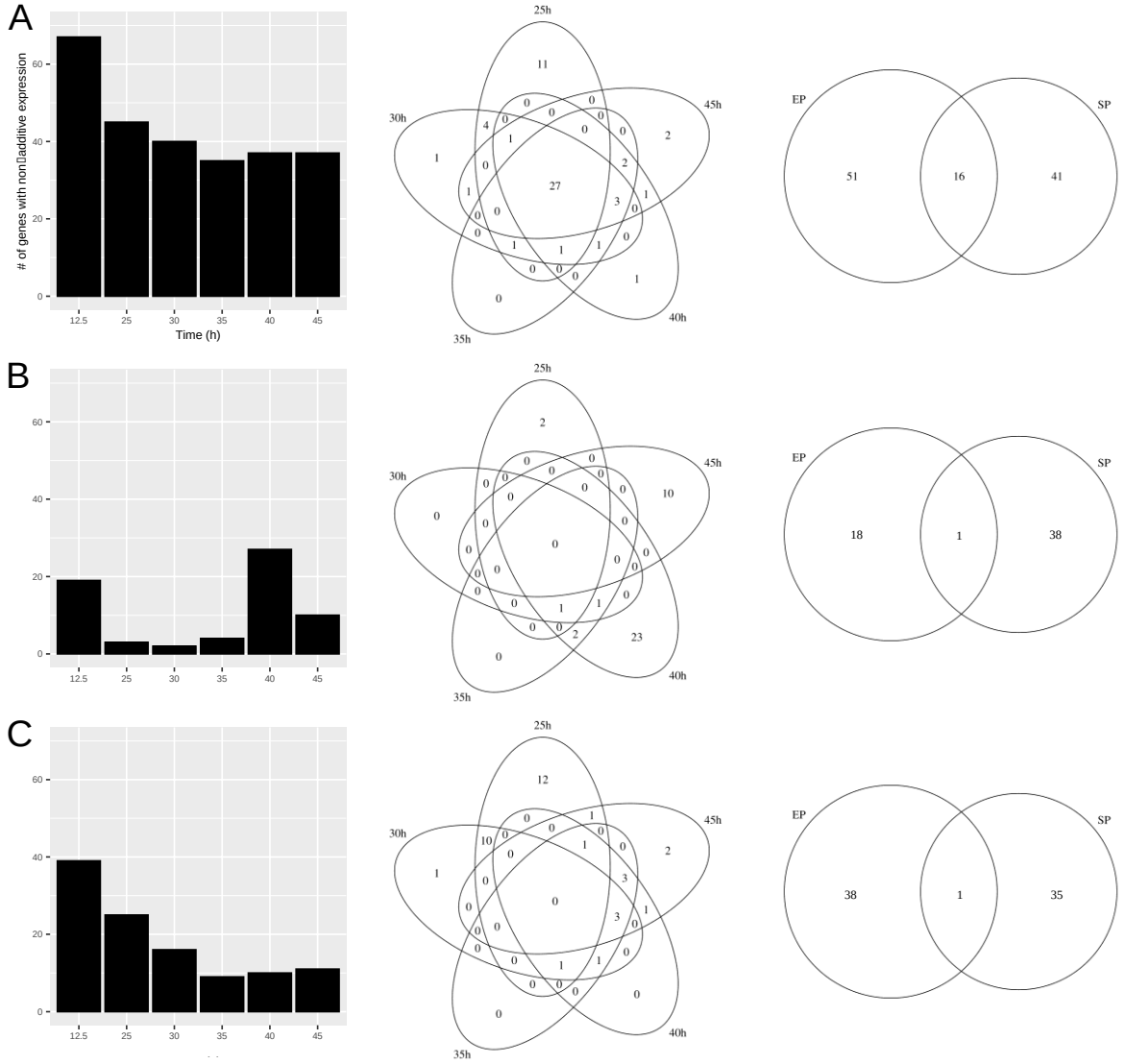

Appendix B Figure 28. Genes have non-additive upregulation in the 3-member community.

Quantity of genes with non-additive upregulation in the 3-member community for *B. thailandensis* (A), *C. violaceum* (B), and *P. syringae* (C) across the time series. The middle column displays a venn diagram representing overlaps and differences between non-additive upregulated genes between stationary phase timepoints. The last column displays a venn

Appendix B Figure 28 (cont'd)

diagram representing overlaps and differences between non-additive upregulated genes between the exponential phase timepoint (EP) and the stationary phase time points (SP).

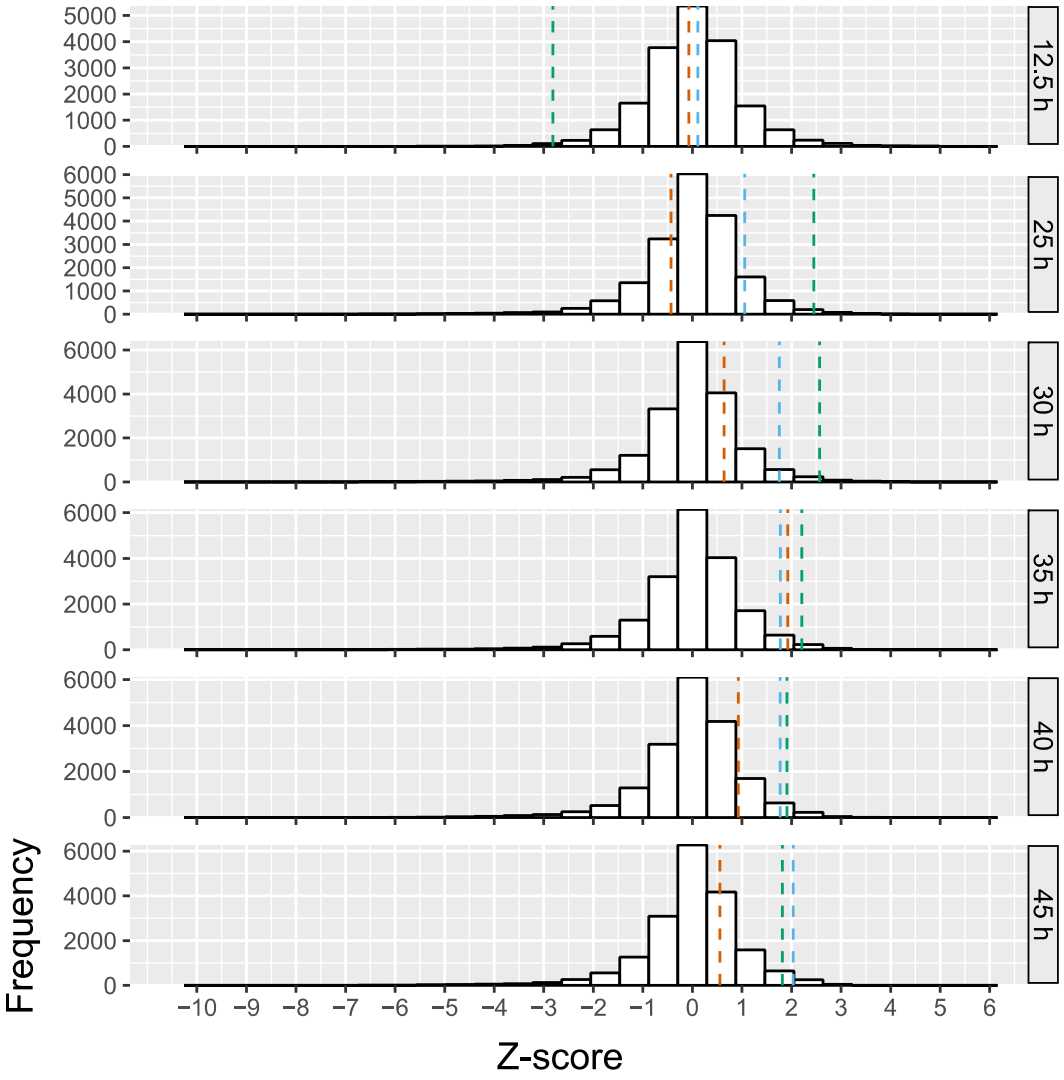

Appendix B Figure 29. Z-score distrubutions of exometabolite fold changes comparing the abundances from the 3-member community to the additive summation across all pairwise cocultures.

The mean fold change at each time point are as follows: 0.59 (12.5 h), 0.59 (25 h), 0.64 (30 h), 0.70 (35 h), 0.54 (40 h), and 0.64 (45 h). Vertical ablines correspond to Z-scored fold changes for thailandamide (cyan), pyochelin (green), and capistruin (red) at each time point.

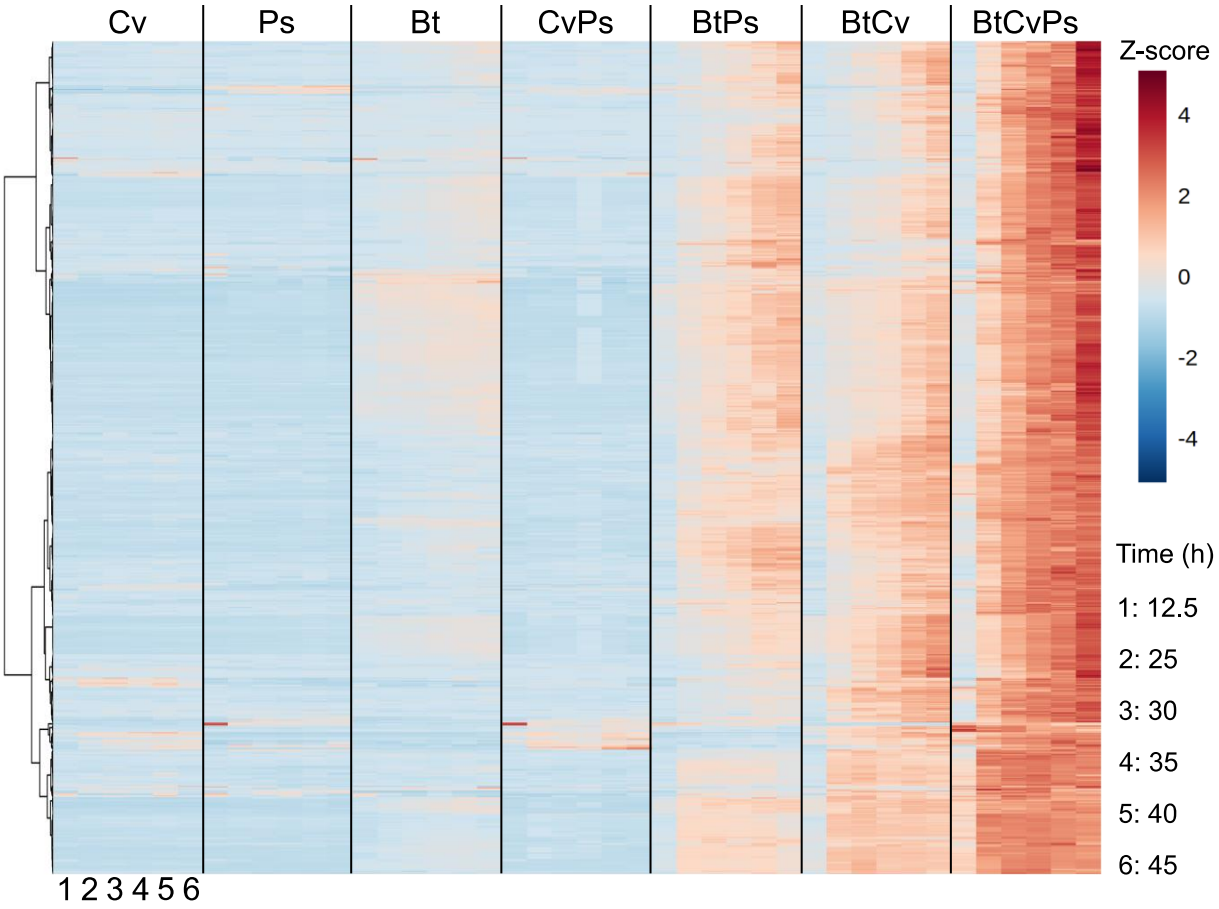

Appendix B Figure 30. Exometabolites accumulate in a non-additive manner.

Exometabolomics features were determined to have non-additive accumulation if the quantity in the 3-member community had a log2 fold-change greater than 1 compared to the summation of exometabolite accumulation in each pairwise coculture. Exometabolites with non-additive accumulation are highlighted in yellow. Samples are in columns and exometabolites are in rows. Data for each sample are the averages from independent time point replicates (n = 2 to 4). Euclidean distance was calculated from Z-scored mass spectral profiles (containing peak areas). Prior to Z-scoring, features were normalized by an ITSD reference feature and cube root transformed. Features were clustered by Ward's method.

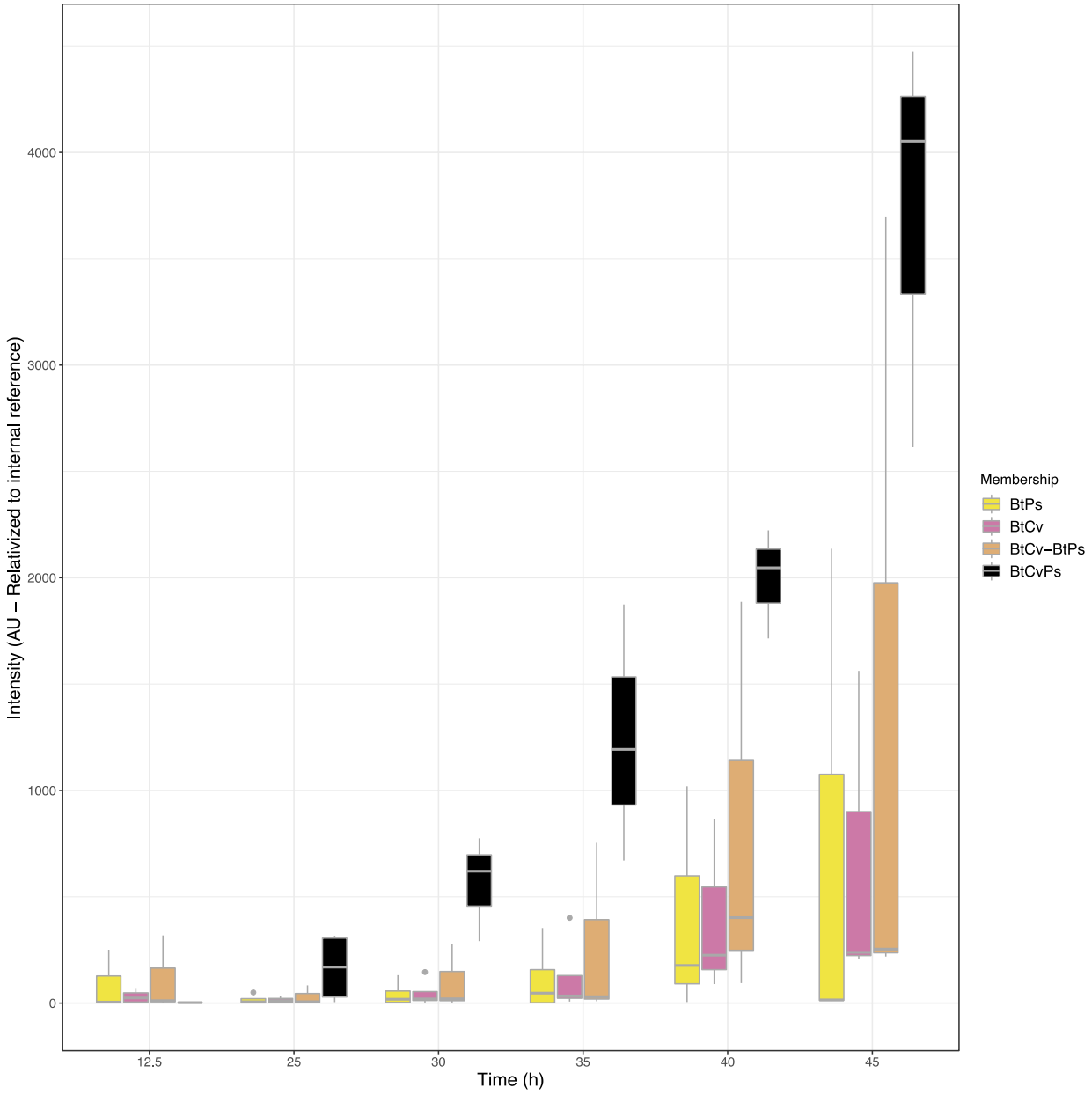

Appendix B Figure 31. Pyochelin accumulates in a non-additive manner.

The accumulation of pyochelin was quantified through time (n = 3-4 integrated peak areas per time point). The bottom and top of the box are the first and third quartiles, respectively, and the line inside the box is the median. The whiskers extend from their respective hinges to the

Appendix B Figure 31 (cont'd)

largest value (top), and smallest value (bottom) was no further away than 1.5× the interquartile range. Colors correspond to the community membership for the *B. thailandensis-P. syringae* coculture (yellow, BtPs), the *B. thailandensis-C. violaceum* coculture (magenta, BtCv), the "expected" exometabolite abundance in the 3-member community obtained from additive peak areas from the *B. thailandensis-P. syringae* and *B. thailandensis-C. violaceum* cocultures (orange, BtCv+BtPs), and the 3-member community (black, BtCvPs).

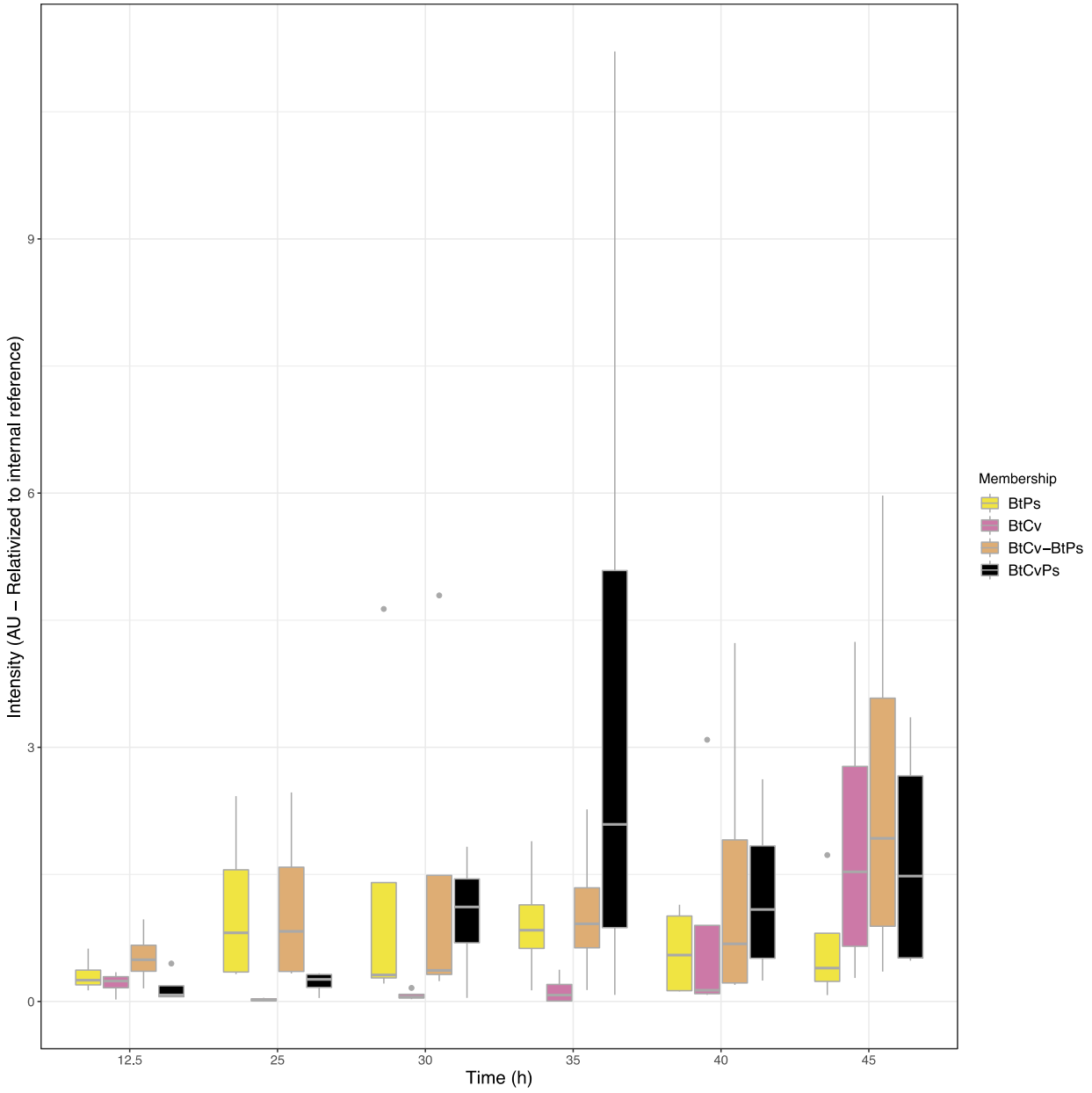

Appendix B Figure 32. Capistruin does not accumulate in a non-additive manner.

The accumulation of pyochelin was quantified through time (n = 4 integrated peak areas per time point). The bottom and top of the box are the first and third quartiles, respectively, and the line inside the box is the median. The whiskers extend from their respective hinges to the largest value (top), and smallest value (bottom) was no further away than 1.5× the interquartile

Appendix B Figure 32 (cont'd)

range. Colors correspond to the community membership for the *B. thailandensis*-*P. syringae* coculture (yellow, BtPs), the *B. thailandensis*-*C. violaceum* coculture (magenta, BtCv), the "expected" exometabolite abundance in the 3-member community obtained from additive peak areas from the *B. thailandensis*-*P. syringae* and *B. thailandensis*-*C. violaceum* cocultures (orange, BtCv+BtPs), and the 3-member community (black, BtCvPs).

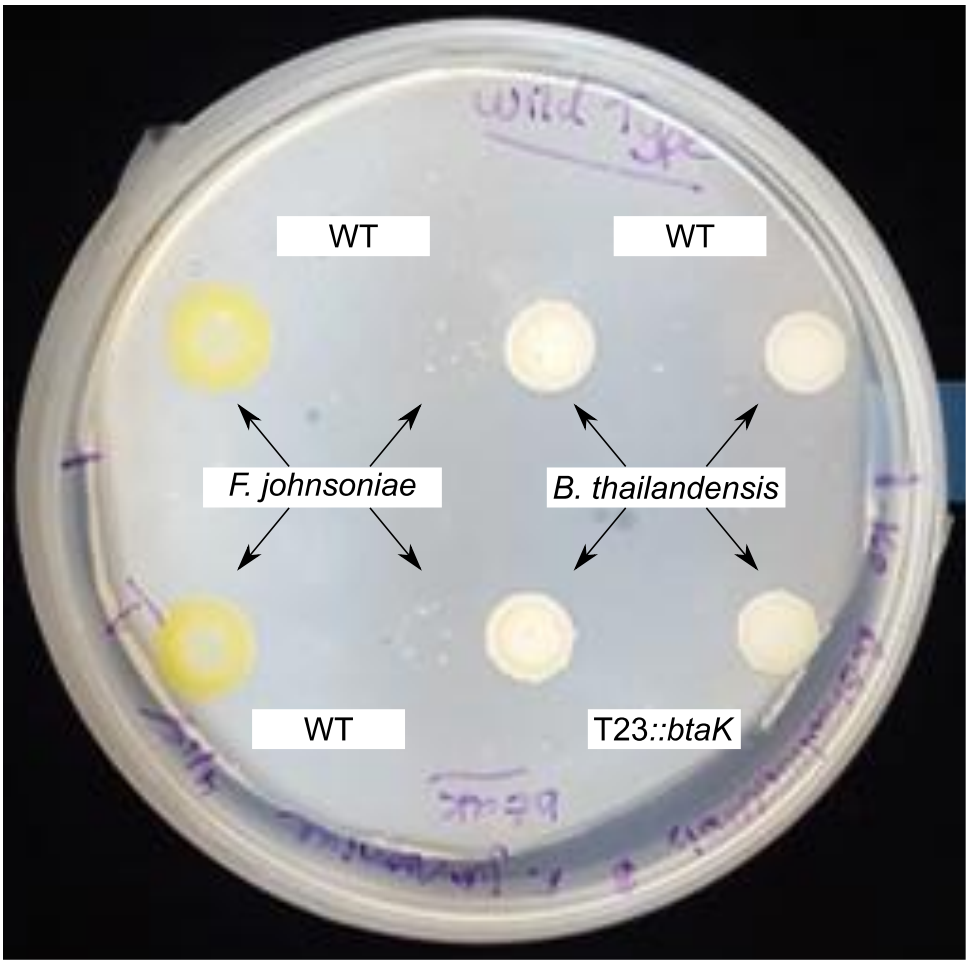

Appendix B Figure 33. A *B. thailandensis* btaK::T23 mutant unable to produce bactobolin still inhibits *F. johnsoniae*.

B. thailandensis WT (top) and *B. thailandensis btaK*::T23 (bottom) was co-plated with *F. johnsoniae* WT. Strains were also plated outside the interspecies interaction zone as growth controls.

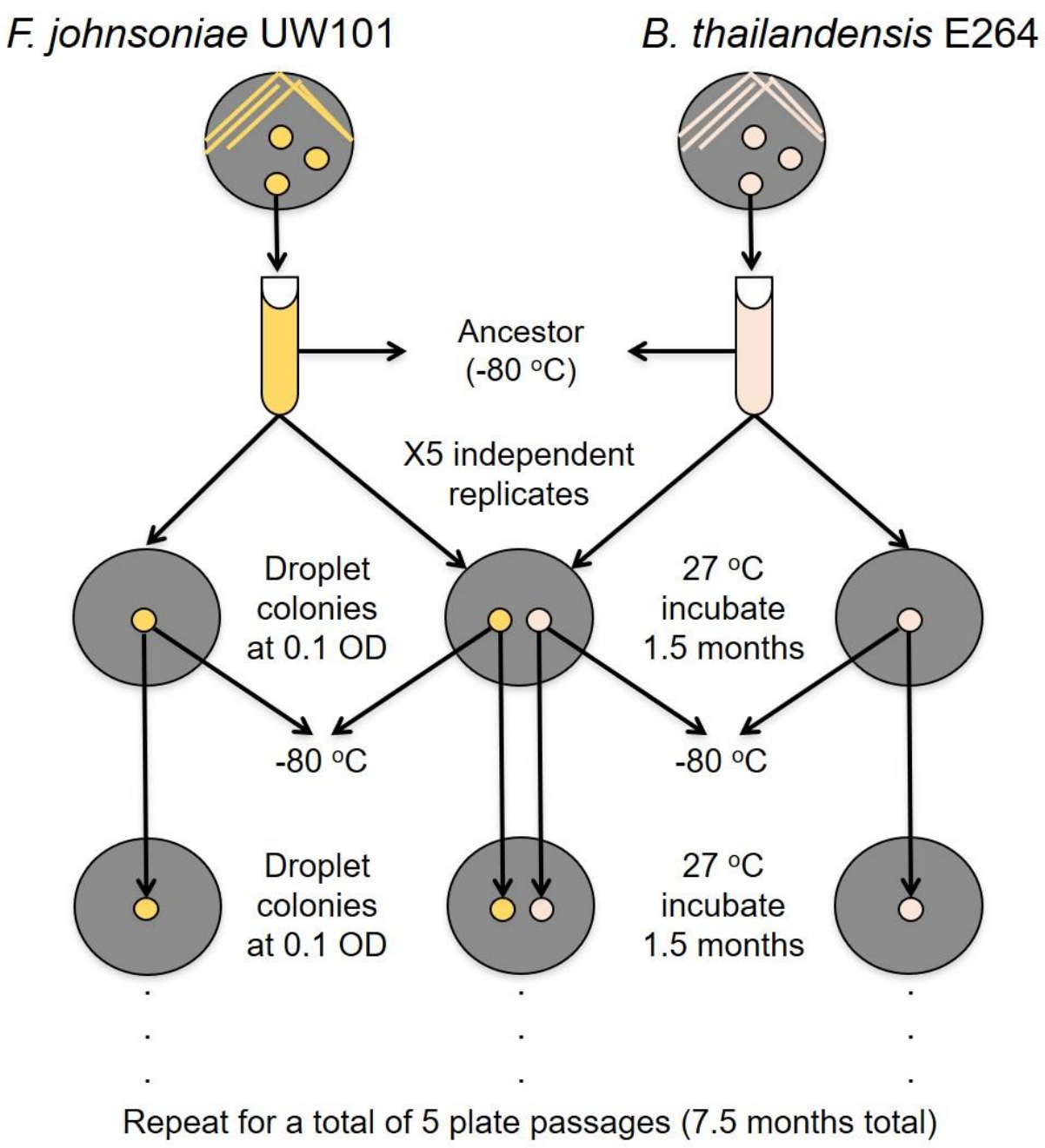

Appendix B Figure 34. Schematic of (co)evolution experiment.

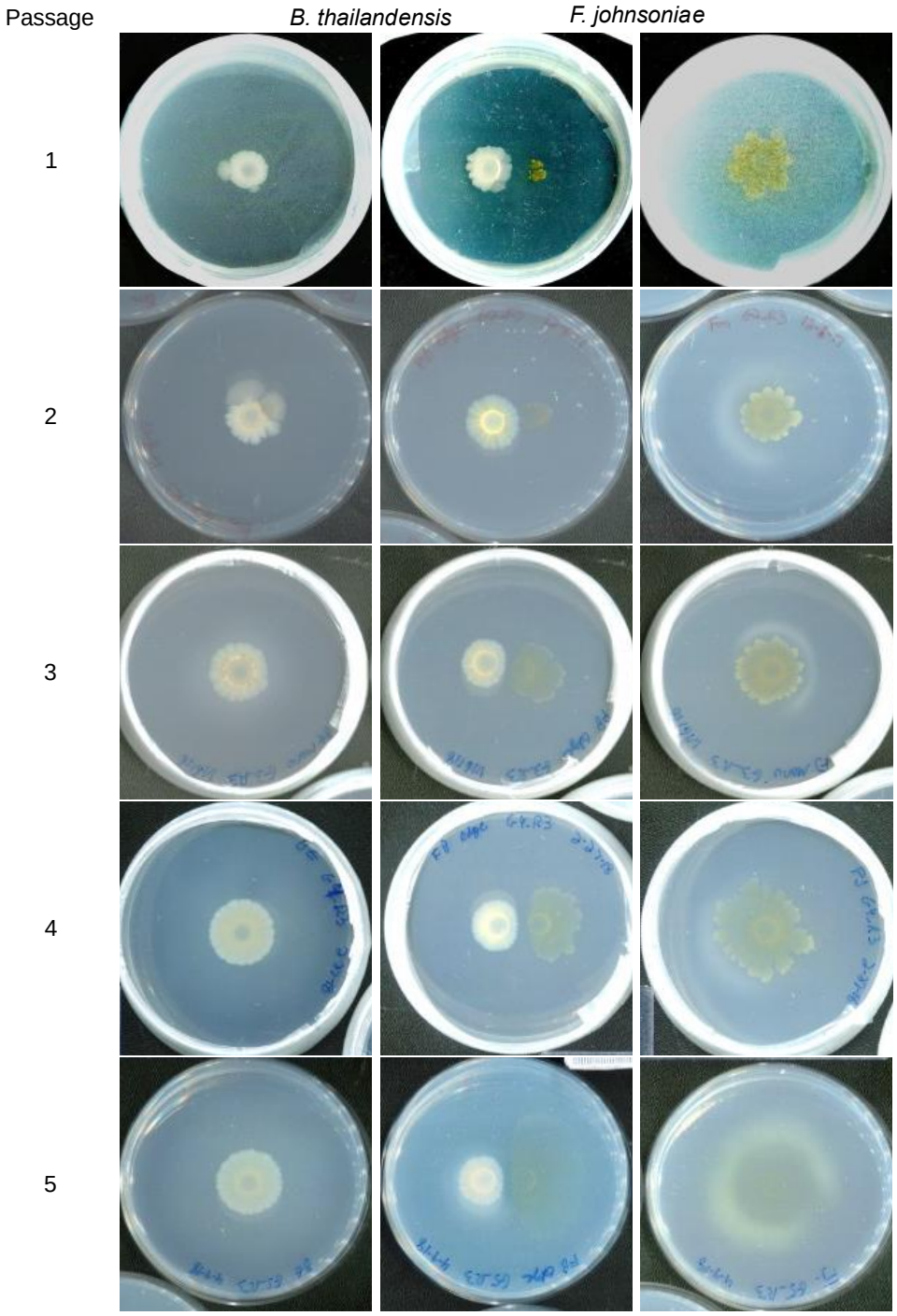

Appendix B Figure 35. Colony morphologies and growth success over the (co)evolution experiment.

Appendix B Figure 35 (cont'd)

Plate images were taken at 1.5 months after each plate passage. Shown are colony morphologies and growth success of *B. thailandensis* monoculture (column 1), co-plated *B. thailandensis-F. johnsoniae* (column 2), and *F. johnsoniae* monoculture (column 3) for a representative independent replicate (rep 3). Each row is plate passage.

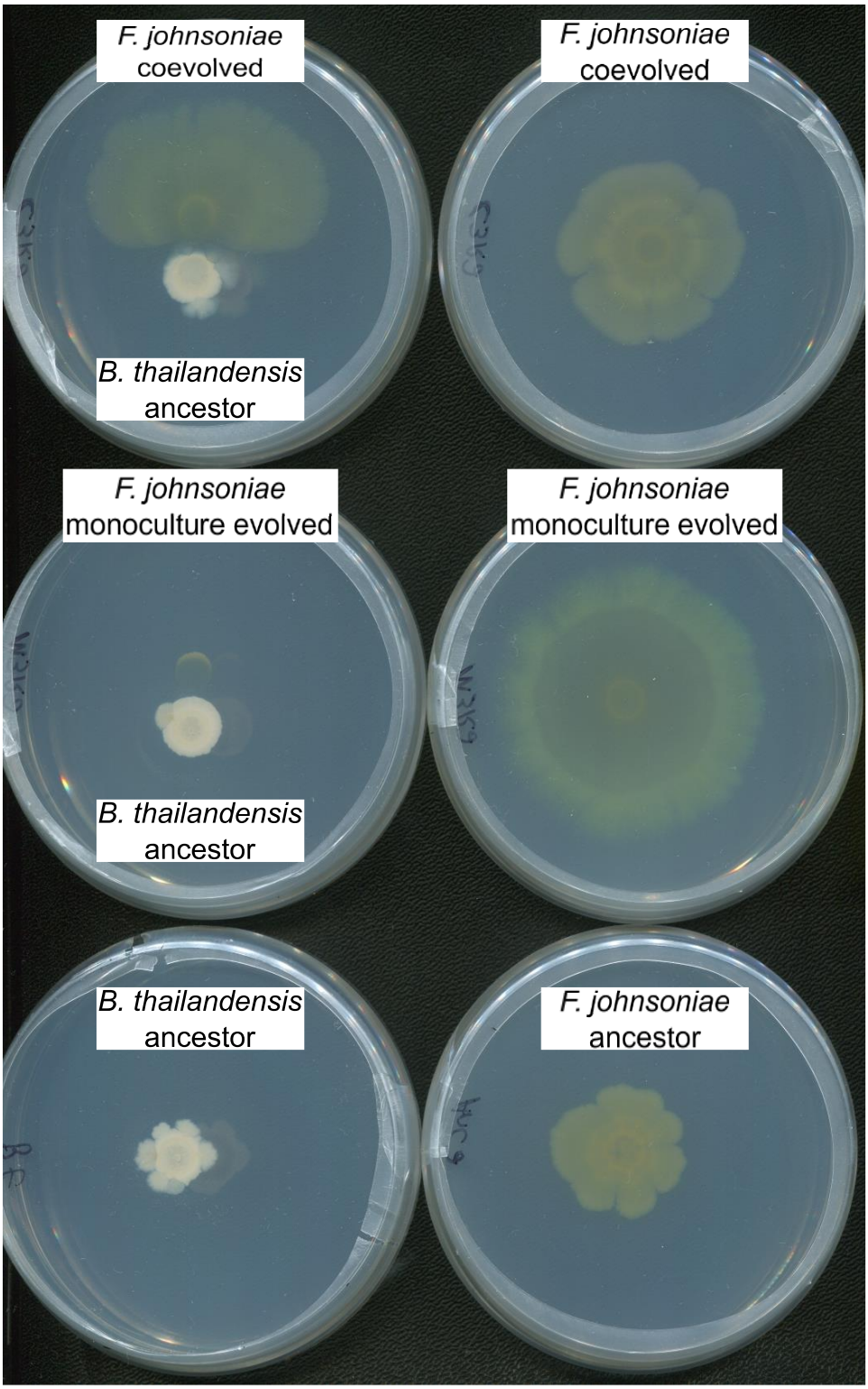

Appendix B Figure 36. Coevolved *F. johnsoniae* has gained resistance to a *B. thailandensis*-produced antibiotic.

Appendix B Figure 36 (cont'd)

Coevolved *F. johnsoniae* can grow better in the presence of *B. thailandensis* (column 1, top row) compared to the monoculture evolved *F. johnsoniae* (column 1, middle row). Monocultures are shown as a comparison of growth success when co-plated. Shown are evolved lines from one of the independent replicates (rep 3) from the fifth plate passage. Images were taken after incubation for 1.5 months.

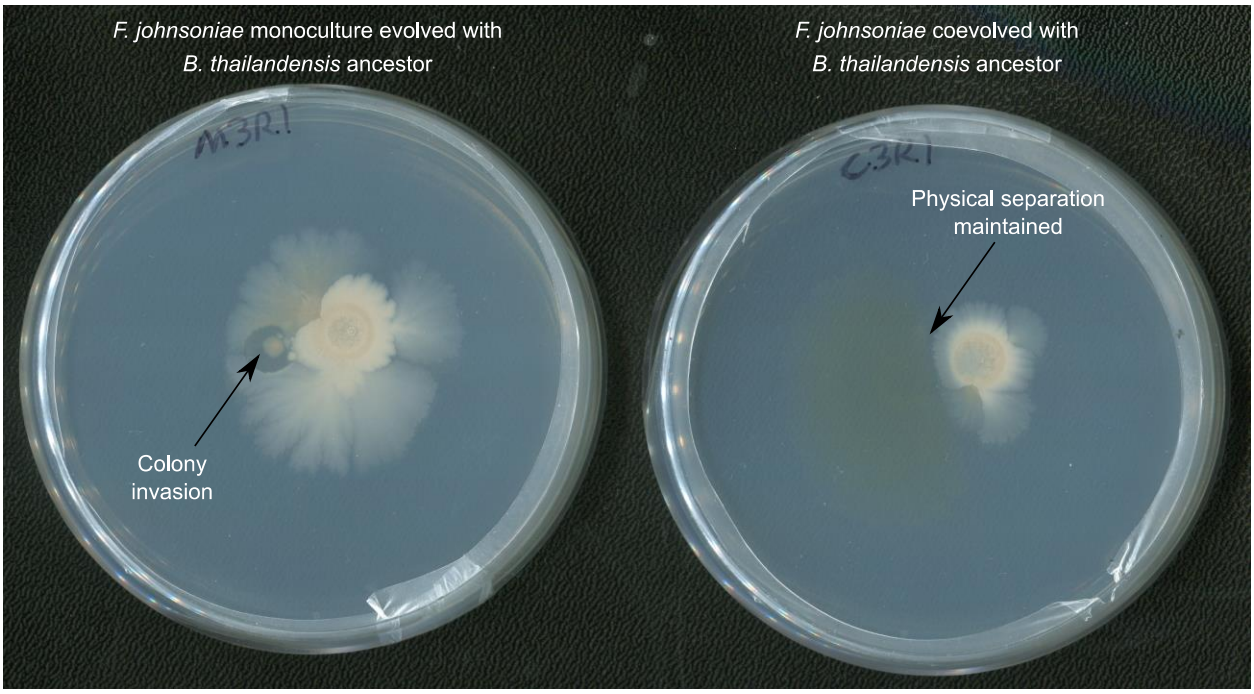

Appendix B Figure 37. Coevolved *F. johnsoniae* can resist colony invasion.

On each plate, *F. johnsoniae* is on the left and *B. thailandensis* (right) is on the right. The *B. thailandensis* ancestor was co-plated with *F. johnsoniae* evolved monoculture (left plate) and *F. johnsoniae* coevolved (right plate) from the fifth plate passage. Plates were incubated for 2.5 months to allow the chance for physical interactions to occur.

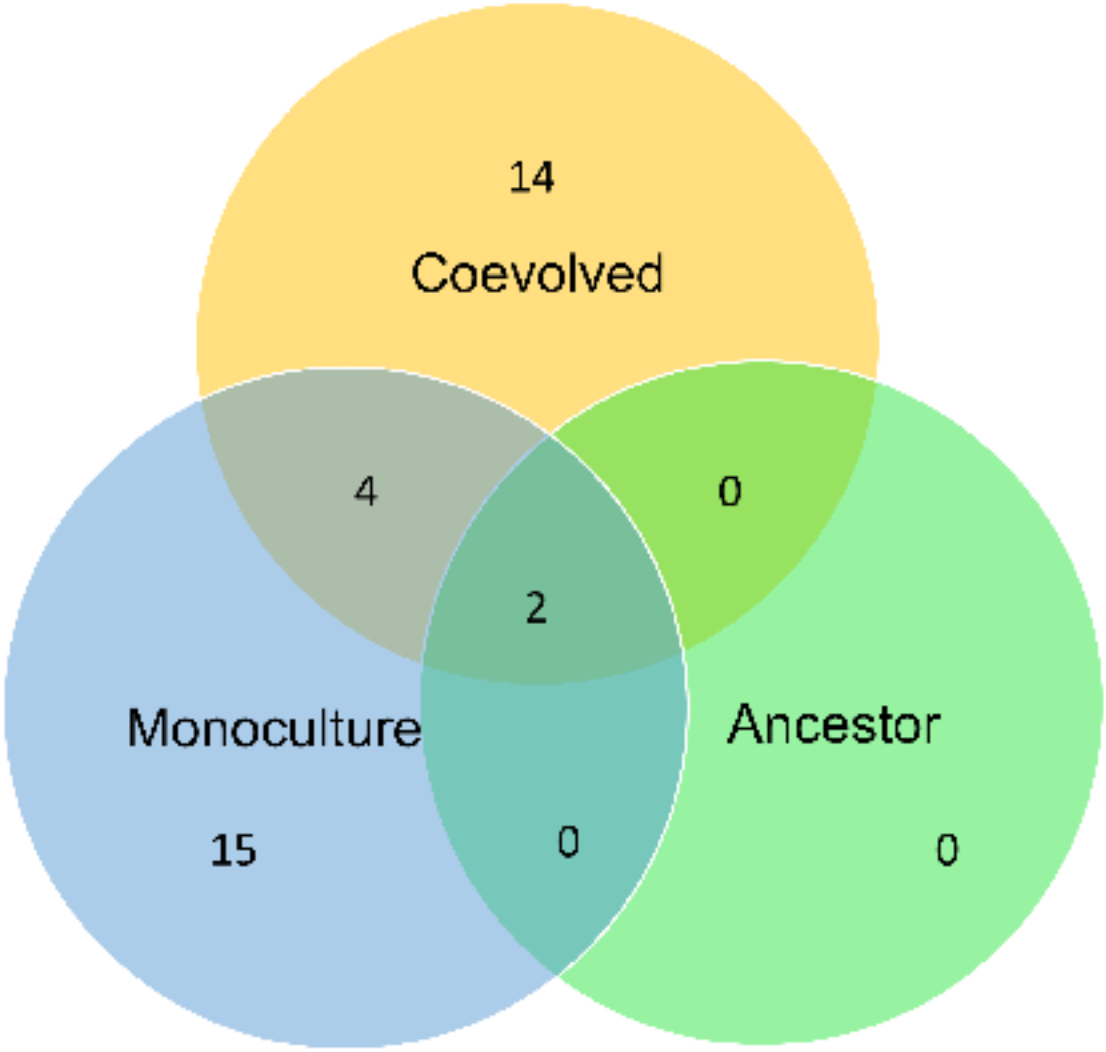

Appendix B Figure 38. Coevolved lines acquire unique mutations as a result of interspecies interactions.

Shown is a Venn diagram comparing distinctions and overlaps of gene loci where mutations were observed in the ancestor, monoculture evolved lines, and coculture evolved lines.

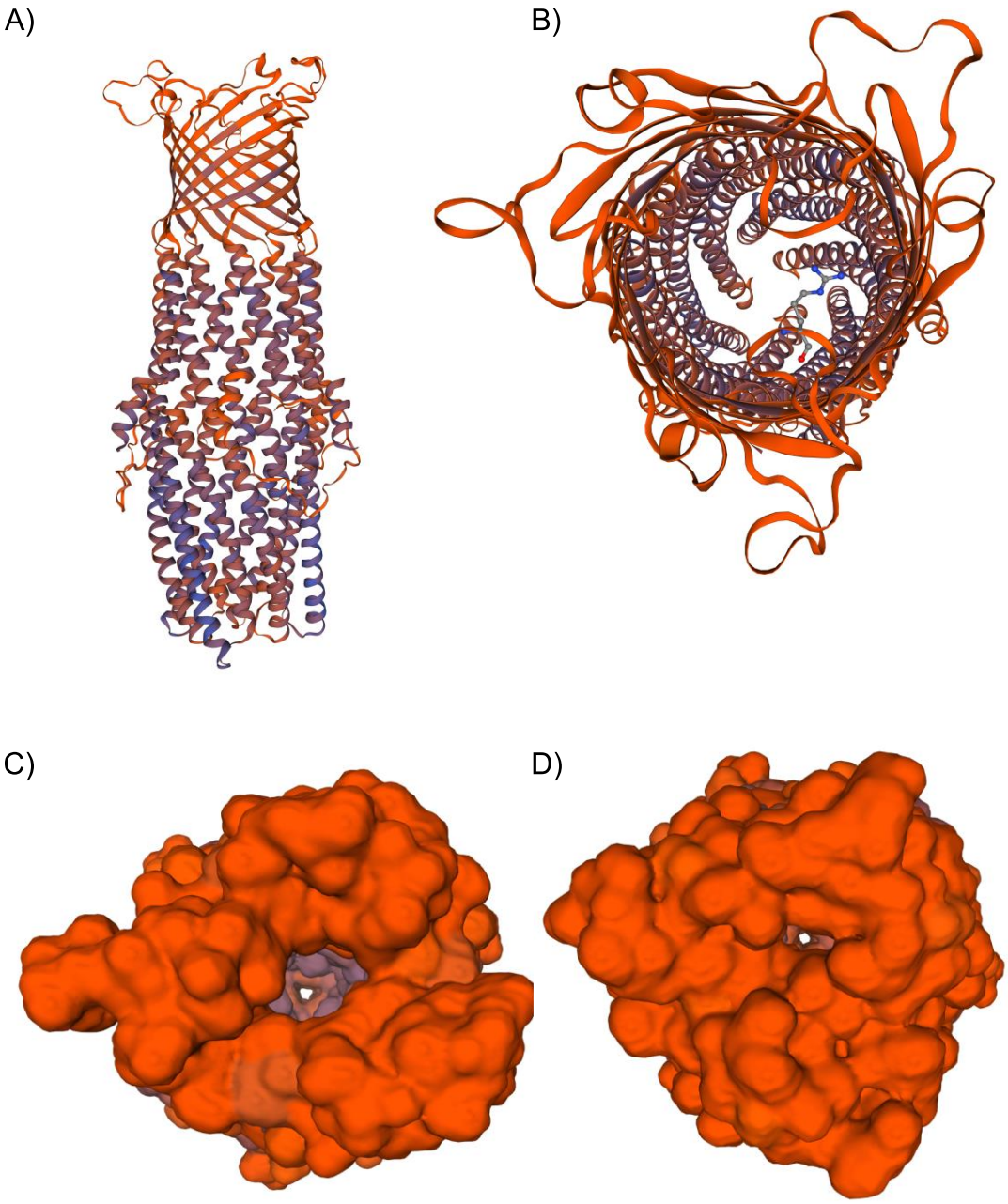

Appendix B Figure 39. A nonsynonymous mutation in TolC narrows the opening of the efflux channel.

A model of TolC (**A**) with the G83R nonsynonymous mutation. TolC is rotated +90 about the x-axis in panels C-D such TolC is viewed from top looking down the channel. The

Appendix B Figure 39 (cont'd)

G83R residue (**B**) is located on one of the extracellular loops of TolC. The opening of the efflux channel in WT TolC (**C)** is predicted to narrow due to G83R (**D**).

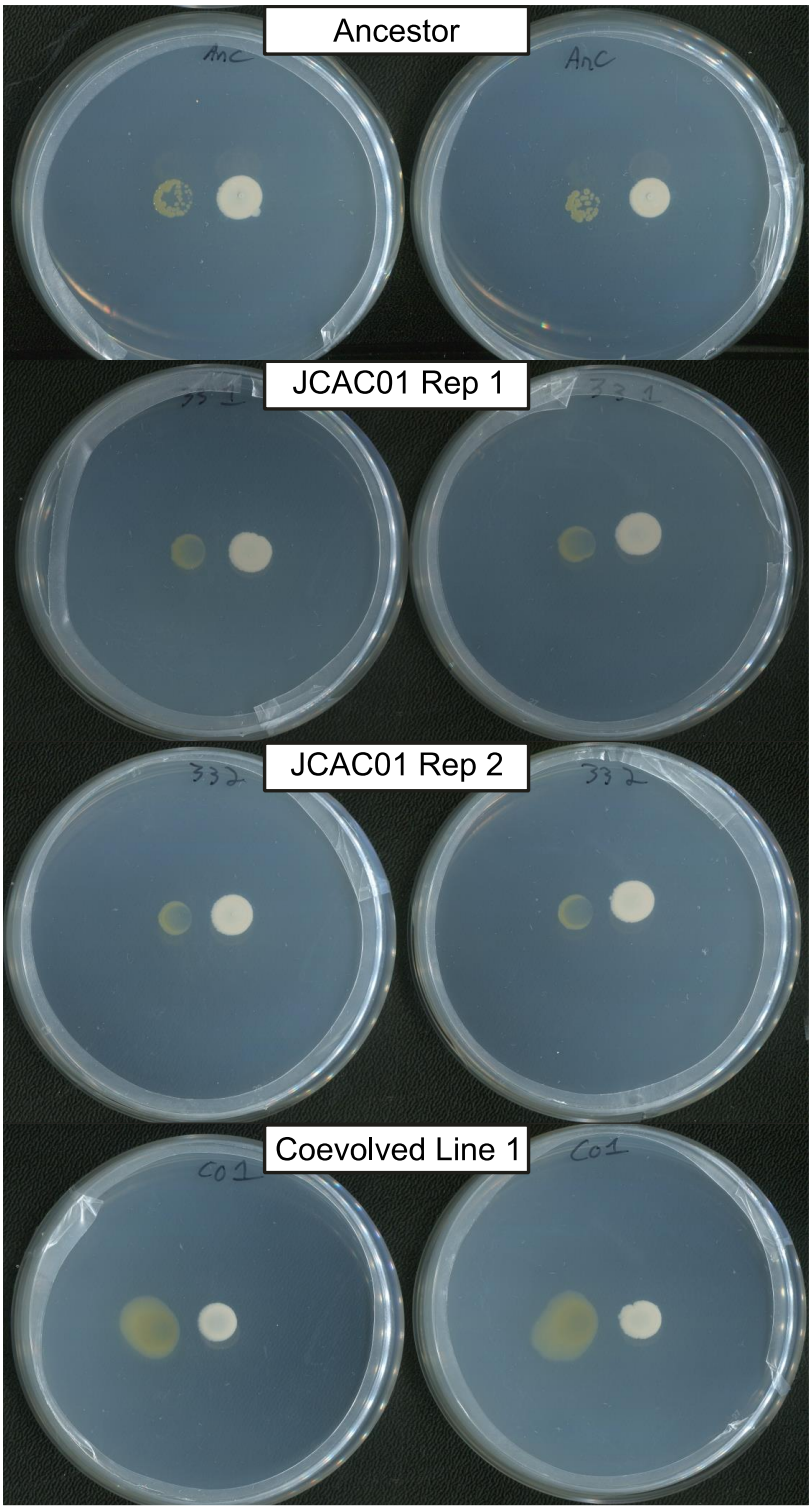

Appendix B Figure 40. *F. johnsoniae* recombinants display antibiotic resistance, but not to the extent observed in coevolved lines.

Appendix B Figure 40 (cont'd)

The 33 bp deletion in FJOH_RS06580 was placed into the *F. johnsoniae* ancestor and co-plated with *B. thailandensis*. Two confirmed successful recombinants (JCAC01 Reps 1&2) have more growth success than the ancestor but not the coevolved line from which FJOH_RS06580 was amplified to create the recombinants. All strains were co-plated with the *B. thailandensis* ancestor. Plates were imaged after a month of incubation.

REFERENCES

REFERENCES

1. Phelan VV, Liu WT, Pogliano K, Dorrestein PC. 2011. Microbial metabolic exchange--the chemotype-to-phenotype link. Nat Chem Biol 8:26–35.

2. Kell DB, Brown M, Davey HM, Dunn WB, Spasic I, Oliver SG. 2005. Metabolic footprinting and systems biology: The medium is the message. Nat Rev Microbiol 3:557–65.

3. Pinu FR, Villas-Boas SG. 2017. Extracellular microbial metabolomics: The state of the art. Metabolites 7:43.

4. Perez-Garcia O, Lear G, Singhal N. 2016. Metabolic network modeling of microbial interactions in natural and engineered environmental systems. Front Microbiol 7:673.

5. Silva LP, Northen TR. 2015. Exometabolomics and MSI: Deconstructing how cells interact to transform their small molecule environment. Curr Opin Biotechnol 34:209–16.

6. Medema MH, Kottmann R, Yilmaz P, Cummings M, Biggins JB, Blin K, De Bruijn I, Chooi YH, Claesen J, Coates RC, Cruz-Morales P, Duddela S, Düsterhus S, Edwards DJ, Fewer DP, Garg N, Geiger C, Gomez-Escribano JP, Greule A, Hadjithomas M, Haines AS, Helfrich EJN, Hillwig ML, Ishida K, Jones AC, Jones CS, Jungmann K, Kegler C, Kim HU, Kötter P, Krug D, Masschelein J, Melnik A V., Mantovani SM, Monroe EA, Moore M, Moss N, Nützmann HW, Pan G, Pati A, Petras D, Reen FJ, Rosconi F, Rui Z, Tian Z, Tobias NJ, Tsunematsu Y, Wiemann P, Wyckoff E, Yan X, Yim G, Yu F, Xie Y, Aigle B, Apel AK, Balibar CJ, Balskus EP, Barona-Gómez F, Bechthold A, Bode HB, Borriss R, Brady SF, Brakhage AA, Caffrey P, Cheng YQ, Clardy J, Cox RJ, De Mot R, Donadio S, Donia MS, Van Der Donk WA, Dorrestein PC, Doyle S, Driessen AJM, Ehling-Schulz M, Entian KD, Fischbach MA, Gerwick L, Gerwick WH, Gross H, Gust B, Hertweck C, Höfte M, Jensen SE, Ju J, Katz L, Kaysser L, Klassen JL, Keller NP, Kormanec J, Kuipers OP, Kuzuyama T, Kyrpides NC, Kwon HJ, Lautru S, Lavigne R, Lee CY, Linquan B, Liu X, Liu W, Luzhetskyy A, Mahmud T, Mast Y, Méndez C, Metsä-Ketelä M, Micklefield J, Mitchell DA, Moore BS, Moreira LM, Müller R, Neilan BA, Nett M, Nielsen J, O'Gara F, Oikawa H, Osbourn A, Osburne MS, Ostash B, Payne SM, Pernodet JL, Petricek M, Piel J, Ploux O, Raaijmakers JM, Salas JA, Schmitt EK, Scott B, Seipke RF, Shen B, Sherman DH, Sivonen K, Smanski MJ, Sosio M, Stegmann E, Süssmuth RD, Tahlan K, Thomas CM, Tang Y, Truman AW, Viaud M, Walton JD, Walsh CT, Weber T, Van Wezel GP, Wilkinson B, Willey JM, Wohlleben W, Wright GD, Ziemert N, Zhang C, Zotchev SB, Breitling R, Takano E, Glöckner FO. 2015. Minimum Information about a Biosynthetic Gene cluster. Nat Chem Biol 11:625–631.

7. Buhian WP, Bensmihen S. 2018. Mini-review: nod factor regulation of phytohormone signaling and homeostasis during rhizobia-legume symbiosis. Front Plant Sci 9:1247.

8. Sasse J, Martinoia E, Northen T. 2018. Feed Your Friends: Do Plant Exudates Shape the Root Microbiome? Trends Plant Sci 23:25–41.

9. Norsworthy AN, Visick KL. 2013. Gimme shelter: how Vibrio fischeri successfully navigates an animal's multiple environments. Front Microbiol 4:356.

10. Lupp C, Ruby EG. 2005. Vibrio fischeri uses two quorum-sensing systems for the regulation of early and late colonization factors. J Bacteriol 187:3620–3629.

11. Cox LM, Yamanishi S, Sohn J, Alekseyenko A V., Leung JM, Cho I, Kim SG, Li H, Gao Z, Mahana D, Zárate Rodriguez JG, Rogers AB, Robine N, Loke P, Blaser MJ. 2014. Altering the intestinal microbiota during a critical developmental window has lasting metabolic consequences. Cell 158:705–721.

12. Olszak T, An D, Zeissig S, Vera MP, Richter J, Franke A, Glickman JN, Siebert R, Baron RM, Kasper DL, Blumberg RS. 2012. Microbial exposure during early life has persistent effects on natural killer T cell function. Science (80-) 336:489–493.

13. Chia LW, Mank M, Blijenberg B, Bongers RS, Van Limpt K, Wopereis H, Tims S, Stahl B, Belzer C, Knol J. 2021. Cross-feeding between Bifidobacterium infantis and Anaerostipes caccae on lactose and human milk oligosaccharides. Benef Microbes 12:69–83.

14. Persson T, Bååth E, Clarholm M, Lundkvist H, Söderström B, Sohlenius B. 1980. Trophic Structure, Biomass Dynamics and Carbon Metabolism of Soil Organisms in a Scots Pine Forest on JSTOR. JSTOR 32:419–459.

15. Azam F, Malfatti F. 2007. Microbial structuring of marine ecosystems. Nat Rev Microbiol 5:782–791.

16. Ariesyady HD, Ito T, Okabe S. 2007. Functional bacterial and archaeal community structures of major trophic groups in a full-scale anaerobic sludge digester. Water Res 41:1554–1568.

17. Tong H, Chen W, Merritt J, Qi F, Shi W, Dong X. 2007. Streptococcus oligofermentans inhibits Streptococcus mutans through conversion of lactic acid into inhibitory H2O2: A possible counteroffensive strategy for interspecies competition. Mol Microbiol 63:872–880.

18. García C, Bautista L, Rendueles M, Díaz M. 2019. A new synbiotic dairy food containing lactobionic acid and Lactobacillus casei. Int J Dairy Technol 72:47–56.

19. Niehus R, Picot A, Oliveira NM, Mitri S, Foster KR. 2017. The evolution of siderophore production as a competitive trait. Evolution (N Y) 71:1443–1455.

20. Smith EE, Sims EH, Spencer DH, Kaul R, Olson M V. 2005. Evidence for diversifying selection at the pyoverdine locus of Pseudomonas aeruginosa. J Bacteriol 187:2138–2147.

21. Cordero OX, Ventouras LA, DeLong EF, Polz MF. 2012. Public good dynamics drive evolution of iron acquisition strategies in natural bacterioplankton populations. Proc Natl Acad Sci U S A 109:20059–20064.

22. Traxler MF, Seyedsayamdost MR, Clardy J, Kolter R. 2012. Interspecies modulation of bacterial development through iron competition and siderophore piracy. Mol Microbiol 86:628–644.

23. Hibbing ME, Fuqua C, Parsek MR, Peterson SB. 2010. Bacterial competition: Surviving and thriving in the microbial jungle. Nat Rev Microbiol 8:15–25.

24. Cornforth DM, Foster KR. 2013. Competition sensing: The social side of bacterial stress responses. Nat Rev Microbiol 11:285–293.

25. Majeed H, Gillor O, Kerr B, Riley MA. 2011. Competitive interactions in Escherichia coli populations: The role of bacteriocins. ISME J 5:71–81.

26. Allen HK, Donato J, Wang HH, Cloud-Hansen KA, Davies J, Handelsman J. 2010. Call of the wild: Antibiotic resistance genes in natural environments. Nat Rev Microbiol 8:251–259.

27. Núñez-Montero K, Barrientos L. 2018. Advances in antarctic research for antimicrobial discovery: A comprehensive narrative review of bacteria from antarctic environments as potential sources of novel antibiotic compounds against human pathogens and microorganisms of industrial importance. Antibiotics 7:90.

28. Mishra AK, Choi J, Choi SJ, Baek KH. 2017. Cyclodipeptides: An overview of their biosynthesis and biological activity. Molecules 22:1796.

29. Abouhamad WN, Manson M, Gibson MM, Higgins CF. 1991. Peptide transport and chemotaxis in Escherichia coli and Salmonella typhimurium: characterization of the dipeptide permease (Dpp) and the dipeptide-binding protein. Mol Microbiol 5:1035–1047.

30. Sun SJ, Liu YC, Weng CH, Sun SW, Li F, Li H, Zhu H. 2020. Cyclic dipeptides mediating quorum sensing and their biological effects in Hypsizygus marmoreus. Biomolecules 10:298.

31. Rhee KH. 2004. Cyclic dipeptides exhibit synergistic, broad spectrum antimicrobial effects and have anti-mutagenic properties. Int J Antimicrob Agents 24:423–427.

32. Gowrishankar S, Sivaranjani M, Kamaladevi A, Ravi AV, Balamurugan K, Karutha Pandian S. 2016. Cyclic dipeptide cyclo(l-leucyl-l-prolyl) from marine Bacillus amyloliquefaciens mitigates biofilm formation and virulence in Listeria monocytogenes. Pathog Dis 74:ftw017.

33. Ortiz-Castro R, Díaz-Pérez C, Martínez-Trujillo M, Del Río RE, Campos-García J, López-Bucio J. 2011. Transkingdom signaling based on bacterial cyclodipeptides with auxin activity in plants. Proc Natl Acad Sci U S A 108:7253–7258.

34. Schmidt R, Ulanova D, Wick LY, Bode HB, Garbeva P. 2019. Microbe-driven chemical ecology: past, present and future. ISME J 13:2656–2663.

35. Sugimoto Y, Camacho FR, Wang S, Chankhamjon P, Odabas A, Biswas A, Jeffrey PD, Donia MS. 2019. A metagenomic strategy for harnessing the chemical repertoire of the human microbiome. Science (80-) 366:eaax9176.

36. Awad H, Khamis MM, El-Aneed A. 2014. Mass Spectrometry, Review of the Basics: Ionization. http://dx.doi.org/101080/057049282014954046 50:158–175.

37. Haag AM. 2016. Mass Analyzers and Mass Spectrometers. Adv Exp Med Biol 919:157–169.

38. McMahon G. 2021. How a Mass Spectrometer Works, Types of Instrumentation and Interpreting Mass Spectral Data | Technology Networks. Technol Networks.

39. Ren JL, Zhang AH, Kong L, Wang XJ. 2018. Advances in mass spectrometry-based metabolomics for investigation of metabolites. RSC Adv 8:22335–22350.

40. Mlynárik V. 2017. Introduction to nuclear magnetic resonance. Anal Biochem 529:4–9.

41. Emwas AH, Roy R, McKay RT, Tenori L, Saccenti E, Nagana Gowda GA, Raftery D, Alahmari F, Jaremko L, Jaremko M, Wishart DS. 2019. Nmr spectroscopy for metabolomics research. Metabolites 9:123.

42. De Roy K, Marzorati M, Van den Abbeele P, Van de Wiele T, Boon N. 2014. Synthetic microbial ecosystems: an exciting tool to understand and apply microbial communities. Environ Microbiol 16:1472–1481.

43. Heather JM, Chain B. 2016. The sequence of sequencers: The history of sequencing DNA. Genomics 107:1–8.

44. Patti GJ, Yanes O, Siuzdak G. 2012. Innovation: Metabolomics: the apogee of the omics trilogy. Nat Rev Mol Cell Biol 13:263–269.

45. Dolinšek J, Goldschmidt F, Johnson DR. 2016. Synthetic microbial ecology and the dynamic interplay between microbial genotypes. FEMS Microbiol Rev 40:961–979.

46. Venturelli OS, Carr A V, Fisher G, Hsu RH, Lau R, Bowen BP, Hromada S, Northen T, Arkin AP. 2018. Deciphering microbial interactions in synthetic human gut microbiome communities. Mol Syst Biol 14:e8157.

47. Kehe J, Kulesa A, Ortiz A, Ackerman CM, Thakku SG, Sellers D, Kuehn S, Gore J, Friedman J, Blainey PC. 2019. Massively parallel screening of synthetic microbial communities. Proc Natl Acad Sci U S A 116:12804–12809.

48. Enke TN, Datta MS, Schwartzman J, Cermak N, Schmitz D, Barrere J, Pascual-García A, Cordero OX. 2019. Modular Assembly of Polysaccharide-Degrading Marine Microbial Communities. Curr Biol 29:1528-1535.e6.

49. Goldford JE, Lu N, Bajić D, Estrela S, Tikhonov M, Sanchez-Gorostiaga A, Segrè D, Mehta P, Sanchez A. 2018. Emergent simplicity in microbial community assembly. Science (80-) 361:469–474.

50. Stasulli NM, Shank EA. 2016. Profiling the metabolic signals involved in chemical communication between microbes using imaging mass spectrometry. FEMS Microbiol Rev 40:807–813.

51. Moutinho TJ, Panagides JC, Biggs MB, Medlock GL, Kolling GL, Papin JA. 2017. Novel co-culture plate enables growth dynamic-based assessment of contact-independent microbial interactions. PLoS One 12:e0182163.

52. Bergkessel M, Basta DW, Newman DK. 2016. The physiology of growth arrest: Uniting molecular and environmental microbiology. Nat Rev Microbiol 14:549–562.

53. Navarro Llorens JM, Tormo A, Martínez-García E. 2010. Stationary phase in gram-negative bacteria. FEMS Microbiol Rev 34:476–495.

54. Schimel JP. 2018. Life in dry soils: Effects of drought on soil microbial communities and processes. Annu Rev Ecol Evol Syst 49:409–432.

55. Fetissov SO. 2017. Role of the gut microbiota in host appetite control: Bacterial growth to animal feeding behaviour. Nat Rev Endocrinol 13:11–25.

56. Ni BJ, Fang F, Rittmann BE, Yu HQ. 2009. Modeling microbial products in activated sludge under feast-famine conditions. Environ Sci Technol 43:2489–2497.

57. Tani TH, Khodursky A, Blumenthal RM, Brown PO, Matthews RG. 2002. Adaptation to famine: A family of stationary-phase genes revealed by microarray analysis. Proc Natl Acad Sci U S A 99:13471–13476.

58. Jaishankar J, Srivastava P. 2017. Molecular basis of stationary phase survival and applications. Front Microbiol 8:2000.

59. Gefen O, Fridman O, Ronin I, Balaban NQ. 2014. Direct observation of single stationary-phase bacteria reveals a surprisingly long period of constant protein production activity. Proc Natl Acad Sci U S A 111:556–561.

60. Link H, Fuhrer T, Gerosa L, Zamboni N, Sauer U. 2015. Real-time metabolome profiling of the metabolic switch between starvation and growth. Nat Methods 12:1091–1097.

61. Quince C, Walker AW, Simpson JT, Loman NJ, Segata N. 2017. Shotgun metagenomics, from sampling to analysis. Nat Biotechnol 35:833–844.

62. Wang Z, Gerstein M, Snyder M. 2009. RNA-Seq: A revolutionary tool for transcriptomics. Nat Rev Genet 10:57–63.

63. Timp W, Timp G. 2020. Beyond mass spectrometry, the next step in proteomics. Sci Adv 6:eaax8978.

64. Johnson CH, Ivanisevic J, Siuzdak G. 2016. Metabolomics: Beyond biomarkers and towards mechanisms. Nat Rev Mol Cell Biol 17:451–459.

65. Sánchez-Romero MA, Casadesús J. 2020. The bacterial epigenome. Nat Rev Microbiol 18:7–20.

66. Bar-Joseph Z, Gitter A, Simon I. 2012. Studying and modelling dynamic biological processes using time-series gene expression data. Nat Rev Genet 13:552–564.

67. Zampieri M, Sauer U. 2017. Metabolomics-driven understanding of genotype-phenotype relations in model organisms. Curr Opin Syst Biol 6:28–36.

68. Brunk E, George KW, Alonso-Gutierrez J, Thompson M, Baidoo E, Wang G, Petzold CJ, McCloskey D, Monk J, Yang L, O'Brien EJ, Batth TS, Martin HG, Feist A, Adams PD, Keasling JD, Palsson BO, Lee TS. 2016. Characterizing Strain Variation in Engineered E. coli Using a Multi-Omics-Based Workflow. Cell Syst 2:335–346.

69. Pinu FR, Beale DJ, Paten AM, Kouremenos K, Swarup S, Schirra HJ, Wishart D. 2019. Systems biology and multi-omics integration: Viewpoints from the metabolomics research community. Metabolites 9:76.

70. Cavill R, Jennen D, Kleinjans J, Briedé JJ. 2016. Transcriptomic and metabolomic data integration. Brief Bioinform 17:891–901.

71. Lenski RE. 2017. Experimental evolution and the dynamics of adaptation and genome evolution in microbial populations. ISME J 11:2181–2194.

72. Barrick JE, Lenski RE. 2013. Genome dynamics during experimental evolution. Nat Rev Genet 14:827–839.

73. Ventola CL. 2015. The antibiotic resistance crisis: causes and threats. P T J 40:277–83.

74. Walsh F. 2013. Investigating antibiotic resistance in non-clinical environments. Front Microbiol 4:19.

75. Granato ET, Meiller-Legrand TA, Foster KR. 2019. The Evolution and Ecology of Bacterial Warfare. Curr Biol 29:R521–R537.

76. Little AE, Robinson CJ, Peterson SB, Raffa KF, and Handelsman J. 2008. Rules of engagement: interspecies interactions that regulate microbial communities. *Annu Rev Microbiol* 62:375–401.

77. Damore JA and Gore J. 2012. Understanding microbial cooperation. *J Theor Biol* 299:31–41.

78. Andrade-Domínguez A, Salazar E, Del Carmen Vargas-Lagunas M, Kolter R, and Encarnación S. 2014. Eco-evolutionary feedbacks drive species interactions. *ISME J* 8:1041–1054.

79. Watve MG, Tickoo R, Jog MM, and Bhole BD. 2001. How many antibiotics are produced by the genus Streptomyces? *Arch Microbiol* 176:386–390.

80. Yang YL, Xu Y, Straight P, and Dorrestein PC. 2009. Translating metabolic exchange with imaging mass spectrometry. *Nat Chem Biol* 5:885–887.

81. Watrous JD and Dorrestein PC. 2011. Imaging mass spectrometry in microbiology. *Nat Rev Microbiol* 9:683–694.

82. Liu WT, Yang YL, Xu Y, Lamsa A, Haste NM, Yang JY, Ng J, Gonzalez D, Ellermeier CD, Straight PD, Pevzner PA, Pogliano J, Nizet V, Pogliano K, and Dorrestein PC. 2010. Imaging mass spectrometry of intraspecies metabolic exchange revealed the cannibalistic factors of *Bacillus subtilis*. *Proc Natl Acad Sci USA* 107:16286–16290.

83. Turnbaugh PJ and Gordon JI. 2008. An invitation to the marriage of metagenomics and metabolomics. *Cell* 134:708–713.

84. Schimel JP and Schaeffer SM. 2012. Microbial control over carbon cycling in soil. *Front Microbiol* 3:348.

85. Norman JS and Friesen ML. 2017. Complex N acquisition by soil diazotrophs: how the ability to release exoenzymes affects N fixation by terrestrial free-living diazotrophs. *ISME J* 11:315–326.

86. Grosskopf T and Soyer OS. 2014. Synthetic microbial communities. *Curr Opin Microbiol* 18:72–77.

87. Datta MS, Sliwerska E, Gore J, Polz MF, and Cordero OX. 2016. Microbial interactions lead to rapid micro-scale successions on model marine particles. *Nat Commun* 7:11965.

88. Lindemann SR, Mobberley JM, Cole JK, Markillie LM, Taylor RC, Huang E, Chrisler WB, Wiley HS, Lipton MS, Nelson WC, Fredrickson JK, and Romine MF. 2017. Predicting species-resolved macronutrient acquisition during succession in a model phototrophic biofilm using an integrated 'omics approach. *Front Microbiol* 8:1–15.

89. Kim HJ, Boedicker JQ, Choi JW, and Ismagilov RF. 2008. Defined spatial structure stabilizes a synthetic multispecies bacterial community. *Proc Natl Acad Sci USA* 105:18188–18193.

90. Klitgord N and Segrè D. 2010. Environments that induce synthetic microbial ecosystems. *PLoS Comput Biol* 6:e1001002.

91. Harcombe WR, Riehl WJ, Dukovski I, Granger BR, Betts A, Lang AH, Bonilla G, Kar A, Leiby N, Mehta P, Marx CJ, and Segrè D. 2014. Metabolic resource allocation in individual microbes determines ecosystem interactions and spatial dynamics. *Cell Rep* 7:1104–1115.

92. Shou W, Ram S, and Vilar JM. 2007. Synthetic cooperation in engineered yeast populations. *Proc Natl Acad Sci USA* 104:1877–1882.

93. Widder S, Allen RJ, Pfeiffer T, Curtis TP, Wiuf C, Sloan WT, Cordero OX, Brown SP, Momeni B, Shou W, Kettle H, Flint HJ, Haas AF, Laroche B, Kreft JU, Rainey PB, Freilich S, Schuster S, Milferstedt K, van der Meer JR, Groβkopf T, Huisman J, Free A, Picioreanu C, Quince C, Klapper I, Labarthe S, Smets BF, Wang H, Isaac Newton Institute Fellows, Soyer OS. 2016. Challenges in microbial ecology: building predictive understanding of community function and dynamics. *ISME J* 10:2557–2568.

94. Lindemann SR, Bernstein HC, Song HS, Fredrickson JK, Fields MW, Shou W, Johnson DR, and Beliaev AS. 2016. Engineering microbial consortia for controllable outputs. *ISME J* 10:2077–2084.

95. McClean KH, Winson MK, Fish L, Taylor A, Chhabra SR, Camara M, Daykin M, Lamb JH, Swift S, Bycroft BW, Stewart GS, and Williams P. 1997. Quorum sensing and *Chromobacterium violaceum*: exploitation of violacein production and inhibition for the detection of N-acylhomoserine lactones. *Microbiology* 143:3703–3711.

96. Smith CA, Want EJ, O'Maille G, Abagyan R, and Siuzdak G. 2006. XCMS: processing mass spectrometry data for metabolite profiling using nonlinear peak alignment, matching, and identification. *Anal Chem* 78:779–787.

97. Scheltema RA, Jankevics A, Jansen RC, Swertz MA, and Breitling R. 2011. PeakML/mzMatch: a file format, Java library, R library, and tool-chain for mass spectrometry data analysis. *Anal Chem* 83:2786–2793.

98. Peres-Neto PR and Jackson DA. 2001. How well do multivariate data sets match? The advantages of a Procrustean superimposition approach over the Mantel test. *Oecologia* 129:169–178.

99. Seyedsayamdost MR, Chandler JR, Blodgett JAV, Lima PS, Duerkop BA, Oinuma K-I, Greenberg EP, and Clardy J. 2010. Quorum-sensing-regulated bactobolin production by *Burkholderia thailandensis* E264. *Org Lett* 12:716–719.

100. Duerkop BA, Varga J, Chandler JR, Peterson SB, Herman JP, Churchill ME, Parsek MR, Nierman WC, and Greenberg EP. 2009. Quorum-sensing control of antibiotic synthesis in *Burkholderia thailandensis*. *J Bacteriol* 191:3909–3918.

101. Smith CA, O'Maille G, Want EJ, Qin C, Trauger SA, Brandon TR, Custodio DE, Abagyan R, and Siuzdak G. 2005. METLIN: a metabolite mass spectral database. *Ther Drug Monit* 27:747–751.

102. Knappe TA, Linne U, Zirah S, Rebuffat S, Xie X, and Marahiel MA. 2008. Isolation and structural characterization of capistruin, a lasso peptide predicted from the genome sequence of *Burkholderia thailandensis* E264. *J Am Chem Soc* 130:11446–11454.

103. Nadell CD, Drescher K, and Foster KR. 2016. Spatial structure, cooperation and competition in biofilms. *Nat Rev Microbiol* 14:589–600.

104. Mitri S, Clarke E, and Foster KR. 2016. Resource limitation drives spatial organization in microbial groups. *ISME J* 10:1471–1482.

105. Bomar L, Maltz M, Colston S, and Graf J. 2011. Directed culturing of microorganisms using metatranscriptomics. *mBio* 2:e00012-11.

106. Nichols D, Cahoon N, Trakhtenberg EM, Pham L, Mehta A, Belanger A, Kanigan T, Lewis K, and Epstein SS. 2010. Use of ichip for high-throughput in situ cultivation of "uncultivable" microbial species. *Appl Environ Microbiol* 76:2445–2450.

107. Maansson M, Vynne NG, Klitgaard A, Nybo JL, Melchiorsen J, Nguyen DD, Sanchez LM, Ziemert N, Dorrestein PC, Andersen MR, and Gram L. 2016. An integrated metabolomic and genomic mining workflow to uncover the biosynthetic potential of bacteria. *mSystems* 1:e00028-15.

108. Khandelwal RA, Olivier BG, Röling WFM, Teusink B, and Bruggeman FJ. 2013. Community flux balance analysis for microbial consortia at balanced growth. *PLoS One* 8:e64567.

109. Buckling A, Kassen R, Bell G, and Rainey PB. 2000. Disturbance and diversity in experimental microcosms. *Nature* 408:961–964.

110. Kassen R, Buckling A, Bell G, and Rainey PB. 2000. Diversity peaks at intermediate productivity in a laboratory microcosm. *Nature* 406:508–512.

111. Violle C, Pu Z, and Jiang L. 2010. Experimental demonstration of the importance of competition under disturbance. *Proc Natl Acad Sci USA* 107:12925–12929.

112. Peay KG, Belisle M, and Fukami T. 2012. Phylogenetic relatedness predicts priority effects in nectar yeast communities. *Proc Biol Sci* 279:749–758.

113. Lenski RE, Rose MR, Simpson SC, and Tadler SC. 1991. Long-term experimental evolution in *Escherichia coli*. I. Adaptation and divergence during. *Am Nat* 138:1315–1341.

114. Jessup CM, Forde SE, and Bohannan BJM. 2005. Microbial experimental systems in ecology. *Adv Ecol Res* 37:273–307.

115. Jessup CM, Kassen R, Forde SE, Kerr B, Buckling A, Rainey PB, and Bohannan BJ. 2004. Big questions, small worlds: microbial model systems in ecology. *Trends Ecol Evol* 19:189–197.

116. Untergasser A, Cutcutache I, Koressaar T, Ye J, Faircloth BC, Remm M, and Rozen SG. 2012. Primer3—new capabilities and interfaces. *Nucleic Acids Res* 40:e115.

117. Want EJ, Wilson ID, Gika H, Theodoridis G, Plumb RS, Shockcor J, Holmes E, and Nicholson JK. 2010. Global metabolic profiling procedures for urine using UPLC-MS. *Nat Protoc* 5:1005–1018.

118. Jankevics A, Merlo ME, de Vries M, Vonk RJ, Takano E, and Breitling R. 2012. Separating the wheat from the chaff: a prioritisation pipeline for the analysis of metabolomics datasets. *Metabolomics* 8:29–36.

119. Xia J, Sinelnikov IV, Han B, and Wishart DS. 2015. MetaboAnalyst 3.0—making metabolomics more meaningful. *Nucleic Acids Res* 43:W251–W257.

120. Dieterle F, Ross A, Schlotterbeck G, and Senn H. 2006. Probabilistic quotient normalization as robust method to account for dilution of complex biological mixtures. Application in ^{1}H NMR metabonomics. *Anal Chem* 78:4281–4290.

121. van den Berg RA, Hoefsloot HC, Westerhuis JA, Smilde AK, and van der Werf MJ. 2006. Centering, scaling, and transformations: improving the biological information content of metabolomics data. *BMC Genomics* 7:142.

122. Anderson MJ. 2001. A new method for non-parametric multivariate analysis of variance. *Aust Ecol* 26:32–46.

123. Oksanen J, Blanchet FG, Kindt R, Legendre P, Minchin PR, O'Hara RB, Simpson GL, Solymos P, Stevens MHH, and Wagner H. 2013. *Vegan: community ecology package. R package version 20-8:254*. http://CRAN.Rproject.org/package=vegan.

124. Benjamini Y and Hochberg Y. 1995. Controlling the false discovery rate: a practical and powerful approach to multiple testing. *J R Stat Soc B Stat Methodol* 57:289–300.

125. Wickham H. 2009, *ggplot2: elegant graphics for data analysis*. Springer, New York, NY.

126. Gika HG, Macpherson E, Theodoridis GA, and Wilson ID. 2008. Evaluation of the repeatability of ultra-performance liquid chromatography-TOF-MS for global metabolic profiling of human urine samples. *J Chromatogr B Analyt Technol Biomed Life Sci* 871:299–305.

127. Wells JS, Trejo WH, Principe PA, Bush K, Georgopapadakou N, Bonner DP, and Sykes RB. 1982. SQ 26,180, a novel monobactam. I. Taxonomy, fermentation and biological properties. *J Antibiot* 35:184–188.

128. Chernin LS, Winson MK, Thompson JM, Haran S, Bycroft BW, Chet I, Williams P, and Stewart GS. 1998. Chitinolytic activity in *Chromobacterium violaceum*: substrate analysis and regulation by quorum sensing. *J Bacteriol* 180:4435–4441.

129. Brett PJ, DeShazer D, and Woods DE. 1998. *Burkholderia thailandensis* sp. nov., a *Burkholderia pseudomallei*-like species. *Int J Syst Bacteriol* 48:317–320.

130. Buell CR, Joardar V, Lindeberg M, Selengut J, Paulsen IT, Gwinn ML, Dodson RJ, Deboy RT, Durkin AS, Kolonay JF, Madupu R, Daugherty S, Brinkac L, Beanan MJ, Haft DH, Nelson WC, Davidsen T, Zafar N, Zhou L, Liu J, Yuan Q, Khouri H, Fedorova N, Tran B, Russell D, Berry K, Utterback T, Van Aken SE, Feldblyum TV, D'Ascenzo M, Deng WL, Ramos AR, Alfano JR, Cartinhour S, Chatterjee AK, Delaney TP, Lazarowitz SG, Martin GB, Schneider DJ, Tang X, Bender CL, White O, Fraser CM, and Collmer A. 2003. The complete genome sequence of the Arabidopsis and tomato pathogen *Pseudomonas syringae* pv. tomato DC3000. *Proc Natl Acad Sci USA* 100:10181–10186.

131. Lewis DL, Gattie DK. 1991. Ecology of quiescent microbes. ASM News 57:27–32.

132. Cole JJ. 1999. Aquatic microbiology for ecosystem scientists: new and recycled paradigms in ecological microbiology. Ecosystems 2:215–225.

133. Blazewicz SJ, Barnard RL, Daly RA, Firestone MK. 2013. Evaluating rRNA as an indicator of microbial activity in environmental communities: limitations and uses. ISME J 7:2061–2068.

134. Göransson H, Godbold DL, Jones DL, Rousk J. 2013. Bacterial growth and respiration responses upon rewetting dry forest soils: impact of drought-legacy. Soil Biol Biochem 57:477–486.

135. Meisner A, Leizeaga A, Rousk J, Bååth E. 2017. Partial drying accelerates bacterial growth recovery to rewetting. Soil Biol Biochem 112:269–276.

136. Chiesa SC, Irvine RL, Manning JF. 1985. Feast/famine growth environments and activated sludge population selection. Biotechnol Bioeng 27:562–568.

137. Breton J, Tennoune N, Lucas N, Francois M, Legrand R, Jacquemot J, Goichon A, Guérin C, Peltier J, Pestel-Caron M, Chan P, Vaudry D, Do Rego JC, Liénard F, Pénicaud L, Fioramonti X, Ebenezer IS, Hökfelt T, Déchelotte P, Fetissov SO. 2016. Gut commensal E. coli proteins activate host satiety pathways following nutrient-induced bacterial growth. Cell Metab 23:324–334.

138. Kolter R, Siegele DA, Tormo A. 1993. The stationary phase of the bacterial life cycle. Annu Rev Microbiol 47:855–874.

139. De Nobili M, Contin M, Mondini C, Brookes PC. 2001. Soil microbial biomass is triggered into activity by trace amounts of substrate. Soil Biol Biochem 33:1163–1170.

140. Świeciło A, Zych-Wezyk I. 2013. Bacterial stress response as an adaptation to life in a soil environment. Pol J Environ Stud 22:1577–1587.

141. Lever MA, Rogers KL, Lloyd KG, Overmann J, Schink B, Thauer RK, Hoehler TM, Jørgensen BB. 2015. Life under extreme energy limitation: a synthesis of laboratory- and field-based investigations. FEMS Microbiol Rev 39:688–728.

142. Rinas U, Hellmuth K, Kang R, Seeger A, Schlieker H. 1995. Entry of Escherichia coli into stationary phase is indicated by endogenous and exogenous accumulation of nucleobases. Appl Environ Microbiol 61:4147–4151.

143. Brauer MJ, Yuan J, Bennett BD, Lu W, Kimball E, Botstein D, Rabinowitz JD. 2006. Conservation of the metabolomic response to starvation across two divergent microbes. Proc Natl Acad Sci U S A 103:19302–19307.

144. Pacheco AR, Moel M, Segrè D. 2019. Costless metabolic secretions as drivers of interspecies interactions in microbial ecosystems. Nat Commun 10:103.

145. Chandler JR, Heilmann S, Mittler JE, Greenberg EP. 2012. Acyl-homoserine lactone-dependent eavesdropping promotes competition in a laboratory co-culture model. ISME J 6:2219–2228.

146. Chodkowski JL, Shade A. 2017. A synthetic community system for probing microbial interactions driven by exometabolites. mSystems 2:e00129-17.

147. Jones AM, Lindow SE, Wildermuth MC. 2007. Salicylic acid, yersiniabactin, and pyoverdin production by the model phytopathogen Pseudomonas syringae pv. tomato DC3000: synthesis, regulation, and impact on tomato and Arabidopsis host plants. J Bacteriol 189:6773–6786.

148. Kothari V, Sharma S, Padia D. 2017. Recent research advances on Chromobacterium violaceum. Asian Pac J Trop Med 10:744–752.

149. Gude S, Pherribo GJ, Taga ME. 2020. Emergence of metabolite provisioning as a by-product of evolved biological functions. mSystems 5:e00259-20.

150. Schink SJ, Biselli E, Ammar C, Gerland U. 2019. Death rate of E. coli during starvation is set by maintenance cost and biomass recycling. Cell Syst 9:64–73.

151. Nyström T. 2004. Stationary-phase physiology. Annu Rev Microbiol 58:161–181.

152. Lewis RA, Bignell CR, Zeng W, Jones AC, Thomas CM. 2002. Chromosome loss from par mutants of Pseudomonas putida depends on growth medium and phase of growth. Microbiology 148:537–548.

153. Shimaya T, Okura R, Wakamoto Y, Takeuchi KA. 2020. Scale invariance during bacterial reductive division observed by an extensive microperfusion system. bioRxiv doi:10.1101/2020.06.25.171710.

154. Piir K, Paier A, Liiv A, Tenson T, Maiväli Ü. 2011. Ribosome degradation in growing bacteria. EMBO Rep 12:458–462.

155. Paczia N, Nilgen A, Lehmann T, Gätgens J, Wiechert W, Noack S. 2012. Extensive exometabolome analysis reveals extended overflow metabolism in various microorganisms. Microb Cell Fact 11:122.

156. Chandler JR, Truong TT, Silva PM, Seyedsayamdost MR, Carr G, Radey M, Jacobs MA, Sims EH, Clardy J, Greenberg EP. 2012. Bactobolin resistance is conferred by mutations in the L2 ribosomal protein. mBio 3:e00499-12.

157. Birch LC. 1957. The meanings of competition. Am Nat 91:5–18.

158. Miller RS. 1967. Pattern and process in competition. Adv Ecol Res 4:1–74.

159. Abe T, Kobayashi K, Kawamura S, Sakaguchi T, Shiiba K, Kobayashi M. 2019. Dipeptide synthesis by internal adenylation domains of a multidomain enzyme involved in nonribosomal peptide synthesis. J Gen Appl Microbiol 65:1–10.

160. Kano S, Suzuki S, Hara R, Kino K. 2019. Synthesis of d-amino acid-containing dipeptides using the adenylation domains of nonribosomal peptide synthetase. Appl Environ Microbiol 85:e00120-19.

161. Waters CM, Bassler BL. 2005. Quorum sensing: cell-to-cell communication in bacteria. Annu Rev Cell Dev Biol 21:319–346.

162. Blaženović I, Kind T, Sa MR, Ji J, Vaniya A, Wancewicz B, Roberts BS, Torbašinović H, Lee T, Mehta SS, Showalter MR, Song H, Kwok J, Jahn D, Kim J, Fiehn O. 2019. Structure annotation of all mass spectra in untargeted metabolomics. Anal Chem 91:2155–2162.

163. Goo E, Majerczyk CD, An JH, Chandler JR, Seo Y-S, Ham H, Lim JY, Kim H, Lee B, Jang MS, Greenberg EP, Hwang I. 2012. Bacterial quorum sensing, cooperativity, and anticipation of stationary-phase stress. Proc Natl Acad Sci U S A 109:19775–19780.

164. Goo E, Kang Y, Lim JY, Ham H, Hwang I. 2017. Lethal consequences of overcoming metabolic restrictions imposed on a cooperative bacterial population. mBio 8:e00042-17.

165. Sass AM, Schmerk C, Agnoli K, Norville PJ, Eberl L, Valvano MA, Mahenthiralingam E. 2013. The unexpected discovery of a novel low-oxygen-activated locus for the anoxic persistence of Burkholderia cenocepacia. ISME J 7:1568–1581.

166. Banerjee D, Raghunathan A. 2019. Constraints-based analysis identifies NAD+ recycling through metabolic reprogramming in antibiotic resistant Chromobacterium violaceum. PLoS One 14:e0210008.

167. Pluskal T, Castillo S, Villar-Briones A, Orešič M. 2010. MZmine 2: modular framework for processing, visualizing, and analyzing mass spectrometry-based molecular profile data. BMC Bioinformatics 11:395.

168. Chong J, Soufan O, Li C, Caraus I, Li S, Bourque G, Wishart DS, Xia J. 2018. MetaboAnalyst 4.0: towards more transparent and integrative metabolomics analysis. Nucleic Acids Res 46:W486–W494.

169. Schymanski EL, Jeon J, Gulde R, Fenner K, Ruff M, Singer HP, Hollender J. 2014. Identifying small molecules via high resolution mass spectrometry: communicating confidence. Environ Sci Technol 48:2097–2098.

170. Wang M, Carver JJ, Phelan VV, Sanchez LM, Garg N, Peng Y, Nguyen DD, Watrous J, Kapono CA, Luzzatto-Knaan T, Porto C, Bouslimani A, Melnik AV, Meehan MJ, Liu WT, Crüsemann M, Boudreau PD, Esquenazi E, Sandoval-Calderón M, Kersten RD, Pace LA, Quinn RA, Duncan KR, Hsu C-C, Floros DJ, Gavilan RG, Kleigrewe K, Northen T, Dutton RJ, Parrot D, Carlson EE, Aigle B, Michelsen CF, Jelsbak L, Sohlenkamp C, Pevzner P, Edlund

A, McLean J, Piel J, Murphy BT, Gerwick L, Liaw CC, Yang YL, Humpf HU, Maansson M, Keyzers RA, Sims AC, Johnson AR, Sidebottom AM, Sedio BE, et al. 2016. Sharing and community curation of mass spectrometry data with Global Natural Products Social Molecular Networking. Nat Biotechnol 34:828–837.

171. Bushnell B. 2015. BBMap (version 37.75). https://sourceforge.net/projects/bbmap/.

172. Bray NL, Pimentel H, Melsted P, Pachter L. 2016. Near-optimal probabilistic RNA-seq quantification. Nat Biotechnol 34:525–527.

173. Love MI, Huber W, Anders S. 2014. Moderated estimation of fold change and dispersion for RNA-seq data with DESeq2. Genome Biol 15:550.

174. Bullard JH, Purdom E, Hansen KD, Dudoit S. 2010. Evaluation of statistical methods for normalization and differential expression in mRNA-Seq experiments. BMC Bioinformatics 11:94.

175. Raithel S, Johnson L, Galliart M, Brown S, Shelton J, Herndon N, Bello NM. 2016. Inferential considerations for low-count RNA-seq transcripts: a case study on the dominant prairie grass Andropogon gerardii. BMC Genomics 17:140.

176. Elbourne LDH, Tetu SG, Hassan KA, Paulsen IT. 2017. TransportDB 2.0: a database for exploring membrane transporters in sequenced genomes from all domains of life. Nucleic Acids Res 45:D320–D324.

177. Blin K, Shaw S, Steinke K, Villebro R, Ziemert N, Lee SY, Medema MH, Weber T. 2019. AntiSMASH 5.0: updates to the secondary metabolite genome mining pipeline. Nucleic Acids Res 47:W81–W87.

178. Oksanen J, Blanchet FG, Friendly M, Kindt R, Legendre P, McGlinn D, Minchin PR, O'Hara RB, Simpson GL, Solymos P, Stevens MHH, Szoecs E, Wagner H. 2019. vegan: community ecology package. R package version 2.5-4.

179. Chen H. 2018. VennDiagram: generate high-resolution Venn and Euler plots. R package version 1.6.20.

180. Herve M. 2020. RVAideMemoire: testing and plotting procedures for biostatistics. R Package version 09-77.

181. Pedersen TL. 2020. patchwork: the composer of plots.

182. Luo W, Brouwer C. 2013. Pathview: an R/Bioconductor package for pathway-based data integration and visualization. Bioinformatics 29:1830–1831.

183. Tenenbaum D. 2018. KEGGREST: client-side REST access to KEGG. R package version 1.22.0.

184. Wickham H. 2019. stringr: simple, consistent wrappers for common string operations. R package version 1.4.0.

185. Wickham H, François R, Henry L, Müller K. 2019. dplyr: a grammar of data manipulation. R package version 0.8.3.

186. Wickham H. 2011. The split-apply-combine strategy for data analysis. J Stat Softw 40:1–29.

187. Wickham H. 2007. Reshaping data with the reshape package. J Stat Softw 21:1–20.

188. Nordberg H, Cantor M, Dusheyko S, Hua S, Poliakov A, Shabalov I, Smirnova T, Grigoriev IV, Dubchak I. 2014. The genome portal of the Department of Energy Joint Genome Institute: 2014 updates. Nucleic Acids Res 42:D26–D31.

189. Stock AM, Robinson VL, Goudreau PN. 2000. Two-component signal transduction. Annu Rev Biochem 69:183–215.

190. Browning DF, Busby SJW. 2004. The regulation of bacterial transcription initiation. Nat Rev Microbiol 2:57–65.

191. Pietschke C, Treitz C, Forêt S, Schultze A, Künzel S, Tholey A, Bosch TCG, Fraune S. 2017. Host modification of a bacterial quorum-sensing signal induces a phenotypic switch in bacterial symbionts. Proc Natl Acad Sci U S A 114:E8488–E8497.

192. Garren M, Son K, Tout J, Seymour JR, Stocker R. 2016. Temperature-induced behavioral switches in a bacterial coral pathogen. ISME J 10:1363–1372.

193. Kato S, Haruta S, Cui ZJ, Ishii M, Igarashi Y. 2005. Stable coexistence of five bacterial strains as a cellulose-degrading community. Appl Environ Microbiol 71:7099–7106.

194. Steinweg J, Dukes JS, Paul EA, Wallenstein MD. 2013. Microbial responses to multi-factor climate change: Effects on soil enzymes. Front Microbiol 4:146.

195. Ma B, Wang Y, Ye S, Liu S, Stirling E, Gilbert JA, Faust K, Knight R, Jansson JK, Cardona C, Röttjers L, Xu J. 2020. Earth microbial co-occurrence network reveals interconnection pattern across microbiomes. Microbiome 8:1–12.

196. Gilbert JA, Steele JA, Caporaso JG, Steinbrück L, Reeder J, Temperton B, Huse S, McHardy AC, Knight R, Joint I, Somerfield P, Fuhrman JA, Field D. 2012. Defining seasonal marine microbial community dynamics. ISME J 6:298–308.

197. Aziz FAA, Suzuki K, Ohtaki A, Sagegami K, Hirai H, Seno J, Mizuno N, Inuzuka Y, Saito Y, Tashiro Y, Hiraishi A, Futamata H. 2015. Interspecies interactions are an integral determinant of microbial community dynamics. Front Microbiol 6:1148.

198. Orr JA, Vinebrooke RD, Jackson MC, Kroeker KJ, Kordas RL, Mantyka-Pringle C, van den Brink PJ, de Laender F, Stoks R, Holmstrup M, Matthaei CD, Monk WA, Penk MR, Leuzinger S, Schäfer RB, Piggott JJ. 2020. Towards a unified study of multiple stressors: Divisions and common goals across research disciplines. Proc R Soc B Biol Sci 287:20200421.

199. Foster KR, Bell T. 2012. Competition, not cooperation, dominates interactions among culturable microbial species. Curr Biol 22:1845–1850.

200. Coyte KZ, Schluter J, Foster KR. 2015. The ecology of the microbiome: Networks, competition, and stability. Science 350:663–666.

201. Tilman D. 1982. Resource Competition and Community Structure. Princeton University Press, Princeton, NJ, U.S.A.

202. Stewart FM, Levin BR. 1973. Partitioning of Resources and the Outcome of Interspecific Competition: A Model and Some General Considerations. Am Nat 107:171–198.

203. Smith HL. 2011. Bacterial competition in serial transfer culture. Math Biosci 229:149–159.

204. Pekkonen M, Korhonen J, Laakso JT. 2011. Increased survival during famine improves fitness of bacteria in a pulsed-resource environment. Evol Ecol Res 13:1–18.

205. Holt RD. 2008. Theoretical perspectives on resource pulses. Ecology 89:671–681.

206. Hiltunen T, Laakso J, Kaitala V, Suomalainen LR, Pekkonen M. 2008. Temporal variability in detritus resource maintains diversity of bacterial communities. Acta Oecologica 33:291–299.

207. Čihák M, Kameník Z, Šmídová K, Bergman N, Benada O, Kofronová O, Petrícková K, Bobek J. 2017. Secondary metabolites produced during the germination of Streptomyces coelicolor. Front Microbiol 8:2495.

208. Okada BK, Seyedsayamdost MR. 2017. Antibiotic dialogues: Induction of silent biosynthetic gene clusters by exogenous small molecules. FEMS Microbiol Rev 41:19–33.

209. Goh EB, Yim G, Tsui W, McClure JA, Surette MG, Davies J. 2002. Transcriptional modulation of bacterial gene expression by subinhibitory concentrations of antibiotics. Proc Natl Acad Sci U S A 99:17025–17030.

210. Chodkowski JL, Shade A. 2020. Exometabolite Dynamics over Stationary Phase Reveal Strain-Specific Responses. mSystems 5:e00493-20.

211. Fischer DS, Theis FJ, Yosef N. 2018. Impulse model-based differential expression analysis of time course sequencing data. Nucleic Acids Res 46:119.

212. Maere S, Heymans K, Kuiper M. 2005. BiNGO: a Cytoscape plugin to assess overrepresentation of gene ontology categories in biological networks. Bioinformatics 21:3448–3449.

213. Blin K, Shaw S, Kloosterman AM, Charlop-Powers Z, van Wezel GP, Medema MH, Weber T. 2021. antiSMASH 6.0: improving cluster detection and comparison capabilities. Nucleic Acids Res 49:W29–W35.

214. Kautsar SA, Blin K, Shaw S, Navarro-Muñoz JC, Terlouw BR, van der Hooft JJJ, van Santen JA, Tracanna V, Suarez Duran HG, Pascal Andreu V, Selem-Mojica N, Alanjary M, Robinson SL, Lund G, Epstein SC, Sisto AC, Charkoudian LK, Collemare J, Linington RG, Weber T, Medema MH. 2020. MIBiG 2.0: a repository for biosynthetic gene clusters of known function. Nucleic Acids Res 48:D454–D458.

215. Faith JJ, Hayete B, Thaden JT, Mogno I, Wierzbowski J, Cottarel G, Kasif S, Collins JJ, Gardner TS. 2007. Large-scale mapping and validation of Escherichia coli transcriptional regulation from a compendium of expression profiles. PLoS Biol 5:e8.

216. Meyer PE, Lafitte F, Bontempi G. 2008. Minet: A r/bioconductor package for inferring large transcriptional networks using mutual information. BMC Bioinformatics 9:461.

217. McClure RS, Overall CC, Mcdermott JE, Hill EA, Markillie LM, Mccue LA, Taylor RC, Ludwig M, Bryant DA, Beliaev AS. 2016. Network analysis of transcriptomics expands regulatory landscapes in Synechococcus sp. PCC 7002. Nucleic Acids Res 44:8810–8825.

218. Shannon P, Markiel A, Ozier O, Baliga NS, Wang JT, Ramage D, Amin N, Schwikowski B, Ideker T. 2003. Cytoscape: A software Environment for integrated models of biomolecular interaction networks. Genome Res 13:2498–2504.

219. Götz S, García-Gómez JM, Terol J, Williams TD, Nagaraj SH, Nueda MJ, Robles M, Talón M, Dopazo J, Conesa A. 2008. High-throughput functional annotation and data mining with the Blast2GO suite. Nucleic Acids Res 36:3420–3435.

220. Zdobnov EM, Apweiler R. 2001. InterProScan - An integration platform for the signature-recognition methods in InterPro. Bioinformatics 17:847–848.

221. Pang Z, Chong J, Zhou G, de Lima Morais DA, Chang L, Barrette M, Gauthier C, Jacques P-É, Li S, Xia J. 2021. MetaboAnalyst 5.0: narrowing the gap between raw spectra and functional insights. Nucleic Acids Res gkab382.

222. Wickham H. 2016. ggplot2: Elegant Graphics for Data Analysis. Springer-Verlag New York.

223. Lawrence M, Gentleman R, Carey V. 2009. rtracklayer: An R package for interfacing with genome browsers. Bioinformatics 25:1841–1842.

224. Garnier S, Ross N, Rudis R, Camargo PA, Sciaini M, Scherer C. 2021. viridis - Colorblind-Friendly Color Maps for R R package:https://sjmgarnier.github.io/viridis/.

225. Wickham H, Averick M, Bryan J, Chang W, McGowan L, François R, Grolemund G, Hayes A, Henry L, Hester J, Kuhn M, Pedersen T, Miller E, Bache S, Müller K, Ooms J, Robinson D, Seidel D, Spinu V, Takahashi K, Vaughan D, Wilke C, Woo K, Yutani H. 2019. Welcome to the Tidyverse. J Open Source Softw 4:1686.

226. Nordberg H, Cantor M, Dusheyko S, Hua S, Poliakov A, Shabalov I, Smirnova T, Grigoriev I V., Dubchak I. 2014. The genome portal of the Department of Energy Joint Genome Institute: 2014 updates. Nucleic Acids Res 42:D26-31.

227. Amunts A, Fiedorczuk K, Truong TT, Chandler J, Peter Greenberg E, Ramakrishnan V. 2015. Bactobolin A binds to a site on the 70S ribosome distinct from previously seen antibiotics. J Mol Biol 427:753–755.

228. Kuznedelov K, Semenova E, Knappe TA, Mukhamedyarov D, Srivastava A, Chatterjee S, Ebright RH, Marahiel MA, Severinov K. 2011. The antibacterial threaded-lasso peptide capistruin inhibits bacterial RNA polymerase. J Mol Biol 412:842–848.

229. Wozniak CE, Lin Z, Schmidt EW, Hughes KT, Liou TG. 2018. Thailandamide, a fatty acid synthesis antibiotic that is coexpressed with a resistant target gene. Antimicrob Agents Chemother 62:e00463-18.

230. Biggins JB, Ternei MA, Brady SF. 2012. Malleilactone, a polyketide synthase-derived virulence factor encoded by the cryptic secondary metabolome of Burkholderia pseudomallei group pathogens. J Am Chem Soc 134:13192–13195.

231. Butt AT, Thomas MS. 2017. Iron acquisition mechanisms and their role in the virulence of Burkholderia species. Front Cell Infect Microbiol 7:460.

232. Dubeau D, Déziel E, Woods DE, Lépine F. 2009. Burkholderia thailandensis harbors two identical rhl gene clusters responsible for the biosynthesis of rhamnolipids. BMC Microbiol 9:1–12.

233. Ghoul M, Mitri S. 2016. The Ecology and Evolution of Microbial Competition. Trends Microbiol 24:833–845.

234. Sanchez-Gorostiaga A, Bajić D, Osborne ML, Poyatos JF, Sanchez A. 2019. High-order interactions distort the functional landscape of microbial consortia. PLoS Biol 17:e3000550.

235. Mickalide H, Kuehn S. 2019. Higher-Order Interaction between Species Inhibits Bacterial Invasion of a Phototroph-Predator Microbial Community. Cell Syst 9:521-533.e10.

236. D'hoe K, Vet S, Faust K, Moens F, Falony G, Gonze D, Lloréns-Rico V, Gelens L, Danckaert J, De Vuyst L, Raes J. 2018. Integrated culturing, modeling and transcriptomics uncovers complex interactions and emergent behavior in a three-species synthetic gut community. Elife 7:e37090.

237. Momeni B, Xie L, Shou W. 2017. Lotka-Volterra pairwise modeling fails to capture diverse pairwise microbial interactions. Elife 6:e25051.

238. Pacheco AR, Osborne ML, Segrè D. 2021. Non-additive microbial community responses to environmental complexity. Nat Commun 12:1–11.

239. Estrela S, Sanchez-Gorostiaga A, Vila JCC, Sanchez A. 2021. Nutrient dominance governs the assembly of microbial communities in mixed nutrient environments. Elife 10:e65948.

240. Ortiz A, Vega NM, Ratzke C, Gore J. 2021. Interspecies bacterial competition regulates community assembly in the C. elegans intestine. ISME J 1–15.

241. Evans KC, Benomar S, Camuy-Vélez LA, Nasseri EB, Wang X, Neuenswander B, Chandler JR. 2018. Quorum-sensing control of antibiotic resistance stabilizes cooperation in Chromobacterium violaceum. ISME J 12:1263–1272.

242. Pettit RK. 2009. Mixed fermentation for natural product drug discovery. Appl Microbiol Biotechnol 83:19–25.

243. Netzker T, Fischer J, Weber J, Mattern DJ, König CC, Valiante V, Schroeckh V, Brakhage AA. 2015. Microbial communication leading to the activation of silent fungal secondary metabolite gene clusters. Front Microbiol. Frontiers Media S.A.

244. Zhu H, Sandiford SK, Van Wezel GP. 2014. Triggers and cues that activate antibiotic production by actinomycetes. J Ind Microbiol Biotechnol 41:371–386.

245. Truong TT, Seyedsayamdost M, Greenberg EP, Chandler JR. 2015. A Burkholderia thailandensis acyl-homoserine lactone-independent orphan LuxR homolog that activates production of the cytotoxin malleilactone. J Bacteriol 197:3456–3462.

246. Alice AF, López CS, Lowe CA, Ledesma MA, Crosa JH. 2006. Genetic and transcriptional analysis of the siderophore malleobactin biosynthesis and transport genes in the human pathogen Burkholderia pseudomallei K96243. J Bacteriol 188:1551–1566.

247. Gupta A, Bedre R, Thapa SS, Sabrin A, Wang G, Dassanayake M, Grove A. 2017. Global Awakening of Cryptic Biosynthetic Gene Clusters in Burkholderia thailandensis. ACS Chem Biol 12:3012–3021.

248. Ishida K, Lincke T, Behnken S, Hertweck C. 2010. Induced biosynthesis of cryptic polyketide metabolites in a Burkholderia thailandensis quorum sensing mutant. J Am Chem Soc 132:13966–13968.

249. Mao D, Bushin LB, Moon K, Wu Y, Seyedsayamdost MR. 2017. Discovery of scmR as a global regulator of secondary metabolism and virulence in Burkholderia thailandensis E264. Proc Natl Acad Sci U S A 114:E2920–E2928.

250. Okada BK, Wu Y, Mao D, Bushin LB, Seyedsayamdost MR. 2016. Mapping the Trimethoprim-Induced Secondary Metabolome of Burkholderia thailandensis. ACS Chem Biol 11:2124–2130.

251. Li A, Mao D, Yoshimura A, Rosen PC, Martin WL, Gallant É, Wühr M, Seyedsayamdost MR. 2020. Multi-omic analyses provide links between low-dose antibiotic treatment and induction of secondary metabolism in Burkholderia thailandensis. MBio 11:e03210-19.

252. McClure RS. 2019. Toward a Better Understanding of Species Interactions through Network Biology. mSystems 4:e00114-19.

253. McClure RS, Overall CC, Hill EA, Song H-S, Charania M, Bernstein HC, McDermott JE, Beliaev AS. 2018. Species-specific transcriptomic network inference of interspecies interactions. ISME J 12:2011–2023.

254. Karas VO, Westerlaken I, Meyer AS. 2015. The DNA-binding protein from starved cells (Dps) utilizes dual functions to defend cells against multiple stresses. J Bacteriol 197:3206–3215.

255. Nair S, Finkel SE. 2004. Dps protects cells against multiple stresses during stationary phase. J Bacteriol 186:4192–4198.

256. Antwis RE, Griffiths SM, Harrison XA, Aranega-Bou P, Arce A, Bettridge AS, Brailsford FL, de Menezes A, Devaynes A, Forbes KM, Fry EL, Goodhead I, Haskell E, Heys C, James C, Johnston SR, Lewis GR, Lewis Z, Macey MC, McCarthy A, McDonald JE, Mejia-Florez NL, O'Brien D, Orland C, Pautasso M, Reid WDK, Robinson HA, Wilson K, Sutherland WJ. 2017. Fifty important research questions in microbial ecology. FEMS Microbiol Ecol 93:fix044.

257. Konopka A. 2009. What is microbial community ecology. ISME J 3:1223–1230.

258. Cornforth DM, Popat R, McNally L, Gurney J, Scott-Phillips TC, Ivens A, Diggle SP, Brown SP. 2014. Combinatorial quorum sensing allows bacteria to resolve their social and physical environment. Proc Natl Acad Sci U S A 111:4280–4284.

259. Bundy BM, Collier LS, Hoover TR, Neidle EL. 2002. Synergistic transcriptional activation by one regulatory protein in response to two metabolites. Proc Natl Acad Sci U S A 99:7693–7698.

260. Morin M, Pierce EC, Dutton RJ. 2018. Changes in the genetic requirements for microbial interactions with increasing community complexity. Elife 7:e37072.

261. Billick I, Case TJ. 1994. Higher order interactions in ecological communities: What are they and how can they be detected? Ecology 75:1529–1543.

262. Bernier SP, Surette MG. 2013. Concentration-dependent activity of antibiotics in natural environments. Front Microbiol. 4:20.

263. Miller TE, Burns JH, Munguia P, Walters EL, Kneitel JM, Richards PM, Mouquet N, Buckley HL. 2005. A critical review of twenty years' use of the resource-ratio theory. Am Nat 165:439–448.

264. De Jong H, Casagranda S, Giordano N, Cinquemani E, Ropers D, Geiselmann J, Gouzé JL. 2017. Mathematical modelling of microbes: Metabolism, gene expression and growth. J R Soc Interface 14:20170502.

265. Jõers A, Liske E, Tenson T. 2020. Dividing subpopulation of Escherichia coli in stationary phase. Res Microbiol 171:153–157.

266. McCall IC, Shah N, Govindan A, Baquero F, Levin BR. 2019. Antibiotic killing of diversely generated populations of nonreplicating bacteria. Antimicrob Agents Chemother 63:e02360-18.

267. Dolinšek J, Goldschmidt F, Johnson DR. 2016. Synthetic microbial ecology and the dynamic interplay between microbial genotypes. FEMS Microbiol Rev 40:961–979.

268. Cairns J, Jokela R, Hultman J, Tamminen M, Virta M, Hiltunen T. 2018. Construction and characterization of synthetic bacterial community for experimental ecology and evolution. Front Genet 9:312.

269. D'Costa VM, McGrann KM, Hughes DW, Wright GD. 2006. Sampling the antibiotic resistome. Science 311:374–377.

270. Waglechner N, McArthur AG, Wright GD. 2019. Phylogenetic reconciliation reveals the natural history of glycopeptide antibiotic biosynthesis and resistance. Nat Microbiol 4:1862–1871.

271. Walsh F. 2013. Investigating antibiotic resistance in non-clinical environments. Front Microbiol 4:19.

272. van der Meij A, Worsley SF, Hutchings MI, van Wezel GP. 2017. Chemical ecology of antibiotic production by actinomycetes. FEMS Microbiol Rev 41:392–416.

273. Baral B, Akhgari A, Metsä-Ketelä M. 2018. Activation of microbial secondary metabolic pathways: Avenues and challenges. Synth Syst Biotechnol 3:163–178.

274. Cornforth DM, Foster KR. 2015. Antibiotics and the art of bacterial war. Proc Natl Acad Sci U S A 112:10827–10828.

275. Andersson DI, Hughes D. 2014. Microbiological effects of sublethal levels of antibiotics. Nat Rev Microbiol 12:465–478.

276. Du D, Wang Z, James NR, Voss JE, Klimont E, Ohene-Agyei T, Venter H, Chiu W, Luisi BF. 2014. Structure of the AcrAB-TolC multidrug efflux pump. Nature 509:512–515.

277. Frimodt-Møller J, Løbner-Olesen A. 2019. Efflux-Pump Upregulation: From Tolerance to High-level Antibiotic Resistance? Trends Microbiol 27:291–293.

278. Ebbensgaard AE, Løbner-Olesen A, Frimodt-Møller J. 2020. The role of efflux pumps in the transition from low-level to clinical antibiotic resistance. Antibiotics 9:1–7.

279. Rueden CT, Schindelin J, Hiner MC, DeZonia BE, Walter AE, Arena ET, Eliceiri KW. 2017. ImageJ2: ImageJ for the next generation of scientific image data. BMC Bioinformatics 18:529.

280. Schneider CA, Rasband WS, Eliceiri KW. 2012. NIH Image to ImageJ: 25 years of image analysis. Nat Methods.

281. Deatherage DE, Barrick JE. 2014. Identification of mutations in laboratory-evolved microbes from next-generation sequencing data using breseq. Methods Mol Biol 1151:165–188.

282. Waterhouse A, Bertoni M, Bienert S, Studer G, Tauriello G, Gumienny R, Heer FT, De Beer TAP, Rempfer C, Bordoli L, Lepore R, Schwede T. 2018. SWISS-MODEL: Homology modelling of protein structures and complexes. Nucleic Acids Res 46:W296–W303.

283. Guex N, Peitsch MC. 1997. SWISS-MODEL and the Swiss-PdbViewer: An environment for comparative protein modeling. Electrophoresis 18:2714–2723.

284. Zhu Y, Thomas F, Larocque R, Li N, Duffieux D, Cladière L, Souchaud F, Michel G, McBride MJ. 2017. Genetic analyses unravel the crucial role of a horizontally acquired alginate lyase for brown algal biomass degradation by Zobellia galactanivorans. Environ Microbiol 19:2164–2181.

285. Rhodes RG, Pucker HG, McBride MJ. 2011. Development and use of a gene deletion strategy for Flavobacterium johnsoniae to identify the redundant gliding motility genes remF, remG, remH, and remI. J Bacteriol 193:2418–2428.

286. Di Tommaso P, Moretti S, Xenarios I, Orobitg M, Montanyola A, Chang JM, Taly JF, Notredame C. 2011. T-Coffee: A web server for the multiple sequence alignment of protein and RNA sequences using structural information and homology extension. Nucleic Acids Res 39:W13-7.

287. Gallagher LA, Ramage E, Patrapuvich R, Weiss E, Brittnacher M, Manoil C. 2013. Sequence-defined transposon mutant library of Burkholderia thailandensis. MBio 4:e00604-13.

288. Aparna V, Dineshkumar K, Mohanalakshmi N, Velmurugan D, Hopper W. 2014. Identification of natural compound inhibitors for multidrug efflux pumps of Escherichia coli and Pseudomonas aeruginosa using In Silico high-throughput virtual screening and In Vitro validation. PLoS One 9:e101840.

289. Bolivar F, Backman K. 1979. Plasmids of Escherichia coli as cloning vectors. Methods Enzymol 68:245–267.

290. Figurski DH, Helinski DR. 1979. Replication of an origin-containing derivative of plasmid RK2 dependent on a plasmid function provided in trans. Proc Natl Acad Sci U S A 76:1648–1652.

291. McBride MJ, Xie G, Martens EC, Lapidus A, Henrissat B, Rhodes RG, Goltsman E, Wang W, Xu J, Hunnicutt DW, Staroscik AM, Hoover TR, Cheng YQ, Stein JL. 2009. Novel features of the polysaccharide-digesting gliding bacterium Flavobacterium johnsoniae as revealed by genome sequence analysis. Appl Environ Microbiol 75:6864–6875.

292. Wu Y, Seyedsayamdost MR. 2018. The Polyene Natural Product Thailandamide A Inhibits Fatty Acid Biosynthesis in Gram-Positive and Gram-Negative Bacteria. Biochemistry 57:4247–4251.

293. Sandoval-Motta S, Aldana M. 2016. Adaptive resistance to antibiotics in bacteria: A systems biology perspective. Wiley Interdiscip Rev Syst Biol Med 8:253–267.

294. Frimodt-Møller J, Rossi E, Haagensen JAJ, Falcone M, Molin S, Johansen HK. 2018. Mutations causing low level antibiotic resistance ensure bacterial survival in antibiotic-treated hosts. Sci Rep 8:1–13.

295. Zhang Q, Lambert G, Liao D, Kim H, Robin K, Tung CK, Pourmand N, Austin RH. 2011. Acceleration of emergence of bacterial antibiotic resistance in connected microenvironments. Science 333:1764–1767.

296. Baym M, Lieberman TD, Kelsic ED, Chait R, Gross R, Yelin I, Kishony R. 2016. Spatiotemporal microbial evolution on antibiotic landscapes. Science 353:1147–1151.

297. Hermsen R, Hwa T. 2010. Sources and sinks: A stochastic model of evolution in heterogeneous environments. Phys Rev Lett 105:248104.

298. Hermsen R, Deris JB, Hwa T. 2012. On the rapidity of antibiotic resistance evolution facilitated by a concentration gradient. Proc Natl Acad Sci U S A 109:10775–10780.

299. Kong D, Masker W. 1994. Deletion between direct repeats in T7 DNA stimulated by double-strand breaks. J Bacteriol 176:5904–5911.

300. Bzymek M, Lovett ST. 2001. Instability of repetitive DNA sequences: The role of replication in multiple mechanisms. Proc Natl Acad Sci U S A 98:8319–8325.

301. Du D, Wang-Kan X, Neuberger A, van Veen HW, Pos KM, Piddock LJV, Luisi BF. 2018. Multidrug efflux pumps: structure, function and regulation. Nat Rev Microbiol 16:523–539.

302. Bavro VN, Pietras Z, Furnham N, Pérez-Cano L, Fernández-Recio J, Pei XY, Misra R, Luisi B. 2008. Assembly and Channel Opening in a Bacterial Drug Efflux Machine. Mol Cell 30:114–121.

303. Pei XY, Hinchliffe P, Symmons MF, Koronakis E, Benz R, Hughes C, Koronakis V. 2011. Structures of sequential open states in a symmetrical opening transition of the TolC exit duct. Proc Natl Acad Sci U S A 108:2112–2117.

304. Krishnamoorthy G, Tikhonova EB, Dhamdhere G, Zgurskaya HI. 2013. On the role of TolC in multidrug efflux: The function and assembly of AcrAB-TolC tolerate significant depletion of intracellular TolC protein. Mol Microbiol 87:982–997.

305. Cuthbertson L, Nodwell JR. 2013. The TetR Family of Regulators. Microbiol Mol Biol Rev 77:440–475.

306. Colclough AL, Scadden J, Blair JMA. 2019. TetR-family transcription factors in Gram-negative bacteria: Conservation, variation and implications for efflux-mediated antimicrobial resistance. BMC Genomics 20:1–12.

307. Yoneyama H, Nakae T. 1993. Mechanism of efficient elimination of protein D2 in outer membrane of imipenem-resistant Pseudomonas aeruginosa. Antimicrob Agents Chemother 37:2385–2390.

308. Castañeda-García A, Rodríguez-Rojas A, Guelfo JR, Blázquez J. 2009. The glycerol-3-phosphate permease GlpT is the only fosfomycin transporter in Pseudomonas aeruginosa. J Bacteriol 191:6968–6974.

309. Bernier SP, Surette MG. 2013. Concentration-dependent activity of antibiotics in natural environments. Front Microbiol 4:20.

310. Andersson DI, Hughes D. 2012. Evolution of antibiotic resistance at non-lethal drug concentrations. Drug Resist Updat 15:162–172.

311. Rutledge PJ, Challis GL. 2015. Discovery of microbial natural products by activation of silent biosynthetic gene clusters. Nat Rev Microbiol 13:509–523.

312. Mungan MD, Alanjary M, Blin K, Weber T, Medema MH, Ziemert N. 2020. ARTS 2.0: Feature updates and expansion of the Antibiotic Resistant Target Seeker for comparative genome mining. Nucleic Acids Res 48:W546–W552.

313. Dawkins R, Krebs JR. 1979. Arms races between and within species. Proc R Soc London - Biol Sci 205:489–511.

314. Tomm HA, Ucciferri L, Ross AC. 2019. Advances in microbial culturing conditions to activate silent biosynthetic gene clusters for novel metabolite production. J Ind Microbiol Biotechnol 46:1381–1400.

315. Mao D, Yoshimura A, Wang R, Seyedsayamdost MR. 2020. Reporter-Guided Transposon Mutant Selection for Activation of Silent Gene Clusters in Burkholderia thailandensis. ChemBioChem 21:1826–1831.

316. Free A, McDonald MA, Pagaling E. 2018. Diversity-Function Relationships in Natural, Applied, and Engineered Microbial Ecosystems. Adv Appl Microbiol 105:131–189.

317. Jackson CR, Tyler HL, Millar JJ. 2013. Determination of microbial extracellular enzyme activity in waters, soils, and sediments using high throughput microplate assays. J Vis Exp 50399.

318. Gross N, Bagousse-Pinguet Y Le, Liancourt P, Berdugo M, Gotelli NJ, Maestre FT. 2017. Functional trait diversity maximizes ecosystem multifunctionality. Nat Ecol Evol 1:132.

319. Gilbert JA, Henry C. 2015. Predicting ecosystem emergent properties at multiple scales. Environ Microbiol Rep 7:20–22.

320. Shade A, Peter H, Allison SD, Baho DL, Berga M, Bürgmann H, Huber DH, Langenheder S, Lennon JT, Martiny JBH, Matulich KL, Schmidt TM, Handelsman J. 2012. Fundamentals of microbial community resistance and resilience. Front Microbiol 3:417.

321. Tognon M, Köhler T, Gdaniec BG, Hao Y, Lam JS, Beaume M, Luscher A, Buckling A, Van Delden C. 2017. Co-evolution with Staphylococcus aureus leads to lipopolysaccharide alterations in Pseudomonas aeruginosa. ISME J 11:2233–2243.

322. Brockhurst MA, Koskella B. 2013. Experimental coevolution of species interactions. Trends Ecol Evol 28:367–375.